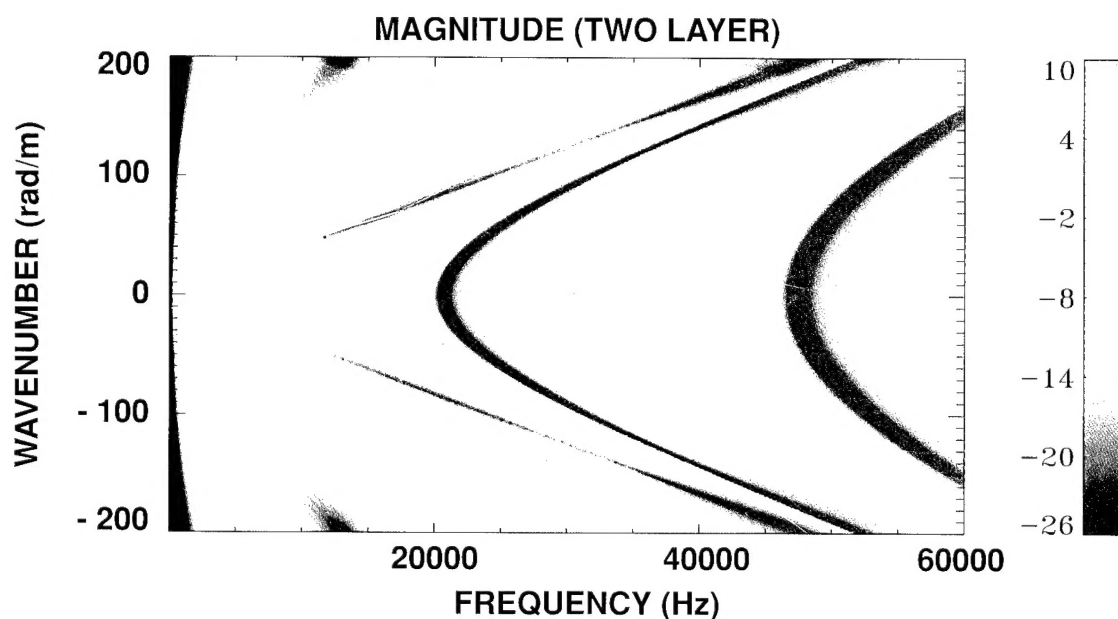


A Closed-Form Dynamic Elasticity Solution to the Fluid/Structure Interaction Problem of a Two-Layer Infinite Viscoelastic Cylinder With Inner and Outer Fluid Loading Subject to Forced Harmonic Excitation

Mark S. Peloquin
Submarine Sonar Department



19960702 076

Naval Undersea Warfare Center Division
Newport, Rhode Island

PREFACE

The research presented in this report was sponsored by the Technology Directorate of the Office of Naval Research (ONR), Program Element 0602314N. The ONR Program Manager for Sensors, Sources, and Arrays is K. G. Dial (ONR 321SS).

The technical reviewer for this report was Dr. Andrew J. Hull (Code 2141) of NUWC Detachment New London.

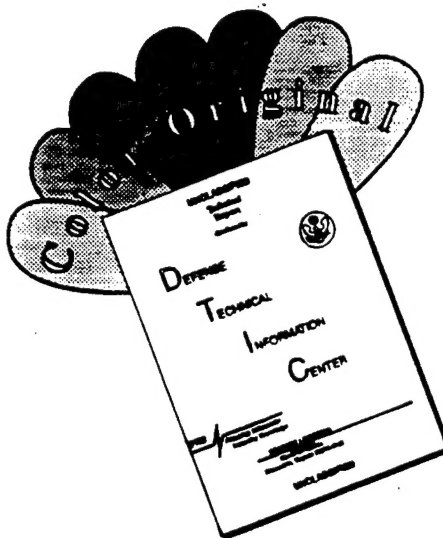
The author gratefully acknowledges Dr. Hull for his careful review of the manuscript. Appreciation is also extended to Karen Holt (Code 5131) of NUWC Detachment New London for her meticulous technical editing.

REVIEWED AND APPROVED: 29 December 1995

A handwritten signature in dark ink, appearing to read 'R. J. Martin', is centered on the page. The signature is fluid and cursive, with the first letters of the first and last names being capitalized and prominent.

R. J. Martin
Acting Head, Submarine Sonar Department

DISCLAIMER NOTICE



THIS DOCUMENT IS BEST QUALITY AVAILABLE. THE COPY FURNISHED TO DTIC CONTAINED A SIGNIFICANT NUMBER OF COLOR PAGES WHICH DO NOT REPRODUCE LEGIBLY ON BLACK AND WHITE MICROFICHE.

REPORT DOCUMENTATION PAGE

Form Approved
OMB No. 0704-0188

Public reporting burden for this collection of information is estimated to average 1 hour per response, including the time for reviewing instructions, searching existing data sources, gathering and maintaining the data needed, and completing and reviewing the collection of information. Send comments regarding this burden estimate or any other aspect of this collection of information, including suggestions for reducing this burden, to Washington Headquarters Services, Directorate for Information Operations and Reports, 1215 Jefferson Davis Highway, Suite 1204, Arlington, VA 22202-4302, and to the Office of Management and Budget, Paperwork Reduction Project (0704-0188), Washington, DC 20503.

1. AGENCY USE ONLY (Leave Blank)		2. REPORT DATE 29 December 1995	3. REPORT TYPE AND DATES COVERED Final	
4. TITLE AND SUBTITLE A Closed-Form Dynamic Elasticity Solution to the Fluid/Structure Interaction Problem of a Two-Layer Infinite Viscoelastic Cylinder With Inner and Outer Fluid Loading Subject to Forced Harmonic Excitation			5. FUNDING NUMBERS PE 0602314N	
6. AUTHOR(S) Mark S. Peloquin				
7. PERFORMING ORGANIZATION NAME(S) AND ADDRESS(ES) Naval Undersea Warfare Center Detachment New London New London, Connecticut 06320			8. PERFORMING ORGANIZATION REPORT NUMBER TR 11,067	
9. SPONSORING/MONITORING AGENCY NAME(S) AND ADDRESS(ES) Office of Naval Research 800 North Quincy Street Arlington, VA 22217-5000			10. SPONSORING/MONITORING AGENCY REPORT NUMBER	
11. SUPPLEMENTARY NOTES				
12a. DISTRIBUTION/AVAILABILITY STATEMENT Approved for public release; distribution is unlimited. DTIC QUALITY INSPECTED 4			12b. DISTRIBUTION CODE	
13. ABSTRACT (Maximum 200 words) <p>This report documents an exact closed-form solution to the problem of a two-layer viscoelastic solid infinite cylinder that is immersed in an infinite ideal inviscid fluid and contains an infinite ideal inviscid fluid within its diameter. The viscoelasticity is modeled with structural damping, which is incorporated by the use of a complex modulus of elasticity. The composite system is subject to forced harmonic vibration at the outer solid/fluid interface. The response to both nonaxisymmetric (described in terms of circumferential order number n) and axisymmetric excitations is derived. The problem is resolved with a three-dimensional dynamic elasticity solution.</p> <p>Simulations of the transfer surfaces for the interior pressure field are performed for radial excitation P_o and longitudinal excitation P_x applied to a single-layer cylinder for $n = 0, 1$, and 2. The circumferential excitation P_θ is applied to the single-layer cylinder for interior pressure simulation with $n = 1$ and 2. Simulations of the circumferential strain are performed for excitations P_o and P_x applied to a two-layer cylinder for $n = 0$. Additionally, the P_o excitation is applied to the two-layer cylinder for $n = 0, 1$, and 2, resulting in simulations for the pressure field in the inner fluid. Simulations are displayed as response transfer surfaces in the longitudinal wavenumber-frequency plane.</p> <p>Comparisons are made between the elasticity models derived in this report and the membrane and bending</p>				
14. SUBJECT TERMS Closed- Form Solution, Dynamic Elasticity Model, Fluid Loading, Fluid/Structure Interaction, Forced Excitation, Infinite Cylinder, Inviscid Fluid, Viscoelastic, Wave Propagation			15. NUMBER OF PAGES 274	
			16. PRICE CODE	
17. SECURITY CLASSIFICATION OF REPORT UNCLASSIFIED	18. SECURITY CLASSIFICATION OF THIS PAGE UNCLASSIFIED	19. SECURITY CLASSIFICATION OF ABSTRACT UNCLASSIFIED	20. LIMITATION OF ABSTRACT SAR	

13. ABSTRACT (Cont'd)

shell models from previous work. The nulls occurring in the interior pressure field at higher frequencies are explored as well as the resonances relating to the thickness of the cylinder.

The two-layer cylinder simulations show that the sensitivity of circumferential strain to longitudinal shear stress is approximately 0 to 40 dB greater than the sensitivity to normal pressure excitation. These simulations also show that the sensitivity of circumferential strain to longitudinal shear stress decreases with increasing frequency, while the sensitivity to normal pressure excitation remains relatively flat with increasing frequency. Such is the case below the first radial resonance frequency of the cylinder.

TABLE OF CONTENTS

	Page
LIST OF ILLUSTRATIONS	v
LIST OF TABLES	xxv
LIST OF SYMBOLS	xxvii
INTRODUCTION	1
THE PHYSICAL MODEL	3
EQUATIONS OF MOTION	5
Displacement Potentials	5
Displacement Potential Summary for Cylinders 1 and 2	9
Particle Displacement/Displacement Potential	10
Stress/Displacement Equations	10
Strain/Displacement Equations	11
Stress, Strain, and Displacements in Terms of Displacement Potential Equations	12
OUTER FLUID	15
INNER FLUID	21
SINGLE-LAYER CYLINDER/FLUID INTERFACES	25
Boundary Conditions	25
System Matrix	30
TWO-LAYER CYLINDER/FLUID INTERFACES	37
Boundary Conditions	37
System Matrix	41
SOLUTION METHODOLOGY	55
Numerical Considerations	55
RESULTS	57
Single-Layer Cylinder Simulations—Radial Pressure Excitations	57
Types of Wave Propagation	57
Cylinder and Fluid Material Properties	58
Circumferential Order Shapes	60
Radial Stress Variation in the Cylinder Wall	63

TABLE OF CONTENTS (CONT'D)

	Page
Model Comparisons—3.00-Inch-Diameter Cylinder	67
Model Comparisons—0.670-Inch-Diameter Cylinder	91
Inner Fluid Pressure Field Evanescence	114
Inner Fluid Density Variation.....	120
High-Frequency Response	127
Elasticity and Bending Shell Model Comparison.....	127
Inner Fluid Pressure Field Nulls	131
Cylinder With Inner and Outer Fluids of Air—Wall Thickness Variation.....	136
Cylinder With Inner and Outer Fluids of Air—Young's Modulus Variation.....	140
Cylinder With Inner and Outer Fluids of Water—Wall Thickness Variation.....	144
Cylinder With Inner and Outer Fluids of Water—Stress and Displacements	147
Single-Layer Cylinder Simulations—Longitudinal Shear Stress Excitation	157
Single-Layer Cylinder Simulations—Circumferential Shear Stress Excitation	166
Two-Layer Cylinder Simulations.....	173
Radial Pressure Excitation	175
Longitudinal and Radial Displacements	191
Longitudinal Shear Stress Excitation.....	198
Comparison of Radial Pressure and Longitudinal Shear Stress Excitations.....	209
CONCLUSIONS AND RECOMMENDATIONS.....	217
Single-Layer Summary	217
Two-Layer Summary	220
REFERENCES	221
APPENDIX A - Bessel Functions of Complex Argument, Series Representation.....	A-1

TABLE OF CONTENTS (CONT'D)

	Page
APPENDIX B - Derivatives of Bessel Functions.....	B-1
APPENDIX C - Output Quantity Equations.....	C-1
APPENDIX D - Two-Layer Model Verification.....	D-1

LIST OF ILLUSTRATIONS

Figure		Page
1	Physical Model Diagram.....	3
2	Outer Fluid Propagating and Nonpropagating Regions of the Wavenumber-Frequency Plane	18
3	Relationship Between Cylinder Vibration and Radiated Pressure p_s	19
4	Inner Fluid Propagating and Nonpropagating Regions of the Wavenumber-Frequency Plane	24
5	Boundary Conditions for Single-Layer Infinite Cylinder and Fluids	27
6	Boundary Conditions for Two-Layer Infinite Cylinder and Fluids	40
7	Circumferential Order Number $n = 0$, First Branch.....	61
8	Circumferential Order Number $n = 0$, Second Branch	61
9	Circumferential Order Number $n = 1$, First Branch.....	62
10	Circumferential Order Number $n = 2$, First Branch.....	62
11	Radial Stress Transfer Surface With Magnitude = $10\text{Log}(\tau_{rr}(r_1)/P_o)^2$ at $r_1 = 1.49$ in. for Elasticity Model, Where $n = 0$ and Diameter = 3.00 in.....	64
12	Radial Stress Transfer Surface With Magnitude = $10\text{Log}(\tau_{rr}(r_1)/P_o)^2$ at $r_1 = 1.35$ in. for Elasticity Model, Where $n = 0$ and Diameter = 3.00 in.....	64
13	Radial Stress Transfer Surface With Magnitude = $10\text{Log}(\tau_{rr}(r_1)/P_o)^2$ at $r_1 = 1.21$ in. for Elasticity Model, Where $n = 0$ and Diameter = 3.00 in.....	64
14	Comparison of Radial Stress Transfer Surfaces With Magnitude = $10\text{Log}(\tau_{rr}(r_1)/P_o)^2$ at Various r for Elasticity Model, Where $n = 0$, Diameter = 3.00 in., and $f = 200$ Hz.....	65
15	Comparison of Radial Stress Transfer Surfaces With Magnitude = $10\text{Log}(\tau_{rr}(r_1)/P_o)^2$ for Elasticity Model, Where $n = 0$, Diameter = 3.00 in., and $k = 0$ rad/m	66

LIST OF ILLUSTRATIONS (CONT'D)

Figure		Page
16	Pressure Transfer Surface With Magnitude = $10\text{Log}(P_i(r_1)/P_o)^2$ at $r_1 = 0.75$ in. for Membrane Shell Model, Where $n = 0$ and Diameter = 3.00 in. (Color Image).....	70
17	Pressure Transfer Surface With Magnitude = $10\text{Log}(P_i(r_1)/P_o)^2$ at $r_1 = 0.75$ in. for Membrane Shell Model, Where $n = 0$ and Diameter = 3.00 in. (Wire Frame Surface).....	70
18	Pressure Transfer Surface With Magnitude = $10\text{Log}(P_i(r_1)/P_o)^2$ at $r_1 = 0.75$ in. for Bending Shell Model, Where $n = 0$ and Diameter = 3.00 in. (Color Image).....	71
19	Pressure Transfer Surface With Magnitude = $10\text{Log}(P_i(r_1)/P_o)^2$ at $r_1 = 0.75$ in. for Bending Shell Model, Where $n = 0$ and Diameter = 3.00 in. (Wire Frame Surface).....	71
20	Pressure Transfer Surface With Magnitude = $10\text{Log}(P_i(r_1)/P_o)^2$ at $r_1 = 0.75$ in. for Elasticity Model, Where $n = 0$ and Diameter = 3.00 in. (Color Image).....	72
21	Pressure Transfer Surface With Magnitude = $10\text{Log}(P_i(r_1)/P_o)^2$ at $r_1 = 0.75$ in. for Elasticity Model, Where $n = 0$ and Diameter = 3.00 in. (Wire Frame Surface).....	72
22	Model Comparison for Figures 16, 18, and 20 at Extended Frequency Range When Magnitude = $10\text{Log}(P_i(r_1)/P_o)^2$ at $r_1 = 0.75$ in. With $n = 0$, Diameter = 3.00 in., and $k = 0$ rad/m	73
23	Model Comparison for Figures 16, 18, and 20 When Magnitude = $10\text{Log}(P_i(r_1)/P_o)^2$ at $r_1 = 0.75$ in. With $n = 0$, Diameter = 3.00 in., and $f = 200$ Hz	74
24	Model Comparison for Figures 16, 18, and 20 When Magnitude = $10\text{Log}(P_i(r_1)/P_o)^2$ at $r_1 = 0.75$ in. With $n = 0$, Diameter = 3.00 in., and $f = 600$ Hz	75
25	Model Comparison for Figures 16, 18, and 20 When Magnitude = $10\text{Log}(P_i(r_1)/P_o)^2$ at $r_1 = 0.75$ in. With $n = 0$, Diameter = 3.00 in., and $f = 4500$ Hz	76

LIST OF ILLUSTRATIONS (CONT'D)

Figure		Page
26	Pressure Transfer Surface With Magnitude = $10\text{Log}(P_i(r_1)/P_o)^2$ at $r_1 = 0.75$ in. for Membrane Shell Model, Where $n = 1$ and Diameter = 3.00 in. (Color Image).....	77
27	Pressure Transfer Surface With Magnitude = $10\text{Log}(P_i(r_1)/P_o)^2$ at $r_1 = 0.75$ in. for Membrane Shell Model, Where $n = 1$ and Diameter = 3.00 in. (Wire Frame Surface).....	77
28	Pressure Transfer Surface With Magnitude = $10\text{Log}(P_i(r_1)/P_o)^2$ at $r_1 = 0.75$ in. for Bending Shell Model, Where $n = 1$ and Diameter = 3.00 in. (Color Image).....	78
29	Pressure Transfer Surface With Magnitude = $10\text{Log}(P_i(r_1)/P_o)^2$ at $r_1 = 0.75$ in. for Bending Shell Model, Where $n = 1$ and Diameter = 3.00 in. (Wire Frame Surface).....	78
30	Pressure Transfer Surface With Magnitude = $10\text{Log}(P_i(r_1)/P_o)^2$ at $r_1 = 0.75$ in. for Elasticity Model, Where $n = 1$ and Diameter = 3.00 in. (Color Image).....	79
31	Pressure Transfer Surface With Magnitude = $10\text{Log}(P_i(r_1)/P_o)^2$ at $r_1 = 0.75$ in. for Elasticity Model, Where $n = 1$ and Diameter = 3.00 in. (Wire Frame Surface).....	79
32	Model Comparison for Figures 26, 28, and 30 When Magnitude = $10\text{Log}(P_i(r_1)/P_o)^2$ at $r_1 = 0.75$ in. With $n = 1$, Diameter = 3.00 in., and $k = 0$ rad/m	80
33	Model Comparison for Figures 26, 28, and 30 When Magnitude = $10\text{Log}(P_i(r_1)/P_o)^2$ at $r_1 = 0.75$ in. With $n = 1$, Diameter = 3.00 in., and $f = 200$ Hz	81
34	Model Comparison for Figures 26, 28, and 30 When Magnitude = $10\text{Log}(P_i(r_1)/P_o)^2$ at $r_1 = 0.75$ in. With $n = 1$, Diameter = 3.00 in., and $f = 600$ Hz	82
35	Model Comparison for Figures 26, 28, and 30 When Magnitude = $10\text{Log}(P_i(r_1)/P_o)^2$ at $r_1 = 0.75$ in. With $n = 1$, Diameter = 3.00 in., and $f = 4500$ Hz	83

LIST OF ILLUSTRATIONS (CONT'D)

Figure		Page
36	Pressure Transfer Surface With Magnitude = $10\text{Log}(P_i(r_1)/P_o)^2$ at $r_1 = 0.75$ in. for Membrane Shell Model, Where $n = 2$ and Diameter = 3.00 in. (Color Image).....	84
37	Pressure Transfer Surface With Magnitude = $10\text{Log}(P_i(r_1)/P_o)^2$ at $r_1 = 0.75$ in. for Membrane Shell Model, Where $n = 2$ and Diameter = 3.00 in. (Wire Frame Surface).....	84
38	Pressure Transfer Surface With Magnitude = $10\text{Log}(P_i(r_1)/P_o)^2$ at $r_1 = 0.75$ in. for Bending Shell Model, Where $n = 2$ and Diameter = 3.00 in. (Color Image).....	85
39	Pressure Transfer Surface With Magnitude = $10\text{Log}(P_i(r_1)/P_o)^2$ at $r_1 = 0.75$ in. for Bending Shell Model, Where $n = 2$ and Diameter = 3.00 in. (Wire Frame Surface).....	85
40	Pressure Transfer Surface With Magnitude = $10\text{Log}(P_i(r_1)/P_o)^2$ at $r_1 = 0.75$ in. for Elasticity Model, Where $n = 2$ and Diameter = 3.00 in. (Color Image).....	86
41	Pressure Transfer Surface With Magnitude = $10\text{Log}(P_i(r_1)/P_o)^2$ at $r_1 = 0.75$ in. for Elasticity Model, Where $n = 2$ and Diameter = 3.00 in. (Wire Frame Surface).....	86
42	Model Comparison for Figures 36, 38, and 40 When Magnitude = $10\text{Log}(P_i(r_1)/P_o)^2$ at $r_1 = 0.75$ in. With $n = 2$, Diameter = 3.00 in., and $k = 0$ rad/m	87
43	Model Comparison for Figures 36, 38, and 40 When Magnitude = $10\text{Log}(P_i(r_1)/P_o)^2$ at $r_1 = 0.75$ in. With $n = 2$, Diameter = 3.00 in., and $f = 200$ Hz	88
44	Model Comparison for Figures 36, 38, and 40 When Magnitude = $10\text{Log}(P_i(r_1)/P_o)^2$ at $r_1 = 0.75$ in. With $n = 2$, Diameter = 3.00 in., and $f = 600$ Hz	89
45	Model Comparison for Figures 36, 38, and 40 When Magnitude = $10\text{Log}(P_i(r_1)/P_o)^2$ at $r_1 = 0.75$ in. With $n = 2$, Diameter = 3.00 in., and $f = 4500$ Hz	90

LIST OF ILLUSTRATIONS (CONT'D)

Figure		Page
46	Pressure Transfer Surface With Magnitude = $10\text{Log}(P_i(r_1)/P_o)^2$ at $r_1 = 0.1$ in. for Membrane Shell Model, Where $n = 0$ and Diameter = 0.670 in. (Color Image).....	93
47	Pressure Transfer Surface With Magnitude = $10\text{Log}(P_i(r_1)/P_o)^2$ at $r_1 = 0.1$ in. for Membrane Shell Model, Where $n = 0$ and Diameter = 0.670 in. (Wire Frame Surface).....	93
48	Pressure Transfer Surface With Magnitude = $10\text{Log}(P_i(r_1)/P_o)^2$ at $r_1 = 0.1$ in. for Bending Shell Model, Where $n = 0$ and Diameter = 0.670 in. (Color Image).....	94
49	Pressure Transfer Surface With Magnitude = $10\text{Log}(P_i(r_1)/P_o)^2$ at $r_1 = 0.1$ in. for Bending Shell Model, Where $n = 0$ and Diameter = 0.670 in. (Wire Frame Surface).....	94
50	Pressure Transfer Surface With Magnitude = $10\text{Log}(P_i(r_1)/P_o)^2$ at $r_1 = 0.1$ in. for Elasticity Model, Where $n = 0$ and Diameter = 0.670 in. (Color Image).....	95
51	Pressure Transfer Surface With Magnitude = $10\text{Log}(P_i(r_1)/P_o)^2$ at $r_1 = 0.1$ in. for Elasticity Model, Where $n = 0$ and Diameter = 0.670 in. (Wire Frame Surface).....	95
52	Model Comparison for Figures 46, 48, and 50 at Extended Frequency Range When Magnitude = $10\text{Log}(P_i(r_1)/P_o)^2$ at $r_1 = 0.1$ in. With $n = 0$, Diameter = 0.670 in., and $k = 0$ rad/m	96
53	Model Comparison for Figures 46, 48, and 50 When Magnitude = $10\text{Log}(P_i(r_1)/P_o)^2$ at $r_1 = 0.1$ in. With $n = 0$, Diameter = 0.670 in., and $f = 200$ Hz	97
54	Model Comparison for Figures 46, 48, and 50 When Magnitude = $10\text{Log}(P_i(r_1)/P_o)^2$ at $r_1 = 0.1$ in. With $n = 0$, Diameter = 0.670 in., and $f = 600$ Hz	98
55	Model Comparison for Figures 46, 48, and 50 When Magnitude = $10\text{Log}(P_i(r_1)/P_o)^2$ at $r_1 = 0.1$ in. With $n = 0$, Diameter = 0.670 in., and $f = 4500$ Hz	99

LIST OF ILLUSTRATIONS (CONT'D)

Figure		Page
56	Pressure Transfer Surface With Magnitude = $10\text{Log}(P_i(r_1)/P_o)^2$ at $r_1 = 0.1$ in. for Membrane Shell Model, Where $n = 1$ and Diameter = 0.670 in. (Color Image).....	100
57	Pressure Transfer Surface With Magnitude = $10\text{Log}(P_i(r_1)/P_o)^2$ at $r_1 = 0.1$ in. for Membrane Shell Model, Where $n = 1$ and Diameter = 0.670 in. (Wire Frame Surface).....	100
58	Pressure Transfer Surface With Magnitude = $10\text{Log}(P_i(r_1)/P_o)^2$ at $r_1 = 0.1$ in. for Bending Shell Model, Where $n = 1$ and Diameter = 0.670 in. (Color Image).....	101
59	Pressure Transfer Surface With Magnitude = $10\text{Log}(P_i(r_1)/P_o)^2$ at $r_1 = 0.1$ in. for Bending Shell Model, Where $n = 1$ and Diameter = 0.670 in. (Wire Frame Surface).....	101
60	Pressure Transfer Surface With Magnitude = $10\text{Log}(P_i(r_1)/P_o)^2$ at $r_1 = 0.1$ in. for Elasticity Model, Where $n = 1$ and Diameter = 0.670 in. (Color Image).....	102
61	Pressure Transfer Surface With Magnitude = $10\text{Log}(P_i(r_1)/P_o)^2$ at $r_1 = 0.1$ in. for Elasticity Model, Where $n = 1$ and Diameter = 0.670 in. (Wire Frame Surface).....	102
62	Model Comparison for Figures 56, 58, and 60 When Magnitude = $10\text{Log}(P_i(r_1)/P_o)^2$ at $r_1 = 0.1$ in. With $n = 1$, Diameter = 0.670 in., and $k = 0$ rad/m	103
63	Model Comparison for Figures 56, 58, and 60 When Magnitude = $10\text{Log}(P_i(r_1)/P_o)^2$ at $r_1 = 0.1$ in. With $n = 1$, Diameter = 0.670 in., and $f = 200$ Hz	104
64	Model Comparison for Figures 56, 58, and 60 When Magnitude = $10\text{Log}(P_i(r_1)/P_o)^2$ at $r_1 = 0.1$ in. With $n = 1$, Diameter = 0.670 in., and $f = 600$ Hz	105
65	Model Comparison for Figures 56, 58, and 60 When Magnitude = $10\text{Log}(P_i(r_1)/P_o)^2$ at $r_1 = 0.1$ in. With $n = 1$, Diameter = 0.670 in., and $f = 4500$ Hz	106

LIST OF ILLUSTRATIONS (CONT'D)

Figure		Page
66	Pressure Transfer Surface With Magnitude = $10\text{Log}(P_i(r_1)/P_o)^2$ at $r_1 = 0.1$ in. for Membrane Shell Model, Where $n = 2$ and Diameter = 0.670 in. (Color Image).....	107
67	Pressure Transfer Surface With Magnitude = $10\text{Log}(P_i(r_1)/P_o)^2$ at $r_1 = 0.1$ in. for Membrane Shell Model, Where $n = 2$ and Diameter = 0.670 in. (Wire Frame Surface).....	107
68	Pressure Transfer Surface With Magnitude = $10\text{Log}(P_i(r_1)/P_o)^2$ at $r_1 = 0.1$ in. for Bending Shell Model, Where $n = 2$ and Diameter = 0.670 in. (Color Image).....	108
69	Pressure Transfer Surface With Magnitude = $10\text{Log}(P_i(r_1)/P_o)^2$ at $r_1 = 0.1$ in. for Bending Shell Model, Where $n = 2$ and Diameter = 0.670 in. (Wire Frame Surface).....	108
70	Pressure Transfer Surface With Magnitude = $10\text{Log}(P_i(r_1)/P_o)^2$ at $r_1 = 0.1$ in. for Elasticity Model, Where $n = 2$ and Diameter = 0.670 in. (Color Image).....	109
71	Pressure Transfer Surface With Magnitude = $10\text{Log}(P_i(r_1)/P_o)^2$ at $r_1 = 0.1$ in. for Elasticity Model, Where $n = 2$ and Diameter = 0.670 in. (Wire Frame Surface).....	109
72	Model Comparison for Figures 66, 68, and 70 When Magnitude = $10\text{Log}(P_i(r_1)/P_o)^2$ at $r_1 = 0.1$ in. With $n = 2$, Diameter = 0.670 in., and $k = 0$ rad/m	110
73	Model Comparison for Figures 66, 68, and 70 When Magnitude = $10\text{Log}(P_i(r_1)/P_o)^2$ at $r_1 = 0.1$ in. With $n = 2$, Diameter = 0.670 in., and $f = 200$ Hz	111
74	Model Comparison for Figures 66, 68, and 70 When Magnitude = $10\text{Log}(P_i(r_1)/P_o)^2$ at $r_1 = 0.1$ in. With $n = 2$, Diameter = 0.670 in., and $f = 600$ Hz	112
75	Model Comparison for Figures 66, 68, and 70 When Magnitude = $10\text{Log}(P_i(r_1)/P_o)^2$ at $r_1 = 0.1$ in. With $n = 2$, Diameter = 0.670 in., and $f = 4500$ Hz	113

LIST OF ILLUSTRATIONS (CONT'D)

Figure		Page
76	Pressure Transfer Surface With Magnitude = $10\text{Log}(P_i(r_1)/P_o)^2$ at $r_1 = 1.1$ in. Where $n = 0$ and Diameter = 3.00 in. for Field Decay Comparison (Color Image).....	115
77	Pressure Transfer Surface With Magnitude = $10\text{Log}(P_i(r_1)/P_o)^2$ at $r_1 = 1.1$ in. Where $n = 0$ and Diameter = 3.00 in. for Field Decay Comparison (Wire Frame Surface).....	115
78	Pressure Transfer Surface With Magnitude = $10\text{Log}(P_i(r_1)/P_o)^2$ at $r_1 = 0.01$ in. Where $n = 0$ and Diameter = 3.00 in. for Field Decay Comparison (Color Image).....	116
79	Pressure Transfer Surface With Magnitude = $10\text{Log}(P_i(r_1)/P_o)^2$ at $r_1 = 0.01$ in. Where $n = 0$ and Diameter = 3.00 in. for Field Decay Comparison (Wire Frame Surface).....	116
80	Field Decay Comparison for Figures 76 and 78 When Magnitude = $10\text{Log}(P_i(r_1)/P_o)^2$ at Various r_1 With $n = 0$, Diameter = 3.00 in., and $f = 300$ Hz	117
81	Field Decay Comparison for Figures 76 and 78 When Magnitude = $10\text{Log}(P_i(r_1)/P_o)^2$ at Various r_1 With $n = 0$, Diameter = 3.00 in., and $f = 900$ Hz	118
82	Field Decay Comparison for Figures 76 and 78 When Magnitude = $10\text{Log}(P_i(r_1)/P_o)^2$ at Various r_1 With $n = 0$, Diameter = 3.00 in., and $f = 4500$ Hz	119
83	Pressure Transfer Surface With Magnitude = $10\text{Log}(P_i(r_1)/P_o)^2$ at $r_1 = 0.01$ in. for $\rho_i = 500$ kg/m ³ , $n = 0$, and Diameter = 3.00 in. (Color Image)	121
84	Pressure Transfer Surface With Magnitude = $10\text{Log}(P_i(r_1)/P_o)^2$ at $r_1 = 0.01$ in. for $\rho_i = 1000$ kg/m ³ , $n = 0$, and Diameter = 3.00 in. (Color Image)	121
85	Pressure Transfer Surface With Magnitude = $10\text{Log}(P_i(r_1)/P_o)^2$ at $r_1 = 0.01$ in. for $\rho_i = 2000$ kg/m ³ , $n = 0$, and Diameter = 3.00 in. (Color Image)	122
86	Effect of Inner Fluid Density When Magnitude = $10\text{Log}(P_i(r_1)/P_o)^2$ at $r_1 = 0.01$ in. for $n = 0$, Diameter = 3.00 in., and $k = 0$ rad/m	123

LIST OF ILLUSTRATIONS (CONT'D)

Figure		Page
87	Effect of Inner Fluid Density When Magnitude = $10\text{Log}(P_i(r_1)/P_o)^2$ at $r_1 = 0.01$ in. for $n = 0$, Diameter = 3.00 in., and $f = 300$ Hz	124
88	Effect of Inner Fluid Density When Magnitude = $10\text{Log}(P_i(r_1)/P_o)^2$ at $r_1 = 0.01$ in. for $n = 0$, Diameter = 3.00 in., and $f = 3000$ Hz	125
89	Effect of Inner Fluid Density When Magnitude = $10\text{Log}(P_i(r_1)/P_o)^2$ at $r_1 = 0.01$ in. for $n = 0$, Diameter = 3.00 in., and $f = 4500$ Hz	126
90	Pressure Transfer Surface Up to 60 kHz When Magnitude = $10\text{Log}(P_i(r_1)/P_o)^2$ at $r_1 = 1.1$ in. for Bending Shell Model, Where $n = 0$ and Diameter = 3.00 in. (Color Image).....	128
91	Pressure Transfer Surface Up to 60 kHz When Magnitude = $10\text{Log}(P_i(r_1)/P_o)^2$ at $r_1 = 1.1$ in. for Bending Shell Model, Where $n = 0$ and Diameter = 3.00 in. (Wire Frame Surface).....	128
92	Pressure Transfer Surface Up to 60 kHz When Magnitude = $10\text{Log}(P_i(r_1)/P_o)^2$ at $r_1 = 1.1$ in. for Elasticity Model, Where $n = 0$ and Diameter = 3.00 in. (Color Image).....	129
93	Pressure Transfer Surface Up to 60 kHz When Magnitude = $10\text{Log}(P_i(r_1)/P_o)^2$ at $r_1 = 1.1$ in. for Elasticity Model, Where $n = 0$ and Diameter = 3.00 in. (Wire Frame Surface).....	129
94	Model Comparison Up to 60 kHz for Figures 90 and 92 When Magnitude = $10\text{Log}(P_i(r_1)/P_o)^2$ at $r_1 = 1.1$ in. With $n = 0$, Diameter = 3.00 in., and $k = 0$ rad/m	130
95	Pressure Transfer Surface Up to 60 kHz When Magnitude = $10\text{Log}(P_i(r_1)/P_o)^2$ at $r_1 = 0.55$ in. With $n = 0$ and Diameter = 3.00 in. (Color Image)	133
96	Pressure Transfer Surface Up to 60 kHz When Magnitude = $10\text{Log}(P_i(r_1)/P_o)^2$ at $r_1 = 0.55$ in. With $n = 0$ and Diameter = 3.00 in. (Wire Frame Surface)	133
97	Pressure Transfer Surface Up to 60 kHz When Magnitude = $10\text{Log}(P_i(r_1)/P_o)^2$ at $r_1 = 0.01$ in. With $n = 0$ and Diameter = 3.00 in. (Color Image)	134

LIST OF ILLUSTRATIONS (CONT'D)

Figure		Page
98	Pressure Transfer Surface Up to 60 kHz When Magnitude = $10\text{Log}(P_i(r_1)/P_o)^2$ at $r_1 = 0.01$ in. With $n = 0$ and Diameter = 3.00 in. (Wire Frame Surface)	134
99	Comparison of Inner Fluid Pressure Field for Figures 92, 95, and 97 When Magnitude = $10\text{Log}(P_i(r_1)/P_o)^2$ at Various r_1 With $n = 0$, Diameter = 3.00 in., and $k = 0$ rad/m	135
100	Radial Stress Transfer Surface Up to 60 kHz When Magnitude = $10\text{Log}(\tau_{rr}^{C1}(r_1)/P_o)^2$ at $r_1 = 1.21$ in. With $h_1 = 0.3$ in., $n = 0$, and Diameter = 3.00 in. (Color Image).....	138
101	Radial Stress Transfer Surface Up to 60 kHz When Magnitude = $10\text{Log}(\tau_{rr}^{C1}(r_1)/P_o)^2$ at $r_1 = 1.21$ in. With $h_1 = 0.6$ in., $n = 0$, and Diameter = 3.00 in. (Color Image).....	138
102	Effect of Variation of Wall Thickness on the Cylinder Response for Figures 100 and 101 When Magnitude = $10\text{Log}(\tau_{rr}^{C1}(r_1)/P_o)^2$ at $r_1 = 1.21$ in. With $n = 0$, Diameter = 3.00 in., and $k = 0$ rad/m.....	139
103	Radial Stress Transfer Surface Up to 60 kHz When Magnitude = $10\text{Log}(\tau_{rr}^{C1}(r_1)/P_o)^2$ at $r_1 = 1.21$ in. With $E_1 = 1 \times 10^9$ Pa, $h_1 = 0.6$ in., $n = 0$, and Diameter = 3.00 in. (Color Image)	142
104	Radial Stress Transfer Surface Up to 60 kHz When Magnitude = $10\text{Log}(\tau_{rr}^{C1}(r_1)/P_o)^2$ at $r_1 = 1.21$ in. With $E_1 = 1 \times 10^8$ Pa, $h_1 = 0.6$ in., $n = 0$, and Diameter = 3.00 in. (Color Image)	142
105	Effect of Variation of Young's Modulus on the Cylinder Response for Figures 103 and 104 When Magnitude = $10\text{Log}(\tau_{rr}^{C1}(r_1)/P_o)^2$ at $r_1 = 1.21$ in. With $n = 0$, Diameter = 3.00 in., and $k = 0$ rad/m	143
106	Pressure Transfer Surface Up to 60 kHz When Magnitude = $10\text{Log}(P_i(r_1)/P_o)^2$ at $r_1 = 0.01$ in. With $h_1 = 0.3$ in., $n = 0$, and Diameter = 3.00 in. (Color Image).....	145
107	Pressure Transfer Surface Up to 60 kHz When Magnitude = $10\text{Log}(P_i(r_1)/P_o)^2$ at $r_1 = 0.01$ in. With $h_1 = 0.6$ in., $n = 0$, and Diameter = 3.00 in. (Color Image).....	145

LIST OF ILLUSTRATIONS (CONT'D)

Figure		Page
108	Effect of Variation of Wall Thickness on the Cylinder Response for Figures 106 and 107 When Magnitude = $10\text{Log}(P_i(r_1)/P_o)^2$ at $r_1 = 0.01$ in. With $n = 0$, Diameter = 3.00 in., and $k = 0$ rad/m	146
109	Radial Stress Transfer Surface Up to 60 kHz When Magnitude = $10\text{Log}(\tau_{rr}^{C1}(r_1)/P_o)^2$ at $r_1 = 1.21$ in. With $n = 0$ and Diameter = 3.00 in. (Color Image)	149
110	Radial Stress Transfer Surface Up to 60 kHz When Magnitude = $10\text{Log}(\tau_{rr}^{C1}(r_1)/P_o)^2$ at $r_1 = 1.21$ in. With $n = 0$ and Diameter = 3.00 in. (Wire Frame Surface)	149
111	Longitudinal Displacement Transfer Surface Up to 60 kHz When Magnitude = $10\text{Log}(w_c^{C1}(r_1)/P_o)^2$ at $r_1 = 1.21$ in. With $n = 0$ and Diameter = 3.00 in. (Color Image).....	150
112	Longitudinal Displacement Transfer Surface Up to 60 kHz When Magnitude = $10\text{Log}(w_c^{C1}(r_1)/P_o)^2$ at $r_1 = 1.21$ in. With $n = 0$ and Diameter = 3.00 in. (Wire Frame Surface).....	150
113	Radial Displacement Transfer Surface Up to 60 kHz When Magnitude = $10\text{Log}(u_c^{C1}(r_1)/P_o)^2$ at $r_1 = 1.21$ in. With $n = 0$ and Diameter = 3.00 in. (Color Image)	151
114	Radial Displacement Transfer Surface Up to 60 kHz When Magnitude = $10\text{Log}(u_c^{C1}(r_1)/P_o)^2$ at $r_1 = 1.21$ in. With $n = 0$ and Diameter = 3.00 in. (Wire Frame Surface)	151
115	Cylinder Displacement Comparison for Figures 111 and 113 When Magnitude = $10\text{Log}(X/P_o)^2$ for Values of $X = w_c^{C1}(r_1)$ and $u_c^{C1}(r_1)$ at $r_1 = 1.21$ in. With $n = 0$, Diameter = 3.00 in., and $f = 2000$ Hz	152
116	Cylinder Displacement Comparison for Figures 111 and 113 When Magnitude = $10\text{Log}(X/P_o)^2$ for Values of $X = w_c^{C1}(r_1)$ and $u_c^{C1}(r_1)$ at $r_1 = 1.21$ in. With $n = 0$, Diameter = 3.00 in., and $f = 10000$ Hz	153
117	Cylinder Displacement Comparison for Figures 111 and 113 When Magnitude = $10\text{Log}(X/P_o)^2$ for Values of $X = w_c^{C1}(r_1)$ and $u_c^{C1}(r_1)$ at $r_1 = 1.21$ in. With $n = 0$, Diameter = 3.00 in., and $k = 50$ rad/m	154

LIST OF ILLUSTRATIONS (CONT'D)

Figure		Page
118	Cylinder Displacement Comparison for Figures 111 and 113 When Magnitude = $10\text{Log}(X/P_o)^2$ for Values of $X = w_c^{C1}(r_1)$ and $u_c^{C1}(r_1)$ at $r_1 = 1.21$ in. With $n = 0$, Diameter = 3.00 in., and $k = 100$ rad/m	155
119	Radial Stress Transfer Surface With Magnitude = $10\text{Log}(\tau_{rr}^{C1}(r_1)/P_o)^2$ at $r_1 = 1.21$ in. With $n = 0$ and Diameter = 3.00 in. (Wire Frame Surface of Figure 13).....	156
120	Pressure Transfer Surface With Magnitude = $10\text{Log}(P_i(r_1)/P_x)^2$ at $r_1 = 0.75$ in. for $n = 0$ and Diameter = 3.00 in. (Color Image)	159
121	Pressure Transfer Surface With Magnitude = $10\text{Log}(P_i(r_1)/P_x)^2$ at $r_1 = 0.75$ in. for $n = 0$ and Diameter = 3.00 in. (Wire Frame Surface)	159
122	Pressure Transfer Surface With Magnitude = $10\text{Log}(P_i(r_1)/P_x)^2$ at $r_1 = 0.75$ in. for $n = 1$ and Diameter = 3.00 in. (Color Image)	160
123	Pressure Transfer Surface With Magnitude = $10\text{Log}(P_i(r_1)/P_x)^2$ at $r_1 = 0.75$ in. for $n = 1$ and Diameter = 3.00 in. (Wire Frame Surface)	160
124	Pressure Transfer Surface With Magnitude = $10\text{Log}(P_i(r_1)/P_x)^2$ at $r_1 = 0.75$ in. for $n = 2$ and Diameter = 3.00 in. (Color Image)	161
125	Pressure Transfer Surface With Magnitude = $10\text{Log}(P_i(r_1)/P_x)^2$ at $r_1 = 0.75$ in. for $n = 2$ and Diameter = 3.00 in. (Wire Frame Surface)	161
126	Comparison of Longitudinal Shear Stress Excitation for Figures 120, 122, and 124 When Magnitude = $10\text{Log}(P_i(r_1)/P_x)^2$ at $r_1 = 0.75$ in. for Various n With Diameter = 3.00 in. and $f = 50$ Hz	162
127	Comparison of Longitudinal Shear Stress Excitation for Figures 120, 122, and 124 When Magnitude = $10\text{Log}(P_i(r_1)/P_x)^2$ at $r_1 = 0.75$ in. for Various n With Diameter = 3.00 in. and $f = 500$ Hz	163
128	Comparison of Longitudinal Shear Stress Excitation for Figures 120, 122, and 124 When Magnitude = $10\text{Log}(P_i(r_1)/P_x)^2$ at $r_1 = 0.75$ in. for Various n With Diameter = 3.00 in. and $f = 2000$ Hz	164

LIST OF ILLUSTRATIONS (CONT'D)

Figure		Page
129	Comparison of Longitudinal Shear Stress Excitation for Figures 120, 122, and 124 When Magnitude = $10\text{Log}(P_i(r_1)/P_x)^2$ at $r_1 = 0.75$ in. for Various n With Diameter = 3.00 in. and $f = 5000$ Hz	165
130	Pressure Transfer Surface With Magnitude = $10\text{Log}(P_i(r_1)/P_\theta)^2$ at $r_1 = 0.75$ in. for $n = 1$ and Diameter = 3.00 in. (Color Image)	167
131	Pressure Transfer Surface With Magnitude = $10\text{Log}(P_i(r_1)/P_\theta)^2$ at $r_1 = 0.75$ in. for $n = 1$ and Diameter = 3.00 in. (Wire Frame Surface)	167
132	Pressure Transfer Surface With Magnitude = $10\text{Log}(P_i(r_1)/P_\theta)^2$ at $r_1 = 0.75$ in. for $n = 2$ and Diameter = 3.00 in. (Color Image)	168
133	Pressure Transfer Surface With Magnitude = $10\text{Log}(P_i(r_1)/P_\theta)^2$ at $r_1 = 0.75$ in. for $n = 2$ and Diameter = 3.00 in. (Wire Frame Surface)	168
134	Comparison of Circumferential Shear Stress Excitation for Figures 130 and 132 When Magnitude = $10\text{Log}(P_i(r_1)/P_\theta)^2$ at $r_1 = 0.75$ in. for Various n With Diameter = 3.00 in. and $f = 50$ Hz	169
135	Comparison of Circumferential Shear Stress Excitation for Figures 130 and 132 When Magnitude = $10\text{Log}(P_i(r_1)/P_\theta)^2$ at $r_1 = 0.75$ in. for Various n With Diameter = 3.00 in. and $f = 500$ Hz	170
136	Comparison of Circumferential Shear Stress Excitation for Figures 130 and 132 When Magnitude = $10\text{Log}(P_i(r_1)/P_\theta)^2$ at $r_1 = 0.75$ in. for Various n With Diameter = 3.00 in. and $f = 2000$ Hz	171
137	Comparison of Circumferential Shear Stress Excitation for Figures 130 and 132 When Magnitude = $10\text{Log}(P_i(r_1)/P_\theta)^2$ at $r_1 = 0.75$ in. for Various n With Diameter = 3.00 in. and $f = 5000$ Hz	172
138	Circumferential Strain Transfer Surface With Magnitude = $10\text{Log}(\epsilon_{\theta\theta}^C(r_1)/P_\theta)^2$ at $r_1 = 0.324$ in. With $n = 0$ and Diameter = 0.650 in. (Color Image)	177

LIST OF ILLUSTRATIONS (CONT'D)

Figure		Page
139	Circumferential Strain Transfer Surface With Magnitude = $10\text{Log}(\epsilon_{\theta\theta}^{C2}(r_1)/P_o)^2$ at $r_1 = 0.324$ in. With $n = 0$ and Diameter = 0.650 in. (Wire Frame Surface)	177
140	Comparison of Circumferential Strain Distribution for Figure 138 When Magnitude = $10\text{Log}(\epsilon_{\theta\theta}^{C2}(r_1)/P_o)^2$ at $r_1 = 0.324$ in. With $n = 0$ and Diameter = 0.650 in.	178
141	Circumferential Strain Transfer Surface With Magnitude = $10\text{Log}(\epsilon_{\theta\theta}^{C1}(r_1)/P_o)^2$ at $r_1 = 0.259$ in. With $n = 0$ and Diameter = 0.650 in. (Color Image)	179
142	Circumferential Strain Transfer Surface With Magnitude = $10\text{Log}(\epsilon_{\theta\theta}^{C1}(r_1)/P_o)^2$ at $r_1 = 0.259$ in. With $n = 0$ and Diameter = 0.650 in. (Wire Frame Surface)	179
143	Comparison of Circumferential Strain Distribution for Figure 141 When Magnitude = $10\text{Log}(\epsilon_{\theta\theta}^{C1}(r_1)/P_o)^2$ at $r_1 = 0.259$ in. With $n = 0$ and Diameter = 0.650 in.	180
144	Circumferential Strain Transfer Surface With Magnitude = $10\text{Log}(\epsilon_{\theta\theta}^{C1}(r_1)/P_o)^2$ at $r_1 = 0.250$ in. With $n = 0$ and Diameter = 0.650 in. (Color Image)	181
145	Circumferential Strain Transfer Surface With Magnitude = $10\text{Log}(\epsilon_{\theta\theta}^{C1}(r_1)/P_o)^2$ at $r_1 = 0.250$ in. With $n = 0$ and Diameter = 0.650 in. (Wire Frame Surface)	181
146	Comparison of Circumferential Strain Distribution for Figure 144 When Magnitude = $10\text{Log}(\epsilon_{\theta\theta}^{C1}(r_1)/P_o)^2$ at $r_1 = 0.250$ in. With $n = 0$ and Diameter = 0.650 in.	182
147	Circumferential Strain Transfer Surface With Magnitude = $10\text{Log}(\epsilon_{\theta\theta}^{C1}(r_1)/P_o)^2$ at $r_1 = 0.161$ in. With $n = 0$ and Diameter = 0.650 in. (Color Image)	183
148	Circumferential Strain Transfer Surface With Magnitude = $10\text{Log}(\epsilon_{\theta\theta}^{C1}(r_1)/P_o)^2$ at $r_1 = 0.161$ in. With $n = 0$ and Diameter = 0.650 in. (Wire Frame Surface)	183
149	Comparison of Circumferential Strain Distribution for Figure 147 When Magnitude = $10\text{Log}(\epsilon_{\theta\theta}^{C1}(r_1)/P_o)^2$ at $r_1 = 0.161$ in. With $n = 0$ and Diameter = 0.650 in.	184

LIST OF ILLUSTRATIONS (CONT'D)

Figure		Page
150	Comparison of Circumferential Strain Distribution for Figures 138, 141, 144, and 147 When Magnitude = $10\text{Log}(\epsilon_{\theta\theta}^{Ci}(r_1)/P_o)^2$ at Various r_1 With $i = 1$ or 2 , $n = 0$, Diameter = 0.650 in., and $k = 0$ rad/m	185
151	Comparison of Circumferential Strain Distribution for Figures 138, 141, 144, and 147 When Magnitude = $10\text{Log}(\epsilon_{\theta\theta}^{Ci}(r_1)/P_o)^2$ at Various r_1 With $i = 1$ or 2 , $n = 0$, Diameter = 0.650 in., and $f = 1000$ Hz	186
152	Comparison of Circumferential Strain Distribution for Figures 138, 141, 144, and 147 When Magnitude = $10\text{Log}(\epsilon_{\theta\theta}^{Ci}(r_1)/P_o)^2$ at Various r_1 With $i = 1$ or 2 , $n = 0$, Diameter = 0.650 in., and $f = 3000$ Hz	187
153	Comparison of Circumferential Strain Distribution for Figures 138, 141, 144, and 147 When Magnitude = $10\text{Log}(\epsilon_{\theta\theta}^{Ci}(r_1)/P_o)^2$ at Various r_1 With $i = 1$ or 2 , $n = 0$, Diameter = 0.650 in., and $f = 6000$ Hz	188
154	Comparison of Circumferential Strain Distribution for Figures 138, 141, 144, and 147 When Magnitude = $10\text{Log}(\epsilon_{\theta\theta}^{Ci}(r_1)/P_o)^2$ at Various r_1 With $i = 1$ or 2 , $n = 0$, Diameter = 0.650 in., and $f = 7500$ Hz	189
155	Attenuation of Circumferential Strain From Figures 138 and 141 When Magnitude = $(10\text{Log}(\epsilon_{\theta\theta}^{C1}(0.259)/P_o)^2$ - $10\text{Log}(\epsilon_{\theta\theta}^{C2}(0.324)/P_o)^2$) at Various f With $n = 0$ and Diameter = 0.650 in.	190
156	Longitudinal Displacement Transfer Surface With Magnitude = $10\text{Log}(w_c^{C1}(r_1)/P_o)^2$ at $r_1 = 0.259$ in. With $n = 0$ and Diameter = 0.650 in. (Color Image)	192
157	Longitudinal Displacement Transfer Surface With Magnitude = $10\text{Log}(w_c^{C1}(r_1)/P_o)^2$ at $r_1 = 0.259$ in. With $n = 0$ and Diameter = 0.650 in. (Wire Frame Surface)	192
158	Radial Displacement Transfer Surface With Magnitude = $10\text{Log}(u_c^{C1}(r_1)/P_o)^2$ at $r_1 = 0.259$ in. With $n = 0$ and Diameter = 0.650 in. (Color Image)	193
159	Radial Displacement Transfer Surface With Magnitude = $10\text{Log}(u_c^{C1}(r_1)/P_o)^2$ at $r_1 = 0.259$ in. With $n = 0$ and Diameter = 0.650 in. (Wire Frame Surface)	193

LIST OF ILLUSTRATIONS (CONT'D)

Figure		Page
160	Comparison of Displacement Distribution for Figures 156 and 158 When Magnitude = $10\text{Log}(X/P_o)^2$ for Values of $X = w_c^{C1}(r_1)$ and $u_c^{C1}(r_1)$ at $r_1 = 0.259$ in. With $n = 0$, Diameter = 0.650 in., and $f = 1000$ Hz	194
161	Comparison of Displacement Distribution for Figures 156 and 158 When Magnitude = $10\text{Log}(X/P_o)^2$ for Values of $X = w_c^{C1}(r_1)$ and $u_c^{C1}(r_1)$ at $r_1 = 0.259$ in. With $n = 0$, Diameter = 0.650 in., and $f = 3000$ Hz	195
162	Comparison of Displacement Distribution for Figures 156 and 158 When Magnitude = $10\text{Log}(X/P_o)^2$ for Values of $X = w_c^{C1}(r_1)$ and $u_c^{C1}(r_1)$ at $r_1 = 0.259$ in. With $n = 0$, Diameter = 0.650 in., and $f = 6000$ Hz	196
163	Comparison of Displacement Distribution for Figures 156 and 158 When Magnitude = $10\text{Log}(X/P_o)^2$ for Values of $X = w_c^{C1}(r_1)$ and $u_c^{C1}(r_1)$ at $r_1 = 0.259$ in. With $n = 0$, Diameter = 0.650 in., and $f = 7500$ Hz	197
164	Circumferential Strain Transfer Surface With Magnitude = $10\text{Log}(\epsilon_{\theta\theta}^{C2}(r_1)/P_x)^2$ at $r_1 = 0.324$ in. With $n = 0$ and Diameter = 0.650 in. (Color Image)	199
165	Circumferential Strain Transfer Surface With Magnitude = $10\text{Log}(\epsilon_{\theta\theta}^{C2}(r_1)/P_x)^2$ at $r_1 = 0.324$ in. With $n = 0$ and Diameter = 0.650 in. (Wire Frame Surface)	199
166	Comparison of Circumferential Strain Distribution for Figure 164 When Magnitude = $10\text{Log}(\epsilon_{\theta\theta}^{C2}(r_1)/P_x)^2$ at $r_1 = 0.324$ in. With $n = 0$ and Diameter = 0.650 in.	200
167	Circumferential Strain Transfer Surface With Magnitude = $10\text{Log}(\epsilon_{\theta\theta}^{C1}(r_1)/P_x)^2$ at $r_1 = 0.259$ in. With $n = 0$ and Diameter = 0.650 in. (Color Image)	201
168	Circumferential Strain Transfer Surface With Magnitude = $10\text{Log}(\epsilon_{\theta\theta}^{C1}(r_1)/P_x)^2$ at $r_1 = 0.259$ in. With $n = 0$ and Diameter = 0.650 in. (Wire Frame Surface)	201
169	Comparison of Circumferential Strain Distribution for Figure 167 When Magnitude = $10\text{Log}(\epsilon_{\theta\theta}^{C1}(r_1)/P_x)^2$ at $r_1 = 0.259$ in. With $n = 0$ and Diameter = 0.650 in.	202

LIST OF ILLUSTRATIONS (CONT'D)

Figure		Page
170	Comparison of Circumferential Strain Distribution for Figures 164 and 167 When Magnitude = $10\text{Log}(\epsilon_{\theta\theta}^{Ci}(r_1)/P_x)^2$ at Various r_1 With $i = 1$ or 2 , $n = 0$, Diameter = 0.650 in., and $k = 0$ rad/m.....	203
171	Comparison of Circumferential Strain Distribution for Figures 164 and 167 When Magnitude = $10\text{Log}(\epsilon_{\theta\theta}^{Ci}(r_1)/P_x)^2$ at Various r_1 With $i = 1$ or 2 , $n = 0$, Diameter = 0.650 in., and $f = 1000$ Hz	204
172	Comparison of Circumferential Strain Distribution for Figures 164 and 167 When Magnitude = $10\text{Log}(\epsilon_{\theta\theta}^{Ci}(r_1)/P_x)^2$ at Various r_1 With $i = 1$ or 2 , $n = 0$, Diameter = 0.650 in., and $f = 3000$ Hz	205
173	Comparison of Circumferential Strain Distribution for Figures 164 and 167 When Magnitude = $10\text{Log}(\epsilon_{\theta\theta}^{Ci}(r_1)/P_x)^2$ at Various r_1 With $i = 1$ or 2 , $n = 0$, Diameter = 0.650 in., and $f = 6000$ Hz	206
174	Comparison of Circumferential Strain Distribution for Figures 164 and 167 When Magnitude = $10\text{Log}(\epsilon_{\theta\theta}^{Ci}(r_1)/P_x)^2$ at Various r_1 With $i = 1$ or 2 , $n = 0$, Diameter = 0.650 in., and $f = 7500$ Hz	207
175	Attenuation of Circumferential Strain From Figures 164 and 167 When Magnitude = $(10\text{Log}(\epsilon_{\theta\theta}^{C1}(0.259)/P_x)^2 - 10\text{Log}(\epsilon_{\theta\theta}^{C2}(0.324)/P_x)^2)$ at Various f With $n = 0$ and Diameter = 0.650 in.	208
176	Comparison of Circumferential Strain Distribution for Figures 141 and 167 When Magnitude = $10\text{Log}(\epsilon_{\theta\theta}^{C1}(r_1)/P_i)^2$ With $i = o$ or x , $n = 0$, Diameter = 0.650 in., and $f = 40$ Hz.....	210
177	Comparison of Circumferential Strain Distribution for Figures 141 and 167 When Magnitude = $10\text{Log}(\epsilon_{\theta\theta}^{C1}(r_1)/P_i)^2$ With $i = o$ or x , $n = 0$, Diameter = 0.650 in., and $f = 500$ Hz.....	211
178	Comparison of Circumferential Strain Distribution for Figures 141 and 167 When Magnitude = $10\text{Log}(\epsilon_{\theta\theta}^{C1}(r_1)/P_i)^2$ With $i = o$ or x , $n = 0$, Diameter = 0.650 in., and $f = 1000$ Hz.....	212

LIST OF ILLUSTRATIONS (CONT'D)

Figure		Page
179	Comparison of Circumferential Strain Distribution for Figures 141 and 167 When Magnitude = $10\text{Log}(\epsilon_{\theta\theta}^{C1}(r_1)/P_i)^2$ With $i = o$ or x , $n = 0$, Diameter = 0.650 in., and $f = 3000$ Hz.....	213
180	Comparison of Circumferential Strain Distribution for Figures 141 and 167 When Magnitude = $10\text{Log}(\epsilon_{\theta\theta}^{C1}(r_1)/P_i)^2$ With $i = o$ or x , $n = 0$, Diameter = 0.650 in., and $f = 6000$ Hz.....	214
181	Comparison of Circumferential Strain Distribution for Figures 141 and 167 When Magnitude = $10\text{Log}(\epsilon_{\theta\theta}^{C1}(r_1)/P_i)^2$ With $i = o$ or x , $n = 0$, Diameter = 0.650 in., and $f = 7500$ Hz.....	215
D-1	Pressure Transfer Surface With Magnitude = $10\text{Log}(P_i(r_1)/P_o)^2$ at $r_1 = 1.1$ in. for Elasticity Model, Where $n = 0$ and Diameter = 3.00 in. (Two-Layer Cylinder)	D-3
D-2	Pressure Transfer Surface With Magnitude = $10\text{Log}(P_i(r_1)/P_o)^2$ at $r_1 = 1.1$ in. for Elasticity Model, Where $n = 0$ and Diameter = 3.00 in. (Single-Layer Cylinder)	D-3
D-3	Comparison of Two-Layer and Single-Layer Elasticity Models With Magnitude = $(10\text{Log}(P_i(r_1)/P_o)^2)$ at $r_1 = 1.1$ in., Where $n = 0$ and Diameter = 3.00 in.	D-4
D-4	Relative Difference Between Two-Layer and Single-Layer Surfaces With Magnitude = $(10\text{Log}(P_i^{M2}(r_1)/P_o)^2 -$ $10\text{Log}(P_i^{M1}(r_1)/P_o)^2)$ at $r_1 = 1.1$ in. for Elasticity Model, Where $n = 0$ and Diameter = 3.00 in.....	D-4
D-5	Pressure Transfer Surface With Magnitude = $10\text{Log}(P_i(r_1)/P_o)^2$ at $r_1 = 1.1$ in. for Elasticity Model, Where $n = 1$ and Diameter = 3.00 in. (Two-Layer Cylinder)	D-5
D-6	Pressure Transfer Surface With Magnitude = $10\text{Log}(P_i(r_1)/P_o)^2$ at $r_1 = 1.1$ in. for Elasticity Model, Where $n = 1$ and Diameter = 3.00 in. (Single-Layer Cylinder)	D-5

LIST OF ILLUSTRATIONS (CONT'D)

Figure		Page
D-7	Comparison of Two-Layer and Single-Layer Elasticity Models With Magnitude = $(10\text{Log}(P_i(r_1)/P_o)^2)$ at $r_1 = 1.1$ in., Where $n = 1$ and Diameter = 3.00 in.	D-6
D-8	Relative Difference Between Two-Layer and Single-Layer Surfaces With Magnitude = $(10\text{Log}(P_i^{M2}(r_1)/P_o)^2 - 10\text{Log}(P_i^{M1}(r_1)/P_o)^2)$ at $r_1 = 1.1$ in. for Elasticity Model, Where $n = 1$ and Diameter = 3.00 in.....	D-6
D-9	Pressure Transfer Surface With Magnitude = $10\text{Log}(P_i(r_1)/P_o)^2$ at $r_1 = 1.1$ in. for Elasticity Model, Where $n = 2$ and Diameter = 3.00 in. (Two-Layer Cylinder)	D-7
D-10	Pressure Transfer Surface With Magnitude = $10\text{Log}(P_i(r_1)/P_o)^2$ at $r_1 = 1.1$ in. for Elasticity Model, Where $n = 2$ and Diameter = 3.00 in. (Single-Layer Cylinder)	D-7
D-11	Comparison of Two-Layer and Single-Layer Elasticity Models With Magnitude = $(10\text{Log}(P_i(r_1)/P_o)^2)$ at $r_1 = 1.1$ in., Where $n = 2$ and Diameter = 3.00 in.	D-8
D-12	Relative Difference Between Two-Layer and Single-Layer Surfaces With Magnitude = $(10\text{Log}(P_i^{M2}(r_1)/P_o)^2 - 10\text{Log}(P_i^{M1}(r_1)/P_o)^2)$ at $r_1 = 1.1$ in. for Elasticity Model, Where $n = 2$ and Diameter = 3.00 in.....	D-8

LIST OF TABLES

Table		Page
1	Single-Layer-Cylinder/Fluid Phase Velocities.....	58
2	Single-Layer-Cylinder Properties—3.00-in. Diameter.....	59
3	Single-Layer-Cylinder Properties—0.670-in. Diameter.....	59
4	Single-Layer-Cylinder Outer Fluid Properties (Water)	60
5	Single-Layer-Cylinder Inner Fluid Properties (Water)	60
6	Effect of Inner Fluid Density on Breathing Wave Phase Velocity From Figure 87	120
7	Null Frequencies Corresponding to the First Two Roots of J_0	131
8	Outer Fluid Properties for Wall Thickness Variation (Air).....	136
9	Inner Fluid Properties for Wall Thickness Variation (Air)	136
10	Thickness Resonance Table for $h_1 = 0.3$ in. From Figure 100	137
11	Thickness Resonance Table for $h_1 = 0.6$ in. From Figure 101	137
12	Young's Modulus and Dilatational Phase Velocity.....	140
13	Comparison of First Radial Resonance Frequency f_r	141
14	Thickness Resonance Table for Air and Water With $h_1 = 0.3$ and 0.6 in.	144
15	Fluid P-Wave Phase and Group Velocity Versus Frequency From Figure 13	148
16	Two-Layer-Cylinder Properties—0.650-in. Diameter	173
17	Two-Layer-Cylinder Inner Fluid Properties (Air)	174
18	Two-Layer-Cylinder Outer Fluid Properties (Water).....	174
19	Two-Layer-Cylinder/Fluid Phase Velocities.....	174
20	Extensional Wave Phase Velocity From Figure 138.....	175
D-1	Two-Layer-Cylinder Properties—3.00-in. Diameter for Model Comparison.....	D-1
D-2	Two-Layer-Cylinder Outer Fluid Properties (Water) for Model Comparison	D-2

LIST OF TABLES (CONT'D)

Table		Page
D-3	Two-Layer-Cylinder Inner Fluid Properties (Water) for Model Comparison	D-2

LIST OF SYMBOLS

Cylinder			
\bar{a} = Mean radius of a cylinder	fb_i	=	Body forces
a = Inner radius of cylinder 1	τ_{ij}	=	Components of the stress tensor
b = Outer radius of cylinder 1	ϵ_{ij}	=	Components of the strain tensor
b = Inner radius of cylinder 2	u	=	Displacement vector
c = Outer radius of cylinder 2	u_i	=	Components of the displacement vector
c_e = Extensional wave speed	\ddot{u}_i	=	Components of the acceleration vector = $\frac{\partial^2 u_i}{\partial t^2}$
c_l = Dilatational wave speed	ϕ	=	Scalar displacement potential = $\phi(r, \theta, x, t)$
c_t = Shear or transverse wave speed	ψ	=	Vector displacement potential = $\psi(r, \theta, x, t)$
k_e = Extensional wavenumber	$\Psi_r, \Psi_\theta, \Psi_x$	=	Components of the vector displacement potential
L_e = Extensional wavelength	$u_c^{C1}, v_c^{C1}, w_c^{C1}$	=	Radial, tangential, and longitudinal displacement of cylinder 1 (field quantity)
r = Radial coordinate	$u_c^{C2}, v_c^{C2}, w_c^{C2}$	=	Radial, tangential, and longitudinal displacement of cylinder 2 (field quantity)
x = Axial coordinate	$\epsilon_{rr}^{C1}, \epsilon_{\theta\theta}^{C1}, \epsilon_{xx}^{C1}$	=	Radial, tangential, and longitudinal strain of cylinder 1 (field quantity)
θ = Angular coordinate	$\epsilon_{rr}^{C2}, \epsilon_{\theta\theta}^{C2}, \epsilon_{xx}^{C2}$	=	Radial, tangential, and longitudinal strain of cylinder 2 (field quantity)
E_c = General Young's modulus	$\tau_{rr}^{C1}, \tau_{\theta\theta}^{C1}, \tau_{xx}^{C1}$	=	Radial, tangential, and longitudinal stress of cylinder 1 (field quantity)
E_j^* = Complex Young's modulus	$\tau_{rr}^{C2}, \tau_{\theta\theta}^{C2}, \tau_{xx}^{C2}$	=	Radial, tangential, and longitudinal stress of cylinder 2 (field quantity)
μ_c = General Lamé constant (shear modulus)	$A_1^{C1}, A_2^{C1}, B_1^{C1}, B_2^{C1}, C_1^{C1}, C_2^{C1}$	=	Arbitrary constants for cylinder 1
λ_c = General Lamé constant	$A_1^{C2}, A_2^{C2}, B_1^{C2}, B_2^{C2}, C_1^{C2}, C_2^{C2}$	=	Arbitrary constants for cylinder 2
ν_c = General Poisson ratio			
ρ_c = General density			
ρ_1 = Density of cylinder 1			
ζ_1 = Structural loss factor for cylinder 1			
μ_1 = Lamé constant of cylinder 1 (shear modulus)			
λ_1 = Lamé constant of cylinder 1			
ν_1 = Poisson ratio of cylinder 1			
h_1 = Thickness of cylinder 1			
ρ_2 = Density of cylinder 2			
ζ_2 = Structural loss factor for cylinder 2			
μ_2 = Lamé constant of cylinder 2 (shear modulus)			
λ_2 = Lamé constant of cylinder 2			
ν_2 = Poisson ratio of cylinder 2			
h_2 = Thickness of cylinder 2			
f_r = First radial natural frequency of the cylinder			
ft_i = Thickness resonance frequencies			

LIST OF SYMBOLS (CONT'D)

Fluid

β	= Bulk modulus
c_f	= Speed of sound in a general fluid
c_s	= Speed of sound in the outer fluid
c_i	= Speed of sound in the inner fluid
k_s	= Outer fluid wavenumber
L_s	= Wavelength in the outer fluid
k_r	= Radial wavenumber
ρ_f	= General fluid density
ρ_s	= Outer fluid density
ρ_i	= Inner fluid density
ϕ_f	= General fluid displacement potential
ϕ_s	= Outer fluid displacement potential
ϕ_i	= Inner fluid displacement potential
u_f	= Particle displacement of a general fluid
u_s	= Particle displacement of the outer fluid
u_i	= Particle displacement of the inner fluid
p_f	= General fluid pressure
p_s	= Outer fluid pressure field
p_i	= Inner fluid pressure field
P_i	= Amplitude of the inner fluid pressure field
P_o	= Amplitude of the normal pressure excitation field
P_x	= Amplitude of the axial shear stress excitation field
P_θ	= Amplitude of the circumferential shear stress excitation field
λ_f	= Lamé constant
μ_f	= Lamé constant (shear modulus)
σ_{ij}	= Components of the stress tensor for the fluid
ϵ_{kk}	= Components of the strain tensor for the fluid

 δ_{ij} = Kronecker delta H, M = Outer fluid displacement potential field constants D = Inner fluid displacement potential field constant**Cylinder and Fluid** α = Angle relative to radial coordinate r ω = Angular frequency t = Time f_n = Inner fluid pressure field null frequencies k = Axial wavenumber ($2\pi/L$) L = Axial wavelength i = $\sqrt{-1}$ n = Circumferential order number u_{int} = Radial displacement at the cylinder/fluid interface J_n = Bessel function of the first kind Y_n = Bessel function of the second kind I_n = Modified Bessel function K_n = Modified Bessel function $H_n^{(1)}$ = Hankel function of the first kind r_1 = Calculation radius

**A CLOSED-FORM DYNAMIC ELASTICITY SOLUTION TO THE FLUID/
STRUCTURE INTERACTION PROBLEM OF A TWO-LAYER INFINITE
VISCOELASTIC CYLINDER WITH INNER AND OUTER FLUID LOADING
SUBJECT TO FORCED HARMONIC EXCITATION**

INTRODUCTION

This research treats the two-layer cylinder with inner and outer fluid loading subject to forced harmonic vibration within the scope of the linearized theory of dynamic elasticity. In previous efforts, investigations of the statically loaded single-layer cylinder were documented by numerous authors, and the forced vibration response of the single-layer cylinder was investigated by Holden,¹ Kaul and McCoy,² and others.

In the theoretical development presented in this report, the case of nonaxisymmetric vibration is discussed in terms of circumferential order number n . Results are presented for the first three-order numbers, namely, $n = 0, 1$, and 2 . Three excitation states are considered: the normal pressure P_0 , the longitudinal shear stress P_x , and the circumferential shear stress P_θ .

The development proceeds using scalar and vector displacement potentials to describe the motion of the solid. The boundary conditions are specified in terms of the stresses and displacements, and thus must be rewritten in terms of the displacement potentials.

For the case of the two-layered cylinder, the problem is reduced to solving a 13-by-13 system matrix for the undetermined complex coefficients. This matrix requires inversion at each location in the wavenumber and frequency plane, allowing all dynamic quantities (stress, strain, and displacement) to be calculated from the coefficients. Even though the solution is closed-form, a sizeable numerical computation is still necessary to extract information from the governing equations.

THE PHYSICAL MODEL

The physical model under analysis is shown in figure 1. A fluid-filled inner cylinder (cylinder 1) of inner radius a and outer radius b is joined to a second cylinder (cylinder 2). Cylinder 2 is in intimate contact with cylinder 1 at radius $r = b$. At radial distance c , cylinder 2 is in contact with an outer fluid. The outer fluid extends to infinity in radial coordinate r . The cylinders and fluids extend to plus and minus infinity in the longitudinal x -direction.

As stated earlier, the system is treated within the context of the linearized theory of elasticity. The assumption of linearity implies that both the cylinders and fluids obey linear constitutive

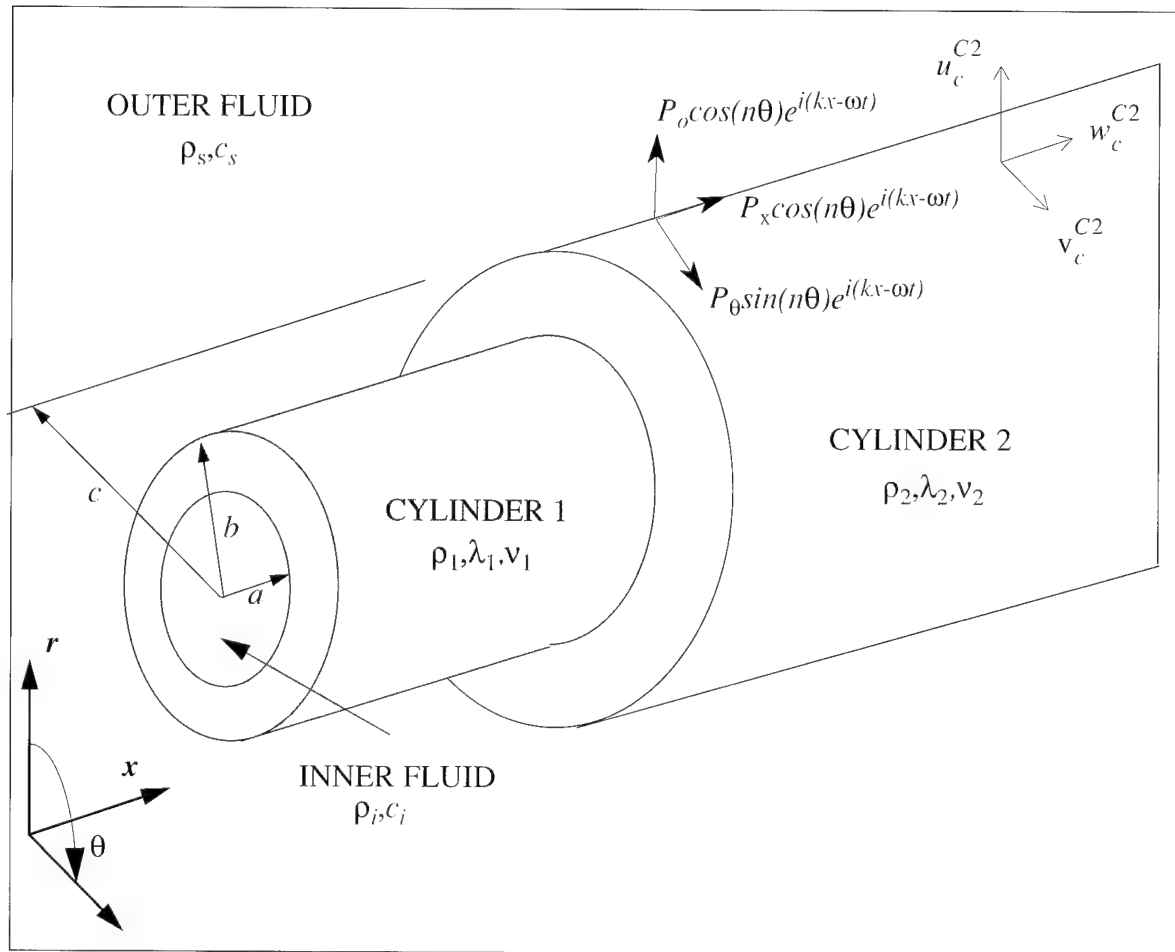


Figure 1. Physical Model Diagram

equations. For the cylinders, this means that there is a linear relationship between stress and strain. For the fluids, deviations from the hydrostatic pressure are a linear function of the condensation (fractional density change) and similarly the dilatation (volume strain). Strains are assumed to be small compared to unity for both the cylinders and the fluids; the response therefore is linearly related to the excitation. Both media are restricted to small signal analysis, i.e., excitation levels on the acoustic scale.

Damping is included by the use of a complex modulus of elasticity—the well-known structural damping form. The fluids are modeled as inviscid for the purpose of fluid loading the moving structure. The radial velocity of the fluids and the cylinders is identically equal at $r = a$ and $r = c$. Under the inviscid assumption, the fluids interact with only the radial motion of the cylinders and are uncoupled from the circumferential and longitudinal motions. A perfect slip condition is allowed between the cylinders and the fluids for the longitudinal and circumferential directions. This assumption allows us to avoid the use of boundary layer physics within the context of this development.

As described in the Introduction, three harmonic excitations are applied by the outer fluid to cylinder 2 at $r = c$: radial pressure P_o , longitudinal shear stress P_x , and circumferential shear stress P_θ . In practice, P_x and P_θ would only be developed by the viscosity of a real outer fluid. The amplitude distribution (at $r = c$) of the excitations in the wavenumber and frequency domain must be known *a priori*; otherwise a calculated quantity is normalized by an excitation stress magnitude. As shown in figure 1, the excitations are at a definite wavenumber (k) and frequency (ω) and are of circumferential order number n . The response of the cylinder will therefore be a function of k , ω , and n , as well as of the geometric and material properties of the composite system.

EQUATIONS OF MOTION

DISPLACEMENT POTENTIALS

The equations governing the motion of a homogeneous, isotropic, linearly elastic body are formulated with the strain-displacement relations (equation (1)), the constitutive relations (equation (2)), and the stress equations of motion (equation (3)) from reference 3:

$$\epsilon_{ij} = \frac{1}{2} (u_{i,j} + u_{j,i}) , \quad (1)$$

$$\tau_{ij} = \lambda_c \epsilon_{kk} \delta_{ij} + 2\mu_c \epsilon_{ij} , \quad (2)$$

and

$$\tau_{ij,j} + \rho_c f b_i = \rho_c \ddot{u}_i , \quad (3)$$

where ϵ_{ij} are the components of the strain tensor, τ_{ij} are the components of the stress tensor, u_i are the components of the displacement, and ρ_c is the density of the cylinder. The components of acceleration are indicated by \ddot{u}_i and the body forces are indicated by $f b_i$. The commas in equations (1) and (3) denote partial differentiation as

$$u_{i,j} = \frac{\partial u_i}{\partial x_j} , \quad \tau_{ij,j} = \frac{\partial \tau_{ij}}{\partial x_j} , \quad (4)$$

where the components of the vector of spatial coordinates x_j are equal to $x_1 = r$, $x_2 = \theta$, and $x_3 = x$.

To obtain an equation only in terms of the displacements and their derivatives, equations (1) and (2) are substituted into equation (3), resulting in⁴

$$\mu_c u_{i,jj} + (\lambda_c + \mu_c) u_{j,ji} = \rho_c \ddot{u}_i . \quad (5)$$

Equation (5) is expressed in vector notation as

$$\mu_c \nabla^2 \mathbf{u} + (\lambda_c + \mu_c) \nabla \nabla \cdot \mathbf{u} = \rho_c \ddot{\mathbf{u}} . \quad (6)$$

The displacement vector is decomposed with the scalar and vector relationship

$$\mathbf{u} = \nabla\phi + \nabla \times \boldsymbol{\psi}, \quad (7)$$

where $\phi = \phi(r, \theta, x, t)$ is the scalar displacement potential and $\boldsymbol{\psi} = \boldsymbol{\psi}(r, \theta, x, t)$ is the vector displacement potential. Equations (6) and (7) reduce to

$$\nabla \cdot ((\lambda_c + 2\mu_c) \nabla^2 \phi - \rho_c \ddot{\phi}) + \nabla \times (\mu_c \nabla^2 \boldsymbol{\psi} - \rho_c \ddot{\boldsymbol{\psi}}) = 0. \quad (8)$$

From equation (8), we obtain the following scalar and vector displacement potentials:

$$\nabla^2 \phi = \frac{1}{c_l^2} \ddot{\phi} \quad (9)$$

and

$$\nabla^2 \boldsymbol{\psi} = \frac{1}{c_t^2} \ddot{\boldsymbol{\psi}}. \quad (10)$$

The dilatational and shear wave phase velocities are given by

$$c_l^2 = \frac{\lambda_c + 2\mu_c}{\rho_c}, \quad c_t^2 = \frac{\mu_c}{\rho_c}, \quad (11)$$

where the Lamé constants λ_c and μ_c are equal to $\lambda_c = \frac{E_c \nu_c}{(1 + \nu_c)(1 - 2\nu_c)}$ and the shear modulus of the material, respectively.⁵

For the present cylindrical geometry, we have the following scalar and uncoupled vector potentials:

$$\nabla^2 \phi = \frac{1}{c_l^2} \ddot{\phi} \quad (12)$$

and

$$\nabla^2 \boldsymbol{\psi}_x = \frac{1}{c_t^2} \ddot{\boldsymbol{\psi}}_x. \quad (13)$$

Two coupled vector potentials in r and θ are

$$\nabla^2 \psi_r - \frac{\psi_r}{r^2} - \frac{2}{r^2} \frac{\partial \psi_\theta}{\partial \theta} = \frac{1}{c_t^2} \frac{\partial^2 \psi_r}{\partial t^2} \quad (14)$$

and

$$\nabla^2 \psi_\theta - \frac{\psi_\theta}{r^2} + \frac{2}{r^2} \frac{\partial \psi_r}{\partial \theta} = \frac{1}{c_t^2} \frac{\partial^2 \psi_\theta}{\partial t^2}. \quad (15)$$

The Laplacian is defined in cylindrical coordinates as

$$\nabla^2 = \frac{\partial^2}{\partial r^2} + \frac{1}{r} \frac{\partial}{\partial r} + \frac{1}{r^2} \frac{\partial^2}{\partial \theta^2} + \frac{\partial^2}{\partial x^2}. \quad (16)$$

Considering the scalar potential given by equation (12) and the harmonic nature of the forcing functions in figure 1, we will assume a separation-of-variables-type solution in r and θ . The scalar potential $\varphi(r, \theta, x, t)$ is then of the form

$$\varphi = \Omega(r) \Theta(\theta) e^{i(kx - \omega t)}. \quad (17)$$

Equation (12) yields the following two equations:

$$\frac{d^2 \Omega}{dr^2} + \frac{1}{r} \frac{d\Omega}{dr} + \left(\frac{\omega^2}{c_t^2} - k^2 \right) \Omega - \frac{n^2}{r^2} \Omega = 0 \quad (18)$$

and

$$\frac{d^2 \Theta}{d\theta^2} + n^2 \Theta = 0. \quad (19)$$

The solution of equation (18) is in terms of Bessel functions. For a solid cylinder, the field quantities must be finite at the center ($r = 0$); therefore only Bessel functions of the first kind, J_n , would be retained. However, for hollow cylinders, such as cylinders 1 and 2, Bessel functions of

both the first and second kind are retained. The solution to equation (19) is in terms of the sine and cosine of argument $n\theta$. The total solution is therefore

$$\phi = [\cos(n\theta) + \sin(n\theta)] (A_1 J_n(pr) + A_2 Y_n(pr)) e^{i(kx - \omega t)}, \quad (20)$$

with p defined as

$$p^2 = \frac{\omega^2}{c_l^2} - k^2. \quad (21)$$

A similar solution for the x -component of the vector potential, ψ_x , is

$$\psi_x = [\cos(n\theta) + \sin(n\theta)] (B_1 J_n(qr) + B_2 Y_n(qr)) e^{i(kx - \omega t)}, \quad (22)$$

with q defined as

$$q^2 = \frac{\omega^2}{c_t^2} - k^2. \quad (23)$$

The potentials for ψ_r and ψ_θ can be uncoupled by noting that ψ_r and ψ_θ contain trigonometric functions of θ and that a sine dependence on θ in ψ_r is equivalent to a cosine dependence on θ in ψ_θ , and vice versa.⁶ With the use of the condition $\nabla \cdot \psi = 0$ to eliminate an extra constant, ψ_r and ψ_θ become

$$\psi_r = [C_1 J_{n+1}(qr) + C_2 Y_{n+1}(qr)] \sin(n\theta) e^{i(kx - \omega t)} \quad (24)$$

and

$$\psi_\theta = [-C_1 J_{n+1}(qr) - C_2 Y_{n+1}(qr)] \cos(n\theta) e^{i(kx - \omega t)}. \quad (25)$$

Displacement Potential Summary for Cylinders 1 and 2

As stated earlier, cylinders 1 and 2 require Bessel functions of the first and second kind.⁷ The summary of the scalar and vector displacement potentials is

$$\phi = [A_1 J_n(pr) + A_2 Y_n(pr)] \cos(n\theta) e^{i(kx - \omega t)},$$

$$\psi_x = [B_1 J_n(qr) + B_2 Y_n(qr)] \sin(n\theta) e^{i(kx - \omega t)},$$

$$\psi_r = [C_1 J_{n+1}(qr) + C_2 Y_{n+1}(qr)] \sin(n\theta) e^{i(kx - \omega t)},$$

$$\psi_\theta = [-C_1 J_{n+1}(qr) + -C_2 Y_{n+1}(qr)] \cos(n\theta) e^{i(kx - \omega t)},$$

$$p^2 = \frac{\omega^2}{c_l^2} - k^2, \quad q^2 = \frac{\omega^2}{c_t^2} - k^2. \quad (26)$$

PARTICLE DISPLACEMENT/DISPLACEMENT POTENTIAL

Intermediate relationships between the particle displacements and the displacement potentials are given by equations (27) through (29),⁸ where u_c is the displacement in the r -direction, v_c is the displacement in the circumferential θ -direction, and w_c is the displacement in the longitudinal x -direction:

$$u_c = \frac{\partial \phi}{\partial r} + \frac{1}{r} \frac{\partial \psi_x}{\partial \theta} - \frac{\partial \psi_\theta}{\partial x}, \quad (27)$$

$$v_c = \frac{1}{r} \frac{\partial \phi}{\partial \theta} + \frac{\partial \psi_r}{\partial x} - \frac{\partial \psi_x}{\partial r}, \quad (28)$$

and

$$w_c = \frac{\partial \phi}{\partial x} + \frac{1}{r} \frac{\partial}{\partial r} (\psi_\theta r) - \frac{1}{r} \frac{\partial \psi_r}{\partial \theta}. \quad (29)$$

STRESS/DISPLACEMENT EQUATIONS

In the problem posed, the boundary conditions are prescribed with the stresses and displacements. Equations (30) through (35) relate the stress components to the particle displacements. We now have a complete progression from displacement potentials to stresses, which will allow us to solve for the motion of the composite system:

$$\tau_{rr} = \lambda_c \left(\frac{\partial u_c}{\partial r} + \frac{u_c}{r} + \frac{1}{r} \frac{\partial v_c}{\partial \theta} + \frac{\partial w_c}{\partial x} \right) + 2\mu_c \frac{\partial u_c}{\partial r}, \quad (30)$$

$$\tau_{\theta\theta} = \lambda_c \left(\frac{\partial u_c}{\partial r} + \frac{u_c}{r} + \frac{1}{r} \frac{\partial v_c}{\partial \theta} + \frac{\partial w_c}{\partial x} \right) + 2\mu_c \left(\frac{u_c}{r} + \frac{1}{r} \frac{\partial v_c}{\partial \theta} \right), \quad (31)$$

$$\tau_{xx} = \lambda_c \left(\frac{\partial u_c}{\partial r} + \frac{u_c}{r} + \frac{1}{r} \frac{\partial v_c}{\partial \theta} + \frac{\partial w_c}{\partial x} \right) + 2\mu_c \frac{\partial w_c}{\partial x}, \quad (32)$$

$$\tau_{r\theta} = \mu_c \left(\frac{\partial v_c}{\partial r} - \frac{v_c}{r} + \frac{1}{r} \frac{\partial u_c}{\partial \theta} \right), \quad (33)$$

$$\tau_{\theta x} = \mu_c \left(\frac{1}{r} \frac{\partial w_c}{\partial \theta} + \frac{\partial v_c}{\partial x} \right), \quad (34)$$

and

$$\tau_{rx} = \mu_c \left(\frac{\partial u_c}{\partial x} + \frac{\partial w_c}{\partial r} \right). \quad (35)$$

The indicial notation is interpreted in the following manner. The first index refers to the plane normal to the coordinate identified by the first index. The second index refers to the direction in which the stress acts. Stresses τ_{rr} , $\tau_{\theta\theta}$, and τ_{xx} are normal stresses, with τ_{rr} acting in the plane perpendicular to the radial coordinate in the radial direction. The remaining three stresses ($\tau_{r\theta}$, $\tau_{\theta x}$, and τ_{rx}) are shear stresses, with $\tau_{r\theta}$ acting in the plane perpendicular to the radial coordinate in the circumferential θ -direction.

STRAIN/DISPLACEMENT EQUATIONS

The relationships between strain and displacement in radial coordinates are

$$\epsilon_{rr} = \frac{\partial u_c}{\partial r}, \quad (36)$$

$$\epsilon_{\theta\theta} = \frac{u_c}{r} + \frac{1}{r} \frac{\partial v_c}{\partial \theta}, \quad (37)$$

and

$$\epsilon_{xx} = \frac{\partial w_c}{\partial x}. \quad (38)$$

STRESS, STRAIN, AND DISPLACEMENTS IN TERMS OF DISPLACEMENT POTENTIAL EQUATIONS

The stress and displacement equations needed to compose a suitable set for the application of the boundary conditions are written in terms of the displacement potentials by substituting equations (27) through (29) into equations (30), (33), and (35) to obtain equations (39), (40), and (41):

$$\tau_{rr} = \lambda_c \left(\frac{\partial^2 \phi_c}{\partial r^2} + \frac{1}{r} \frac{\partial \phi_c}{\partial r} + \frac{1}{r^2} \frac{\partial^2 \phi_c}{\partial \theta^2} + \frac{\partial^2 \phi_c}{\partial x^2} \right) + 2\mu_c \left(\frac{\partial^2 \phi_c}{\partial r^2} - \frac{1}{r^2} \frac{\partial \psi_x}{\partial \theta} + \frac{1}{r} \frac{\partial^2 \psi_x}{\partial \theta \partial r} - \frac{\partial^2 \psi_\theta}{\partial x \partial r} \right), \quad (39)$$

$$\tau_{r\theta} = \mu_c \left(-\frac{2}{r^2} \frac{\partial \phi_c}{\partial \theta} + \frac{2}{r} \frac{\partial^2 \phi_c}{\partial \theta \partial r} + \frac{\partial^2 \psi_r}{\partial x \partial r} - \frac{1}{r} \frac{\partial \psi_r}{\partial x} - \frac{1}{r} \frac{\partial^2 \psi_\theta}{\partial x \partial \theta} - \frac{\partial^2 \psi_x}{\partial r^2} + \frac{1}{r} \frac{\partial \psi_x}{\partial r} + \frac{1}{r^2} \frac{\partial^2 \psi_x}{\partial \theta^2} \right), \quad (40)$$

$$\tau_{rx} = \mu_c \left(2 \frac{\partial^2 \phi_c}{\partial r \partial x} + \frac{1}{r^2} \frac{\partial \psi_r}{\partial \theta} - \frac{1}{r} \frac{\partial^2 \psi_r}{\partial \theta \partial r} - \frac{\partial^2 \psi_\theta}{\partial x^2} + \frac{\partial^2 \psi_\theta}{\partial r^2} - \frac{1}{r^2} \psi_\theta + \frac{1}{r} \frac{\partial \psi_\theta}{\partial r} + \frac{1}{r} \frac{\partial^2 \psi_x}{\partial \theta \partial x} \right). \quad (41)$$

This same substitution is performed on strain equations (36), (37), and (38) to obtain equations (42), (43), and (44):

$$\epsilon_{rr} = \frac{\partial^2 \phi_c}{\partial r^2} - \frac{1}{r^2} \frac{\partial \psi_x}{\partial \theta} + \frac{1}{r} \frac{\partial^2 \psi_x}{\partial \theta \partial r} - \frac{\partial^2 \psi_\theta}{\partial x \partial r}, \quad (42)$$

$$\epsilon_{\theta\theta} = \frac{1}{r} \frac{\partial \phi_c}{\partial r} + \frac{1}{r^2} \frac{\partial \psi_x}{\partial \theta} - \frac{1}{r} \frac{\partial \psi_\theta}{\partial x} + \frac{1}{r^2} \frac{\partial^2 \phi_c}{\partial \theta^2} + \frac{1}{r} \frac{\partial^2 \psi_r}{\partial x \partial \theta} - \frac{1}{r} \frac{\partial^2 \psi_x}{\partial \theta \partial r}, \quad (43)$$

$$\epsilon_{xx} = \frac{\partial^2 \phi_c}{\partial x^2} + \frac{\partial^2 \psi_\theta}{\partial x \partial r} + \frac{1}{r} \frac{\partial \psi_\theta}{\partial x} - \frac{1}{r} \frac{\partial^2 \psi_r}{\partial x \partial \theta}. \quad (44)$$

Equations (45), (46), and (47) are now repeated to aid the reader:

$$u_c = \frac{\partial \phi_c}{\partial r} + \frac{1}{r} \frac{\partial \psi_x}{\partial \theta} - \frac{\partial \psi_\theta}{\partial x}, \quad (45)$$

$$v_c = \frac{1}{r} \frac{\partial \phi_c}{\partial \theta} + \frac{\partial \psi_r}{\partial x} - \frac{\partial \psi_x}{\partial r}, \quad (46)$$

and

$$w_c = \frac{\partial \phi_c}{\partial x} + \frac{\partial \psi_\theta}{\partial r} + \frac{1}{r} \psi_\theta - \frac{1}{r} \frac{\partial \psi_r}{\partial \theta}. \quad (47)$$

OUTER FLUID

As the surface of the cylinder is set into motion by the excitation of a pressure wave of magnitude P_o , a pressure field p_s is generated in the outer fluid by the cylinder surface. When the longitudinal wavenumber associated with the vibration of the cylinder surface is smaller than ω/c_s , the pressure radiated into the outer fluid is in the form of a propagating wave. If the longitudinal wavenumber of the cylinder vibration is greater than ω/c_s , the pressure field decays exponentially from the surface of the cylinder in the positive radial direction. The outer fluid is modeled as an ideal (nonviscous) linearly elastic media that cannot sustain shear stress, even when it is in motion.⁹ The equation of state is then

$$\sigma_{ij} = -p_f \delta_{ij}, \quad (48)$$

whose components are given by Hooke's law ($\sigma_{ij} = \lambda_f \epsilon_{kk} \delta_{ij} + 2\mu_f \epsilon_{ij}$) by setting $\mu_f = 0$:

$$\begin{aligned} \sigma_{11} = \sigma_{22} = \sigma_{33} &= \lambda_f \epsilon_{kk} = -p_f, \\ \sigma_{12} = \sigma_{13} = \sigma_{23} &= 0. \end{aligned} \quad (49)$$

The following scalar displacement potential describes the dynamic motion of the fluid in cylindrical coordinates:¹⁰

$$\nabla^2 \phi_f = \frac{1}{c_f^2} \frac{\partial^2 \phi_f}{\partial t^2}, \quad (50)$$

where

$$\nabla^2 = \frac{\partial^2}{\partial r^2} + \frac{1}{r} \frac{\partial}{\partial r} + \frac{1}{r^2} \frac{\partial^2}{\partial \theta^2} + \frac{\partial^2}{\partial z^2}. \quad (51)$$

In the case of fluids, $c_f = \sqrt{\lambda_f/\rho_f}$, which is equivalent to $c_f = \sqrt{\beta/\rho_f}$, where β is the bulk modulus of the fluid. The particle displacement and the pressure in the fluid can be expressed in terms of the displacement potential as follows:

$$u_f = \nabla \phi_f \quad (52)$$

and

$$p_f = -\rho_f \frac{d^2 \phi_f}{dt^2}. \quad (53)$$

For propagating wavenumbers in the outer fluid field, denoted by subscript s , the scalar displacement potential is given by¹¹

$$\phi_s = M \left(H_n^{(1)}(g_2 r) \right) \cos(n\theta) e^{i(kx - \omega t)}, \quad g_2^2 = \frac{\omega^2}{c_s^2} - k^2, \quad \text{for} \quad \frac{\omega^2}{c_s^2} > k^2. \quad (54)$$

For an outgoing wave described by $e^{i(k_r r - \omega t)}$, the pressure field in the outer fluid is physically a radiation from the surface of the moving cylinder. The radial dependence in equation (54) is a Hankel function of the first kind, indicated by superscript (1); i.e., $H_n^{(1)}(g_2 r) = J_n(g_2 r) + iY_n(g_2 r)$.

Differentiating equation (54) with respect to radius and time yields equations (55) through (57) for the fluid pressure, particle displacement, and particle acceleration, respectively:

$$p_s = \omega^2 \rho_s M \left(H_n^{(1)}(g_2 r) \right) \cos(n\theta) e^{i(kx - \omega t)}, \quad (55)$$

$$u_s = M \frac{\partial}{\partial r} \left(H_n^{(1)}(g_2 r) \right) \cos(n\theta) e^{i(kx - \omega t)}, \quad (56)$$

and

$$\frac{\partial^2 u_s}{\partial t^2} = \omega^2 M \frac{\partial}{\partial r} \left(H_n^{(1)}(g_2 r) \right) \cos(n\theta) e^{i(kx - \omega t)}. \quad (57)$$

For nonpropagating wavenumbers in the outer fluid, the evanescent field is given by the following displacement potential, where the radial dependence is in the form of the modified Bessel function K_n :

$$\phi_s = HK_n(f_2 r) \cos(n\theta) e^{i(kx - \omega t)}, \quad f_2^2 = k^2 - \frac{\omega^2}{c_s^2}, \quad \text{for} \quad k^2 > \frac{\omega^2}{c_s^2}. \quad (58)$$

Similar to the above discussion of the propagating case, the pressure, particle displacement, and particle acceleration are given by equations (59) through (61) as

$$p_s = \omega^2 \rho_s H K_n(f_2 r) \cos(n\theta) e^{i(kx - \omega t)}, \quad (59)$$

$$u_s = H \frac{\partial}{\partial r} K_n(f_2 r) \cos(n\theta) e^{i(kx - \omega t)}, \quad (60)$$

and

$$\frac{\partial^2 u_s}{\partial t^2} = H \frac{\partial}{\partial r} K_n(f_2 r) \cos(n\theta) e^{i(kx - \omega t)}. \quad (61)$$

Figure 2 connects the wavenumber-frequency plane with the time-space characteristics of the field properties in the outer fluid. The vertical axis represents wavenumber with respect to the longitudinal x -axis of the cylinder. The horizontal axis is the frequency axis. The positive wavenumber direction corresponds to propagation in the positive x -direction, and the negative wavenumber direction corresponds to propagation in the negative x -direction. There are two distinct regions in the wavenumber-frequency plane corresponding to propagating and non-propagating fields in the outer fluid.

In review, variable k refers to the wavenumber that exists on the surface of the cylinder. The vibrating cylinder surface will initiate a propagating field in the outer fluid if $\omega^2/c_s^2 > k^2$. When this condition exists, the radial displacement (u_c) of the cylinder surface must project (u_c') onto the propagation direction of the field in the outer fluid. For a given frequency, the wavelength of cylinder vibration must be greater than the corresponding wavelength of vibration that the fluid will propagate. The axisymmetric $n = 0$ vibration produces a symmetric field in the outer fluid as a function of θ . The spatial representation of a point (k_1, ω_1) in the region of propagating wavenumber-frequency pairs given by $|k_s| > |k_1| > 0$, is shown in figure 3, where L_1 is the wavelength and c_1 is the velocity of propagation. In the limit of $|k_1| \rightarrow 0$, the radiated field is physically a series of cylindrical, radially spreading wavefronts, emanating outward from and parallel to the surface of the cylinder. The intermediate range shown in figure 3 results in the

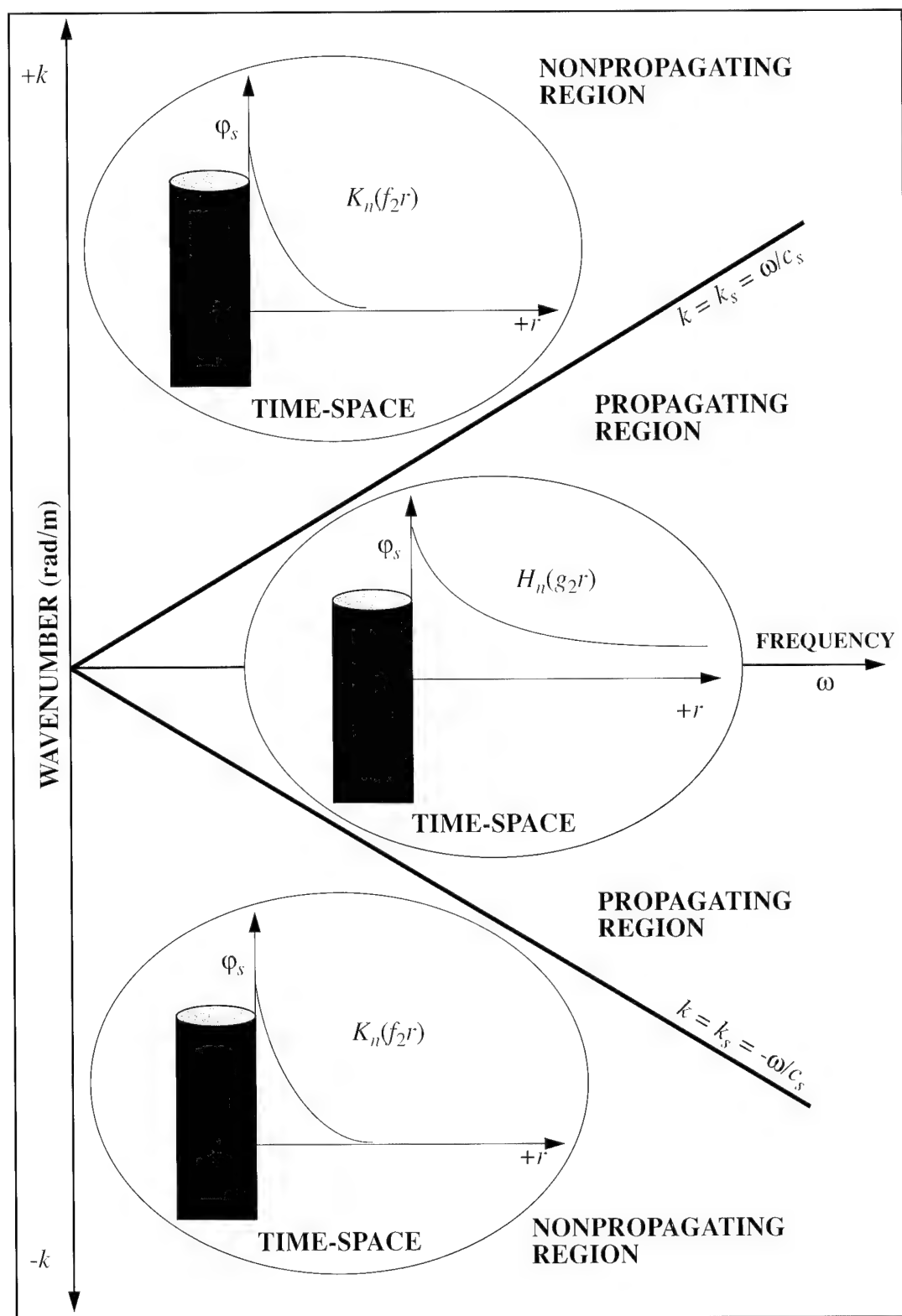


Figure 2. Outer Fluid Propagating and Nonpropagating Regions of the Wavenumber-Frequency Plane

wavefronts propagating out along conical planes, forming an angle α with the longitudinal x -axis of the cylinder. The direction, α , of the radiated field will be given by equation (62) as

$$\alpha = \arccos \frac{L_s}{L_1} = \arccos \frac{c_s}{c_1} = \arccos \frac{k_1}{k_s}, \quad (62)$$

where

$$k_s = \frac{2\pi}{L_s} = \frac{\omega}{c_s}. \quad (63)$$

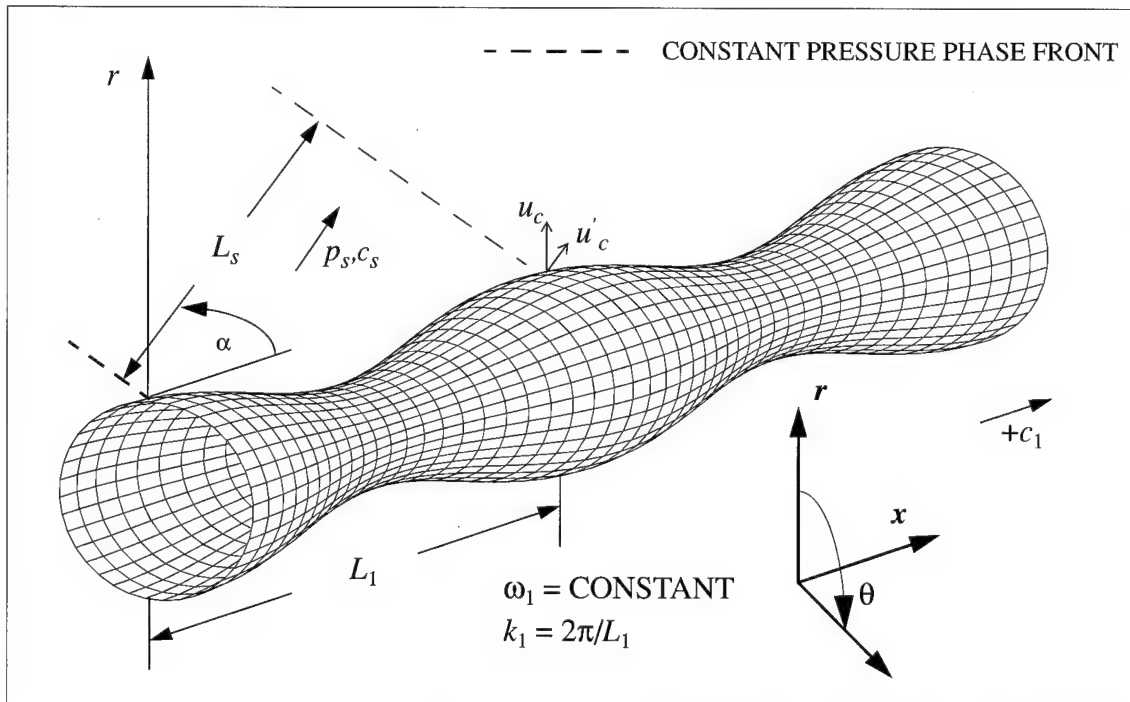


Figure 3. Relationship Between Cylinder Vibration and Radiated Pressure p_s

Propagation ceases when $k_1 = k_s$. This condition requires that $c_1 = c_s$; therefore, the propagation in the fluid would be along the longitudinal x -direction. However, there is only coupling between the cylinder motion and a propagating fluid pressure field if the radial

displacement u can be projected onto the propagation direction of the fluid pressure wave. This is not possible when $k_1 = k_s$ since u and x are orthogonal to each other; this condition is the onset of the nonpropagating region shown in figure 2.

The Hankel function variation of the outer fluid displacement potential can be observed in the inset TIME-SPACE diagrams in figure 2. These diagrams depict the radial spatial variation of the magnitude of the field quantities at a frozen instant of time.

As a line of constant frequency is traversed in figure 2, the cylinder wavelength L_1 becomes shorter, ultimately reaching a length less than the length of the corresponding fluid wavelength that supports propagation. Under this condition, there is no longer a component of the radial displacement of the cylinder that can be projected onto the propagation direction of the field in the outer fluid; equation (62) is no longer valid; and the field in the outer fluid, p_s , induced by cylinder vibration ceases to propagate. The radial variation of the field quantities is, according to the modified Bessel function depicted in figure 2, for the nonpropagating regions. The magnitude of all field quantities, such as the displacement potential and all parameters related to it, undergo the same qualitative spatial variation.

INNER FLUID

Similar to the behavior of the outer fluid, as the surface of the cylinder is set into motion by the excitation of a pressure wave of magnitude P_o , a pressure field (p_i) is generated in the inner fluid by the cylinder surface. When the longitudinal wavenumber associated with the vibration of the cylinder surface is smaller than ω/c_i , the pressure radiated into the inner fluid is in the form of a propagating wave. If the longitudinal wavenumber of the cylinder vibration is greater than ω/c_i , the pressure field decays exponentially from the surface of the cylinder in the direction of decreasing radius.

When considering the behavior of the field at $r = 0$, we make the observation that Y_n and K_n approach infinity as the argument of the functions approaches zero. However, because the interior pressure field must be finite at $r = 0$, these solutions are inappropriate and must be discarded. Bessel functions J_n and I_n will be retained to describe the displacement potentials in the inner fluid.

For the case of inner fluid, $c_i = \sqrt{\beta_i/\rho_i}$, where β_i is the bulk modulus of the fluid and ρ_i is the density. The particle displacement and the pressure in the fluid can be expressed in terms of the displacement potential as follows:

$$u_i = \nabla \phi_i \quad (64)$$

and

$$p_i = -\rho_i \frac{d^2 \phi_i}{dt^2} \quad (65)$$

For propagating wavenumbers, the scalar displacement potential is given by

$$\phi_i = DJ_n(g_1 r) \cos(n\theta) e^{i(kx - \omega t)}, \quad g_1^2 = \frac{\omega^2}{c_i^2} - k^2, \quad \text{for} \quad \frac{\omega^2}{c_i^2} > k^2. \quad (66)$$

Differentiating equation (66) with respect to radius and time yields equations (67) through (69) for the fluid pressure, particle displacement, and particle acceleration, respectively:

$$p_i = \omega^2 \rho_i D J_n(g_1 r) \cos(n\theta) e^{i(kx - \omega t)}, \quad (67)$$

$$u_i = D \frac{\partial}{\partial r} J_n(g_1 r) \cos(n\theta) e^{i(kx - \omega t)}, \quad (68)$$

and

$$\frac{\partial^2 u_i}{\partial t^2} = \omega^2 D \frac{\partial}{\partial r} J_n(g_1 r) \cos(n\theta) e^{i(kx - \omega t)}. \quad (69)$$

For nonpropagating wavenumbers in the inner fluid (imaginary g_1), the field decays evanescently and is described by the following displacement potential, where the radial dependence is in the form of the modified Bessel function I_n , evaluated for real argument m :

$$\phi_i = G I_n(mr) \cos(n\theta) e^{i(kx - \omega t)}, \quad m^2 = k^2 - \frac{\omega^2}{c_i^2}, \quad \text{for} \quad k^2 > \frac{\omega^2}{c_i^2}. \quad (70)$$

In this case, I_n replaces J_n using the identity $I_n(x) = i^{-n} J_n(ix)$. Similar to the discussion of the propagating case, the pressure, particle displacement, and particle acceleration are given by equations (71) through (73) as

$$p_i = \omega^2 \rho_i G I_n(mr) \cos(n\theta) e^{i(kx - \omega t)}, \quad (71)$$

$$u_i = G \frac{\partial}{\partial r} I_n(mr) \cos(n\theta) e^{i(kx - \omega t)}, \quad (72)$$

and

$$\frac{\partial^2 u_i}{\partial t^2} = G \frac{\partial}{\partial r} I_n(mr) \cos(n\theta) e^{i(kx - \omega t)}. \quad (73)$$

The FORTRAN algorithm that is used to evaluate the J_n Bessel function numerically accepts complex arguments. Thus, equations (70) through (73), which use Bessel function I_n to replace J_n as the argument of the function becomes imaginary, are not used in the FORTRAN algorithms developed to implement the solution of the inner fluid displacement potentials. The development presented above is provided in the event that the complex argument Bessel function routines might not be available to the reader.

Figure 4 connects the wavenumber-frequency plane with the time-space characteristics of the field properties in the inner fluid. The vertical axis represents wavenumber with respect to the longitudinal x -axis of the cylinder. The horizontal axis is the frequency axis. The positive wavenumber direction corresponds to propagation in the positive x -direction, and the negative wavenumber direction corresponds to propagation in the negative x -direction. There are two distinct regions in the wavenumber-frequency plane corresponding to propagating and non-propagating fields in the inner fluid.

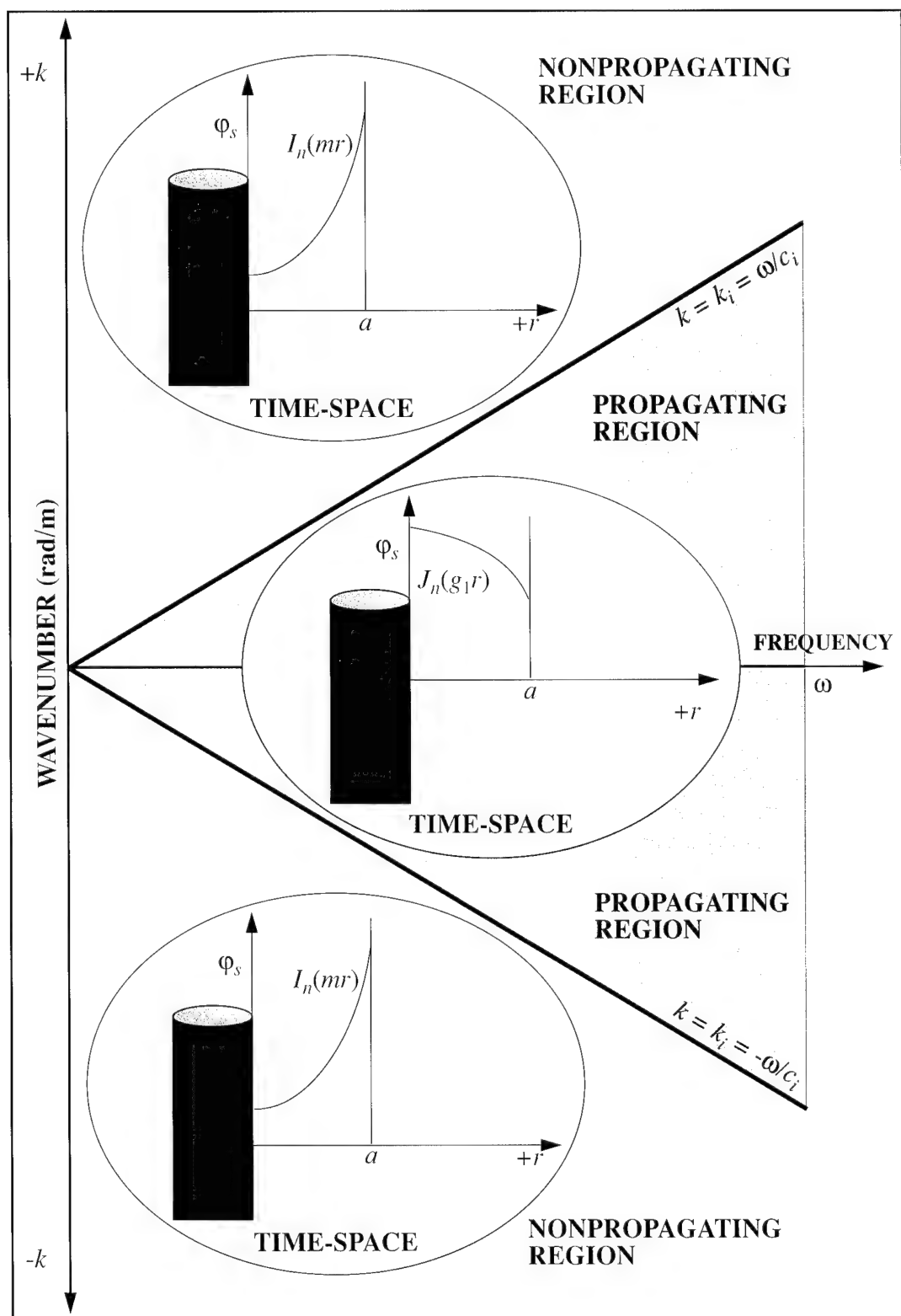


Figure 4. Inner Fluid Propagating and Nonpropagating Regions of the Wavenumber-Frequency Plane

SINGLE-LAYER CYLINDER/FLUID INTERFACES

BOUNDARY CONDITIONS

The solution to the solid cylinder in contact with an outer fluid is obtained by solving for the constants $A_1^{C1}, A_2^{C1}, B_1^{C1}, B_2^{C1}, C_1^{C1}$ and C_2^{C1} in equation (26), M in equation (54), and D in equation (66) for the pertinent boundary conditions by considering the state of stress and displacement at the cylinder and fluid interfaces $r = a$ and $r = b$. (Note from this point on in the derivations that subscript c (Lame constants) has been replaced with 1 or 2 to indicate cylinder 1 or 2. Superscript $C1$ or $C2$ has been added to all other pertinent quantities to distinguish the first from the second cylinder.)

The final problem contains a total of seven unknown constants. There are seven boundary conditions, which are reflected in rows 1 through 7, respectively, of system matrix $smc1$. Initially the problem was set up with eight boundary conditions, where the eighth equated the radial displacement of the cylinder to the outer fluid at $r = b$. However, due to the properties of the cylinder used for the trial problem and the limited precision available for the calculation, rows 4 and 8 of this original matrix were not sufficiently different to enable the required inversion, a condition referred to as algorithmically singular.

To circumvent this original inversion problem, the radial displacement boundary condition evaluated at $r = b$,

$$u_c^{C1} \Big|_{r=b} = \frac{\partial \phi_s}{\partial r} \Big|_{r=b}, \quad (74)$$

was assembled and written in terms of the unknown fluid constant M , assuming $\omega^2/c_s^2 > k^2$, as follows:

$$M = \frac{1}{\frac{\partial}{\partial r} \left(H_n^{(1)}(g_2 b) \right)} \left(A_1^{C1} \frac{\partial}{\partial r} J_n(p_1 b) + A_2^{C1} \frac{\partial}{\partial r} Y_n(p_1 b) + B_1^{C1} \frac{n}{b} J_n(q_1 b) + B_2^{C1} \frac{n}{b} Y_n(q_1 b) \right. \\ \left. + C_1^{C1} i k J_{n+1}(q_1 b) + C_2^{C1} i k Y_{n+1}(q_1 b) \right). \quad (75)$$

Equation (75) was used in the assembly of boundary condition 1 (equation (76)) to eliminate the outer fluid constant M . This added a fluid term to each of the terms in boundary condition 1, making it sufficiently different from boundary condition 4 to allow the numerical inverse of matrix $smc1$ to exist. Thus, the system was reduced from eight equations for the boundary conditions to seven, which also decreased the time needed for computation.

The seven boundary conditions are given by equations (76) through (82) as

$$\text{Boundary condition 1} \quad \tau_{rr}^{C1} \Big|_{r=b} = (-P_o - p_s) \Big|_{r=b}. \quad (76)$$

$$\text{Boundary condition 2} \quad \tau_{rx}^{C1} \Big|_{r=b} = -P_x \Big|_{r=b}. \quad (77)$$

$$\text{Boundary condition 3} \quad \tau_{r\theta}^{C1} \Big|_{r=b} = -P_\theta \Big|_{r=b}. \quad (78)$$

$$\text{Boundary condition 4} \quad \tau_{rr}^{C1} \Big|_{r=a} = -p_i \Big|_{r=a}. \quad (79)$$

$$\text{Boundary condition 5} \quad \tau_{rx}^{C1} \Big|_{r=a} = 0 \Big|_{r=a}. \quad (80)$$

$$\text{Boundary condition 6} \quad \tau_{r\theta}^{C1} \Big|_{r=a} = 0 \Big|_{r=a}. \quad (81)$$

$$\text{Boundary condition 7} \quad u_c^{C1} \Big|_{r=a} = \frac{\partial \phi_i}{\partial r} \Big|_{r=a}. \quad (82)$$

The seven boundary conditions are shown diagrammatically in figure 5. All boundary conditions are in effect over the entire area of contact between the cylinder and the fluids.

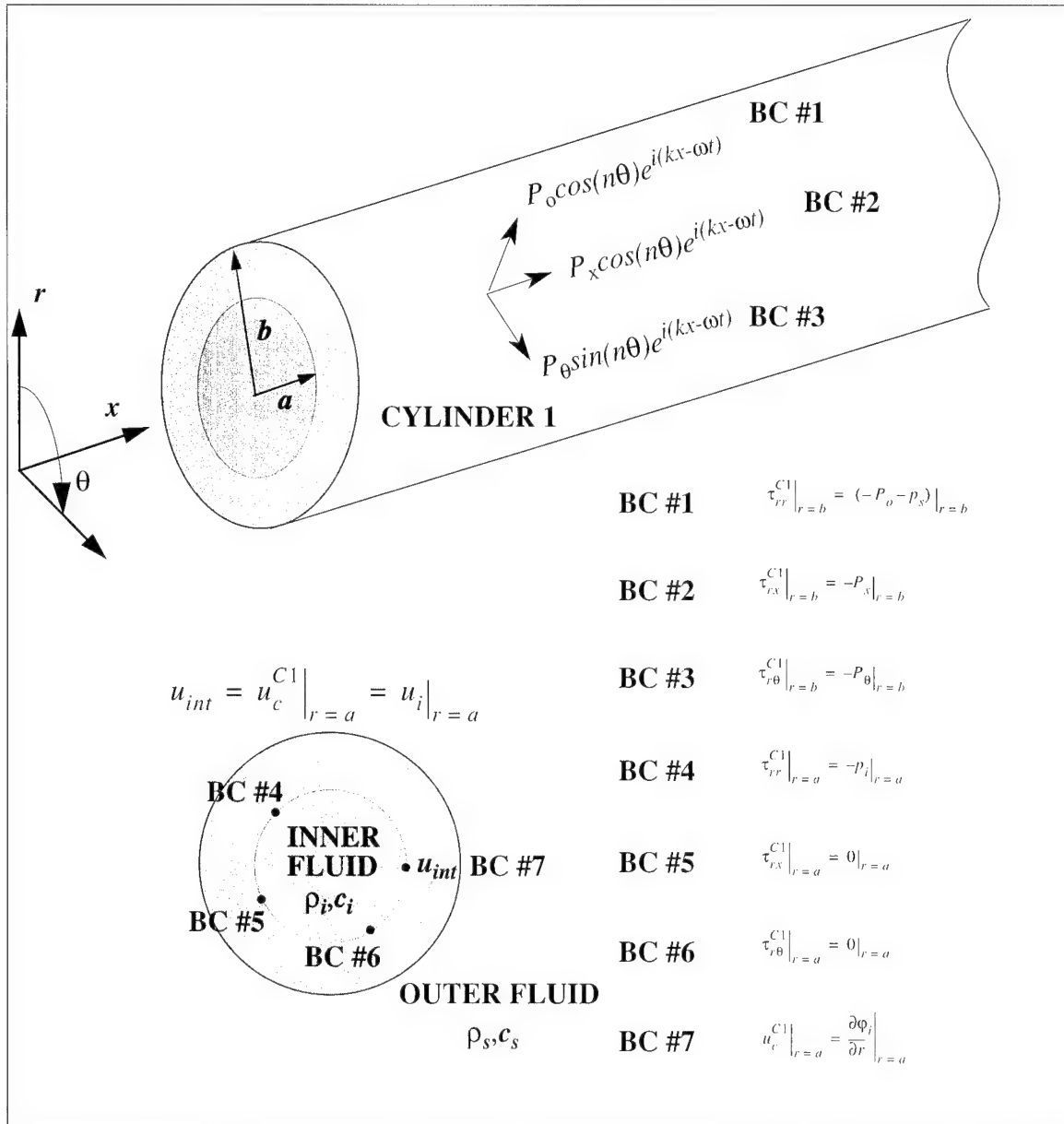


Figure 5. Boundary Conditions for Single-Layer Infinite Cylinder and Fluids

The fourth boundary condition (equation (79)) for radial stress is assembled by substituting equation (67) and the appropriate derivatives of equation (26) into equation (39). The resulting expression is in terms of the unknown constants for the displacement potentials and is given as

$$\begin{aligned}
& \left(A_1^{C1} \left[(\lambda_1 + 2\mu_1) \frac{\partial^2}{\partial r^2} J_n(p_1 a) + \frac{\lambda_1}{a} \frac{\partial}{\partial r} J_n(p_1 a) - \lambda_1 J_n(p_1 a) \left(\frac{n^2}{a^2} + k^2 \right) \right] \right. \\
& + A_2^{C1} \left[(\lambda_1 + 2\mu_1) \frac{\partial^2}{\partial r^2} Y_n(p_1 a) + \frac{\lambda_1}{a} \frac{\partial}{\partial r} Y_n(p_1 a) - \lambda_1 Y_n(p_1 a) \left(\frac{n^2}{a^2} + k^2 \right) \right] \\
& - B_1^{C1} \left[\frac{2\mu_1 n}{a^2} \left(J_n(q_1 a) - a \frac{\partial}{\partial r} J_n(q_1 a) \right) \right] - B_2^{C1} \left[\frac{2\mu_1 n}{a^2} \left(Y_n(q_1 a) - a \frac{\partial}{\partial r} Y_n(q_1 a) \right) \right] \\
& + C_1^{C1} 2\mu_1 i k \frac{\partial}{\partial r} J_{n+1}(q_1 a) + C_2^{C1} 2\mu_1 i k \frac{\partial}{\partial r} Y_{n+1}(q_1 a) \left. \right) \cos(n\theta) e^{i(kx - \omega t)} \\
& = -\omega^2 \rho_i D J_n(g_1 a) \cos(n\theta) e^{i(kx - \omega t)}. \tag{83}
\end{aligned}$$

As previously described, the first boundary condition, equation (76), is assembled by using equation (75) to eliminate the outer fluid constant M , resulting in

$$\begin{aligned}
& \left(A_1^{C1} \left[(\lambda_1 + 2\mu_1) \frac{\partial^2}{\partial r^2} J_n(p_1 b) + \frac{\partial}{\partial r} J_n(p_1 b) \left(\frac{\lambda_1}{b} + \rho_s \omega^2 \frac{H_n^{(1)}(g_2 b)}{\frac{\partial}{\partial r} (H_n^{(1)}(g_2 b))} \right) - \lambda_1 J_n(p_1 b) \left(\frac{n^2}{b^2} + k^2 \right) \right] \right. \\
& + A_2^{C1} \left[(\lambda_1 + 2\mu_1) \frac{\partial^2}{\partial r^2} Y_n(p_1 b) + \frac{\partial}{\partial r} Y_n(p_1 b) \left(\frac{\lambda_1}{b} + \rho_s \omega^2 \frac{H_n^{(1)}(g_2 b)}{\frac{\partial}{\partial r} (H_n^{(1)}(g_2 b))} \right) - \lambda_1 Y_n(p_1 b) \left(\frac{n^2}{b^2} + k^2 \right) \right] \\
& - B_1^{C1} \left[\frac{2\mu_1 n}{b^2} \left(J_n(q_1 b) - b \frac{\partial}{\partial r} J_n(q_1 b) \right) - \frac{n \rho_s \omega^2}{b} \frac{H_n^{(1)}(g_2 b)}{\frac{\partial}{\partial r} (H_n^{(1)}(g_2 b))} J_n(q_1 b) \right] \\
& - B_2^{C1} \left[\frac{2\mu_1 n}{b^2} \left(Y_n(q_1 b) - b \frac{\partial}{\partial r} Y_n(q_1 b) \right) - \frac{n \rho_s \omega^2}{b} \frac{H_n^{(1)}(g_2 b)}{\frac{\partial}{\partial r} (H_n^{(1)}(g_2 b))} Y_n(q_1 b) \right] \\
& + C_1^{C1} \left[2\mu_1 i k \frac{\partial}{\partial r} J_{n+1}(q_1 b) + i k \rho_s \omega^2 \frac{H_n^{(1)}(g_2 b)}{\frac{\partial}{\partial r} (H_n^{(1)}(g_2 b))} J_{n+1}(q_1 b) \right] \\
& \left. + C_2^{C1} \left[2\mu_1 i k \frac{\partial}{\partial r} Y_{n+1}(q_1 b) + i k \rho_s \omega^2 \frac{H_n^{(1)}(g_2 b)}{\frac{\partial}{\partial r} (H_n^{(1)}(g_2 b))} Y_{n+1}(q_1 b) \right] \right) \cos(n\theta) e^{i(kx - \omega t)} = 0. \quad (84)
\end{aligned}$$

SYSTEM MATRIX

The seven boundary conditions in equations (76) through (82) are assembled in matrix form in equation (85):

$$\begin{bmatrix} smc1(1,1) & smc1(1,2) & smc1(1,3) & smc1(1,4) & smc1(1,5) & smc1(1,6) & 0 \\ smc1(2,1) & smc1(2,2) & smc1(2,3) & smc1(2,4) & smc1(2,5) & smc1(2,6) & 0 \\ smc1(3,1) & smc1(3,2) & smc1(3,3) & smc1(3,4) & smc1(3,5) & smc1(3,6) & 0 \\ smc1(4,1) & smc1(4,2) & smc1(4,3) & smc1(4,4) & smc1(4,5) & smc1(4,6) & smc1(1,7) \\ smc1(5,1) & smc1(5,2) & smc1(5,3) & smc1(5,4) & smc1(5,5) & smc1(5,6) & 0 \\ smc1(6,1) & smc1(6,2) & smc1(6,3) & smc1(6,4) & smc1(6,5) & smc1(6,6) & 0 \\ smc1(7,1) & smc1(7,2) & smc1(7,3) & smc1(7,4) & smc1(7,5) & smc1(7,6) & smc1(1,7) \end{bmatrix} \begin{bmatrix} A_1^{C1} \\ A_2^{C1} \\ B_1^{C1} \\ B_2^{C1} \\ C_1^{C1} \\ C_2^{C1} \\ D \end{bmatrix} = \begin{bmatrix} -P_o \\ -P_x \\ -P_\theta \\ 0 \\ 0 \\ 0 \\ 0 \end{bmatrix} \quad (85)$$

Elements of the *smc1* matrix are shown in equations (86) through (134). Solution of equation (85) at each point in the wavenumber-frequency plane for the vector of unknown constants allows the displacement potentials of the system to be evaluated with equations (26), (54), and (58). Equation (85) will be evaluated for only one nonzero forcing function at a time. The coefficients will be normalized by the forcing function stress, which will cast the output in terms of a transfer surface for the particular cylinder variable chosen, i.e., displacement, velocity, stress, or strain.

From boundary condition 1,

$$\begin{aligned} smc1(1,1) = & (\lambda_1 + 2\mu_1) \frac{\partial^2}{\partial r^2} J_n(p_1 b) + \frac{\partial}{\partial r} J_n(p_1 b) \left(\frac{\lambda_1}{b} + \rho_s \omega^2 \frac{H_n^{(1)}(g_2 b)}{\frac{\partial}{\partial r} (H_n^{(1)}(g_2 b))} \right) \\ & - \lambda_1 J_n(p_1 b) \left(\frac{n^2}{b^2} + k^2 \right), \end{aligned} \quad (86)$$

$$\begin{aligned}
smc1(1, 2) = & (\lambda_1 + 2\mu_1) \frac{\partial^2}{\partial r^2} Y_n(p_1 b) + \frac{\partial}{\partial r} Y_n(p_1 b) \left(\frac{\lambda_1}{b} + \rho_s \omega^2 \frac{H_n^{(1)}(g_2 b)}{\frac{\partial}{\partial r} (H_n^{(1)}(g_2 b))} \right) \\
& - \lambda_1 Y_n(p_1 b) \left(\frac{n^2}{b^2} + k^2 \right), \quad (87)
\end{aligned}$$

$$smc1(1, 3) = -2\mu_1 \frac{n}{b^2} \left(J_n(q_1 b) - b \frac{\partial}{\partial r} J_n(q_1 b) \right) + \frac{n\rho_s \omega^2}{b} \frac{H_n^{(1)}(g_2 b)}{\frac{\partial}{\partial r} (H_n^{(1)}(g_2 b))} J_n(q_1 b), \quad (88)$$

$$smc1(1, 4) = -2\mu_1 \frac{n}{b^2} \left(Y_n(q_1 b) - b \frac{\partial}{\partial r} Y_n(q_1 b) \right) + \frac{n\rho_s \omega^2}{b} \frac{H_n^{(1)}(g_2 b)}{\frac{\partial}{\partial r} (H_n^{(1)}(g_2 b))} Y_n(q_1 b), \quad (89)$$

$$smc1(1, 5) = i2\mu_1 k \frac{\partial}{\partial r} J_{n+1}(q_1 b) + ik\rho_s \omega^2 \frac{H_n^{(1)}(g_2 b)}{\frac{\partial}{\partial r} (H_n^{(1)}(g_2 b))} J_{n+1}(q_1 b), \quad (90)$$

$$smc1(1, 6) = i2\mu_1 k \frac{\partial}{\partial r} Y_{n+1}(q_1 b) + ik\rho_s \omega^2 \frac{H_n^{(1)}(g_2 b)}{\frac{\partial}{\partial r} (H_n^{(1)}(g_2 b))} J_{n+1}(q_1 b), \quad (91)$$

and

$$smc1(1, 7) = 0. \quad (92)$$

From boundary condition 2,

$$smc1(2, 1) = i2\mu_1 k \frac{\partial}{\partial r} J_n(p_1 b), \quad (93)$$

$$smc1(2, 2) = i2\mu_1 k \frac{\partial}{\partial r} Y_n(p_1 b), \quad (94)$$

$$smc1(2, 3) = \frac{i\mu_1 kn}{b} J_n(q_1 b), \quad (95)$$

$$smc1(2, 4) = \frac{i\mu_1 kn}{b} Y_n(q_1 b), \quad (96)$$

$$smc1(2, 5) = \mu_1 \left(J_{n+1}(q_1 b) \left(\frac{n+1}{b^2} - k^2 \right) - \frac{\partial}{\partial r} J_{n+1}(q_1 b) \left(\frac{n+1}{b} \right) - \frac{\partial^2}{\partial r^2} J_{n+1}(q_1 b) \right), \quad (97)$$

$$smc1(2, 6) = \mu_1 \left(Y_{n+1}(q_1 b) \left(\frac{n+1}{b^2} - k^2 \right) - \frac{\partial}{\partial r} Y_{n+1}(q_1 b) \left(\frac{n+1}{b} \right) - \frac{\partial^2}{\partial r^2} Y_{n+1}(q_1 b) \right), \quad (98)$$

and

$$smc1(2, 7) = 0. \quad (99)$$

From boundary condition 3,

$$smc1(3, 1) = \frac{2\mu_1 n}{b} \left(\frac{1}{b} J_n(p_1 b) - \frac{\partial}{\partial r} J_n(p_1 b) \right), \quad (100)$$

$$smc1(3, 2) = \frac{2\mu_1 n}{b} \left(\frac{1}{b} Y_n(p_1 b) - \frac{\partial}{\partial r} Y_n(p_1 b) \right), \quad (101)$$

$$smc1(3, 3) = \mu_1 \left(-\frac{\partial^2}{\partial r^2} J_n(q_1 b) + \frac{1}{b} \frac{\partial}{\partial r} J_n(q_1 b) - \frac{n^2}{b^2} J_n(q_1 b) \right), \quad (102)$$

$$smc1(3, 4) = \mu_1 \left(-\frac{\partial^2}{\partial r^2} Y_n(q_1 b) + \frac{1}{b} \frac{\partial}{\partial r} Y_n(q_1 b) - \frac{n^2}{b^2} Y_n(q_1 b) \right), \quad (103)$$

$$smc1(3, 5) = ik\mu_1 \left(\frac{\partial}{\partial r} J_{n+1}(q_1 b) - J_{n+1}(q_1 b) \left(\frac{1+n}{b} \right) \right), \quad (104)$$

$$smc1(3, 6) = ik\mu_1 \left(\frac{\partial}{\partial r} Y_{n+1}(q_1 b) - Y_{n+1}(q_1 b) \left(\frac{1+n}{b} \right) \right), \quad (105)$$

and

$$smc1(3, 7) = 0. \quad (106)$$

From boundary condition 4,

$$smc1(4, 1) = (\lambda_1 + 2\mu_1) \frac{\partial^2}{\partial r^2} J_n(p_1 a) + \frac{\lambda_1}{a} \frac{\partial}{\partial r} J_n(p_1 a) - \frac{\lambda_1 n^2}{a^2} J_n(p_1 a) - k^2 \lambda_1 J_n(p_1 a), \quad (107)$$

$$smc1(4, 2) = (\lambda_1 + 2\mu_1) \frac{\partial^2}{\partial r^2} Y_n(p_1 a) + \frac{\lambda_1}{a} \frac{\partial}{\partial r} Y_n(p_1 a) - \frac{\lambda_1 n^2}{a^2} Y_n(p_1 a) - k^2 \lambda_1 Y_n(p_1 a), \quad (108)$$

$$smc1(4, 3) = -2\mu_1 \frac{n}{a^2} \left(J_n(q_1 a) - a \frac{\partial}{\partial r} J_n(q_1 a) \right), \quad (109)$$

$$smc1(4, 4) = -2\mu_1 \frac{n}{a^2} \left(Y_n(q_1 a) - a \frac{\partial}{\partial r} Y_n(q_1 a) \right), \quad (110)$$

$$smc1(4, 5) = 2\mu_1 i k \frac{\partial}{\partial r} J_{n+1}(q_1 a), \quad (111)$$

$$smc1(4, 6) = 2\mu_1 i k \frac{\partial}{\partial r} Y_{n+1}(q_1 a), \quad (112)$$

and

$$smc1(4, 7) = \omega^2 \rho_i D J_n(g_1 a). \quad (113)$$

From boundary condition 5,

$$smc1(5, 1) = i 2\mu_1 k \frac{\partial}{\partial r} J_n(p_1 a), \quad (114)$$

$$smc1(5, 2) = i 2\mu_1 k \frac{\partial}{\partial r} Y_n(p_1 a), \quad (115)$$

$$smc1(5, 3) = \frac{i \mu_1 k n}{a} J_n(q_1 a), \quad (116)$$

$$smc1(5, 4) = \frac{i\mu_1 kn}{a} Y_n(q_1 a), \quad (117)$$

$$smc1(5, 5) = \mu_1 \left(J_{n+1}(q_1 a) \left(\frac{n+1}{a^2} - k^2 \right) - \frac{\partial}{\partial r} J_{n+1}(q_1 a) \left(\frac{n+1}{a} \right) - \frac{\partial^2}{\partial r^2} J_{n+1}(q_1 a) \right), \quad (118)$$

$$smc1(5, 6) = \mu_1 \left(Y_{n+1}(q_1 a) \left(\frac{n+1}{a^2} - k^2 \right) - \frac{\partial}{\partial r} Y_{n+1}(q_1 a) \left(\frac{n+1}{a} \right) - \frac{\partial^2}{\partial r^2} Y_{n+1}(q_1 a) \right), \quad (119)$$

and

$$smc1(5, 7) = 0. \quad (120)$$

From boundary condition 6,

$$smc1(6, 1) = \frac{2\mu_1 n}{a} \left(\frac{1}{a} J_n(p_1 a) - \frac{\partial}{\partial r} J_n(p_1 a) \right), \quad (121)$$

$$smc1(6, 2) = \frac{2\mu_1 n}{a} \left(\frac{1}{a} Y_n(p_1 a) - \frac{\partial}{\partial r} Y_n(p_1 a) \right), \quad (122)$$

$$smc1(6, 3) = \mu_1 \left(-\frac{\partial^2}{\partial r^2} J_n(q_1 a) + \frac{1}{a} \frac{\partial}{\partial r} J_n(q_1 a) - \frac{n^2}{a^2} J_n(q_1 a) \right), \quad (123)$$

$$smc1(6, 4) = \mu_1 \left(-\frac{\partial^2}{\partial r^2} Y_n(q_1 a) + \frac{1}{a} \frac{\partial}{\partial r} Y_n(q_1 a) - \frac{n^2}{a^2} Y_n(q_1 a) \right), \quad (124)$$

$$smc1(6, 5) = ik\mu_1 \left(\frac{\partial}{\partial r} J_{n+1}(q_1 a) - J_{n+1}(q_1 a) \left(\frac{1+n}{a} \right) \right), \quad (125)$$

$$smc1(6, 6) = ik\mu_1 \left(\frac{\partial}{\partial r} Y_{n+1}(q_1 a) - Y_{n+1}(q_1 a) \left(\frac{1+n}{a} \right) \right), \quad (126)$$

and

$$smc1(6, 7) = 0. \quad (127)$$

From boundary condition 7,

$$smc1(7, 1) = \frac{\partial}{\partial r} J_n(p_1 a), \quad (128)$$

$$smc1(7, 2) = \frac{\partial}{\partial r} Y_n(p_1 a), \quad (129)$$

$$smc1(7, 3) = \frac{n}{a} J_n(q_1 a), \quad (130)$$

$$smc1(7, 4) = \frac{n}{a} Y_n(q_1 a), \quad (131)$$

$$smc1(7, 5) = ik J_{n+1}(q_1 a), \quad (132)$$

$$smc1(7, 6) = ik Y_{n+1}(q_1 a), \quad (133)$$

and

$$smc1(7, 7) = -\frac{\partial}{\partial r} J_n(g_1 a). \quad (134)$$

TWO-LAYER CYLINDER/FLUID INTERFACES

BOUNDARY CONDITIONS

In this section, we will formulate the 13 boundary conditions required for the two-cylinder problem shown in figure 1. At radius $r = c$ (the second cylinder/fluid interface), the radial stress in cylinder 2 is set equal to the negative of the magnitude of the pressure in the fluid. Also at radius $r = c$, the radial displacement of the cylinder equals the radial displacement of the fluid. At radius $r = b$, there is a continuity of displacements and stress components between each cylinder in the plane of contact perpendicular to the radial coordinate. At radius $r = a$ (the first cylinder/fluid interface), the radial stress in cylinder 1 is set equal to the negative of the pressure in the inner fluid. Additionally, the radial particle displacement of the fluid and cylinder is equated. The shear stresses $\tau_{r\theta}$ and τ_{rx} vanish due to the inviscid assumption. For the composite problem, the following description at the boundaries exists:

$$\text{Boundary condition 1} \quad \tau_{rr}^{C2} \Big|_{r=c} = (-P_o - p_s) \Big|_{r=c}. \quad (135)$$

$$\text{Boundary condition 2} \quad \tau_{rx}^{C2} \Big|_{r=c} = -P_x \Big|_{r=c}. \quad (136)$$

$$\text{Boundary condition 3} \quad \tau_{r\theta}^{C2} \Big|_{r=c} = -P_\theta \Big|_{r=c}. \quad (137)$$

$$\text{Boundary condition 4} \quad \tau_{rr}^{C2} \Big|_{r=b} = \tau_{rr}^{C1} \Big|_{r=b}. \quad (138)$$

$$\text{Boundary condition 5} \quad \tau_{rx}^{C2} \Big|_{r=b} = \tau_{rx}^{C1} \Big|_{r=b}. \quad (139)$$

$$\text{Boundary condition 6} \quad \tau_{r\theta}^{C2} \Big|_{r=b} = \tau_{r\theta}^{C1} \Big|_{r=b}. \quad (140)$$

$$\text{Boundary condition 7} \quad u_c^{C2} \Big|_{r=b} = u_c^{C1} \Big|_{r=b}. \quad (141)$$

$$\text{Boundary condition 8} \quad v_c^{C2} \Big|_{r=b} = v_c^{C1} \Big|_{r=b}. \quad (142)$$

$$\text{Boundary condition 9} \quad w_c^{C2} \Big|_{r=b} = w_c^{C1} \Big|_{r=b}. \quad (143)$$

$$\text{Boundary condition 10} \quad \tau_{rr}^{C1} \Big|_{r=a} = -p_i \Big|_{r=a}. \quad (144)$$

$$\text{Boundary condition 11} \quad \tau_{rx}^{C1} \Big|_{r=a} = 0. \quad (145)$$

$$\text{Boundary condition 12} \quad \tau_{r\theta}^{C1} \Big|_{r=a} = 0. \quad (146)$$

$$\text{Boundary condition 13} \quad u_c^{C1} \Big|_{r=a} = u_i \Big|_{r=a}. \quad (147)$$

The same procedure employed for the single-layer cylinder, which combined the outer fluid radial displacement condition with the boundary condition for radial stress, is used in the two-layer cylinder problem formulation. At radius $r = c$, the continuity of radial displacement between the cylinder and the outer fluid requires that

$$u_c^{C2} \Big|_{r=c} = \frac{\partial \phi_s}{\partial r} \Big|_{r=c}. \quad (148)$$

This boundary condition is assembled with equations (26), (27), and (54). Solving for M as follows yields

$$M = \frac{1}{\frac{\partial}{\partial r} \left(H_n^{(1)}(g_2 c) \right)} \left(A_1^{C2} \frac{\partial}{\partial r} J_n(p_2 c) + A_2^{C2} \frac{\partial}{\partial r} Y_n(p_2 c) + B_1^{C2} \frac{n}{c} J_n(q_2 c) + B_2^{C2} \frac{n}{c} Y_n(q_2 c) \right. \\ \left. + C_1^{C2} i k J_{n+1}(q_2 c) + C_2^{C2} i k Y_{n+1}(q_2 c) \right). \quad (149)$$

Equation (149) is combined with equation (135) to eliminate the constant M , reducing the size of the system matrix from 14 by 14 to 13 by 13.

The 13 boundary conditions correspond to rows 1 through 13, respectively, of equation (150). The elements of the system matrix, C , are given in equations (151) through (319). Solution of equation (150) at each point in the wavenumber-frequency plane for the vector of unknown constants allows the displacement potentials of the system to be evaluated with equations (26), (54), and (58). Matrix C will be evaluated for only one nonzero forcing function at a time in any given simulation. The coefficients will be normalized by the forcing function stress magnitude (P_o , P_x , or P_θ), which will cast the output in terms of a transfer surface for the particular cylinder or fluid variable chosen, i.e., displacement, velocity, stress, strain, or fluid pressure.

The 13 boundary conditions are shown diagrammatically in figure 6 for the two-layer solid cylinder immersed in an outer fluid. All boundary conditions are in effect over the entire surface of contact for the media at radii $r = a$, b , and c .

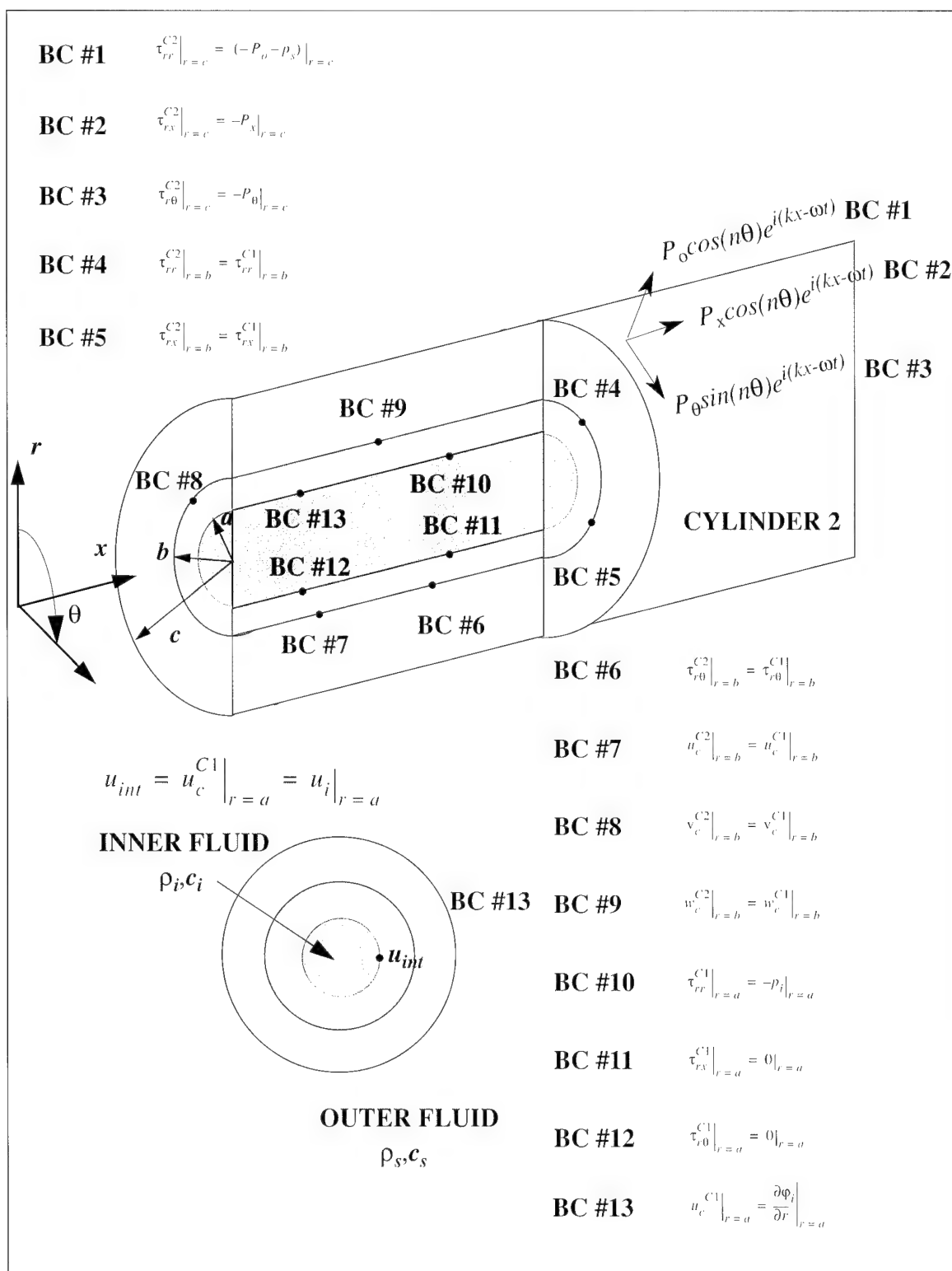


Figure 6. Boundary Conditions for Two-Layer Infinite Cylinder and Fluids

SYSTEM MATRIX

As noted earlier, the 13 boundary conditions are assembled into matrix form in the following expression:

$$\begin{bmatrix}
 C(1,1) & C(1,2) & C(1,3) & C(1,4) & C(1,5) & C(1,6) & 0 & 0 & 0 & 0 & 0 & 0 & 0 \\
 C(2,1) & C(2,2) & C(2,3) & C(2,4) & C(2,5) & C(2,6) & 0 & 0 & 0 & 0 & 0 & 0 & 0 \\
 C(3,1) & C(3,2) & C(3,3) & C(3,4) & C(3,5) & C(3,6) & 0 & 0 & 0 & 0 & 0 & 0 & 0 \\
 C(4,1) & C(4,2) & C(4,3) & C(4,4) & C(4,5) & C(4,6) & C(4,7) & C(4,8) & C(4,9) & C(4,10) & C(4,11) & C(4,12) & 0 \\
 C(5,1) & C(5,2) & C(5,3) & C(5,4) & C(5,5) & C(5,6) & C(5,7) & C(5,8) & C(5,9) & C(5,10) & C(5,11) & C(5,12) & 0 \\
 C(6,1) & C(6,2) & C(6,3) & C(6,4) & C(6,5) & C(6,6) & C(6,7) & C(6,8) & C(6,9) & C(6,10) & C(6,11) & C(6,12) & 0 \\
 C(7,1) & C(7,2) & C(7,3) & C(7,4) & C(7,5) & C(7,6) & C(7,7) & C(7,8) & C(7,9) & C(7,10) & C(7,11) & C(7,12) & 0 \\
 C(8,1) & C(8,2) & C(8,3) & C(8,4) & C(8,5) & C(8,6) & C(8,7) & C(8,8) & C(8,9) & C(8,10) & C(8,11) & C(8,12) & 0 \\
 C(9,1) & C(9,2) & 0 & 0 & C(9,5) & C(9,6) & C(9,7) & C(9,8) & 0 & 0 & C(9,11) & C(9,12) & 0 \\
 0 & 0 & 0 & 0 & 0 & 0 & C(10,7) & C(10,8) & C(10,9) & C(10,10) & C(10,11) & C(10,12) & C(10,13) \\
 0 & 0 & 0 & 0 & 0 & 0 & C(11,7) & C(11,8) & C(11,9) & C(11,10) & C(11,11) & C(11,12) & 0 \\
 0 & 0 & 0 & 0 & 0 & 0 & C(12,7) & C(12,8) & C(12,9) & C(12,10) & C(12,11) & C(12,12) & 0 \\
 0 & 0 & 0 & 0 & 0 & 0 & C(13,7) & C(13,8) & C(13,9) & C(13,10) & C(13,11) & C(13,12) & C(13,13)
 \end{bmatrix}
 \begin{bmatrix}
 A_1^{C2} \\
 A_2^{C2} \\
 B_1^{C2} \\
 B_2^{C2} \\
 C_1^{C2} \\
 C_2^{C2} \\
 A_1^{C1} \\
 A_2^{C1} \\
 B_1^{C1} \\
 B_2^{C1} \\
 C_1^{C1} \\
 C_2^{C1} \\
 D
 \end{bmatrix}
 =
 \begin{bmatrix}
 -P_o \\
 -P_x \\
 -P_\theta \\
 0 \\
 0 \\
 0 \\
 0 \\
 0 \\
 0 \\
 0 \\
 0 \\
 0 \\
 0
 \end{bmatrix}
 \quad (150)$$

The elements of equation (150) are given by equations (151) through (319). From boundary condition 1, the first row yields

$$\begin{aligned}
 C(1,1) = & (\lambda_2 + 2\mu_2) \frac{\partial^2}{\partial r^2} J_n(p_2 c) + \frac{\partial}{\partial r} J_n(p_2 c) \left(\frac{\lambda_2}{c} + \rho_s \omega^2 \frac{H_n^{(1)}(g_2 c)}{\frac{\partial}{\partial r} (H_n^{(1)}(g_2 c))} \right) \\
 & - \lambda_2 J_n(p_2 c) \left(\frac{n^2}{c^2} + k^2 \right),
 \end{aligned} \quad (151)$$

$$\begin{aligned}
 C(1,2) = & (\lambda_2 + 2\mu_2) \frac{\partial^2}{\partial r^2} Y_n(p_2 c) + \frac{\partial}{\partial r} Y_n(p_2 c) \left(\frac{\lambda_2}{c} + \rho_s \omega^2 \frac{H_n^{(1)}(g_2 c)}{\frac{\partial}{\partial r} (H_n^{(1)}(g_2 c))} \right) \\
 & - \lambda_2 Y_n(p_2 c) \left(\frac{n^2}{c^2} + k^2 \right),
 \end{aligned} \quad (152)$$

$$C(1, 3) = -2\mu_2 \frac{n}{c^2} \left(J_n(q_2 c) - c \frac{\partial}{\partial r} J_n(q_2 c) \right) + \frac{n \rho_s \omega^2}{c} \frac{H_n^{(1)}(g_2 c)}{\frac{\partial}{\partial r} (H_n^{(1)}(g_2 c))} J_n(q_2 c), \quad (153)$$

$$C(1, 4) = -2\mu_2 \frac{n}{c^2} \left(Y_n(q_2 c) - c \frac{\partial}{\partial r} Y_n(q_2 c) \right) + \frac{n \rho_s \omega^2}{c} \frac{H_n^{(1)}(g_2 c)}{\frac{\partial}{\partial r} (H_n^{(1)}(g_2 c))} Y_n(q_2 c), \quad (154)$$

$$C(1, 5) = i2\mu_2 k \frac{\partial}{\partial r} J_{n+1}(q_2 c) + ik \rho_s \omega^2 \frac{H_n^{(1)}(g_2 c)}{\frac{\partial}{\partial r} (H_n^{(1)}(g_2 c))} J_{n+1}(q_2 c), \quad (155)$$

$$C(1, 6) = i2\mu_2 k \frac{\partial}{\partial r} Y_{n+1}(q_2 c) + ik \rho_s \omega^2 \frac{H_n^{(1)}(g_2 c)}{\frac{\partial}{\partial r} (H_n^{(1)}(g_2 c))} Y_{n+1}(q_2 c), \quad (156)$$

$$C(1, 7) = 0, \quad (157)$$

$$C(1, 8) = 0, \quad (158)$$

$$C(1, 9) = 0, \quad (159)$$

$$C(1, 10) = 0, \quad (160)$$

$$C(1, 11) = 0, \quad (161)$$

$$C(1, 12) = 0, \quad (162)$$

and

$$C(1, 13) = 0. \quad (163)$$

From boundary condition 2,

$$C(2, 1) = i2\mu_2 k \frac{\partial}{\partial r} J_n(p_2 c), \quad (164)$$

$$C(2, 2) = i2\mu_2 k \frac{\partial}{\partial r} Y_n(p_2 c), \quad (165)$$

$$C(2, 3) = \frac{i\mu_2 kn}{c} J_n(q_2 c), \quad (166)$$

$$C(2, 4) = \frac{i\mu_2 kn}{c} Y_n(q_2 c), \quad (167)$$

$$C(2, 5) = \mu_2 \left(J_{n+1}(q_2 c) \left(\frac{n+1}{c^2} - k^2 \right) - \frac{\partial}{\partial r} J_{n+1}(q_2 c) \left(\frac{n+1}{c} \right) - \frac{\partial^2}{\partial r^2} J_{n+1}(q_2 c) \right), \quad (168)$$

$$C(2, 6) = \mu_2 \left(Y_{n+1}(q_2 c) \left(\frac{n+1}{c^2} - k^2 \right) - \frac{\partial}{\partial r} Y_{n+1}(q_2 c) \left(\frac{n+1}{c} \right) - \frac{\partial^2}{\partial r^2} Y_{n+1}(q_2 c) \right), \quad (169)$$

$$C(2, 7) = 0, \quad (170)$$

$$C(2, 8) = 0, \quad (171)$$

$$C(2, 9) = 0, \quad (172)$$

$$C(2, 10) = 0, \quad (173)$$

$$C(2, 11) = 0, \quad (174)$$

$$C(2, 12) = 0, \quad (175)$$

and

$$C(2, 13) = 0. \quad (176)$$

From boundary condition 3,

$$C(3, 1) = \frac{2\mu_2 n}{c} \left(\frac{1}{c} J_n(p_2 c) - \frac{\partial}{\partial r} J_n(p_2 c) \right), \quad (177)$$

$$C(3, 2) = \frac{2\mu_2 n}{c} \left(\frac{1}{c} Y_n(p_2 c) - \frac{\partial}{\partial r} Y_n(p_2 c) \right), \quad (178)$$

$$C(3, 3) = \mu_2 \left(-\frac{\partial^2}{\partial r^2} J_n(q_2 c) + \frac{1}{c} \frac{\partial}{\partial r} J_n(q_2 c) - \frac{n^2}{c^2} J_n(q_2 c) \right), \quad (179)$$

$$C(3, 4) = \mu_2 \left(-\frac{\partial^2}{\partial r^2} Y_n(q_2 c) + \frac{1}{c} \frac{\partial}{\partial r} Y_n(q_2 c) - \frac{n^2}{c^2} Y_n(q_2 c) \right), \quad (180)$$

$$C(3, 5) = ik\mu_2 \left(\frac{\partial}{\partial r} J_{n+1}(q_2 c) - J_{n+1}(q_2 c) \left(\frac{1+n}{c} \right) \right), \quad (181)$$

$$C(3, 6) = ik\mu_2 \left(\frac{\partial}{\partial r} Y_{n+1}(q_2 c) - Y_{n+1}(q_2 c) \left(\frac{1+n}{c} \right) \right), \quad (182)$$

$$C(3, 7) = 0, \quad (183)$$

$$C(3, 8) = 0, \quad (184)$$

$$C(3, 9) = 0, \quad (185)$$

$$C(3, 10) = 0, \quad (186)$$

$$C(3, 11) = 0, \quad (187)$$

$$C(3, 12) = 0, \quad (188)$$

and

$$C(3, 13) = 0. \quad (189)$$

From boundary condition 4,

$$C(4, 1) = (\lambda_2 + 2\mu_2) \frac{\partial^2}{\partial r^2} J_n(p_2 b) + \frac{\lambda_2}{b} \frac{\partial}{\partial r} J_n(p_2 b) - \lambda_2 J_n(p_2 b) \left(\frac{n^2}{b^2} + k^2 \right), \quad (190)$$

$$C(4, 2) = (\lambda_2 + 2\mu_2) \frac{\partial^2}{\partial r^2} Y_n(p_2 b) + \frac{\lambda_2}{b} \frac{\partial}{\partial r} Y_n(p_2 b) - \lambda_2 Y_n(p_2 b) \left(\frac{n^2}{b^2} + k^2 \right), \quad (191)$$

$$C(4, 3) = -2\mu_2 \frac{n}{b^2} \left(J_n(q_2 b) - b \frac{\partial}{\partial r} J_n(q_2 b) \right), \quad (192)$$

$$C(4, 4) = -2\mu_2 \frac{n}{b^2} \left(Y_n(q_2 b) - b \frac{\partial}{\partial r} Y_n(q_2 b) \right), \quad (193)$$

$$C(4, 5) = i2\mu_2 k \frac{\partial}{\partial r} J_{n+1}(q_2 b), \quad (194)$$

$$C(4, 6) = i2\mu_2 k \frac{\partial}{\partial r} Y_{n+1}(q_2 b), \quad (195)$$

$$C(4, 7) = -(\lambda_1 + 2\mu_1) \frac{\partial^2}{\partial r^2} J_n(p_1 b) - \frac{\lambda_1}{b} \frac{\partial}{\partial r} J_n(p_1 b) + \lambda_1 J_n(p_1 b) \left(\frac{n^2}{b^2} + k^2 \right), \quad (196)$$

$$C(4, 8) = -(\lambda_1 + 2\mu_1) \frac{\partial^2}{\partial r^2} Y_n(p_1 b) - \frac{\lambda_1}{b} \frac{\partial}{\partial r} Y_n(p_1 b) + \lambda_1 Y_n(p_1 b) \left(\frac{n^2}{b^2} + k^2 \right), \quad (197)$$

$$C(4, 9) = 2\mu_1 \frac{n}{b^2} \left(J_n(q_1 b) - b \frac{\partial}{\partial r} J_n(q_1 b) \right), \quad (198)$$

$$C(4, 10) = 2\mu_1 \frac{n}{b^2} \left(Y_n(q_1 b) - b \frac{\partial}{\partial r} Y_n(q_1 b) \right), \quad (199)$$

$$C(4, 11) = -i2\mu_1 k \frac{\partial}{\partial r} J_{n+1}(q_1 b), \quad (200)$$

$$C(4, 12) = -i2\mu_1 k \frac{\partial}{\partial r} Y_{n+1}(q_1 b), \quad (201)$$

and

$$C(4, 13) = 0. \quad (202)$$

From boundary condition 5,

$$C(5, 1) = i2\mu_2 k \frac{\partial}{\partial r} J_n(p_2 b), \quad (203)$$

$$C(5, 2) = i2\mu_2 k \frac{\partial}{\partial r} Y_n(p_2 b), \quad (204)$$

$$C(5, 3) = \frac{i\mu_2 kn}{b} J_n(q_2 b), \quad (205)$$

$$C(5, 4) = \frac{i\mu_2 kn}{b} Y_n(q_2 b), \quad (206)$$

$$C(5, 5) = \mu_2 \left(J_{n+1}(q_2 b) \left(\frac{n+1}{b^2} - k^2 \right) - \frac{\partial}{\partial r} J_{n+1}(q_2 b) \left(\frac{n+1}{b} \right) - \frac{\partial^2}{\partial r^2} J_{n+1}(q_2 b) \right), \quad (207)$$

$$C(5, 6) = \mu_2 \left(Y_{n+1}(q_2 b) \left(\frac{n+1}{b^2} - k^2 \right) - \frac{\partial}{\partial r} Y_{n+1}(q_2 b) \left(\frac{n+1}{b} \right) - \frac{\partial^2}{\partial r^2} Y_{n+1}(q_2 b) \right), \quad (208)$$

$$C(5, 7) = -i2\mu_1 k \frac{\partial}{\partial r} J_n(p_1 b), \quad (209)$$

$$C(5, 8) = -i2\mu_1 k \frac{\partial}{\partial r} Y_n(p_1 b), \quad (210)$$

$$C(5, 9) = -\frac{i\mu_1 kn}{b} J_n(q_1 b), \quad (211)$$

$$C(5, 10) = -\frac{i\mu_1 kn}{b} Y_n(q_1 b), \quad (212)$$

$$C(5, 11) = -\mu_1 \left(J_{n+1}(q_1 b) \left(\frac{n+1}{b^2} - k^2 \right) - \frac{\partial}{\partial r} J_{n+1}(q_1 b) \left(\frac{n+1}{b} \right) - \frac{\partial^2}{\partial r^2} J_{n+1}(q_1 b) \right), \quad (213)$$

$$C(5, 12) = -\mu_1 \left(Y_{n+1}(q_1 b) \left(\frac{n+1}{b^2} - k^2 \right) - \frac{\partial}{\partial r} Y_{n+1}(q_1 b) \left(\frac{n+1}{b} \right) - \frac{\partial^2}{\partial r^2} Y_{n+1}(q_1 b) \right), \quad (214)$$

and

$$C(5, 13) = 0. \quad (215)$$

From boundary condition 6,

$$C(6, 1) = \frac{2\mu_2 n}{b} \left(\frac{1}{b} J_n(p_2 b) - \frac{\partial}{\partial r} J_n(p_2 b) \right), \quad (216)$$

$$C(6, 2) = \frac{2\mu_2 n}{b} \left(\frac{1}{b} Y_n(p_2 b) - \frac{\partial}{\partial r} Y_n(p_2 b) \right), \quad (217)$$

$$C(6, 3) = \mu_2 \left(-\frac{\partial^2}{\partial r^2} J_n(q_2 b) + \frac{1}{b} \frac{\partial}{\partial r} J_n(q_2 b) - \frac{n^2}{b^2} J_n(q_2 b) \right), \quad (218)$$

$$C(6, 4) = \mu_2 \left(-\frac{\partial^2}{\partial r^2} Y_n(q_2 b) + \frac{1}{b} \frac{\partial}{\partial r} Y_n(q_2 b) - \frac{n^2}{b^2} Y_n(q_2 b) \right), \quad (219)$$

$$C(6, 5) = ik\mu_2 \left(\frac{\partial}{\partial r} J_{n+1}(q_2 b) - J_{n+1}(q_2 b) \left(\frac{1+n}{b} \right) \right), \quad (220)$$

$$C(6, 6) = ik\mu_2 \left(\frac{\partial}{\partial r} Y_{n+1}(q_2 b) - Y_{n+1}(q_2 b) \left(\frac{1+n}{b} \right) \right), \quad (221)$$

$$C(6, 7) = -\frac{2\mu_1 n}{b} \left(\frac{1}{b} J_n(p_1 b) - \frac{\partial}{\partial r} J_n(p_1 b) \right), \quad (222)$$

$$C(6, 8) = -\frac{2\mu_1 n}{b} \left(\frac{1}{b} Y_n(p_1 b) - \frac{\partial}{\partial r} Y_n(p_1 b) \right), \quad (223)$$

$$C(6, 9) = -\mu_1 \left(-\frac{\partial^2}{\partial r^2} J_n(q_1 b) + \frac{1}{b} \frac{\partial}{\partial r} J_n(q_1 b) - \frac{n^2}{b^2} J_n(q_1 b) \right), \quad (224)$$

$$C(6, 10) = -\mu_1 \left(-\frac{\partial^2}{\partial r^2} Y_n(q_1 b) + \frac{1}{b} \frac{\partial}{\partial r} Y_n(q_1 b) - \frac{n^2}{b^2} Y_n(q_1 b) \right), \quad (225)$$

$$C(6, 11) = -ik\mu_1 \left(\frac{\partial}{\partial r} J_{n+1}(q_1 b) - J_{n+1}(q_1 b) \left(\frac{1+n}{b} \right) \right), \quad (226)$$

$$C(6, 12) = -ik\mu_1 \left(\frac{\partial}{\partial r} Y_{n+1}(q_1 b) - Y_{n+1}(q_1 b) \left(\frac{1+n}{b} \right) \right), \quad (227)$$

and

$$C(6, 13) = 0. \quad (228)$$

From boundary condition 7,

$$C(7, 1) = \frac{\partial}{\partial r} J_n(p_2 b), \quad (229)$$

$$C(7, 2) = \frac{\partial}{\partial r} Y_n(p_2 b), \quad (230)$$

$$C(7, 3) = \frac{n}{b} J_n(q_2 b), \quad (231)$$

$$C(7, 4) = \frac{n}{b} Y_n(q_2 b), \quad (232)$$

$$C(7, 5) = ik J_{n+1}(q_2 b), \quad (233)$$

$$C(7, 6) = ik Y_{n+1}(q_2 b), \quad (234)$$

$$C(7, 7) = -\frac{\partial}{\partial r} (J_n(p_1 b)), \quad (235)$$

$$C(7, 8) = -\frac{\partial}{\partial r} (Y_n(p_1 b)), \quad (236)$$

$$C(7, 9) = -\frac{n}{b} J_n(q_1 b), \quad (237)$$

$$C(7, 10) = -\frac{n}{b} Y_n(q_1 b), \quad (238)$$

$$C(7, 11) = -ik J_{n+1}(q_1 b), \quad (239)$$

$$C(7, 12) = -ik Y_{n+1}(q_1 b), \quad (240)$$

and

$$C(7, 13) = 0. \quad (241)$$

From boundary condition 8,

$$C(8, 1) = -\frac{n}{b}J_n(p_2b), \quad (242)$$

$$C(8, 2) = -\frac{n}{b}Y_n(p_2b), \quad (243)$$

$$C(8, 3) = -\frac{\partial}{\partial r}J_n(q_2b), \quad (244)$$

$$C(8, 4) = -\frac{\partial}{\partial r}Y_n(q_2b), \quad (245)$$

$$C(8, 5) = ikJ_{n+1}(q_2b), \quad (246)$$

$$C(8, 6) = ikY_{n+1}(q_2b), \quad (247)$$

$$C(8, 7) = \frac{n}{b}J_n(p_1b), \quad (248)$$

$$C(8, 8) = \frac{n}{b}Y_n(p_1b), \quad (249)$$

$$C(8, 9) = \frac{\partial}{\partial r}J_n(q_1b), \quad (250)$$

$$C(8, 10) = \frac{\partial}{\partial r}Y_n(q_1b), \quad (251)$$

$$C(8, 11) = -ikJ_{n+1}(q_1b), \quad (252)$$

$$C(8, 12) = -ikY_{n+1}(q_1b), \quad (253)$$

and

$$C(8, 13) = 0. \quad (254)$$

From boundary condition 9,

$$C(9, 1) = ikJ_n(p_2b), \quad (255)$$

$$C(9, 2) = ikY_n(p_2b), \quad (256)$$

$$C(9, 3) = 0, \quad (257)$$

$$C(9, 4) = 0, \quad (258)$$

$$C(9, 5) = -\frac{\partial}{\partial r}J_{n+1}(q_2b) - \frac{n+1}{b}J_{n+1}(q_2b), \quad (259)$$

$$C(9, 6) = -\frac{\partial}{\partial r}Y_{n+1}(q_2b) - \frac{n+1}{b}Y_{n+1}(q_2b), \quad (260)$$

$$C(9, 7) = -ikJ_n(p_1b), \quad (261)$$

$$C(9, 8) = -ikY_n(p_1b), \quad (262)$$

$$C(9, 9) = 0, \quad (263)$$

$$C(9, 10) = 0, \quad (264)$$

$$C(9, 11) = \frac{\partial}{\partial r}J_{n+1}(q_1b) + \frac{n+1}{b}J_{n+1}(q_1b), \quad (265)$$

$$C(9, 12) = \frac{\partial}{\partial r}Y_{n+1}(q_1b) + \frac{n+1}{b}Y_{n+1}(q_1b), \quad (266)$$

and

$$C(9, 13) = 0. \quad (267)$$

From boundary condition 10,

$$C(10, 1) = 0, \quad (268)$$

$$C(10, 2) = 0, \quad (269)$$

$$C(10, 3) = 0, \quad (270)$$

$$C(10, 4) = 0, \quad (271)$$

$$C(10, 5) = 0, \quad (272)$$

$$C(10, 6) = 0, \quad (273)$$

$$C(10, 7) = (\lambda_1 + 2\mu_1) \frac{\partial^2}{\partial r^2} J_n(p_1 a) + \frac{\lambda_1}{a} \frac{\partial}{\partial r} J_n(p_1 a) - \lambda_1 J_n(p_1 a) \left(\frac{n^2}{a^2} + k^2 \right), \quad (274)$$

$$C(10, 8) = (\lambda_1 + 2\mu_1) \frac{\partial^2}{\partial r^2} Y_n(p_1 a) + \frac{\lambda_1}{a} \frac{\partial}{\partial r} Y_n(p_1 a) - \lambda_1 Y_n(p_1 a) \left(\frac{n^2}{a^2} + k^2 \right), \quad (275)$$

$$C(10, 9) = -2\mu_1 \frac{n}{a^2} \left(J_n(q_1 a) - a \frac{\partial}{\partial r} J_n(q_1 a) \right), \quad (276)$$

$$C(10, 10) = -2\mu_1 \frac{n}{a^2} \left(Y_n(q_1 a) - a \frac{\partial}{\partial r} Y_n(q_1 a) \right), \quad (277)$$

$$C(10, 11) = i2\mu_1 k \frac{\partial}{\partial r} J_{n+1}(q_1 a), \quad (278)$$

$$C(10, 12) = i2\mu_1 k \frac{\partial}{\partial r} Y_{n+1}(q_1 a), \quad (279)$$

and

$$C(10, 13) = \rho_i \omega^2 D J_n(g_1 a). \quad (280)$$

From boundary condition 11,

$$C(11, 1) = 0, \quad (281)$$

$$C(11, 2) = 0, \quad (282)$$

$$C(11, 3) = 0, \quad (283)$$

$$C(11, 4) = 0, \quad (284)$$

$$C(11, 5) = 0, \quad (285)$$

$$C(11, 6) = 0, \quad (286)$$

$$C(11, 7) = i2\mu_1 k \frac{\partial}{\partial r} J_n(p_1 a), \quad (287)$$

$$C(11, 8) = i2\mu_1 k \frac{\partial}{\partial r} Y_n(p_1 a), \quad (288)$$

$$C(11, 9) = \frac{i\mu_1 kn}{a} J_n(q_1 a), \quad (289)$$

$$C(11, 10) = \frac{i\mu_1 kn}{a} Y_n(q_1 a), \quad (290)$$

$$C(11, 11) = \mu_1 \left(J_{n+1}(q_1 a) \left(\frac{n+1}{a^2} - k^2 \right) - \frac{\partial}{\partial r} J_{n+1}(q_1 a) \left(\frac{n+1}{a} \right) - \frac{\partial^2}{\partial r^2} J_{n+1}(q_1 a) \right), \quad (291)$$

$$C(11, 12) = \mu_1 \left(Y_{n+1}(q_1 a) \left(\frac{n+1}{a^2} - k^2 \right) - \frac{\partial}{\partial r} Y_{n+1}(q_1 a) \left(\frac{n+1}{a} \right) - \frac{\partial^2}{\partial r^2} Y_{n+1}(q_1 a) \right), \quad (292)$$

and

$$C(11, 13) = 0. \quad (293)$$

From boundary condition 12,

$$C(12, 1) = 0, \quad (294)$$

$$C(12, 2) = 0, \quad (295)$$

$$C(12, 3) = 0, \quad (296)$$

$$C(12, 4) = 0, \quad (297)$$

$$C(12, 5) = 0, \quad (298)$$

$$C(12, 6) = 0, \quad (299)$$

$$C(12, 7) = \frac{2\mu_1 n}{a} \left(\frac{1}{a} J_n(p_1 a) - \frac{\partial}{\partial r} J_n(p_1 a) \right), \quad (300)$$

$$C(12, 8) = \frac{2\mu_1 n}{a} \left(\frac{1}{a} Y_n(p_1 a) - \frac{\partial}{\partial r} Y_n(p_1 a) \right), \quad (301)$$

$$C(12, 9) = \mu_1 \left(-\frac{\partial^2}{\partial r^2} J_n(q_1 a) + \frac{1}{a} \frac{\partial}{\partial r} J_n(q_1 a) - \frac{n^2}{a^2} J_n(q_1 a) \right), \quad (302)$$

$$C(12, 10) = \mu_1 \left(-\frac{\partial^2}{\partial r^2} Y_n(q_1 a) + \frac{1}{a} \frac{\partial}{\partial r} Y_n(q_1 a) - \frac{n^2}{a^2} Y_n(q_1 a) \right), \quad (303)$$

$$C(12, 11) = ik\mu_1 \left(\frac{\partial}{\partial r} J_{n+1}(q_1 a) - J_{n+1}(q_1 a) \left(\frac{1+n}{a} \right) \right), \quad (304)$$

$$C(12, 12) = ik\mu_1 \left(\frac{\partial}{\partial r} Y_{n+1}(q_1 a) - Y_{n+1}(q_1 a) \left(\frac{1+n}{a} \right) \right), \quad (305)$$

and

$$C(12, 13) = 0. \quad (306)$$

From boundary condition 13,

$$C(13, 1) = 0, \quad (307)$$

$$C(13, 2) = 0, \quad (308)$$

$$C(13, 3) = 0, \quad (309)$$

$$C(13, 4) = 0, \quad (310)$$

$$C(13, 5) = 0, \quad (311)$$

$$C(13, 6) = 0, \quad (312)$$

$$C(13, 7) = \frac{\partial}{\partial r} J_n(p_1 a), \quad (313)$$

$$C(13, 8) = \frac{\partial}{\partial r} Y_n(p_1 a), \quad (314)$$

$$C(13, 9) = \frac{n}{a} J_n(q_1 a), \quad (315)$$

$$C(13, 10) = \frac{n}{a} Y_n(q_1 a), \quad (316)$$

$$C(13, 11) = ik J_{n+1}(q_1 a), \quad (317)$$

$$C(13, 12) = ik Y_{n+1}(q_1 a), \quad (318)$$

and

$$C(13, 13) = -\frac{\partial}{\partial r} J_n(g_1 a). \quad (319)$$

SOLUTION METHODOLOGY

As discussed in the previous sections, the system matrices in equations (85) and (150) provide the undetermined constants that allow for the evaluation of the displacement potentials directly from equations (26), (54), (58), (66), and (70). At this point we can evaluate all of the dynamic quantities of the composite systems, i.e., the single- or two-layer cylinders with fluids. At any cylinder radius, the stresses can be evaluated with equations (39) through (41), the strains with equations (42) through (44), and the displacements with equations (45) through (47). Additionally, the inner fluid pressure field can be evaluated with equations (67) and (71), and the outer fluid pressure field with equations (55) and (59). Fluid velocities can be evaluated in a similar fashion. The Bessel functions are evaluated with the series representations given in appendix A, and the necessary derivatives are formed with the relations given in appendix B. The equations used for calculating the output quantities are given in appendix C. The output quantity is normalized by the particular excitation chosen (equations (85) and (150) are evaluated for only one nonzero excitation at a time). Normalizing the output quantity by the excitation casts the results in a transfer surface when computation is over a range of wavenumbers and frequencies.

The two-layer model is compared against the single-layer model for an equivalent cylinder in appendix D. The two simulations, which are shown overlaying each other, provide a verification of the agreement between the elasticity models.

NUMERICAL CONSIDERATIONS

The procedure described above is repeated over the domain of wavenumber and frequency at regular intervals. The interval used for the simulations extending to 5000 or 8000 Hz is 20.0 Hz and the interval used for the 60,000-Hz simulations is 200 Hz. The wavenumber interval used for the 5000-Hz simulations is 0.257 rad/m; 1.545 rad/m is used for all other simulations. These intervals produce transfer surfaces ranging from 32,000 to 194,000 points each.

When sharp resonances are present, a visual/numerical artifact is apparent in the simulations due to the finite wavenumber and frequency interval used for evaluating the closed-form

solution. This is most evident in the wire frame surface representation of the simulations, which is shown later in the report. Small asymmetries with respect to wavenumber are evident in the magnitude cuts as well. The first problem, which arises when a Cartesian wire frame surface algorithm is used with sloped topography in the xy plane, is inevitable because of the graphics software that is used to display the wire frame surfaces. The second problem results when, for a given frequency, slightly different wavenumber locations are being calculated in the minus and plus wavenumber half-planes. This problem could be minimized by decreasing both the frequency and wavenumber interval by several orders of magnitude, although a corresponding increase in calculation time would result. The image sizes were selected as an appropriate compromise between calculation time and the requirement to convey the physics embodied in the simulations.

Evaluation of the equations requires the use of the quad precision complex data type. The language of choice is FORTRAN (version 3.0) running on a Sun Microsystems SPARC Station model 10SX-512, Operating System Solaris 2.3. The calculation time varies from 45 minutes to 6 hours.

The FORTRAN algorithms developed to produce the simulations contained here are published in a separate document,¹² which is available via e-mail at *peloquin@cascade.nl.nuwc.navy.mil*.

RESULTS

SINGLE-LAYER CYLINDER SIMULATIONS—RADIAL PRESSURE EXCITATIONS

Types of Wave Propagation

In review, an infinite isotropic elastic media will support two distinct types of waves: the dilatational wave and the transverse (or shear) wave. The phase velocity of the dilatational wave is given by equation (320) as

$$c_l = \sqrt{\frac{E_c (1 - \nu_c)}{\rho_c (1 + \nu_c) (1 - 2\nu_c)}}. \quad (320)$$

For a dilatational wave, the particle displacement and the wave propagation vector, which defines the direction of energy propagation, are coincident. For the wavenumber and frequency range shown in the simulations, the manifestation of this wave in the long thin cylinder produces a modified phase velocity, known as the bar velocity or extensional wave phase velocity. It is given in equation (321) as

$$c_e = \sqrt{\frac{E_c}{\rho_c}}. \quad (321)$$

The other wave, the transverse (or shear) wave, is characterized by a particle displacement that is perpendicular to the wave propagation vector. An expression for the shear modulus in terms of the Young's modulus and Poisson ratio of a material is given by equation (322) as

$$\mu_c = \frac{E_c}{2(1 + \nu_c)}. \quad (322)$$

From equation (11), the shear wave phase velocity is calculated. The phase velocities of the dilatational and extensional waves of the cylinder and the dilatational wave of the fluids are listed in table 1 and are based on the data provided in table 2.

Table 1. Single-Layer Cylinder/Fluid Phase Velocities

Wave Type	Phase Velocity (m/sec)
Dilatational Wave c_l	447.51
Transverse Wave c_t	182.68
Extensional Wave c_e	305.71
Dilatational Wave c_i, c_s	1500.0

The system under consideration in this report is infinite in longitudinal coordinate x ; however, it is bounded in r and θ . Furthermore, the cylinder is in contact with fluids. This composite system will produce branches of wave propagation that are related to the dilatational and transverse waves of the media but which do not necessarily propagate at the same velocity. The velocities listed in table 1 will serve as a guide for analyzing the responses that follow.

Mechanical damping in the cylinder is incorporated by the use of the structural loss factor ζ_j . This structural loss factor represents the fraction of the Young's modulus that causes the strain response to be out of phase with the applied stress:

$$E_j^* = E_j (1 + i\zeta_j) , \quad (323)$$

where j equals 1 or 2, corresponding to the first and second layers of the cylinder, respectively. It is therefore possible, with the formulation presented here, to have different structural loss factors for each cylinder. This is, in fact, how the two-layer simulations were performed.

Cylinder and Fluid Material Properties

The material properties for the single-layer cylinder/fluid simulations are listed in tables 2 through 5. The values listed approximate water as both an inner and an outer fluid. The cylinder properties are those of urethane or rubber, much like an ordinary garden or fire hose.

Table 2. Single-Layer-Cylinder Properties—3.00-in. Diameter

Property	Definition
$E_1 = 1.0 \times 10^8 \frac{\text{N}}{\text{m}^2}$	Young's Modulus
$\zeta_1 = 0.3$	Structural Loss Factor
$\rho_1 = 1070 \frac{\text{kg}}{\text{m}^3}$	Density
$\nu_1 = 0.4$	Poisson's Ratio
$a = 1.200 \text{ in.}$	Inner Radius
$b = 1.500 \text{ in.}$	Outer Radius
$h_1 = 0.300 \text{ in.}$	Thickness

Table 3. Single-Layer-Cylinder Properties—0.670-in. Diameter

Property	Definition
$E_1 = 1.0 \times 10^8 \frac{\text{N}}{\text{m}^2}$	Young's Modulus
$\zeta_1 = 0.3$	Structural Loss Factor
$\rho_1 = 1070 \frac{\text{kg}}{\text{m}^3}$	Density
$\nu_1 = 0.4$	Poisson's Ratio
$a = 0.235 \text{ in.}$	Inner Radius
$b = 0.335 \text{ in.}$	Outer Radius
$h_1 = 0.100 \text{ in.}$	Thickness

Table 4. Single-Layer-Cylinder Outer Fluid Properties (Water)

Property	Definition
$\rho_s = 1000.0 \frac{\text{kg}}{\text{m}^3}$	Density
$c_s = 1500.0 \frac{\text{m}}{\text{sec}}$	Velocity of Sound

Table 5. Single-Layer-Cylinder Inner Fluid Properties (Water)

Property	Definition
$\rho_i = 1000.0 \frac{\text{kg}}{\text{m}^3}$	Density
$c_i = 1500.0 \frac{\text{m}}{\text{sec}}$	Velocity of Sound

Circumferential Order Shapes

For the simulations that follow, most of the significant branches of wave propagation will produce cylinder deformation shapes as depicted in figures 7 through 10. Figure 7 depicts the radial u -displacement that occurs in the cylinder as energy is propagating in the first branch of wave propagation, corresponding to circumferential order number $n = 0$. This first branch of wave propagation is commonly referred to as a breathing wave. Figure 8 depicts the longitudinal w -displacement that occurs in the cylinder as energy is propagating in the second branch of wave propagation, corresponding to circumferential order number $n = 0$. This second branch of wave propagation is commonly referred to as an extensional wave. The displacement shapes depicted in figures 9 ($n = 1$) and 10 ($n = 2$) cause the cylinder to undergo a state of bending.

The cylinder deformation in figures 7 through 10 has been magnified for the purpose of visualizing the deformation. It should be remembered that this is a small strain analysis, suitable for analyzing problems undergoing loading on an acoustic scale.

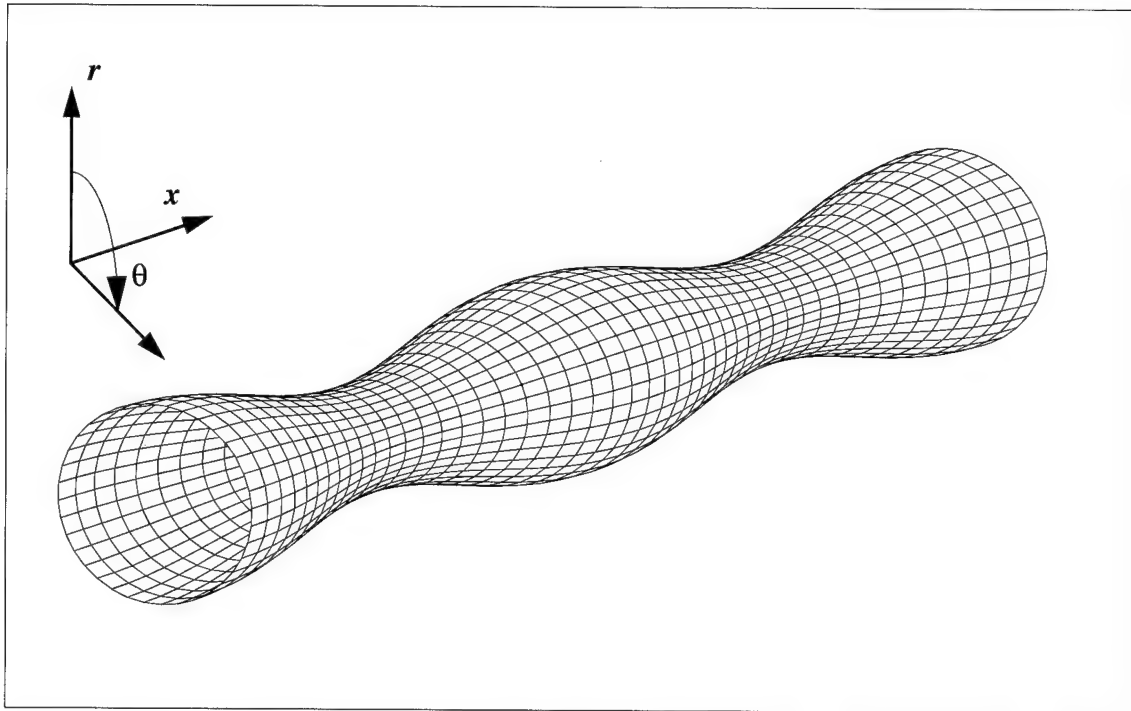


Figure 7. Circumferential Order Number $n = 0$, First Branch

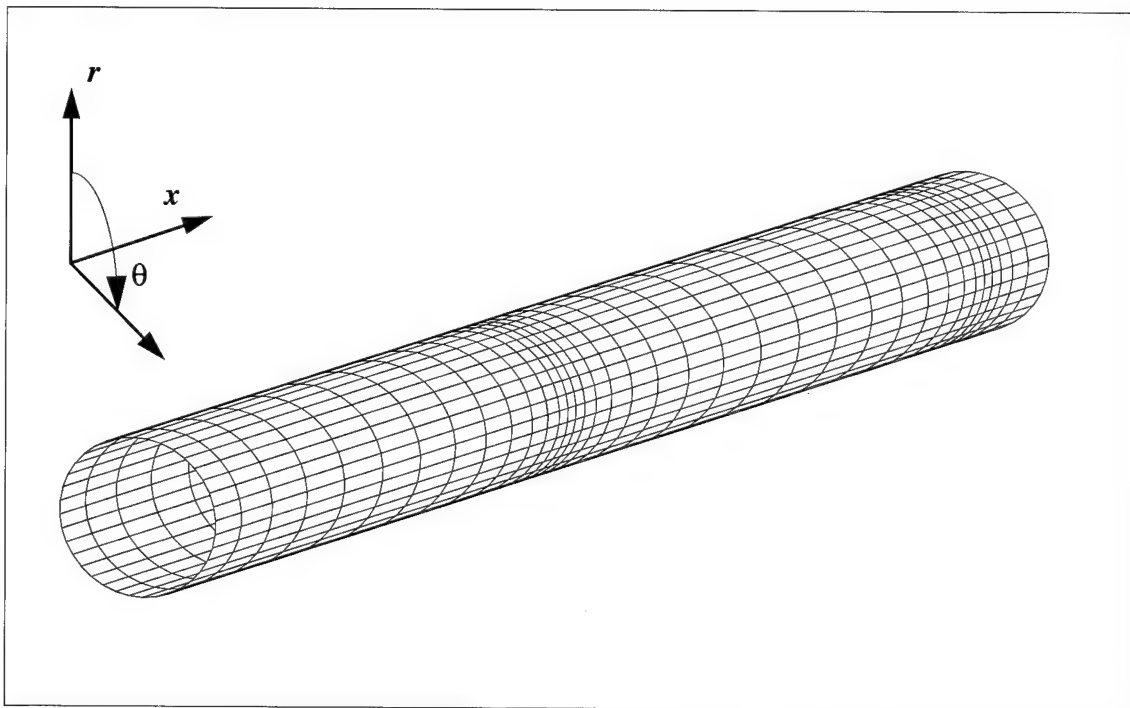


Figure 8. Circumferential Order Number $n = 0$, Second Branch

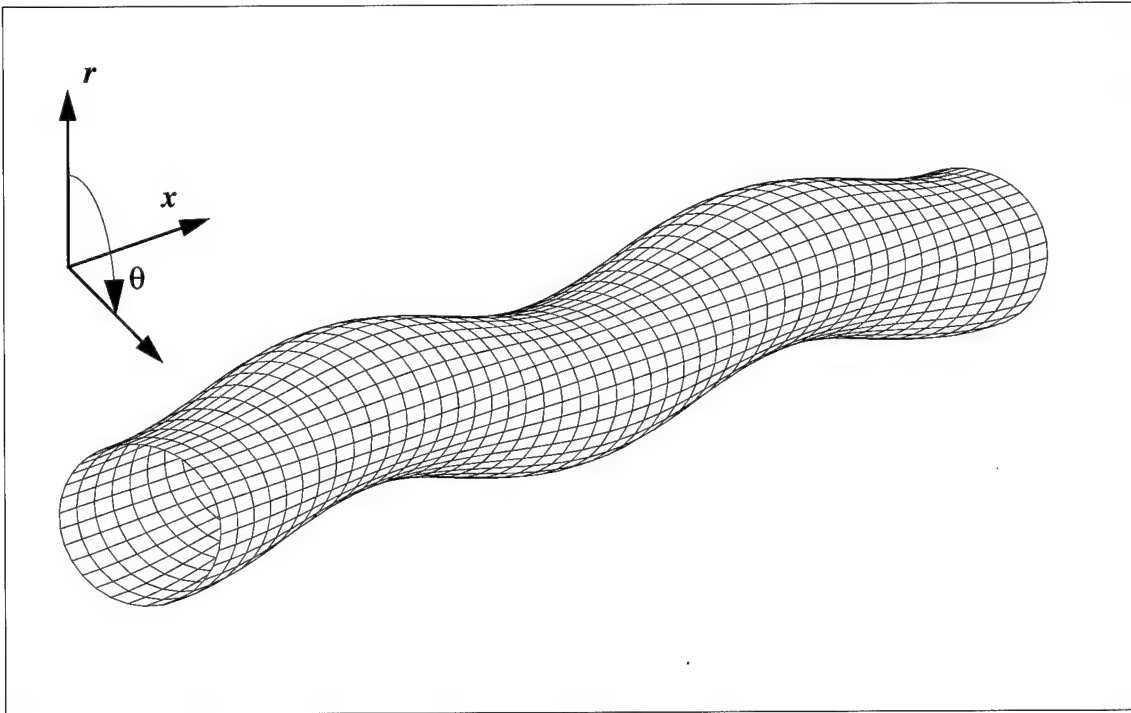


Figure 9. Circumferential Order Number $n = 1$, First Branch

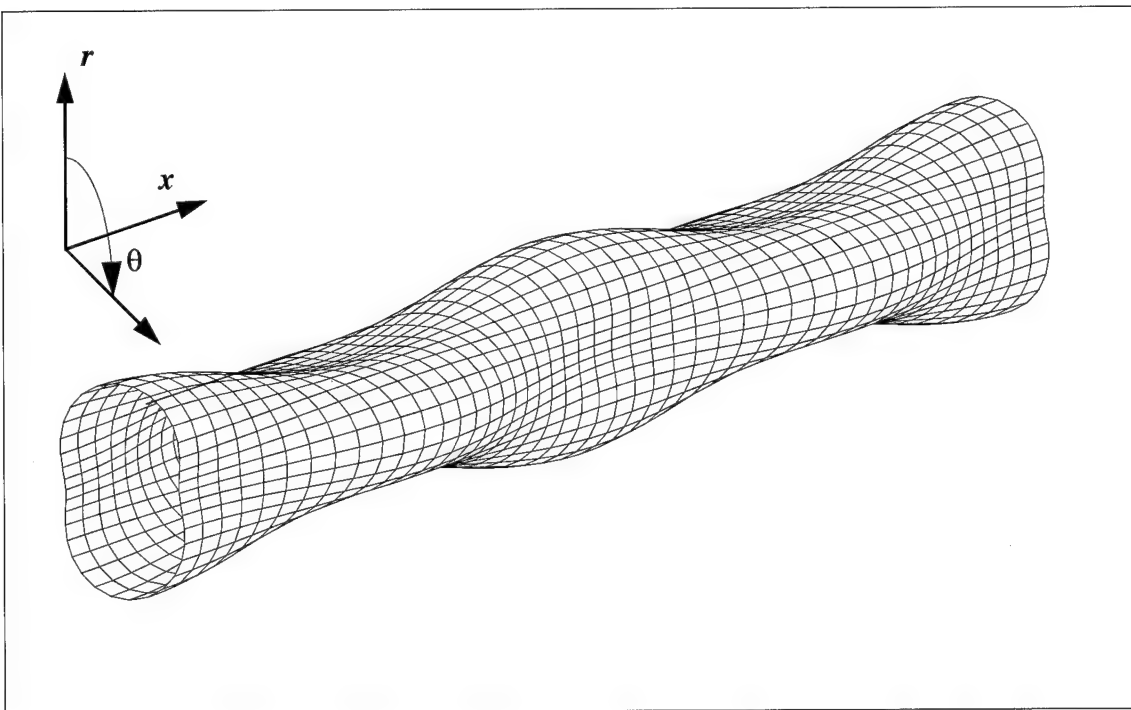


Figure 10. Circumferential Order Number $n = 2$, First Branch

Radial Stress Variation in the Cylinder Wall

This first set of simulations is performed for the data listed in tables 2, 4, and 5. The radial stress transfer surface is calculated at three different radial positions in figures 11, 12, and 13. These positions correspond to the outer, middle, and inner surface of the cylinder wall. In reality, the inner and outer radial positions are 0.01 inch from the actual free surface of the cylinder.

The curves plotted in figures 14 and 15 show the distribution and variation of radial stress as a function of radial position r within the cylinder wall. The principal assumptions made in shell theory,¹³ which ignore the variations of quantities across the cylinder wall thickness, are not made in elasticity theory. The model developed here does not make any assumptions that discard parts of the physical behavior of the system. As can be clearly observed in figures 14 and 15, the radial stress varies across the cylinder wall thickness.

In figure 15, the radial stress increases with decreasing diameter, which amplifies the stress level beneath the outer diameter of the cylinder. This behavior is consistent with the principle of conservation of energy owing to the fact that the circumferential area at a radial location within the cylinder thickness is actually less than the circumferential area at the cylinder outer diameter.

The radial stress boundary conditions imposed on the cylinder wall require the stress to vary from a value equal to the inner fluid pressure field at $r = a$ to a value equal to the outer fluid pressure field at $r = b$. This variation can be observed in the behavior of the curves in figure 14.

The other significant feature in the simulations is the resonance at approximately 2800 Hz, which is clearly apparent in figure 15. The cylinder is experiencing a predominantly radial vibration that is heavily influenced by the presence of the fluids in this case. This resonance will be discussed in some detail in a later section of this report.

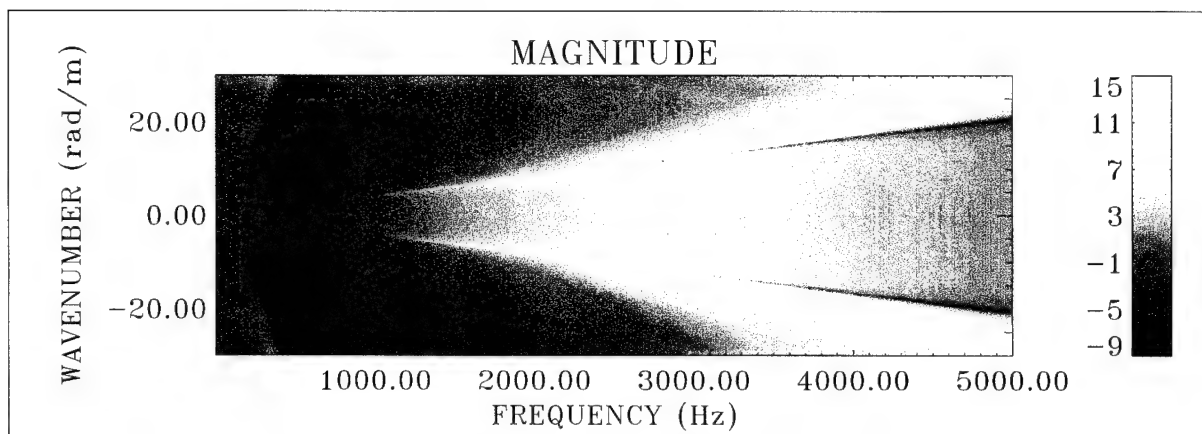


Figure 11. Radial Stress Transfer Surface With Magnitude = $10\text{Log}(\tau_{rr}(r_1)/P_o)^2$ at $r_1 = 1.49$ in. for Elasticity Model, Where $n = 0$ and Diameter = 3.00 in.

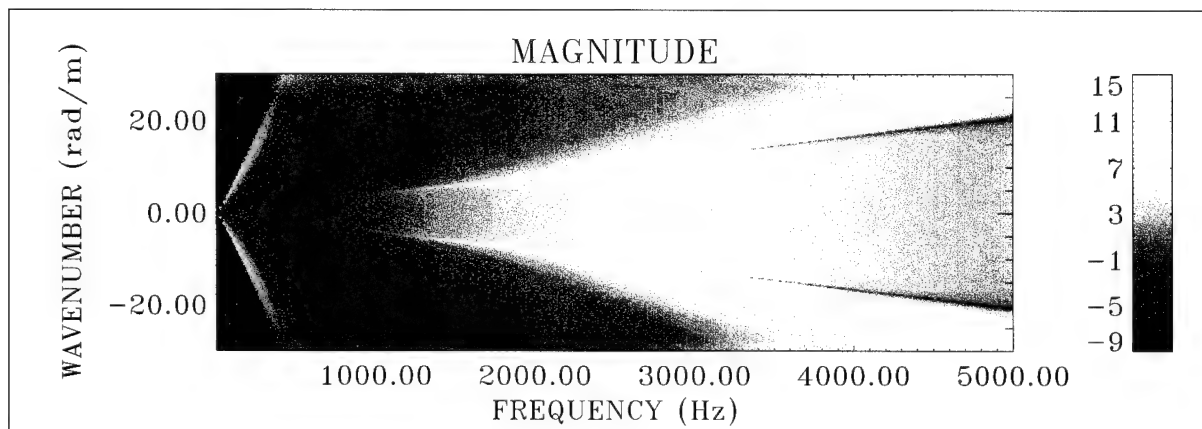


Figure 12. Radial Stress Transfer Surface With Magnitude = $10\text{Log}(\tau_{rr}(r_1)/P_o)^2$ at $r_1 = 1.35$ in. for Elasticity Model, Where $n = 0$ and Diameter = 3.00 in.

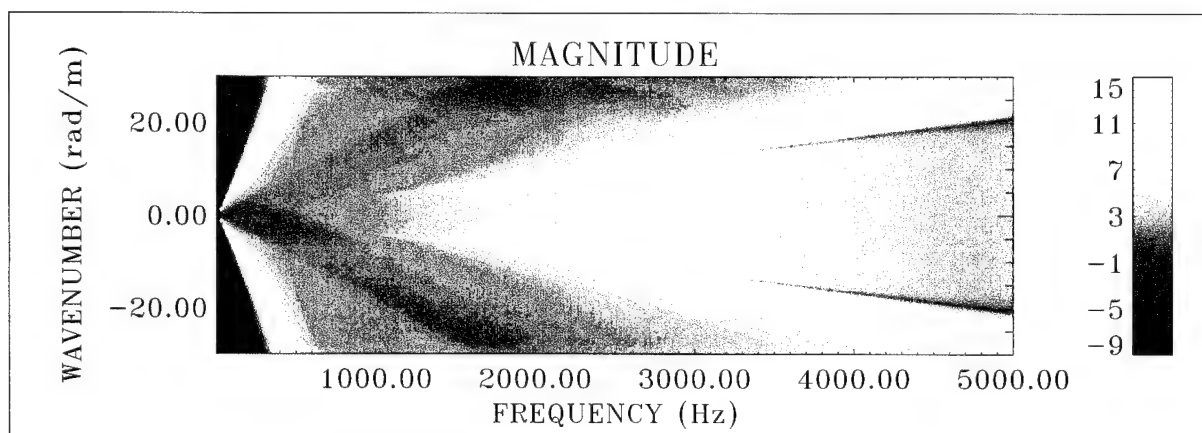
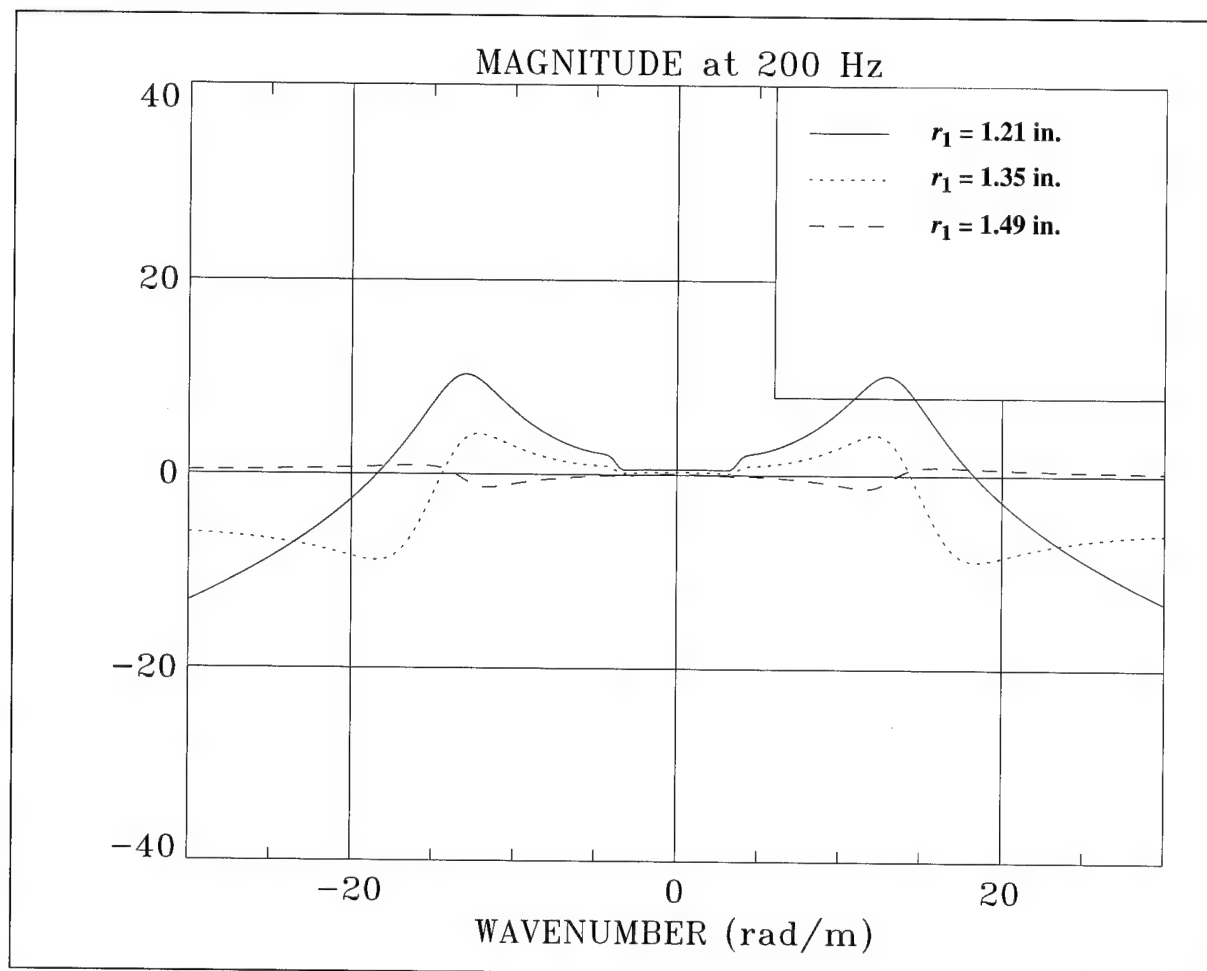
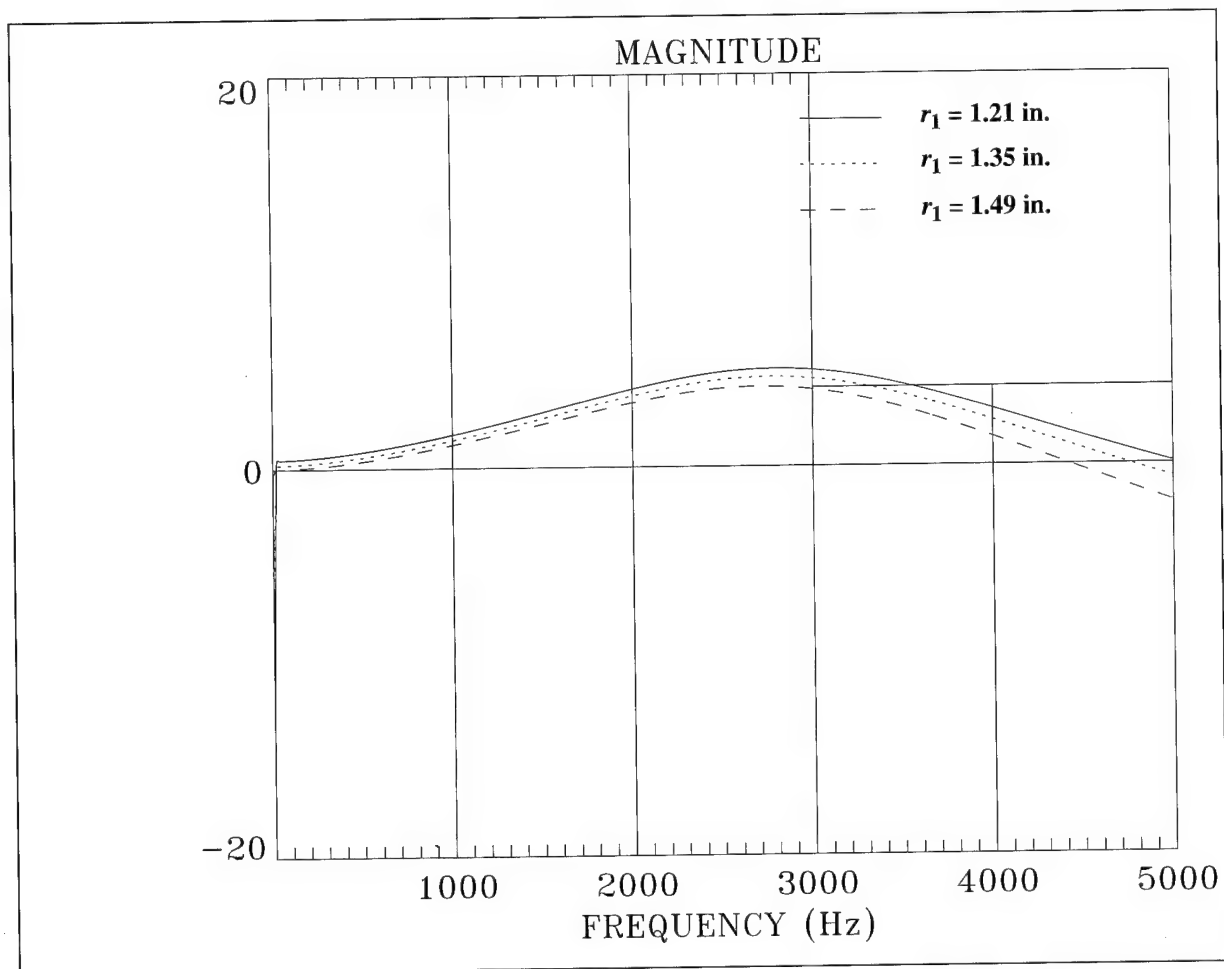


Figure 13. Radial Stress Transfer Surface With Magnitude = $10\text{Log}(\tau_{rr}(r_1)/P_o)^2$ at $r_1 = 1.21$ in. for Elasticity Model, Where $n = 0$ and Diameter = 3.00 in.



**Figure 14. Comparison of Radial Stress Transfer Surfaces With
Magnitude = $10\text{Log}(\tau_{rr}(r_1)/P_o)^2$ at Various r for Elasticity Model,
Where $n = 0$, Diameter = 3.00 in., and $f = 200$ Hz**



**Figure 15. Comparison of Radial Stress Transfer Surfaces With
Magnitude = $10\text{Log}(\tau_{rr}(r_1)/P_o)^2$ for Elasticity Model,
Where $n = 0$, Diameter = 3.00 in., and $k = 0$ rad/m**

Model Comparisons—3.00-Inch-Diameter Cylinder

In this section, we will compare the elasticity model developed in this report to the membrane shell and bending shell models presented in reference 13. As noted previously, the assumptions made for shell theory have limitations on the mean diameter-to-thickness ratio (which should be above 10 for accurate model behavior) as well as on the wavelength-to-diameter and wavelength-to-thickness ratios. The elasticity model represents the true behavior of the cylinder because it does not introduce simplifying assumptions for the elastic behavior of the material. Although it is acknowledged that the shell models will not always be in full agreement with the elasticity model, a further understanding of the fluid/structure interaction is obtained by investigating the agreement that does occur between the models for the 3.00-inch-outer-diameter cylinder (in this section) and the 0.670-inch-outer-diameter cylinder (in the following section).

Each simulation is displayed as a color image, where color indicates magnitude. For clarity, and in an effort to reveal the true character of the surface, the color image is also displayed as a wire frame surface directly below the corresponding color image.

Figures 16 through 21 are the simulations ($n = 0$) for the membrane shell, bending shell, and elasticity models, respectively. In figure 22, which is a comparison of the three models at $k = 0$, both shell models predict the resonance frequency of the cylinder to be higher than does the elasticity model. The shell models indicate the resonance frequency to be at approximately 11 kHz, while the elasticity model is indicating the resonance at 2870 Hz. The combination of urethanelike properties (cylinder) and water (fluids) causes the shell models to incorrectly predict the first radial resonance of the cylinder. If air had been chosen for the inner and outer fluids, the resonance frequencies of the models would have been in close agreement.

The breathing wave, evident in the three model types, is dispersive in all. Figures 23 and 24 compare the breathing wave resonance peaks at 200 and 600 Hz, respectively. The corresponding phase velocity for these two frequencies is 94 and 74 m/sec for the elasticity model, and 126 and 80 m/sec for the shell model. At high frequency, the character of the breathing wave in the membrane model is very different from both the bending shell and elasticity models. Above 1000 Hz, the breathing wave in the membrane model slows dramatically and

falls in amplitude relative to the other two models. In figure 23, at 80 rad/m, the membrane model begins to underpredict the transfer function roll-off, ultimately underpredicting the roll-off relative to the elasticity model prediction by approximately 40 dB at 300 rad/m.

The extensional wave is evident in the elasticity model of figure 24. It appears as low-level peaks on either side of $k = 0$ at a phase velocity of 291 m/sec and exhibits no dispersion. In figure 25, the extensional wave is more clearly visible at 100 rad/m; it is also visible in figure 20. Comparison of the three models in figure 25 indicates significant divergence of the shell solutions from the elasticity solutions above 20 rad/m.

The simulations for circumferential order number $n = 1$ are shown in figures 26 through 31. The first branch of wave propagation places the cylinder in a state of bending, as shown in the wire frame representation of figure 9. Two additional branches of wave propagation are visible in the simulations. The second branch has a cutoff frequency of approximately 1000 Hz and causes the longitudinal displacement to undergo one wavelength of variation around the circumference of the cylinder. The third branch has a cutoff frequency of approximately 2000 Hz, causing the circumferential displacement to undergo one wavelength of variation around the circumference of the cylinder. Both of these branches couple into the radial displacement, which develops a pressure in the inner fluid. However, these pressure field components are weak because of the magnitude of the damping ($\zeta_1 = 0.3$). The reader is referred to reference 13 for a complete set of figures depicting the deformation shapes of the cylinder for these branches of wave propagation. Figures 32 through 34 compare the three models at $k = 0$ and at various cuts in wavenumber. The resonant peak of the first branch of wave propagation compares favorably for all three models up to 600 Hz, as seen in figure 34. The membrane model's roll-off in wavenumber departs from the other two models by approximately 60 rad/m, and at 4500 Hz (figure 35) the significant divergence of the shell models from the elasticity model renders the shell models to be unacceptable predictors of the cylinder's behavior.

Figures 36 through 41 are the simulations for circumferential order number $n = 2$. We see from figures 36 and 42 that the membrane model will not support a cutoff frequency for the first branch of wave propagation. This first branch produces a deformation in the cylinder as shown

in figure 10. Two additional branches are visible, both with cutoff frequencies. Each produces the same kind of deformation in the shell as described for $n = 1$, only now there are two wavelengths of variation around the circumference. In figures 43 through 45, we see that the bending shell model is useful up to 600 Hz, diverging from the elasticity model only at higher frequencies.

To summarize, for the 3.00-inch-diameter cylinder considered here, the shell models are in good agreement with the elasticity model for the region extending to 1000 Hz and ± 75 rad/m. Outside of this region, the difference increases beyond 5 dB, and the elasticity solution should be used. For the $n = 0$ case, the fluid loading influences the first radial natural frequency of the shell models so dramatically that the error relative to the elasticity model is greater than a factor of three, as evidenced by figure 22. For the $n = 2$ case, the membrane model should not be used, owing to the misrepresentation of the behavior of the first branch (i.e., lack of cutoff frequency and appropriate branch structure). Although not shown here, similar behavior will occur with the membrane shell model for $n > 2$.

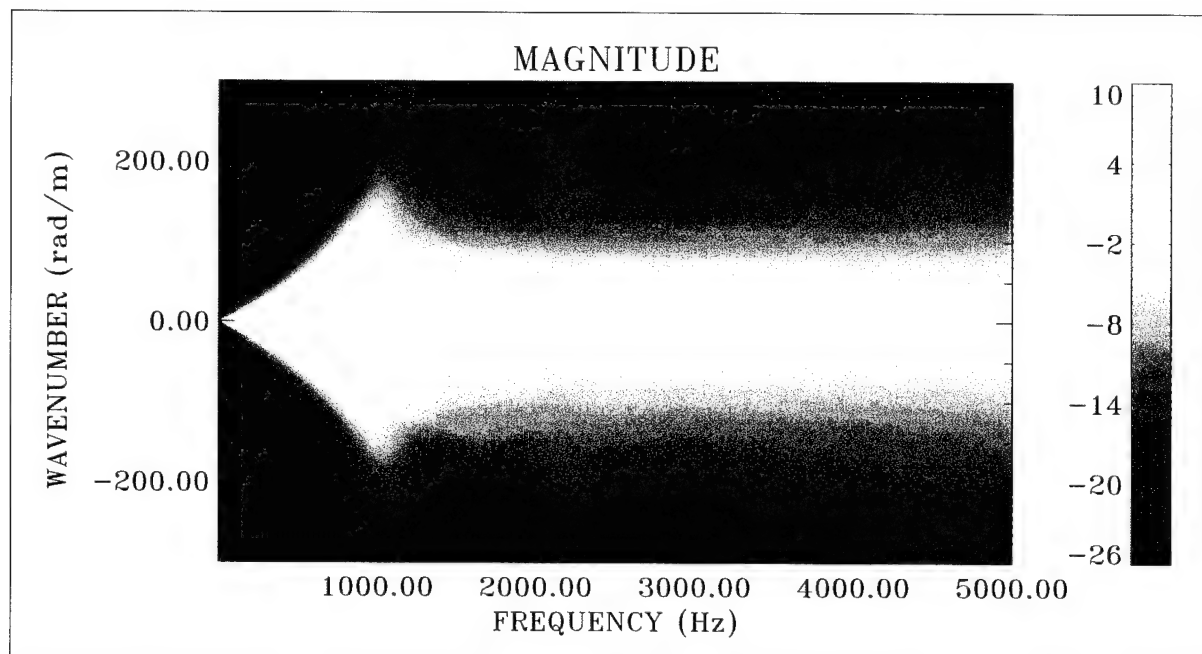


Figure 16. Pressure Transfer Surface With Magnitude = $10\text{Log}(P_i(r_1)/P_o)^2$ at $r_1 = 0.75$ in. for Membrane Shell Model, Where $n = 0$ and Diameter = 3.00 in. (Color Image)

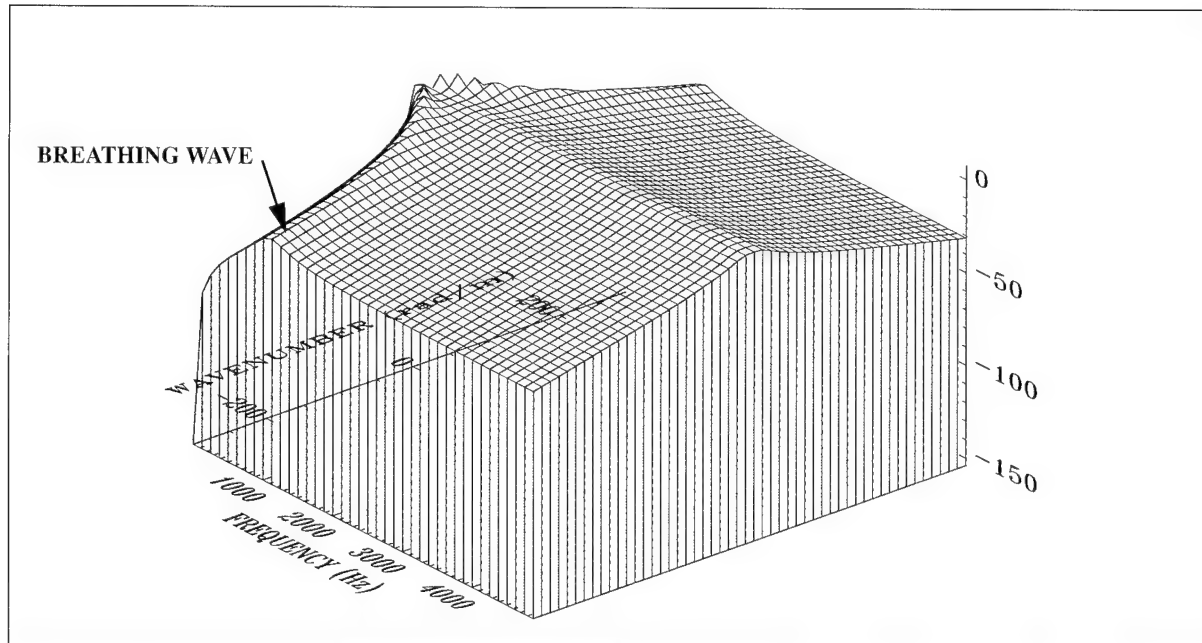


Figure 17. Pressure Transfer Surface With Magnitude = $10\text{Log}(P_i(r_1)/P_o)^2$ at $r_1 = 0.75$ in. for Membrane Shell Model, Where $n = 0$ and Diameter = 3.00 in. (Wire Frame Surface)

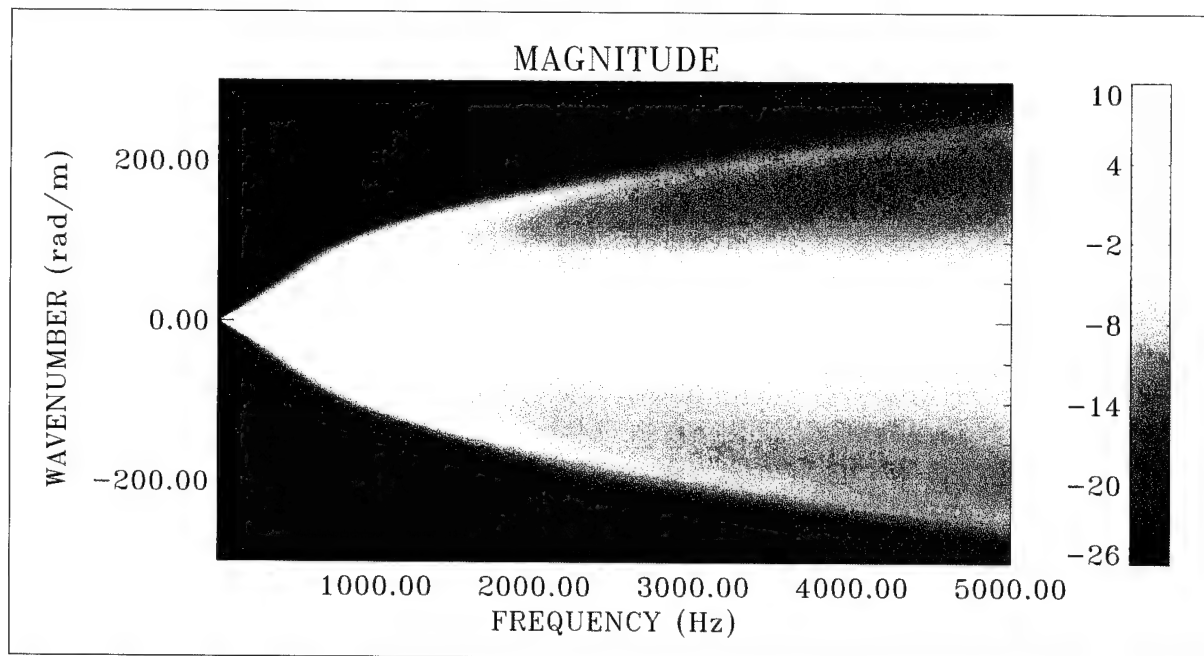


Figure 18. Pressure Transfer Surface With Magnitude = $10\text{Log}(P_i(r_1)/P_o)^2$ at $r_1 = 0.75$ in. for Bending Shell Model, Where $n = 0$ and Diameter = 3.00 in. (Color Image)

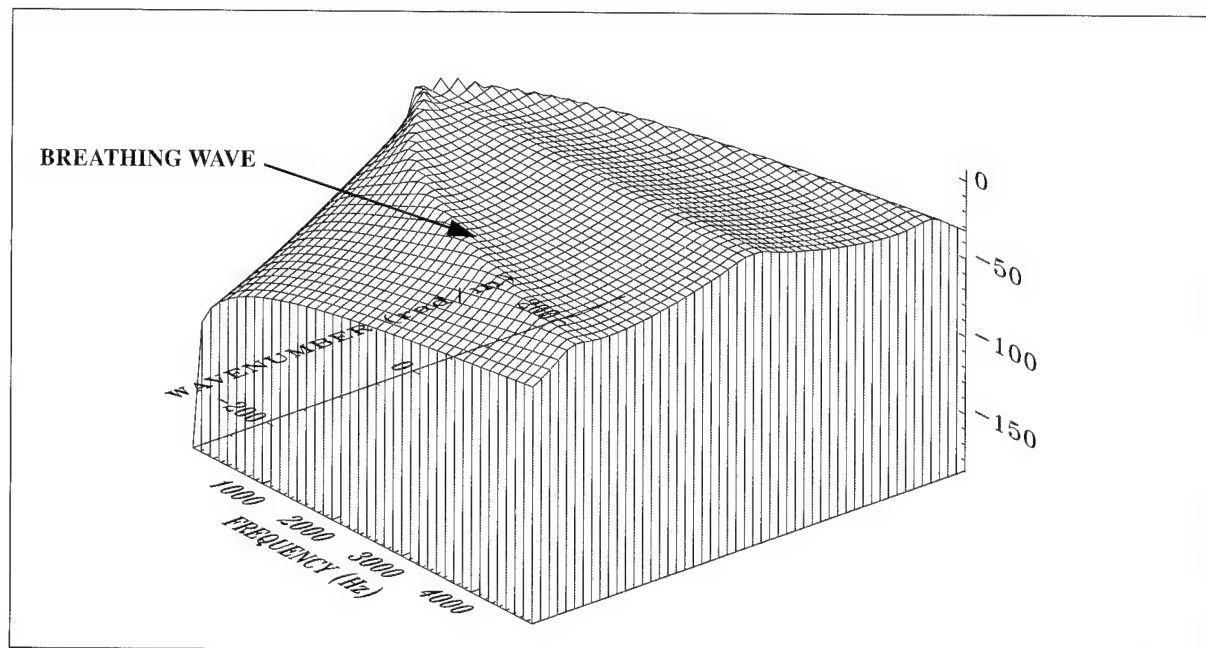


Figure 19. Pressure Transfer Surface With Magnitude = $10\text{Log}(P_i(r_1)/P_o)^2$ at $r_1 = 0.75$ in. for Bending Shell Model, Where $n = 0$ and Diameter = 3.00 in. (Wire Frame Surface)

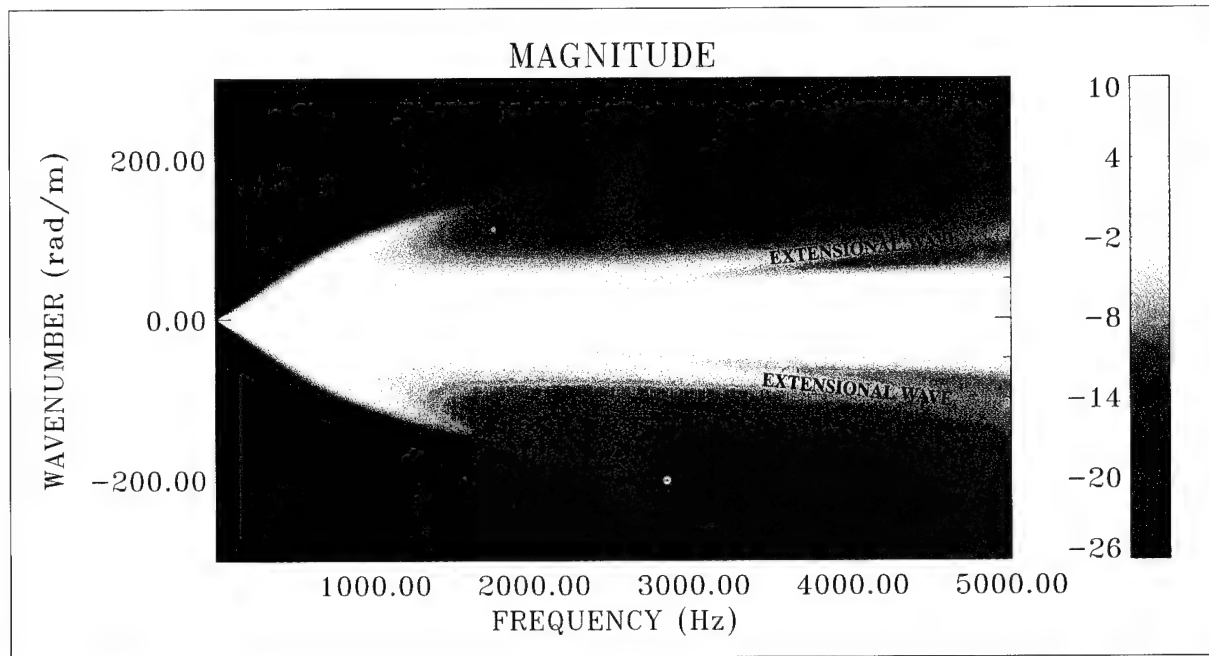


Figure 20. Pressure Transfer Surface With Magnitude = $10\text{Log}(P_i(r_1)/P_o)^2$ at $r_1 = 0.75$ in. for Elasticity Model, Where $n = 0$ and Diameter = 3.00 in. (Color Image)

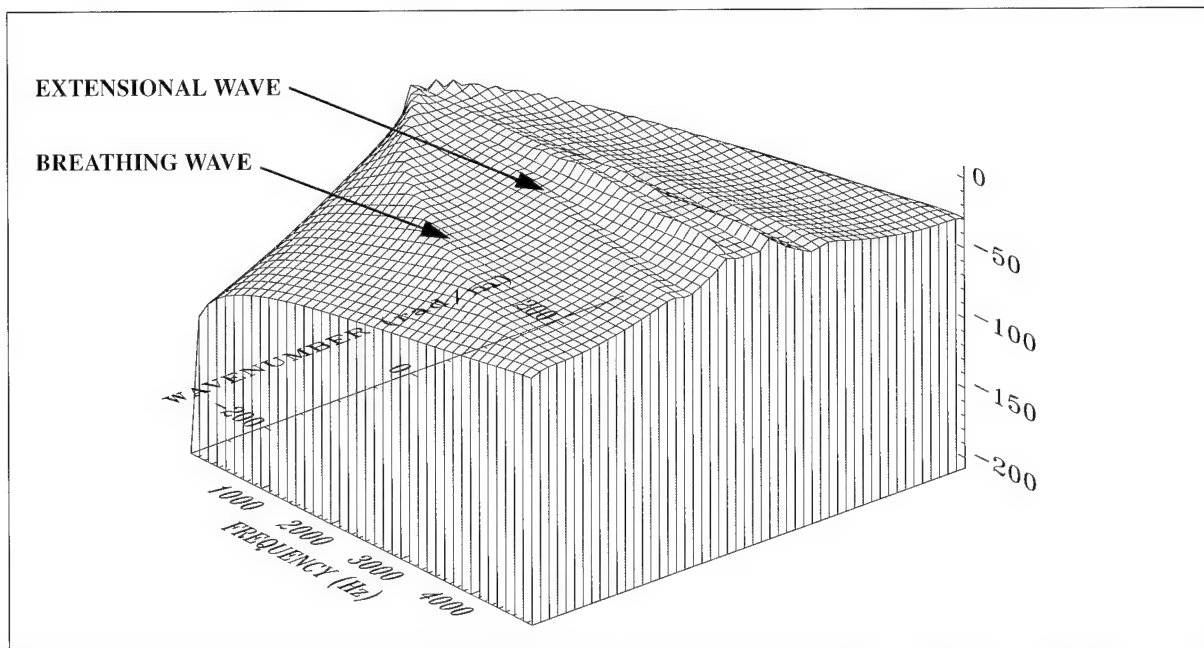


Figure 21. Pressure Transfer Surface With Magnitude = $10\text{Log}(P_i(r_1)/P_o)^2$ at $r_1 = 0.75$ in. for Elasticity Model, Where $n = 0$ and Diameter = 3.00 in. (Wire Frame Surface)

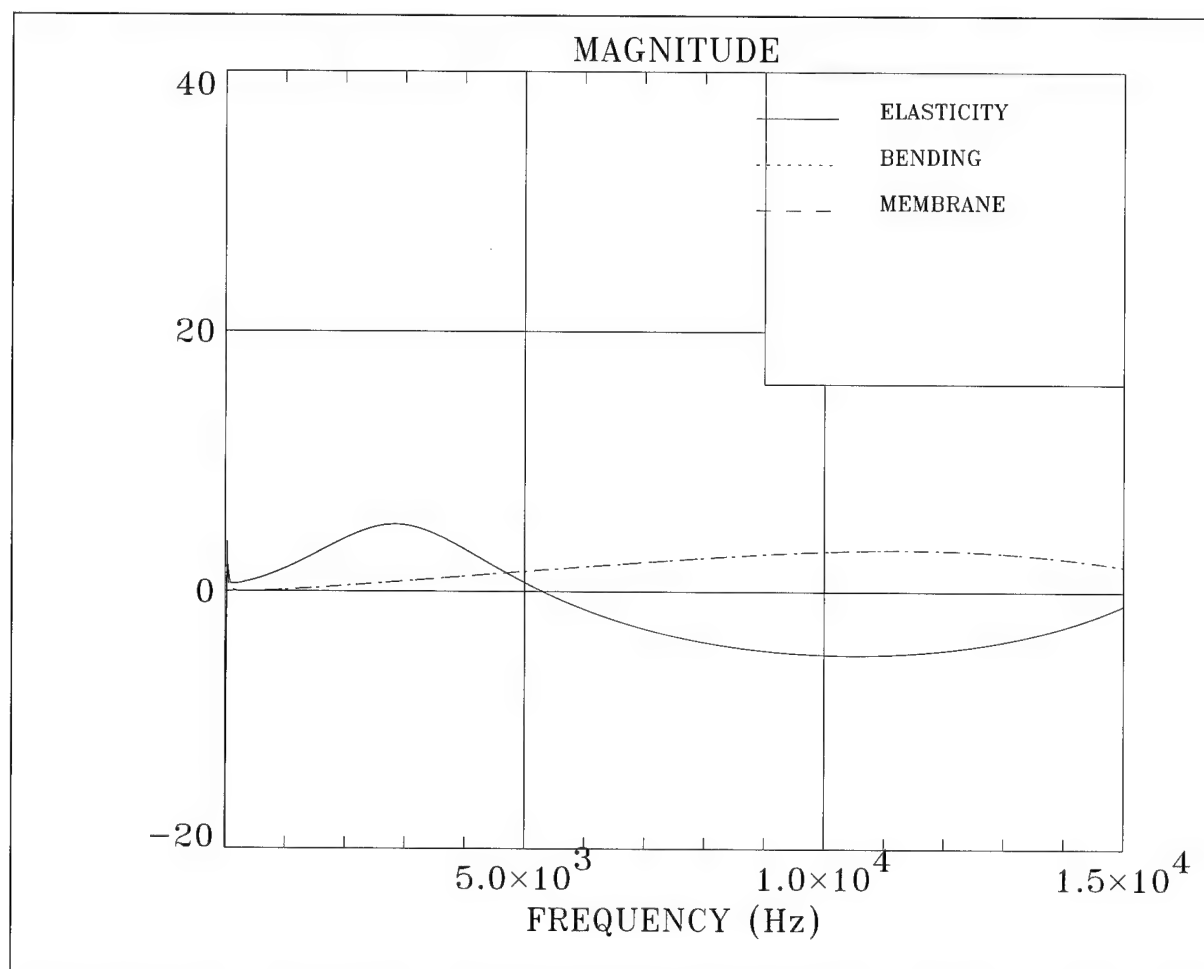
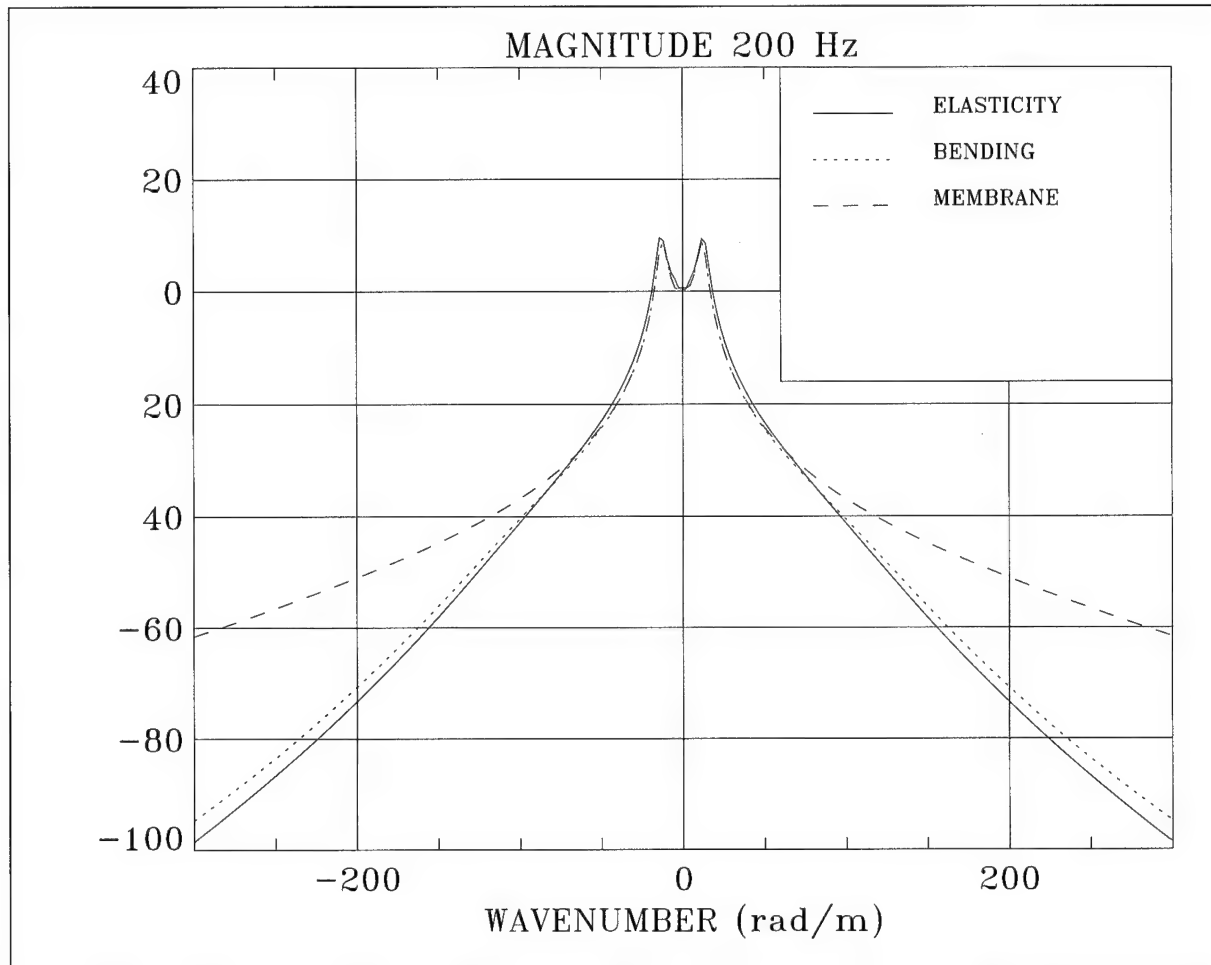
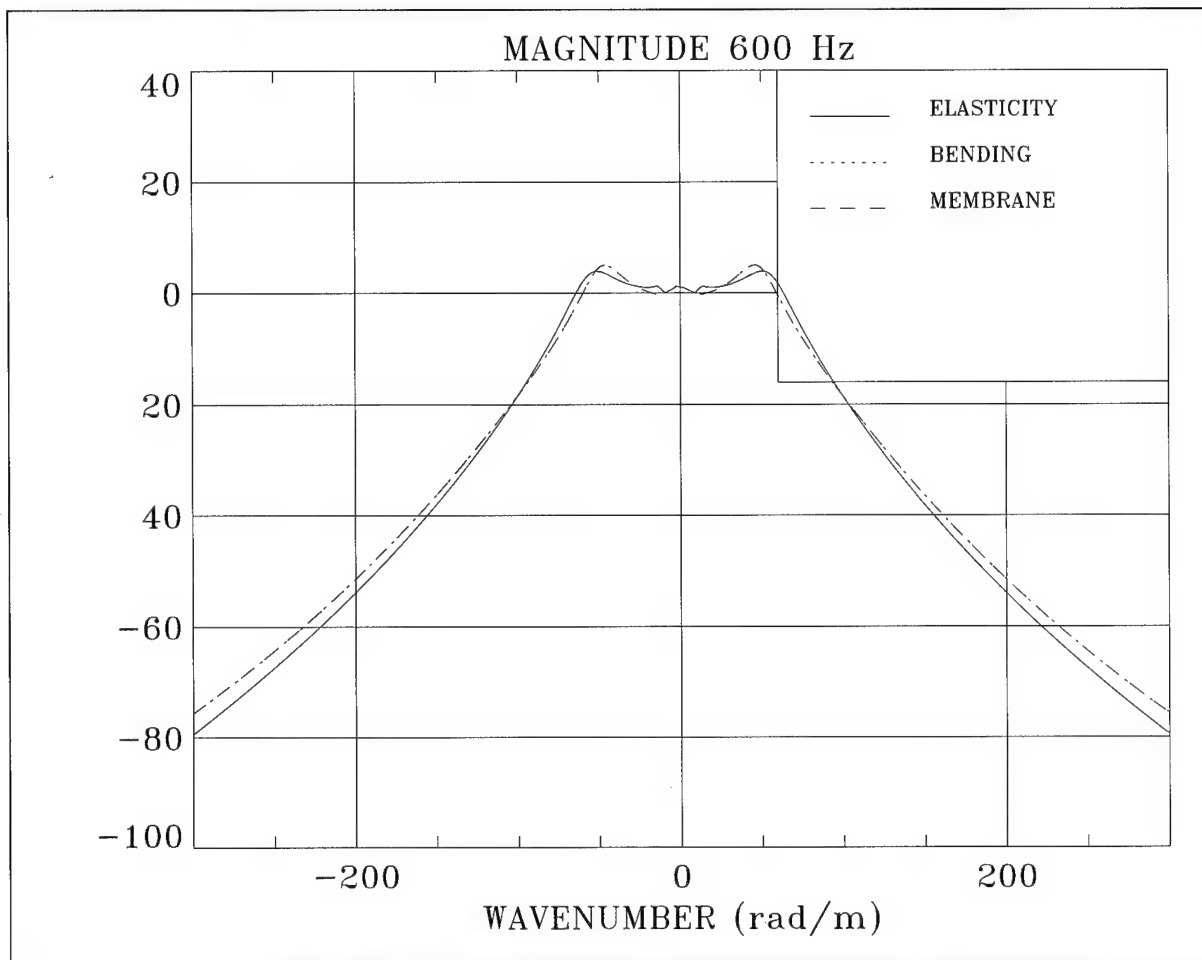


Figure 22. Model Comparison for Figures 16, 18, and 20 at Extended Frequency Range When Magnitude = $10\text{Log}(P_i(r_1)/P_o)^2$ at $r_1 = 0.75$ in. With $n = 0$, Diameter = 3.00 in., and $k = 0$ rad/m



**Figure 23. Model Comparison for Figures 16, 18, and 20 When
Magnitude = $10\text{Log}(P_i(r_1)/P_o)^2$ at $r_1 = 0.75$ in. With $n = 0$,
Diameter = 3.00 in., and $f = 200$ Hz**



**Figure 24. Model Comparison for Figures 16, 18, and 20 When
Magnitude = $10\text{Log}(P_i(r_1)/P_o)^2$ at $r_1 = 0.75$ in. With $n = 0$,
Diameter = 3.00 in., and $f = 600$ Hz**

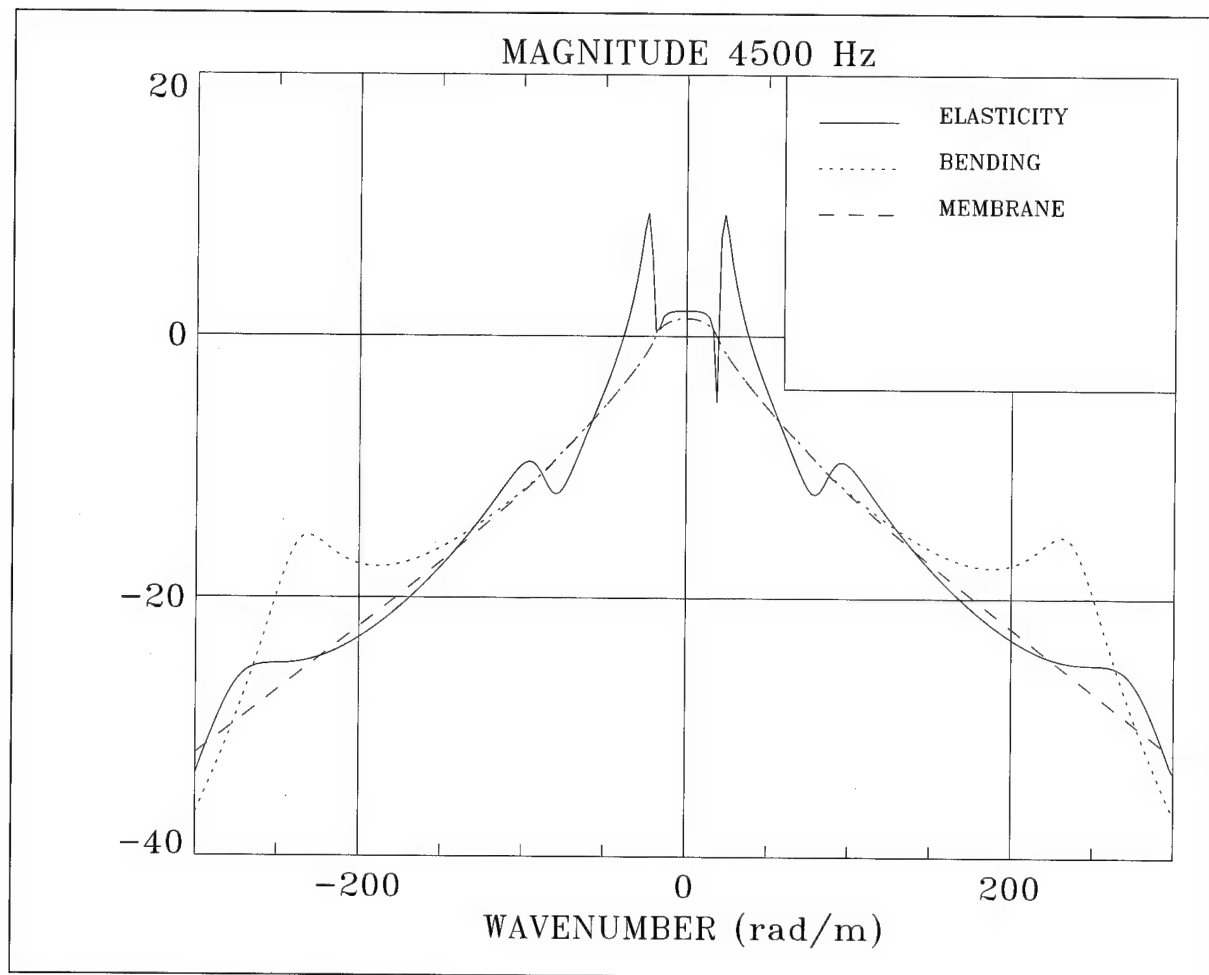


**Figure 25. Model Comparison for Figures 16, 18, and 20 When
 Magnitude = $10\text{Log}(P_i(r_1)/P_o)^2$ at $r_1 = 0.75$ in. With $n = 0$,
 Diameter = 3.00 in., and $f = 4500$ Hz**

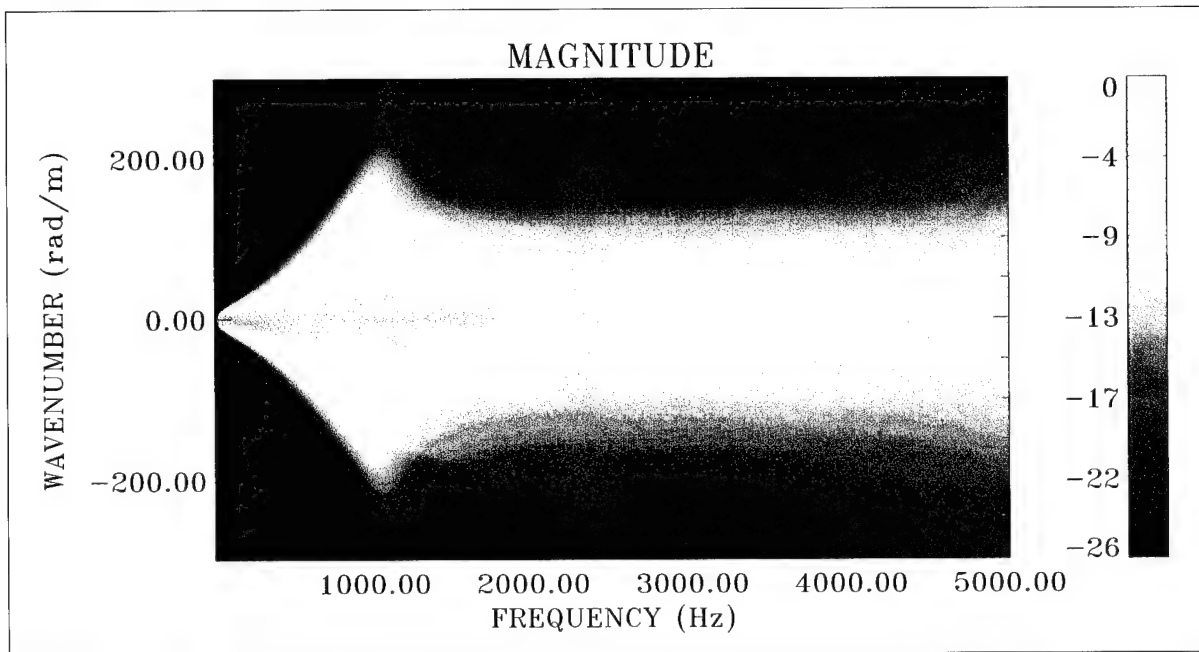


Figure 26. Pressure Transfer Surface With Magnitude = $10\text{Log}(P_i(r_1)/P_o)^2$ at $r_1 = 0.75$ in. for Membrane Shell Model, Where $n = 1$ and Diameter = 3.00 in. (Color Image)

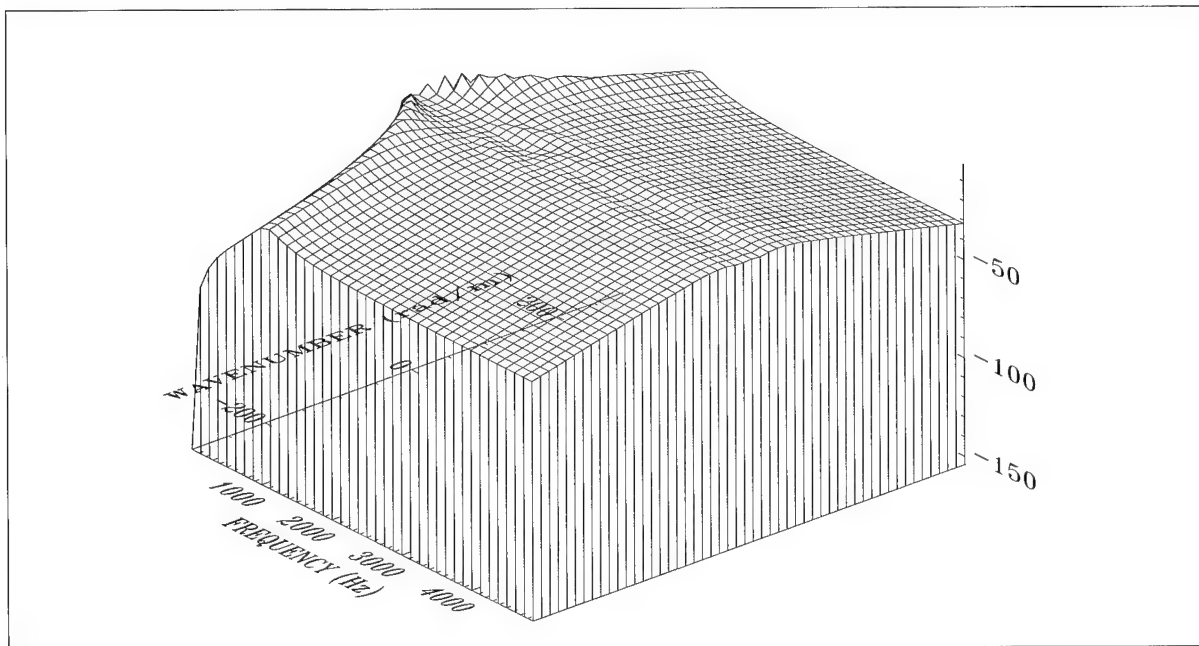


Figure 27. Pressure Transfer Surface With Magnitude = $10\text{Log}(P_i(r_1)/P_o)^2$ at $r_1 = 0.75$ in. for Membrane Shell Model, Where $n = 1$ and Diameter = 3.00 in. (Wire Frame Surface)

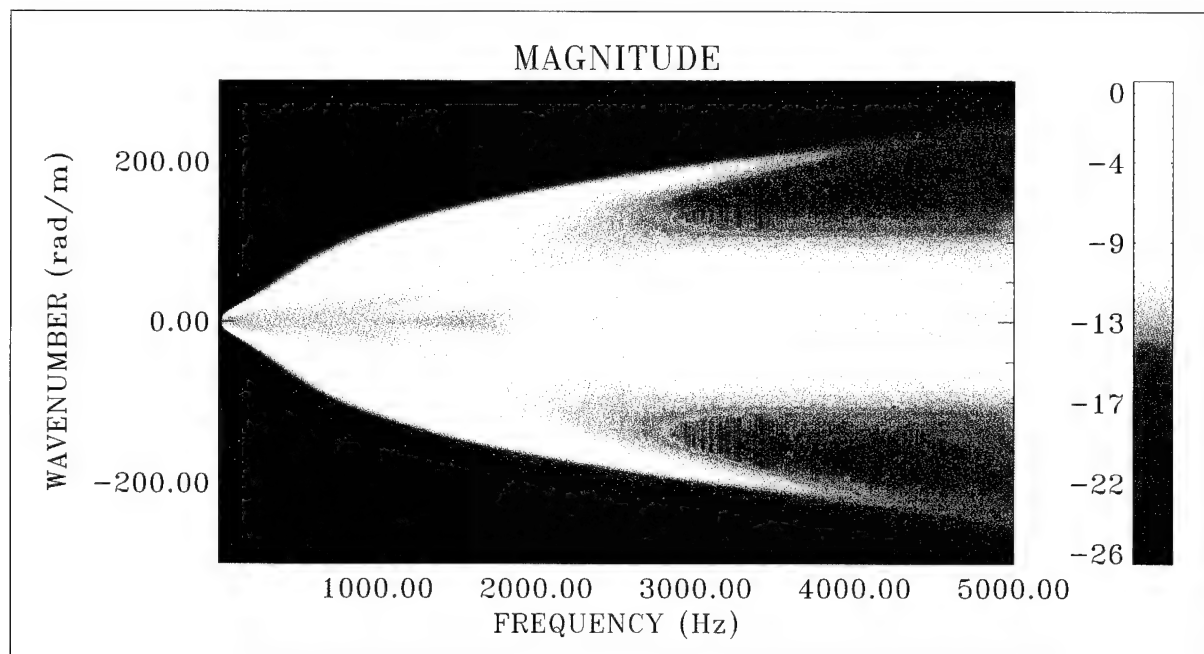


Figure 28. Pressure Transfer Surface With Magnitude = $10\text{Log}(P_i(r_1)/P_o)^2$ at $r_1 = 0.75$ in. for Bending Shell Model, Where $n = 1$ and Diameter = 3.00 in. (Color Image)

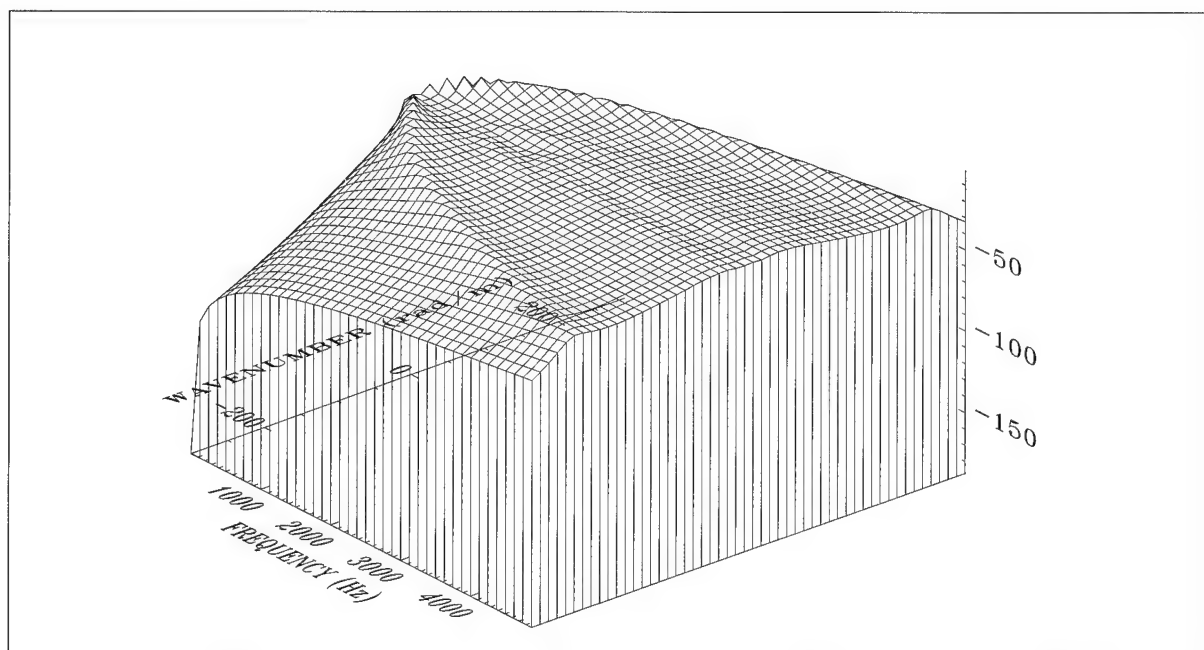


Figure 29. Pressure Transfer Surface With Magnitude = $10\text{Log}(P_i(r_1)/P_o)^2$ at $r_1 = 0.75$ in. for Bending Shell Model, Where $n = 1$ and Diameter = 3.00 in. (Wire Frame Surface)

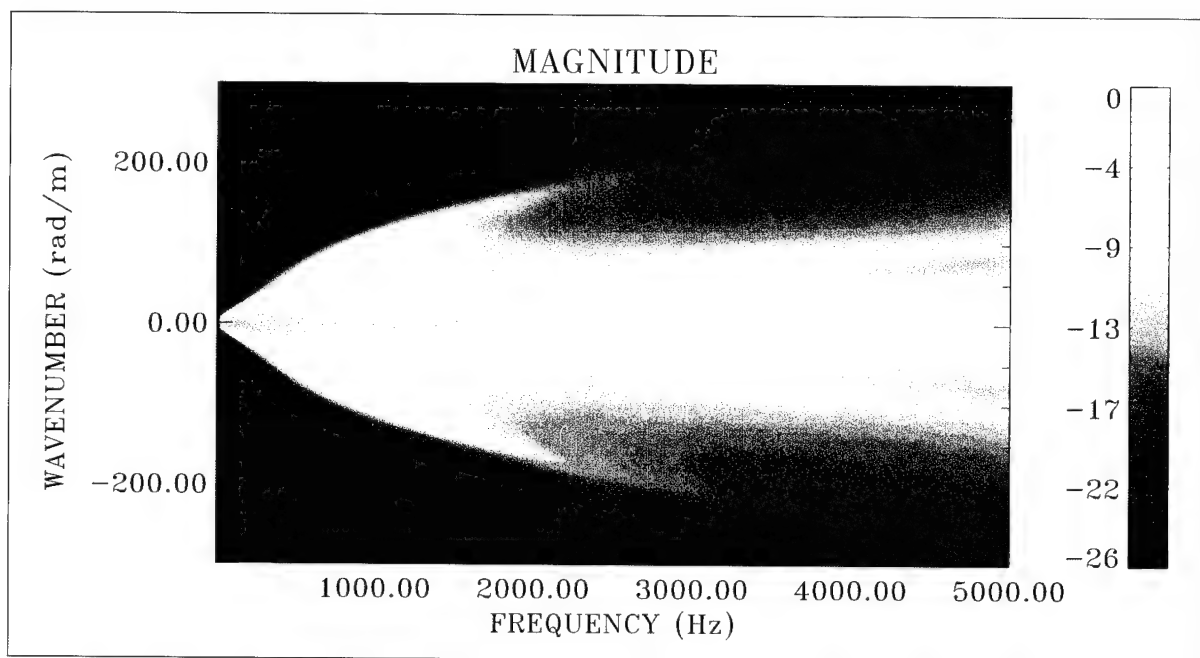


Figure 30. Pressure Transfer Surface With Magnitude = $10\text{Log}(P_i(r_1)/P_o)^2$ at $r_1 = 0.75$ in. for Elasticity Model, Where $n = 1$ and Diameter = 3.00 in. (Color Image)

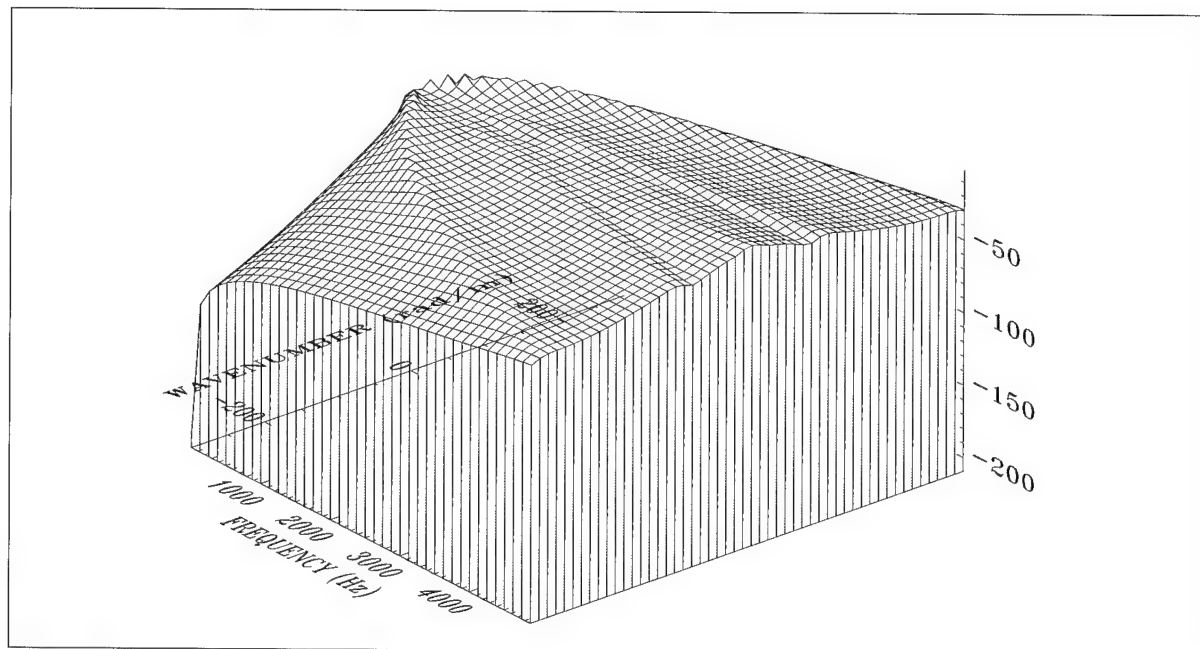
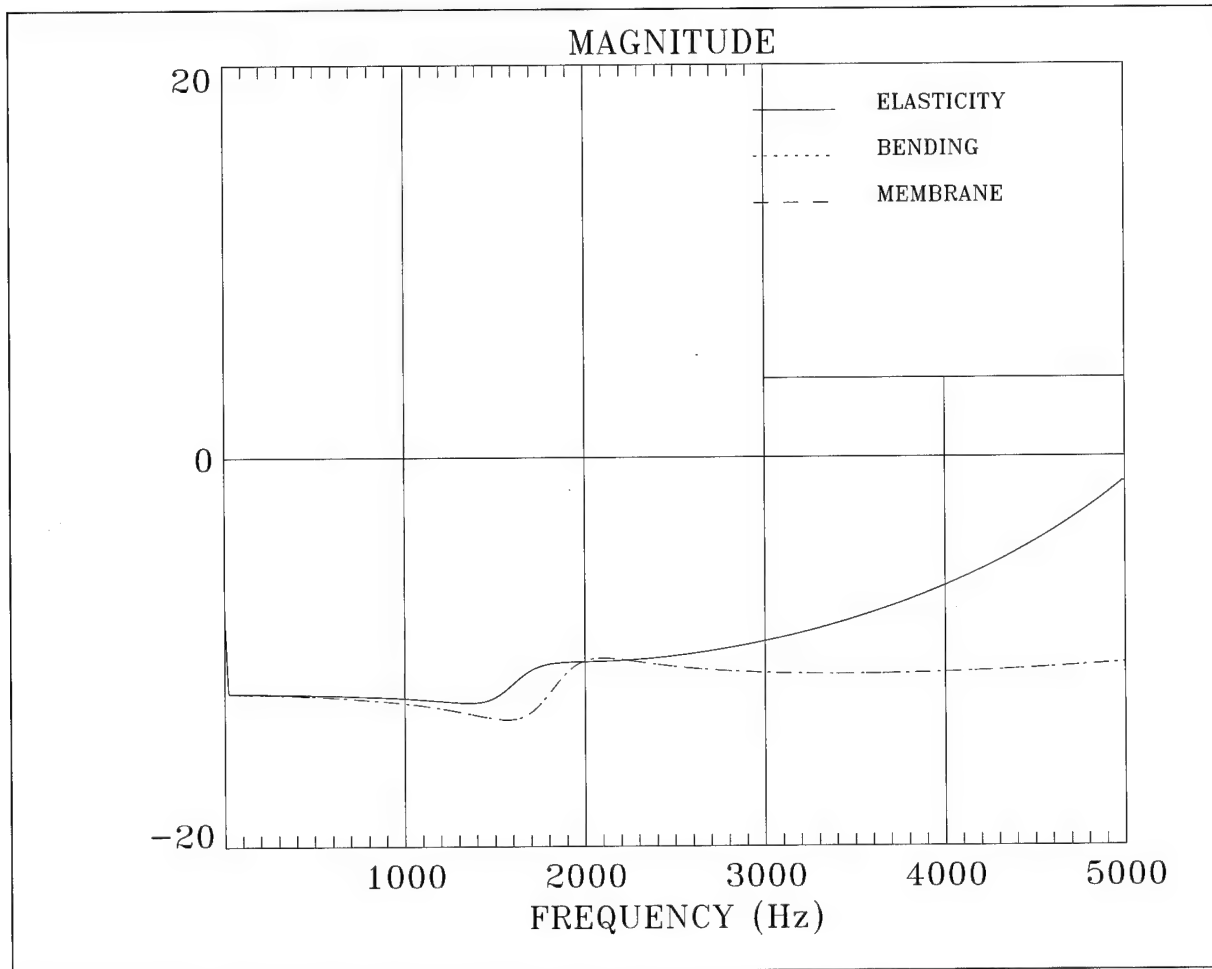
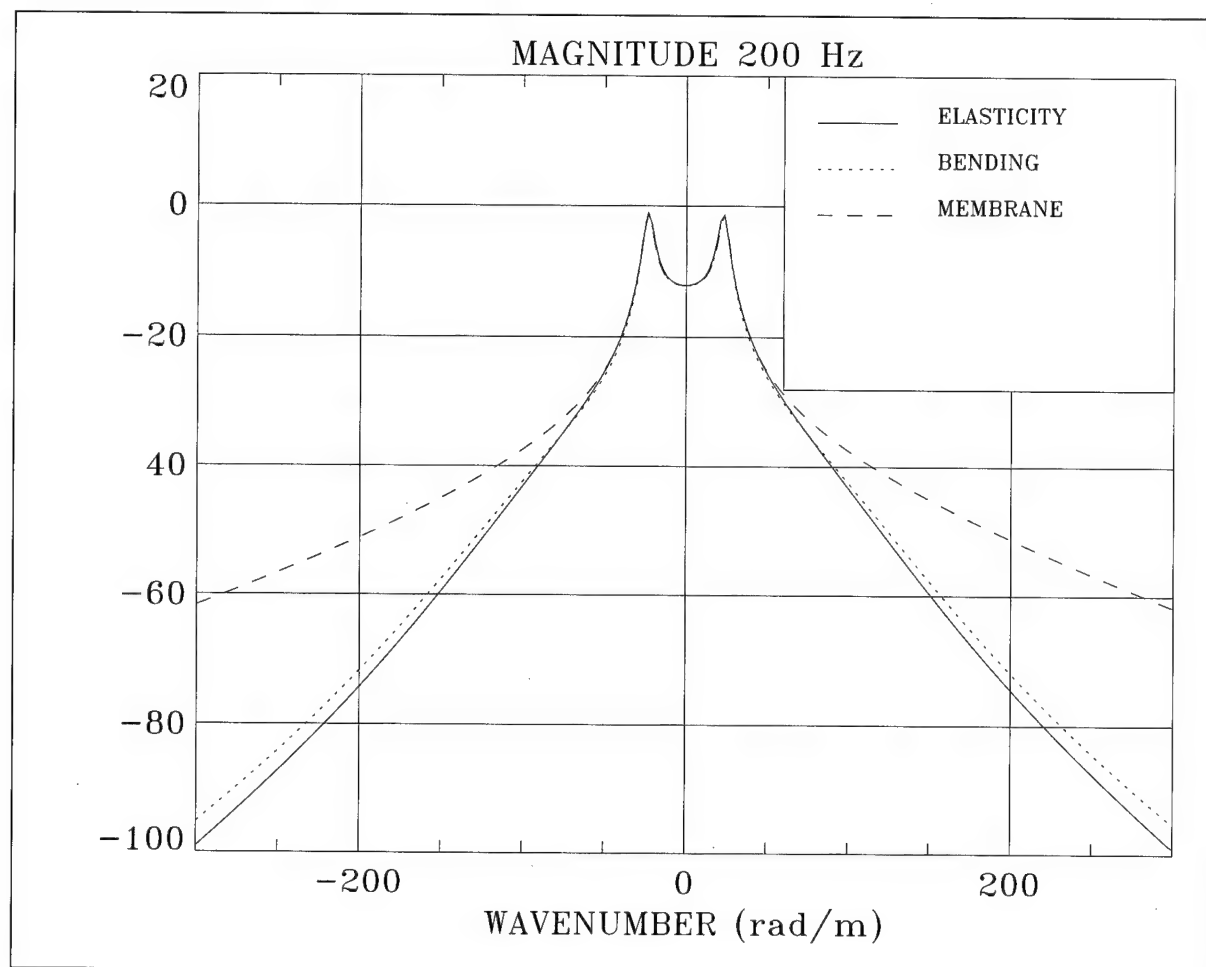


Figure 31. Pressure Transfer Surface With Magnitude = $10\text{Log}(P_i(r_1)/P_o)^2$ at $r_1 = 0.75$ in. for Elasticity Model, Where $n = 1$ and Diameter = 3.00 in. (Wire Frame Surface)



**Figure 32. Model Comparison for Figures 26, 28, and 30 When
Magnitude = $10\text{Log}(P_i(r_1)/P_o)^2$ at $r_1 = 0.75$ in. With $n = 1$,
Diameter = 3.00 in., and $k = 0$ rad/m**



**Figure 33. Model Comparison for Figures 26, 28, and 30 When
Magnitude = $10\text{Log}(P_i(r_1)/P_o)^2$ at $r_1 = 0.75$ in. With $n = 1$,
Diameter = 3.00 in., and $f = 200$ Hz**

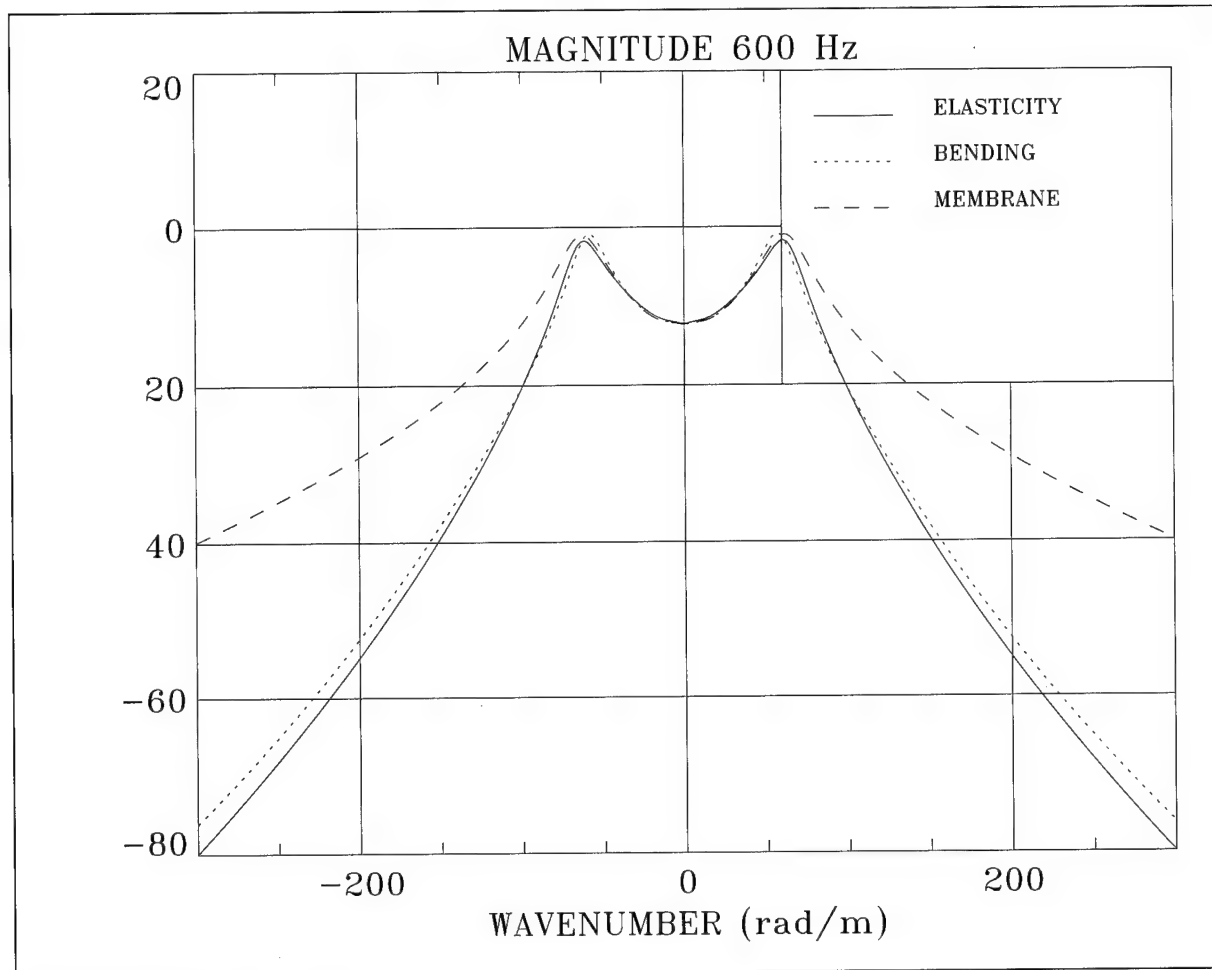


**Figure 34. Model Comparison for Figures 26, 28, and 30 When
Magnitude = $10\text{Log}(P_i(r_1)/P_o)^2$ at $r_1 = 0.75$ in. With $n = 1$,
Diameter = 3.00 in., and $f = 600$ Hz**

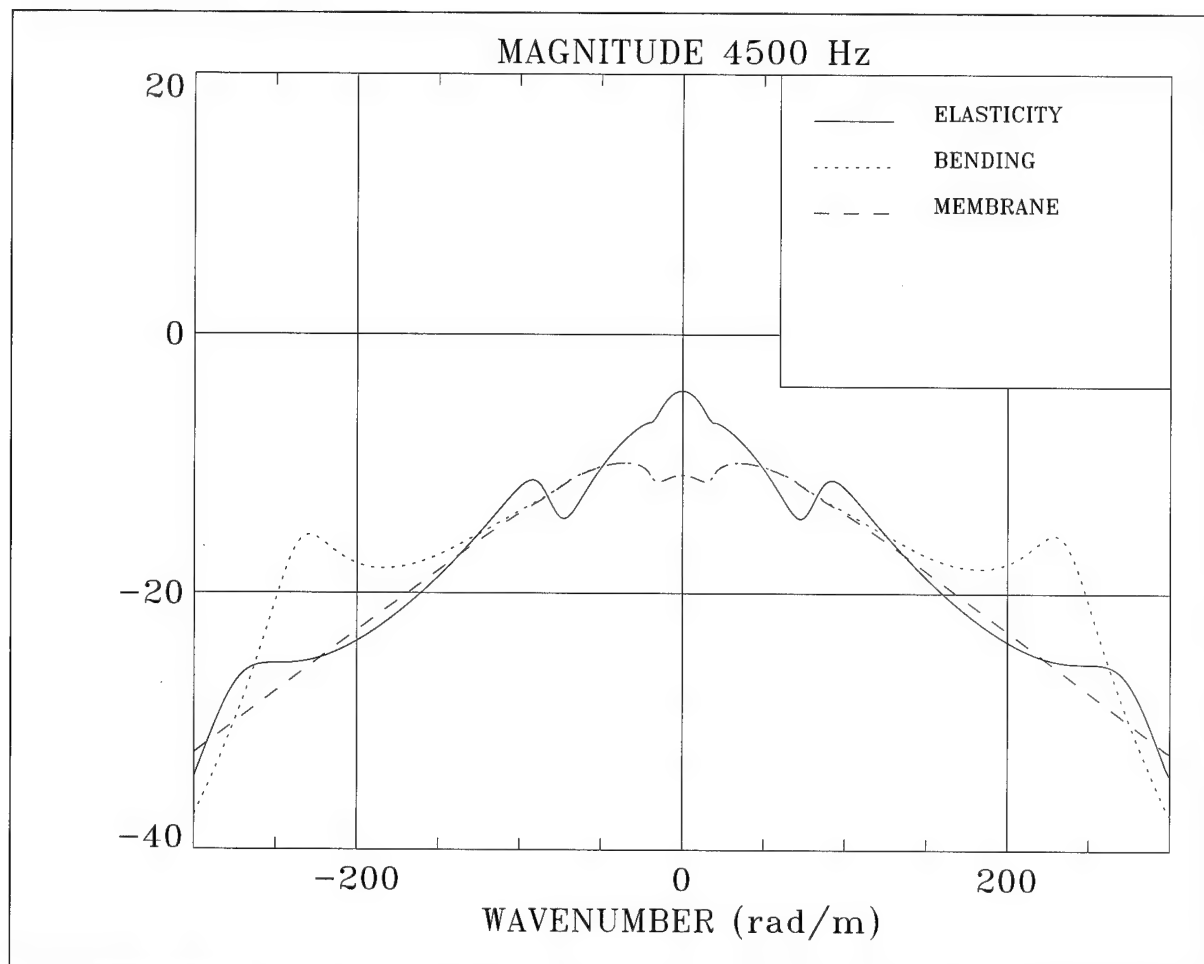


**Figure 35. Model Comparison for Figures 26, 28, and 30 When
Magnitude = $10\text{Log}(P_i(r_1)/P_o)^2$ at $r_1 = 0.75$ in. With $n = 1$,
Diameter = 3.00 in., and $f = 4500$ Hz**

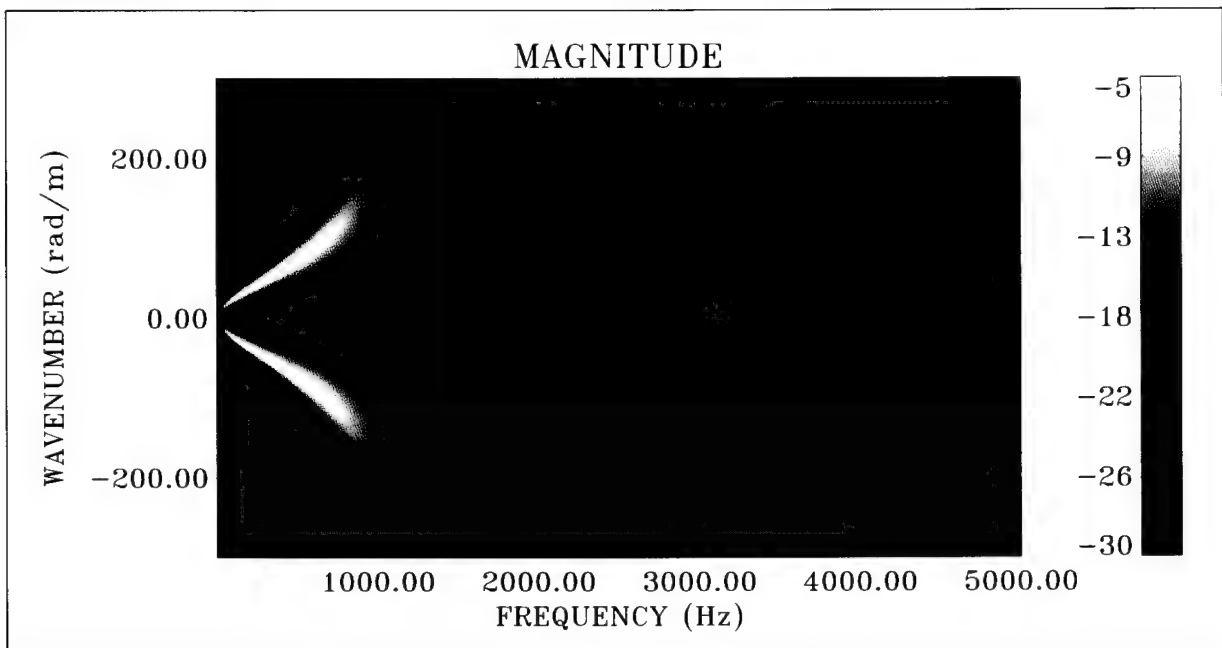


Figure 36. Pressure Transfer Surface With Magnitude = $10\text{Log}(P_i(r_1)/P_o)^2$ at $r_1 = 0.75$ in. for Membrane Shell Model, Where $n = 2$ and Diameter = 3.00 in. (Color Image)

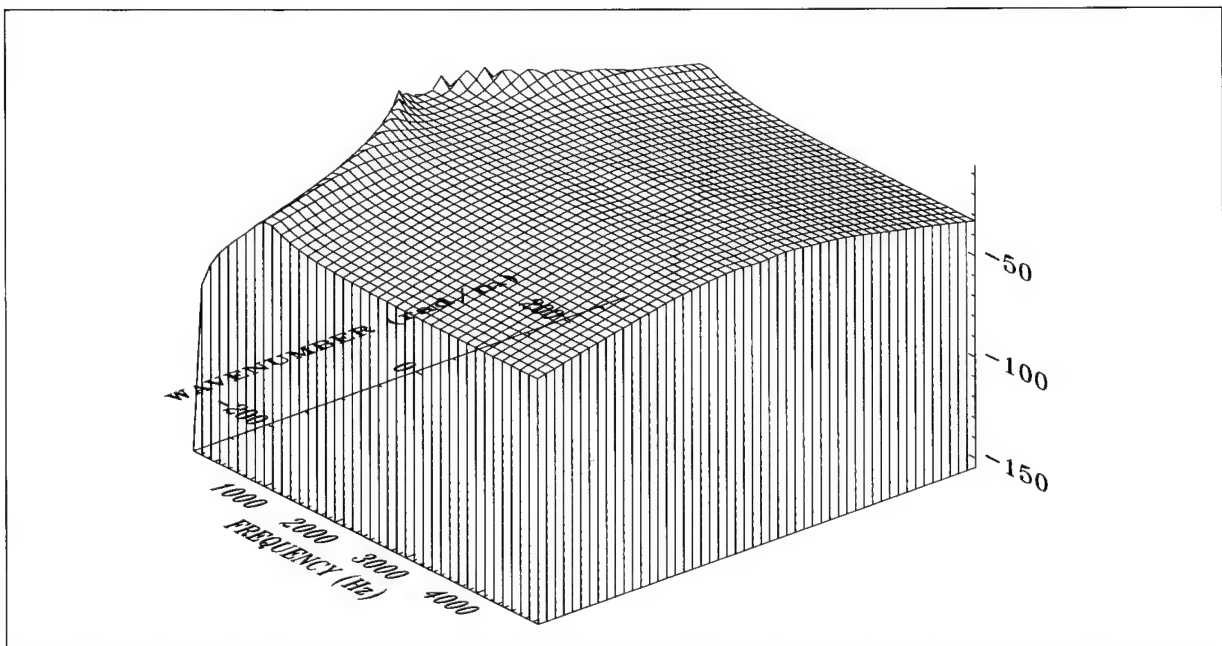


Figure 37. Pressure Transfer Surface With Magnitude = $10\text{Log}(P_i(r_1)/P_o)^2$ at $r_1 = 0.75$ in. for Membrane Shell Model, Where $n = 2$ and Diameter = 3.00 in. (Wire Frame Surface)

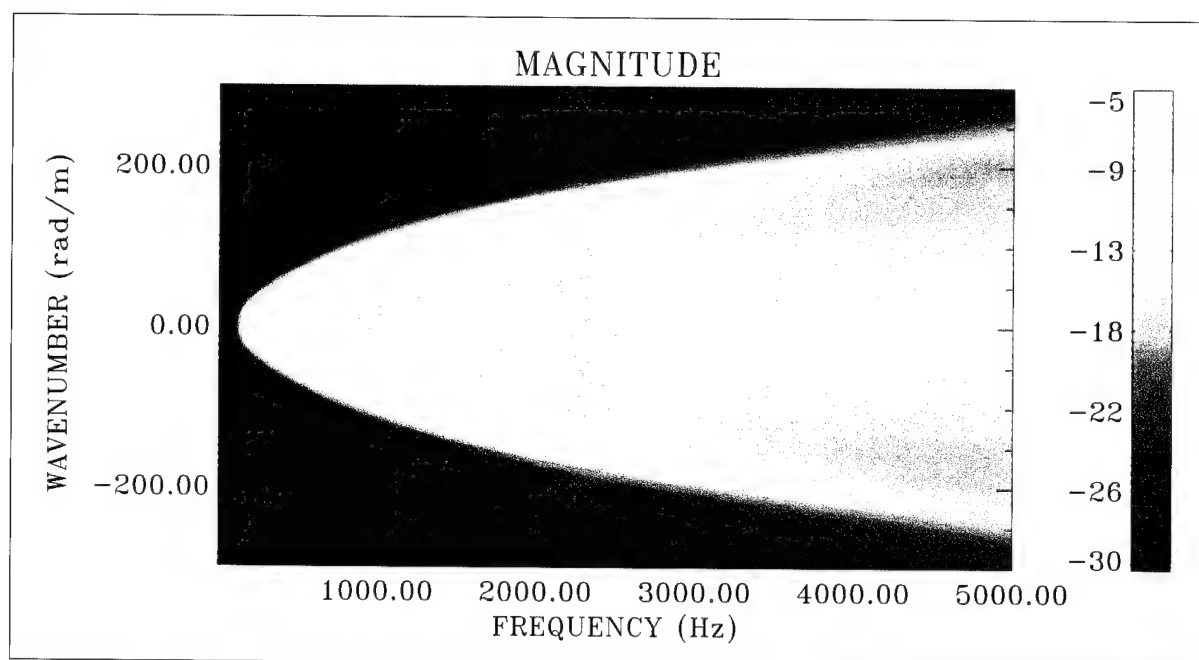


Figure 38. Pressure Transfer Surface With Magnitude = $10\text{Log}(P_i(r_1)/P_o)^2$ at $r_1 = 0.75$ in. for Bending Shell Model, Where $n = 2$ and Diameter = 3.00 in. (Color Image)

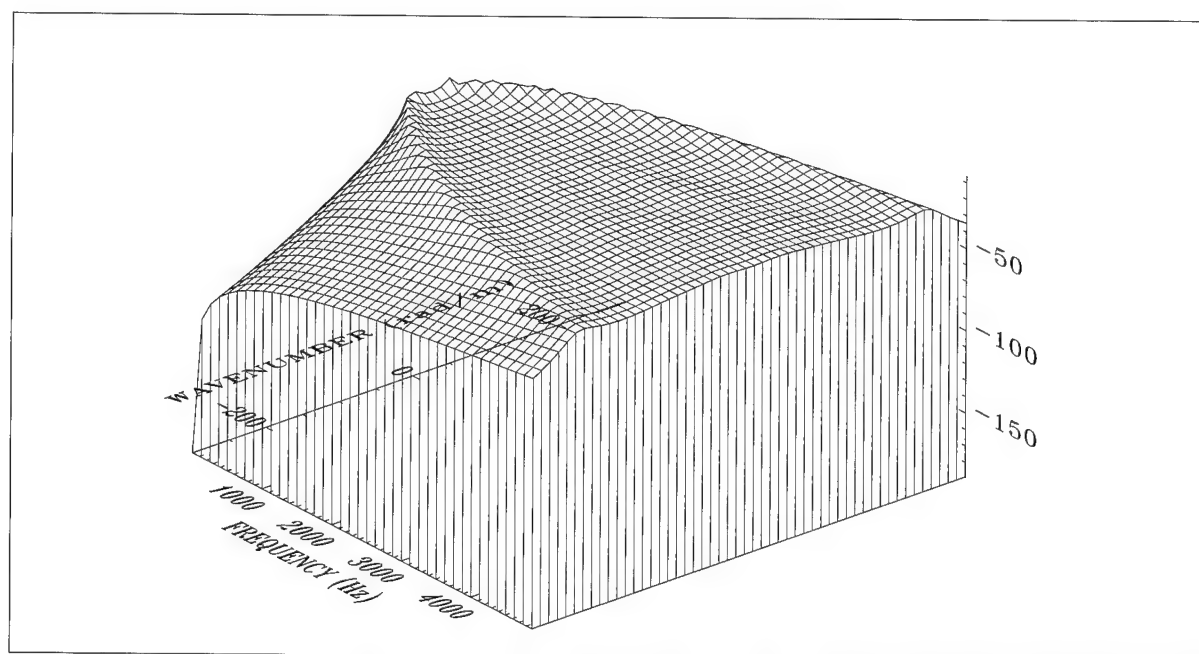


Figure 39. Pressure Transfer Surface With Magnitude = $10\text{Log}(P_i(r_1)/P_o)^2$ at $r_1 = 0.75$ in. for Bending Shell Model, Where $n = 2$ and Diameter = 3.00 in. (Wire Frame Surface)

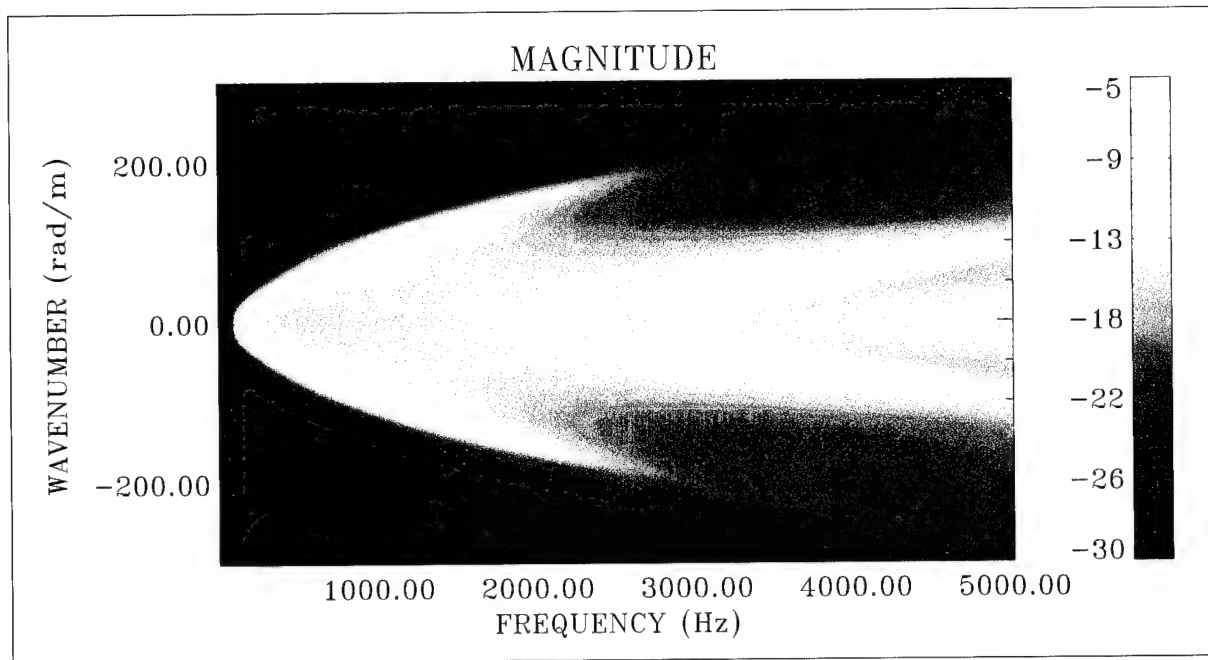


Figure 40. Pressure Transfer Surface With Magnitude = $10\text{Log}(P_i(r_1)/P_o)^2$ at $r_1 = 0.75$ in. for Elasticity Model, Where $n = 2$ and Diameter = 3.00 in. (Color Image)

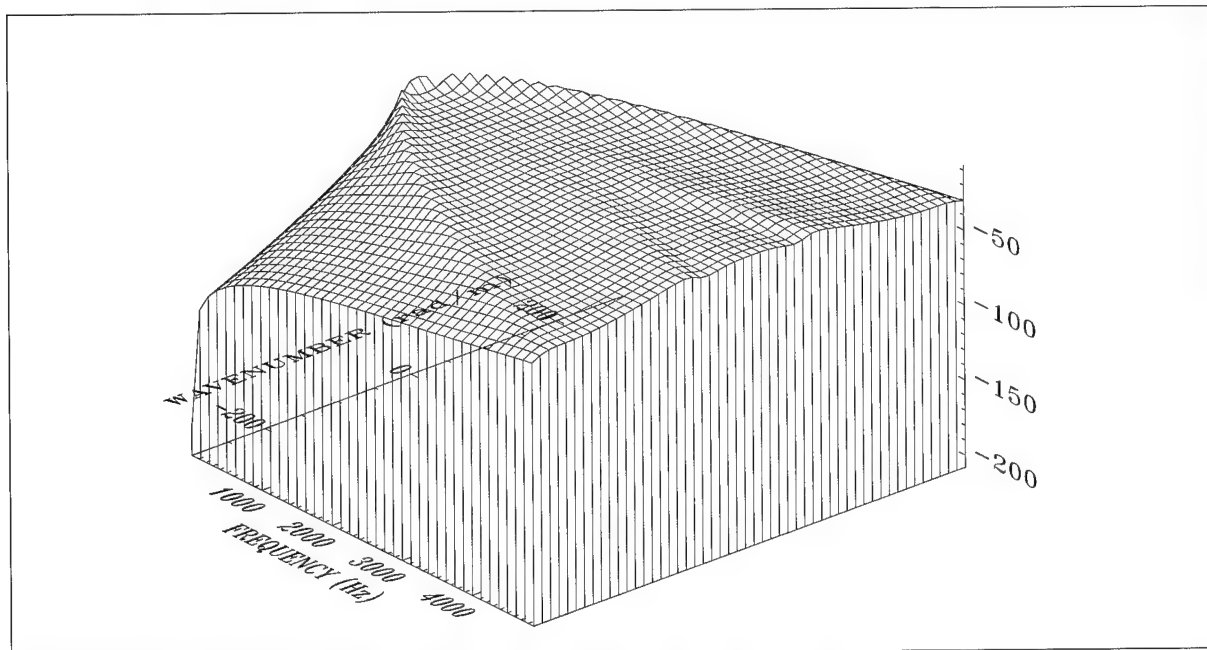
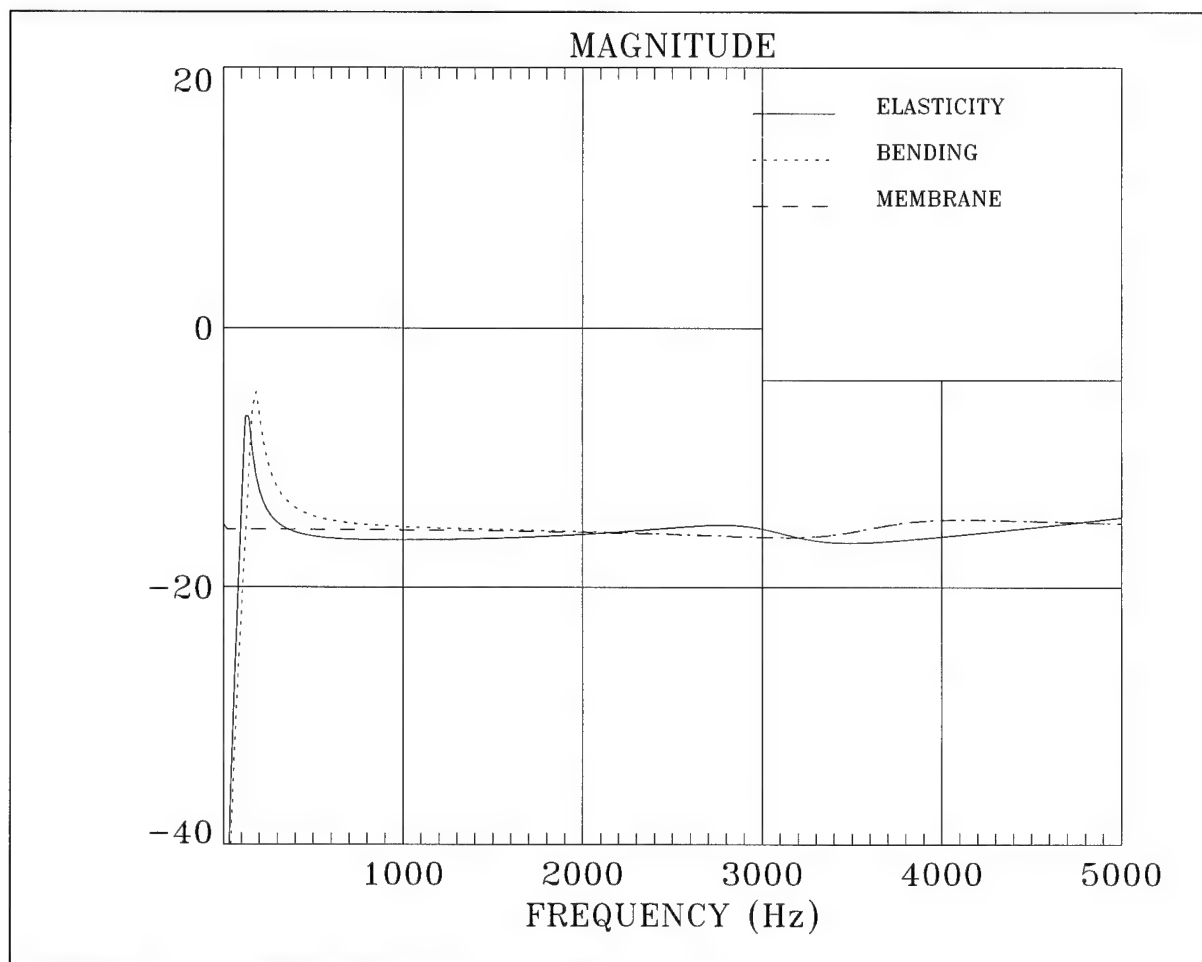
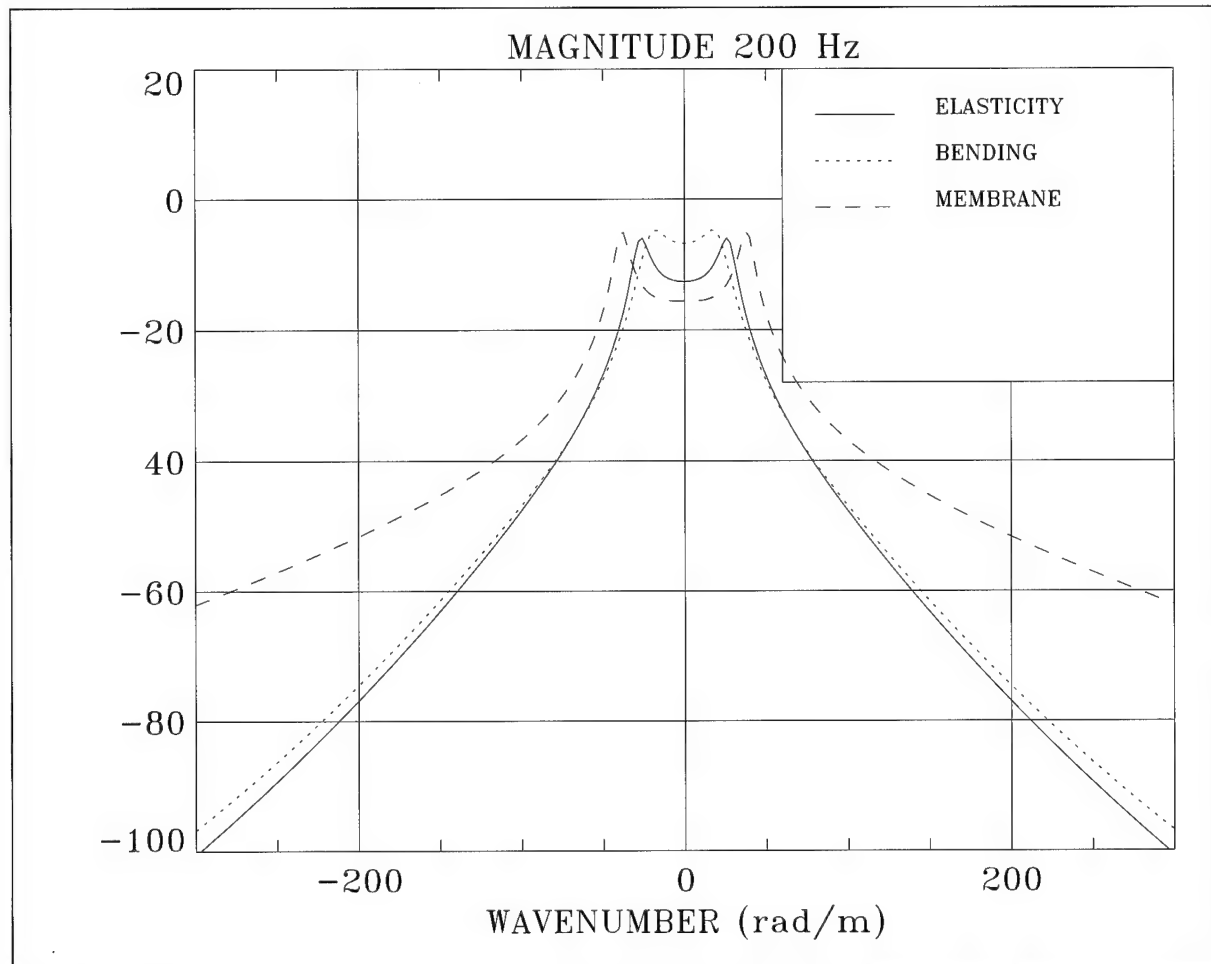


Figure 41. Pressure Transfer Surface With Magnitude = $10\text{Log}(P_i(r_1)/P_o)^2$ at $r_1 = 0.75$ in. for Elasticity Model, Where $n = 2$ and Diameter = 3.00 in. (Wire Frame Surface)



**Figure 42. Model Comparison for Figures 36, 38, and 40 When
Magnitude = $10\text{Log}(P_i(r_1)/P_o)^2$ at $r_1 = 0.75$ in. With $n = 2$,
Diameter = 3.00 in., and $k = 0$ rad/m**



**Figure 43. Model Comparison for Figures 36, 38, and 40 When
Magnitude = $10\text{Log}(P_i(r_1)/P_o)^2$ at $r_1 = 0.75$ in. With $n = 2$,
Diameter = 3.00 in., and $f = 200$ Hz**

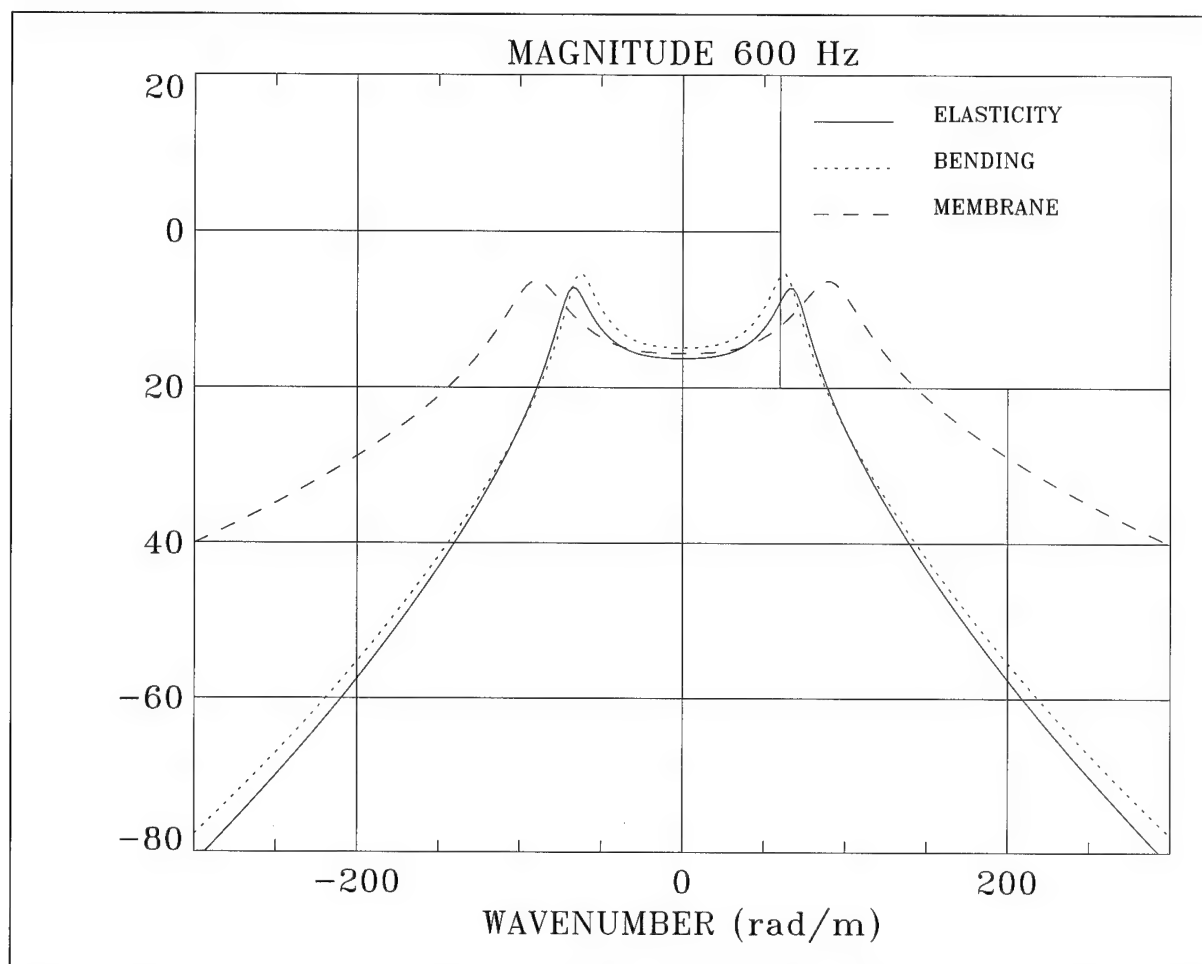


**Figure 44. Model Comparison for Figures 36, 38, and 40 When
Magnitude = $10\text{Log}(P_i(r_1)/P_o)^2$ at $r_1 = 0.75$ in. With $n = 2$,
Diameter = 3.00 in., and $f = 600$ Hz**

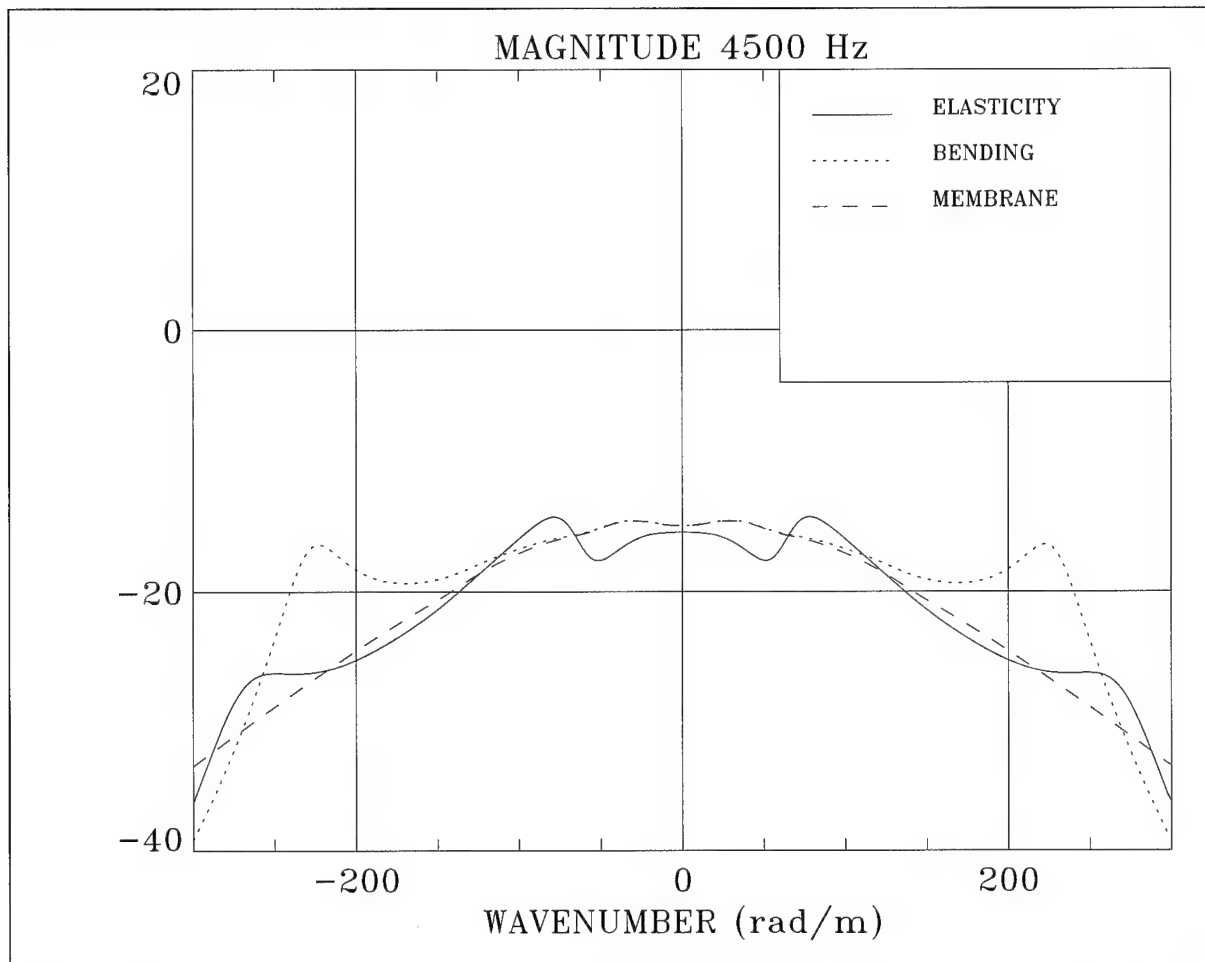


**Figure 45. Model Comparison for Figures 36, 38, and 40 When
Magnitude = $10\text{Log}(P_i(r_1)/P_o)^2$ at $r_1 = 0.75$ in. With $n = 2$,
Diameter = 3.00 in., and $f = 4500$ Hz**

Model Comparisons—0.670-Inch-Diameter Cylinder

Let us now consider the case of a cylinder with the properties listed in table 3, surrounded by fluids with the properties listed in tables 4 and 5. This cylinder, similar to the one previously considered, has properties that are representative of a garden or fire hose, and the fluids have properties consistent with those of water. Figures 46 through 51 are the $n = 0$ simulations for the three models. The output quantity is the pressure in the inner fluid; this field quantity is calculated at $r_1 = 0.1$ inch. Figures 52 through 55 are the comparisons of the three models. The major branch of wave propagation is the breathing wave, indicated on figures 47, 49, and 51. The extensional wave is visible in the elasticity model (figures 51 and 55). All three models are in close agreement up to ± 150 rad/m. Above this point, the membrane shell model diverges; however, the bending shell model continues to remain within 4 dB of the elasticity model up to 4500 Hz and ± 300 rad/m.

The large discrepancy between the shell models and the elasticity model for the first radial natural frequency of the cylinder is apparent in figure 52. The fluid-loaded shell models produce resonances at 53,136 Hz, while the fluid-loaded elasticity model displays this resonance at 10,793 Hz. As was seen in the 3.00-inch-diameter simulations of the previous section, the shell models are not adequate for predicting the first radial natural frequency when the present combination of water and rubberlike cylinder properties is chosen. The elasticity model provides the best solution in this case.

Figures 56 through 61 are the simulations for circumferential order number $n = 1$. Figure 62 is a comparison of the models across frequency, and figures 63 through 65 are comparisons of the models across wavenumber for particular frequencies. The first and dominant branch of wave propagation in the simulations is one in which the cylinder is placed in a state of bending, as depicted by the wire frame representation of figure 9. The shell models are in close agreement with the elasticity model up to ± 150 rad/m and 5000 Hz, as seen in figures 62 through 65. Above these points in the wavenumber-frequency plane, the membrane shell model diverges. The bending shell model, however, remains within 4 dB of the elasticity solution over the entire range of wavenumbers and frequencies considered.

The next branch of wave propagation, faintly visible in the 4500-Hz region, has a cutoff frequency associated with it. As described earlier for the 3.00-inch cylinder, this second branch is causing the longitudinal displacement to undergo one wavelength of variation with respect to the circumference of the cylinder. The predominantly longitudinal displacement does couple into the radial displacement, thereby causing an effect on the pressure field in the inner fluid. The value of the damping selected for the cylinder has diminished the sharpness of this branch.

Figures 66 through 71 contain the simulations for circumferential order number $n = 2$. As in the case for the cylinder considered in the previous section, the membrane shell model will not support a cutoff frequency for the first branch of wave propagation (figures 66 and 72). This is due to the assumption that neglects bending stiffness terms, which are inherent in a membrane formulation. Figures 73 through 75 are comparisons across wavenumber, and once again we see the divergence of the membrane shell model and the close agreement between the bending shell and elasticity solutions.

To summarize, the membrane shell model generally falls within 4 dB of the elasticity model for the $n = 0$ circumferential order number in the region ± 150 rad/m and 0 to 5000 Hz. If it is necessary to obtain a simulation with an error of less than 4 dB, the elasticity model should be used. Furthermore, the elasticity model (not the shell models) should also be used for the determination of the first radial natural frequency of this cylinder/fluid combination. For the higher circumferential order numbers, it should be remembered that the membrane model will not support a cutoff frequency for the first branch of wave propagation. The bending shell model will be within 4 dB of the elasticity solution. If an error of less than 4 dB is required, the elasticity model should be used.

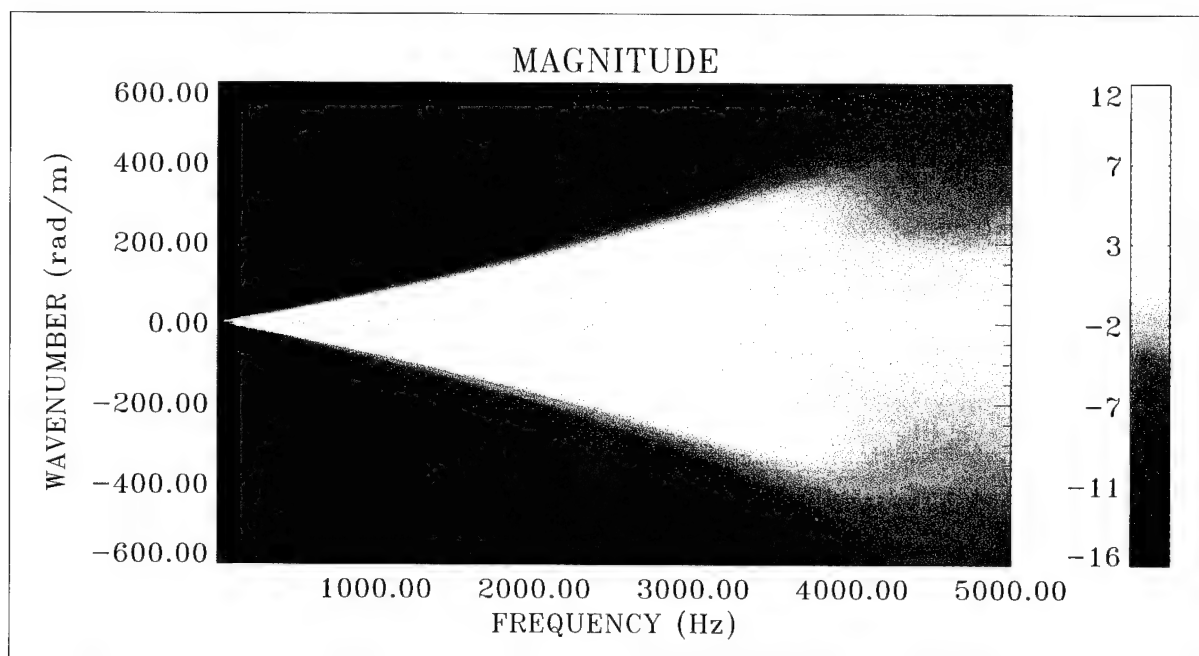


Figure 46. Pressure Transfer Surface With Magnitude = $10\text{Log}(P_i(r_1)/P_o)^2$ at $r_1 = 0.1$ in. for Membrane Shell Model, Where $n = 0$ and Diameter = 0.670 in. (Color Image)

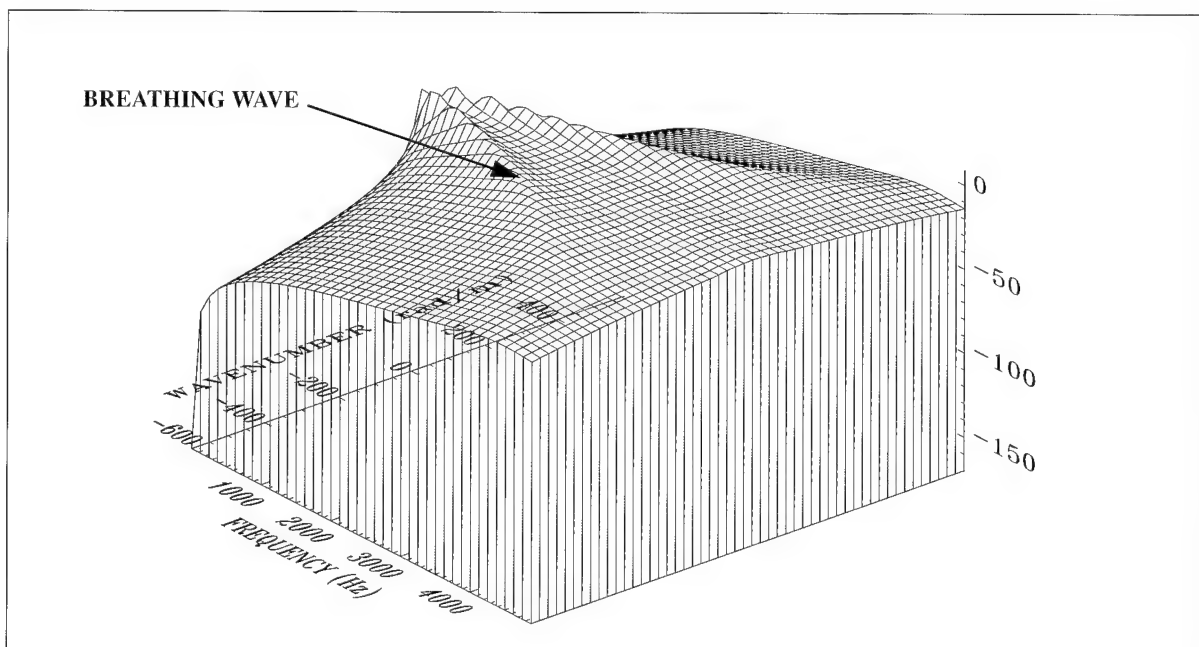


Figure 47. Pressure Transfer Surface With Magnitude = $10\text{Log}(P_i(r_1)/P_o)^2$ at $r_1 = 0.1$ in. for Membrane Shell Model, Where $n = 0$ and Diameter = 0.670 in. (Wire Frame Surface)

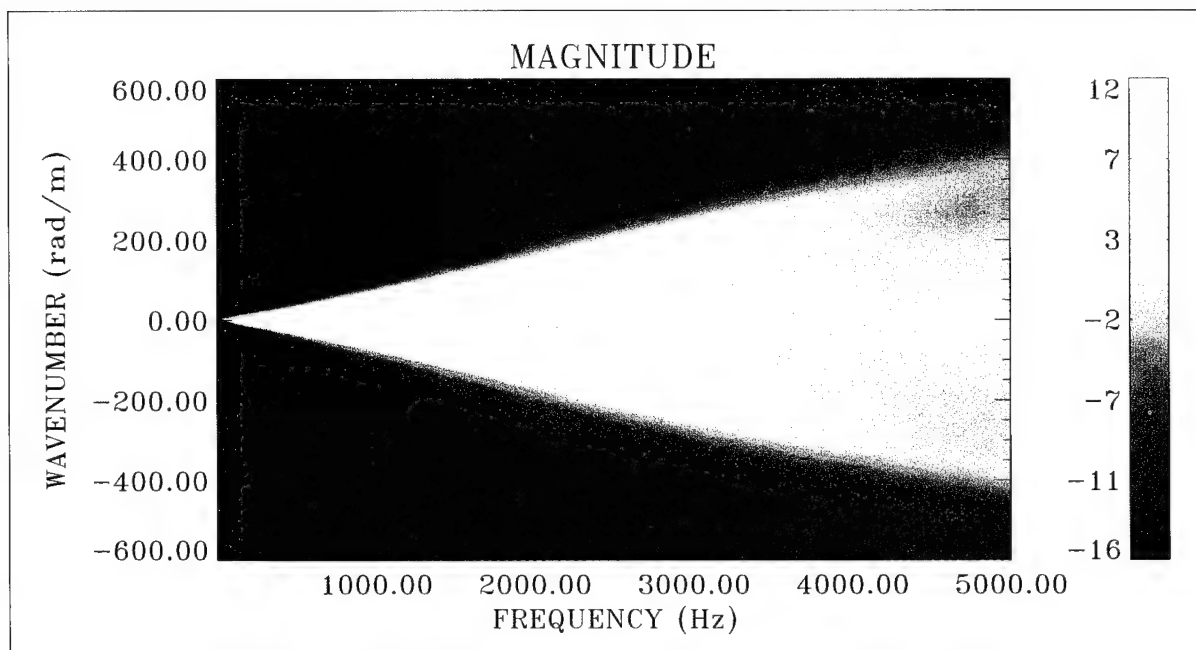


Figure 48. Pressure Transfer Surface With Magnitude = $10\text{Log}(P_i(r_1)/P_o)^2$ at $r_1 = 0.1$ in. for Bending Shell Model, Where $n = 0$ and Diameter = 0.670 in. (Color Image)

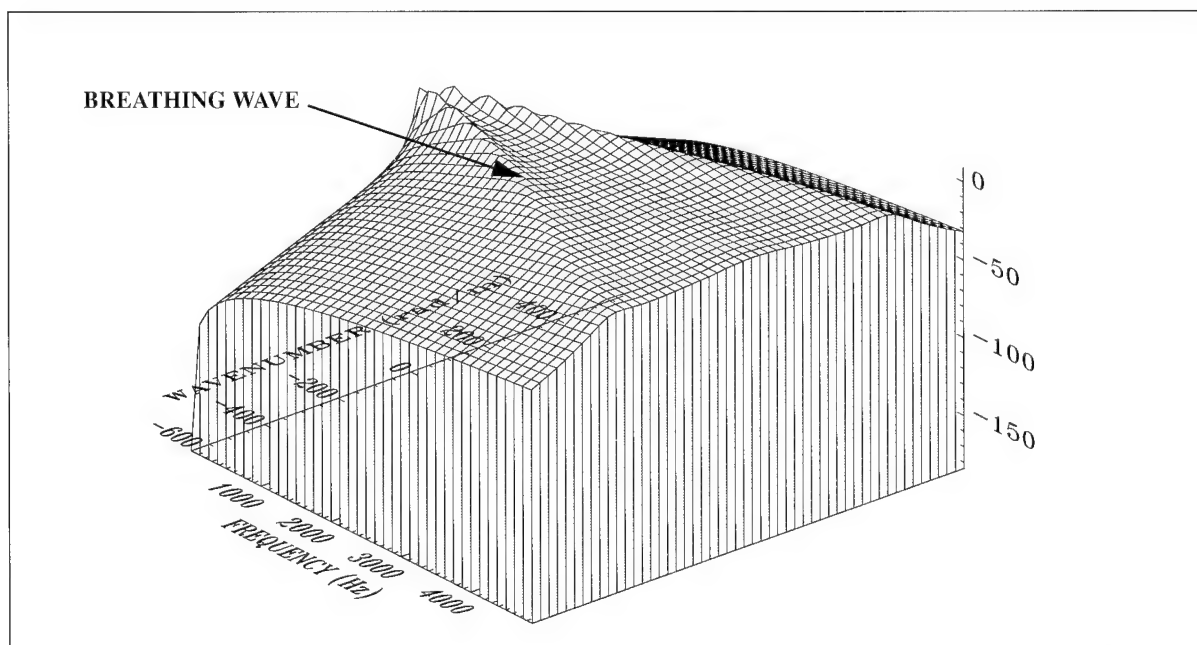


Figure 49. Pressure Transfer Surface With Magnitude = $10\text{Log}(P_i(r_1)/P_o)^2$ at $r_1 = 0.1$ in. for Bending Shell Model, Where $n = 0$ and Diameter = 0.670 in. (Wire Frame Surface)

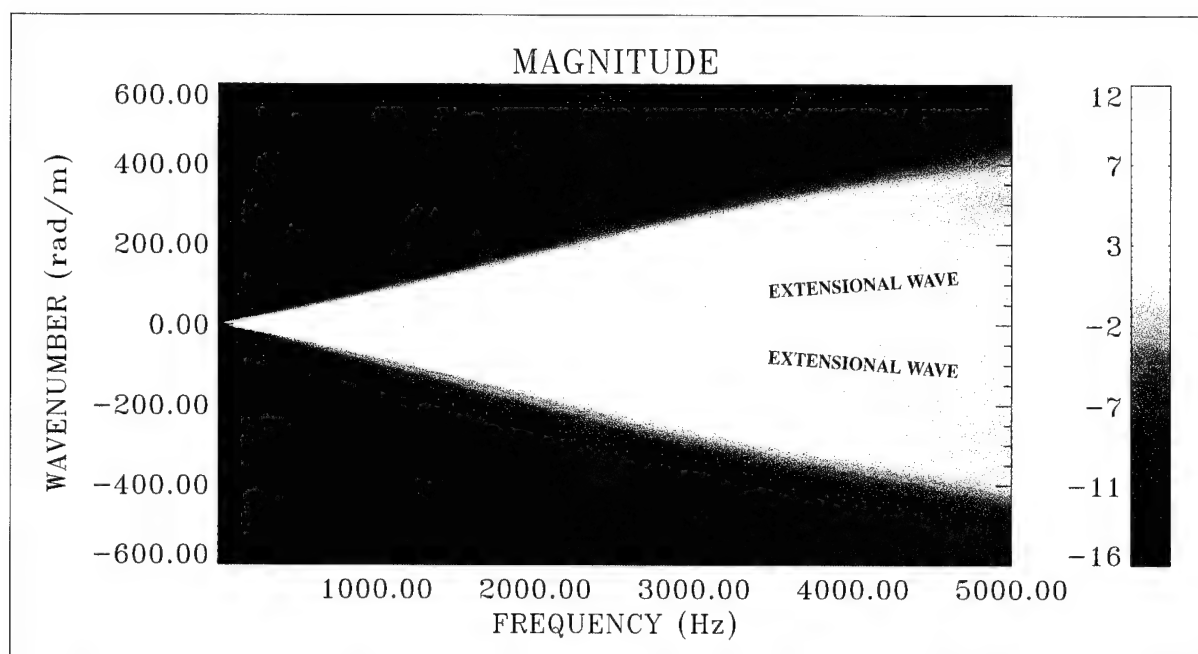


Figure 50. Pressure Transfer Surface With Magnitude = $10\text{Log}(P_i(r_1)/P_o)^2$ at $r_1 = 0.1$ in. for Elasticity Model, Where $n = 0$ and Diameter = 0.670 in. (Color Image)

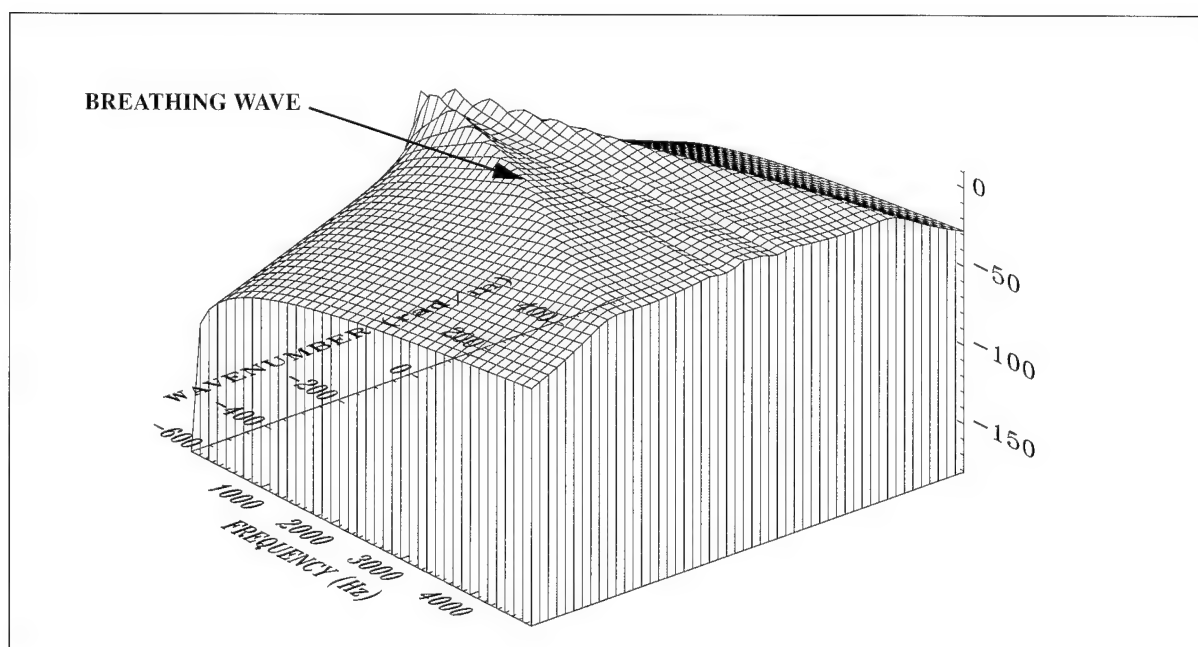


Figure 51. Pressure Transfer Surface With Magnitude = $10\text{Log}(P_i(r_1)/P_o)^2$ at $r_1 = 0.1$ in. for Elasticity Model, Where $n = 0$ and Diameter = 0.670 in. (Wire Frame Surface)

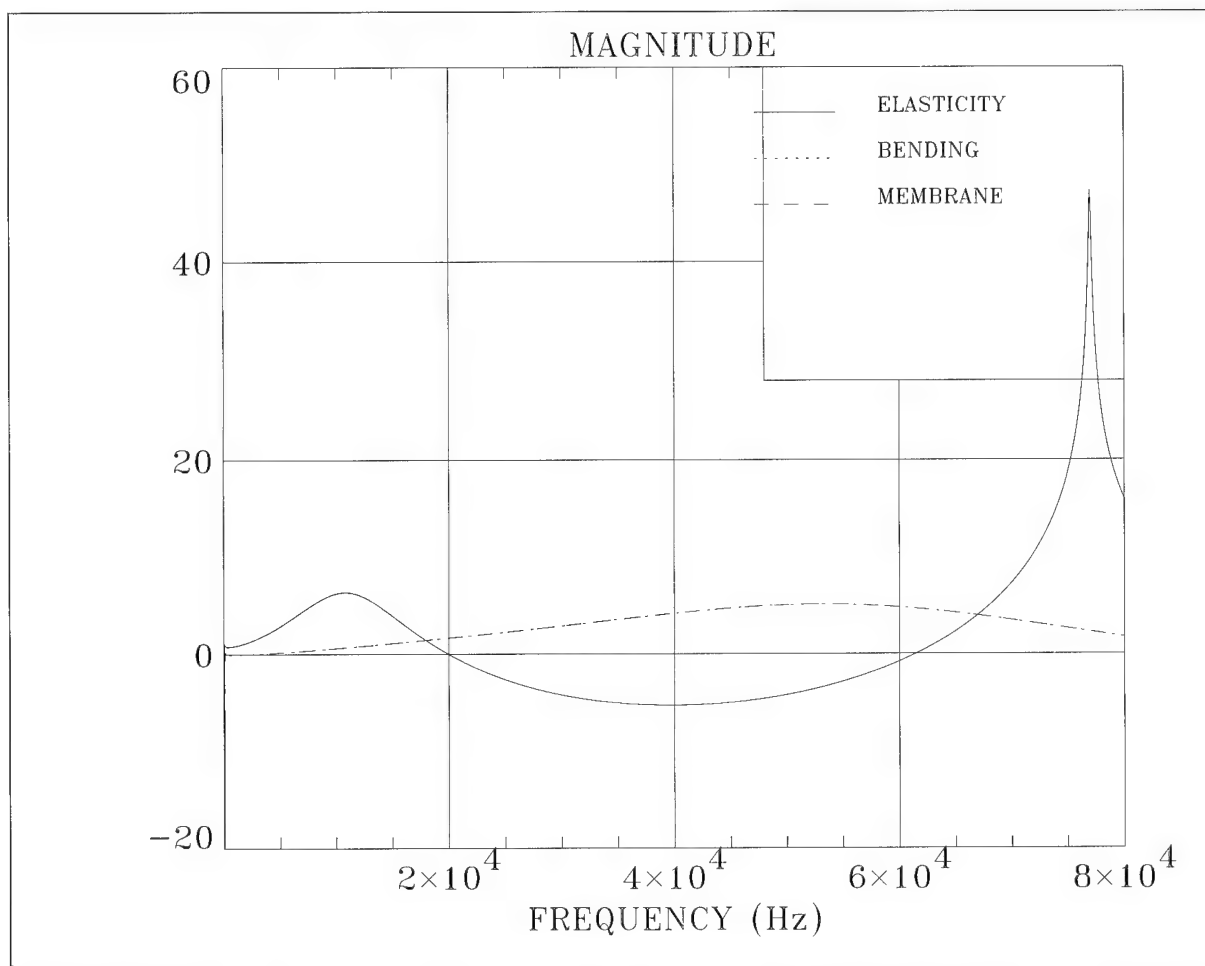
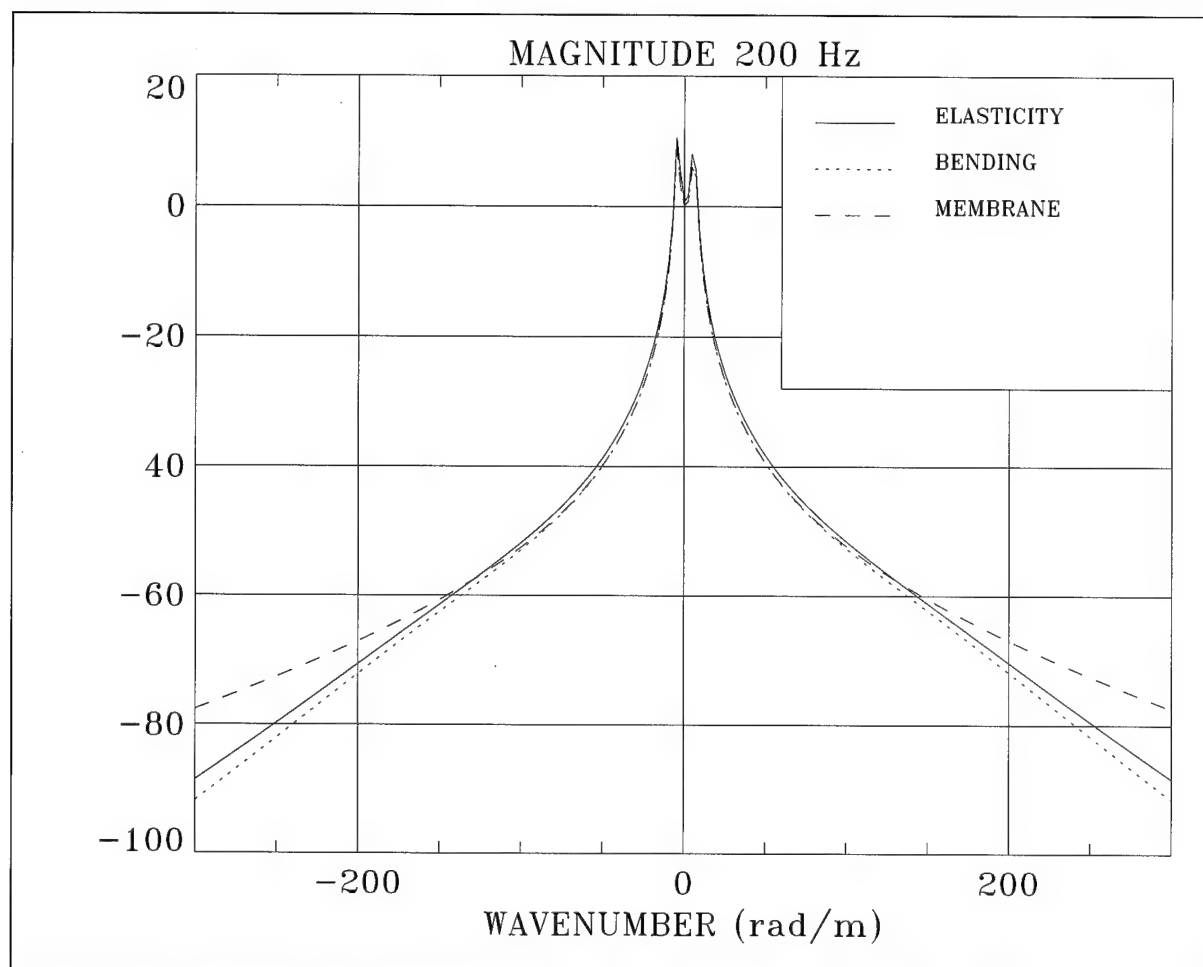
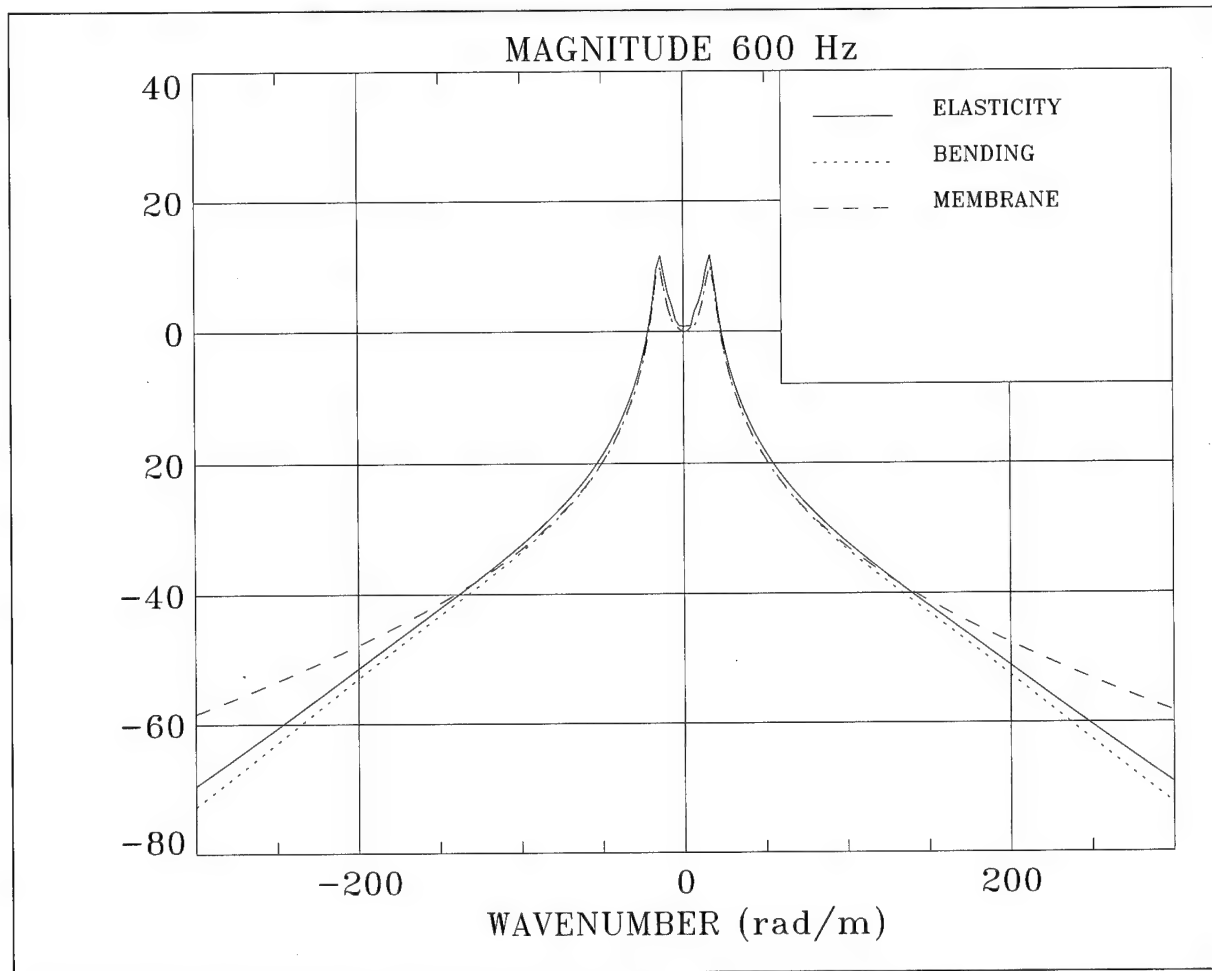


Figure 52. Model Comparison for Figures 46, 48, and 50 at Extended Frequency Range When Magnitude = $10\text{Log}(P_i(r_1)/P_o)^2$ at $r_1 = 0.1$ in. With $n = 0$, Diameter = 0.670 in., and $k = 0$ rad/m



**Figure 53. Model Comparison for Figures 46, 48, and 50 When
Magnitude = $10\text{Log}(P_i(r_1)/P_o)^2$ at $r_1 = 0.1$ in. With $n = 0$,
Diameter = 0.670 in., and $f = 200$ Hz**



**Figure 54. Model Comparison for Figures 46, 48, and 50 When
 Magnitude = $10\text{Log}(P_i(r_1)/P_o)^2$ at $r_1 = 0.1$ in. With $n = 0$,
 Diameter = 0.670 in., and $f = 600$ Hz**

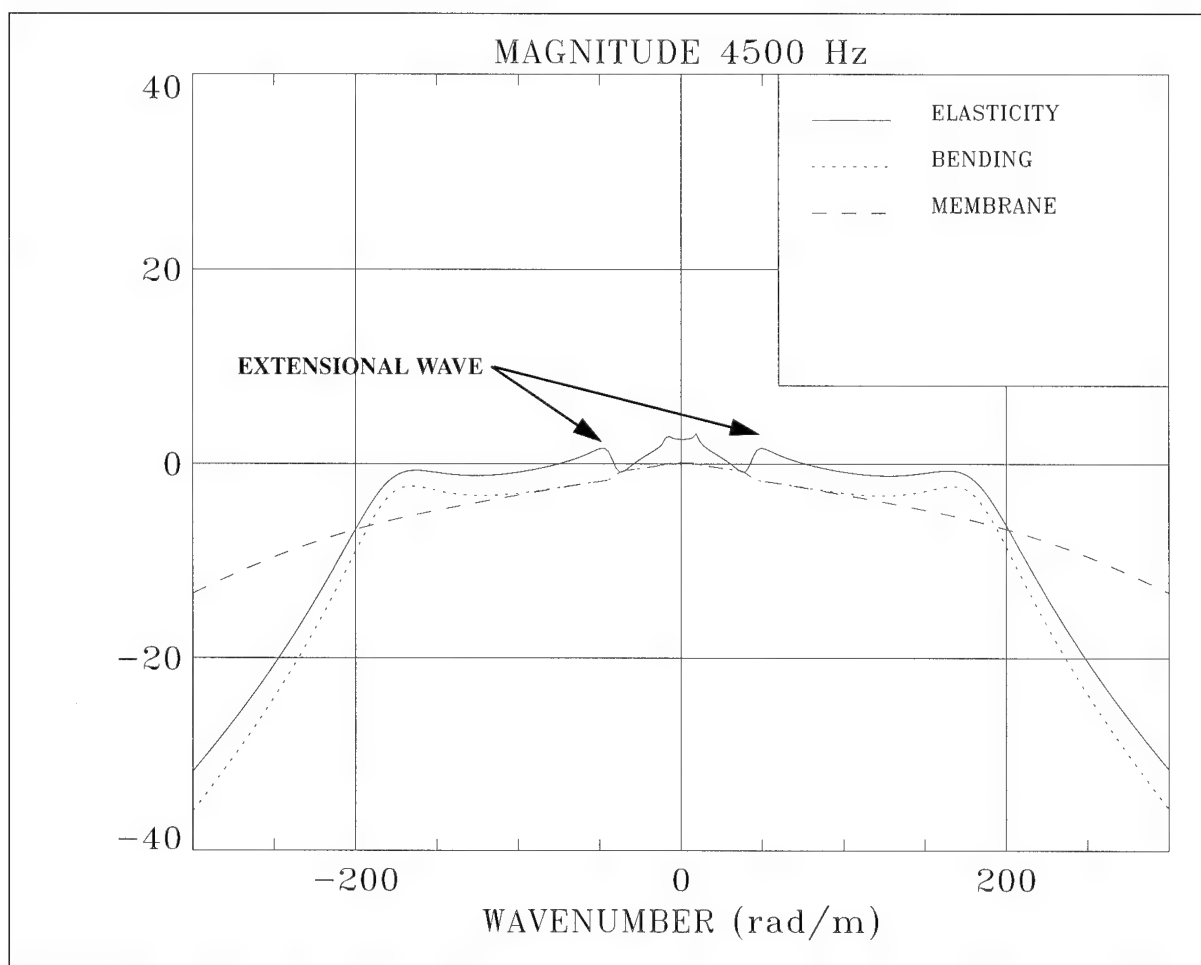


**Figure 55. Model Comparison for Figures 46, 48, and 50 When
 Magnitude = $10\text{Log}(P_i(r_1)/P_o)^2$ at $r_1 = 0.1$ in. With $n = 0$,
 Diameter = 0.670 in., and $f = 4500$ Hz**

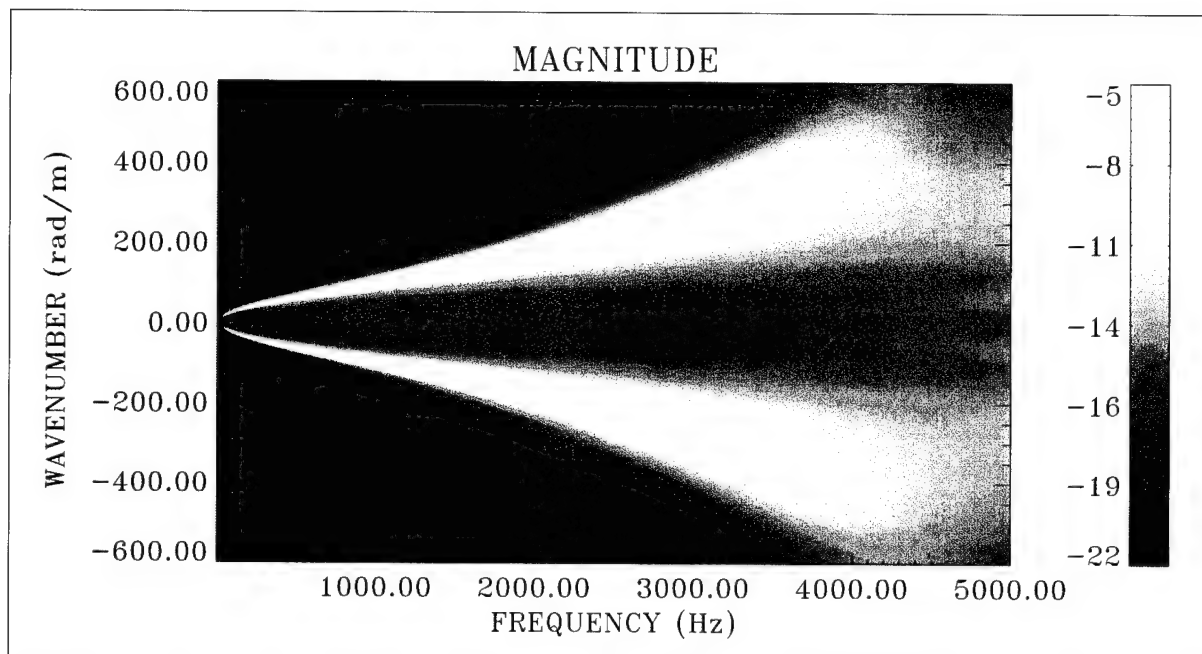


Figure 56. Pressure Transfer Surface With Magnitude = $10\text{Log}(P_i(r_1)/P_o)^2$ at $r_1 = 0.1$ in. for Membrane Shell Model, Where $n = 1$ and Diameter = 0.670 in. (Color Image)

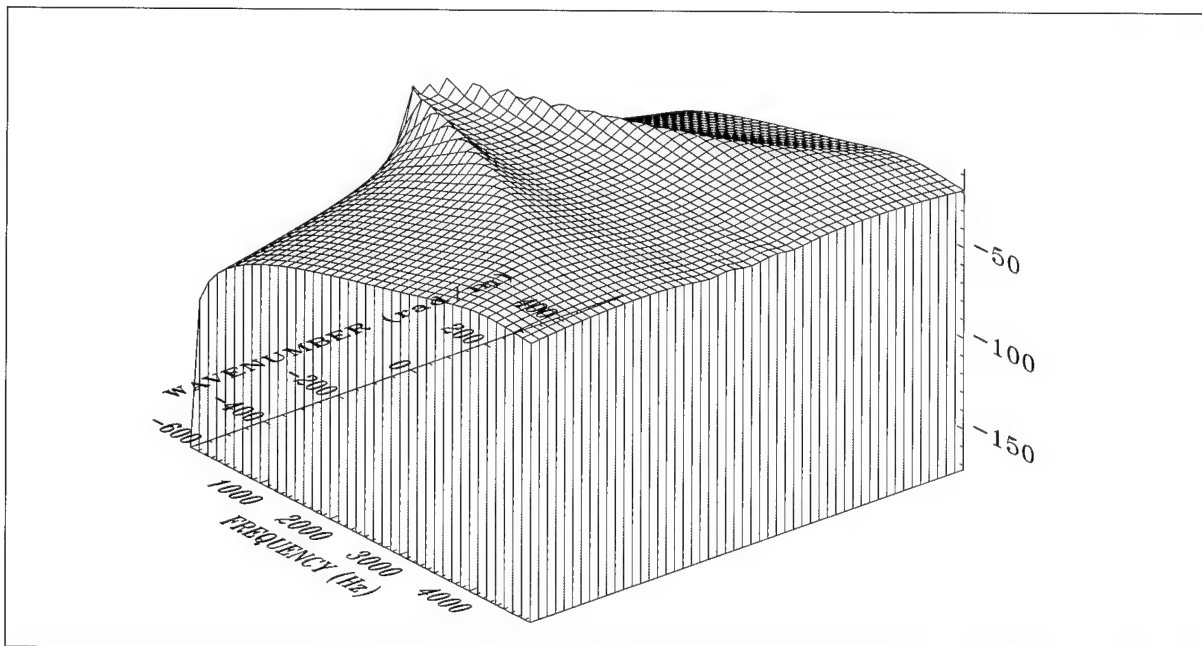


Figure 57. Pressure Transfer Surface With Magnitude = $10\text{Log}(P_i(r_1)/P_o)^2$ at $r_1 = 0.1$ in. for Membrane Shell Model, Where $n = 1$ and Diameter 0.670 in. (Wire Frame Surface)

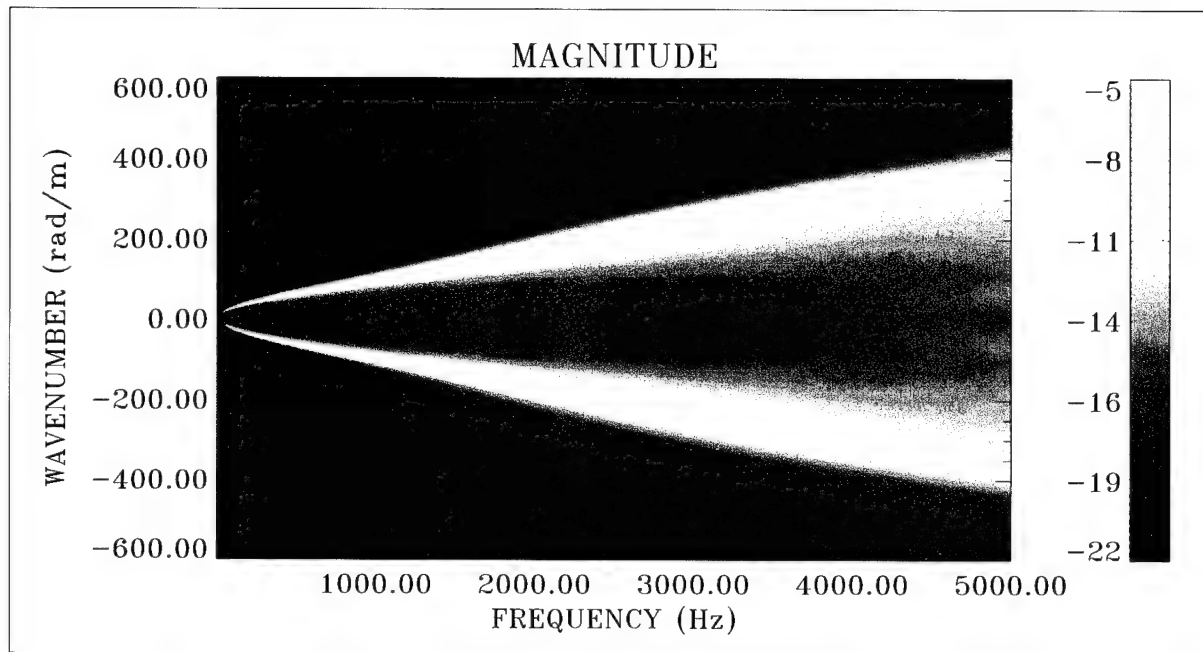


Figure 58. Pressure Transfer Surface With Magnitude = $10\text{Log}(P_i(r_1)/P_o)^2$ at $r_1 = 0.1$ in. for Bending Shell Model, Where $n = 1$ and Diameter = 0.670 in. (Color Image)

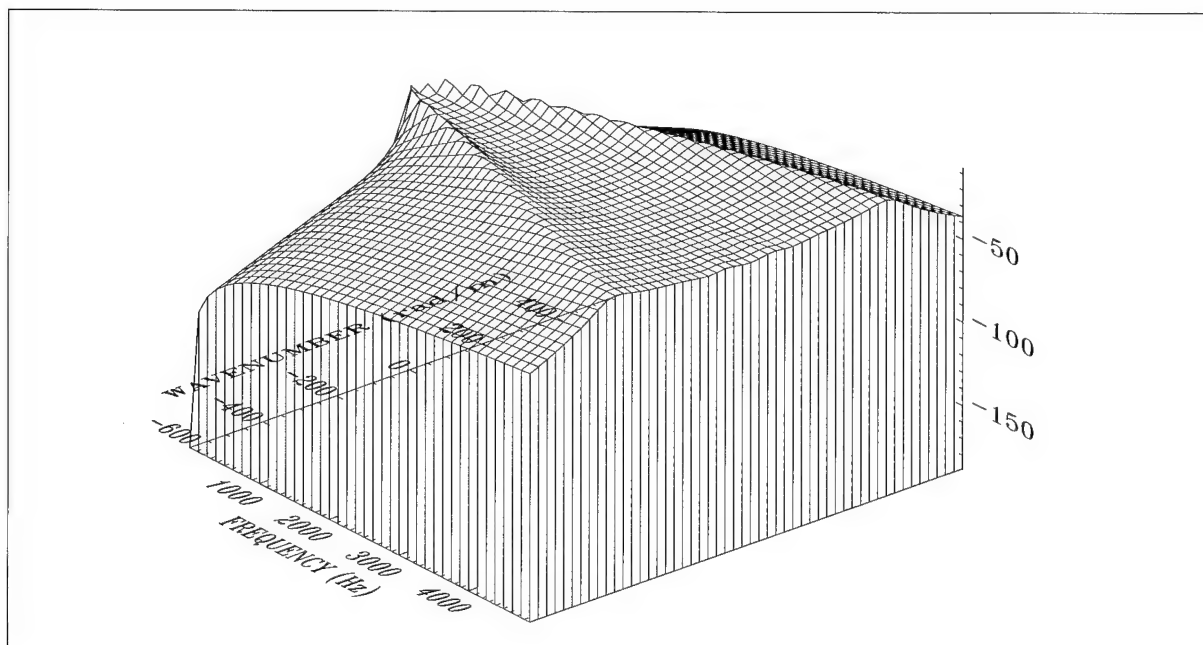


Figure 59. Pressure Transfer Surface With Magnitude = $10\text{Log}(P_i(r_1)/P_o)^2$ at $r_1 = 0.1$ in. for Bending Shell Model, Where $n = 1$ and Diameter = 0.670 in. (Wire Frame Surface)

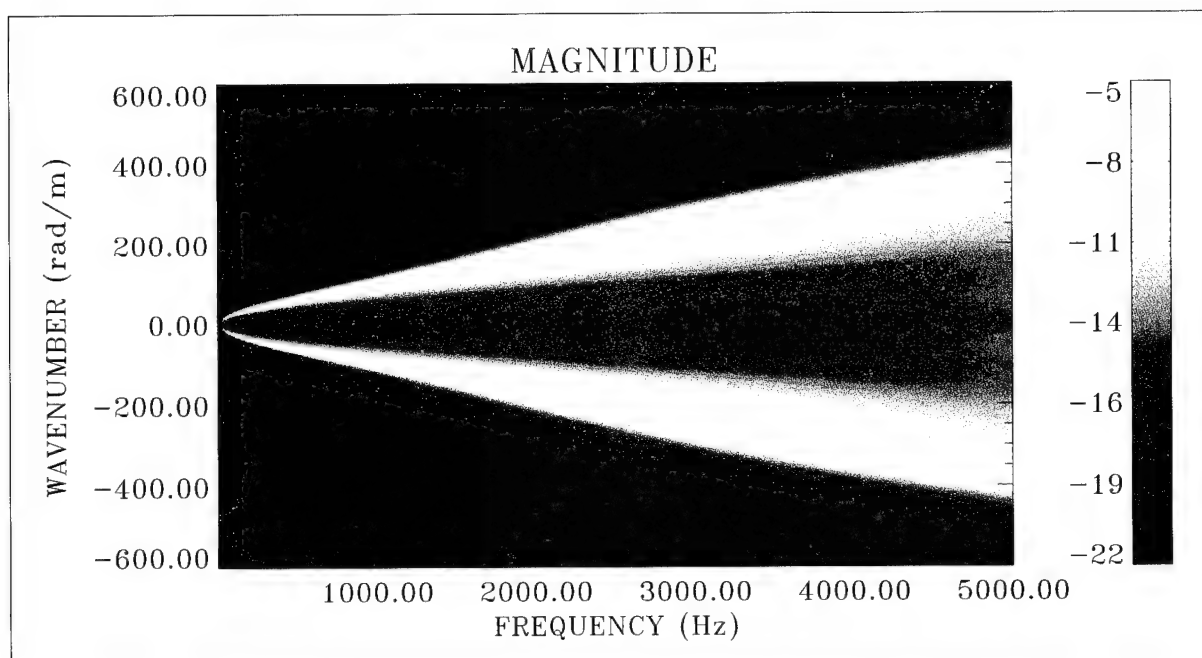


Figure 60. Pressure Transfer Surface With Magnitude = $10 \log(P_i(r_1)/P_o)^2$ at $r_1 = 0.1$ in. for Elasticity Model, Where $n = 1$ and Diameter = 0.670 in. (Color Image)

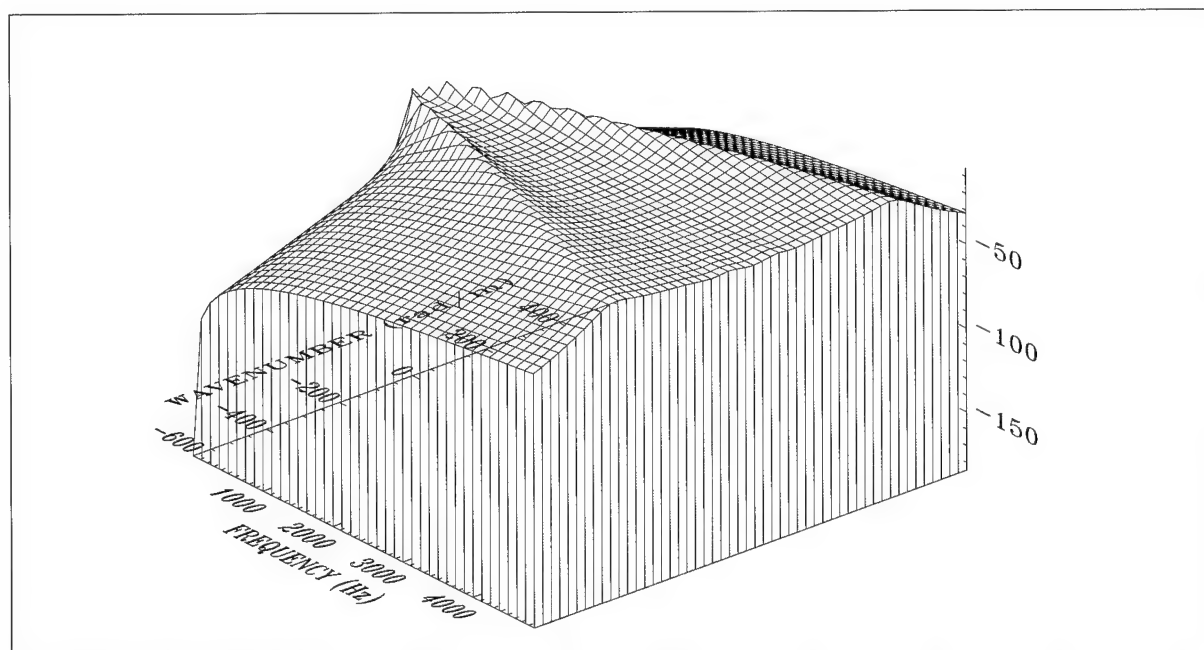
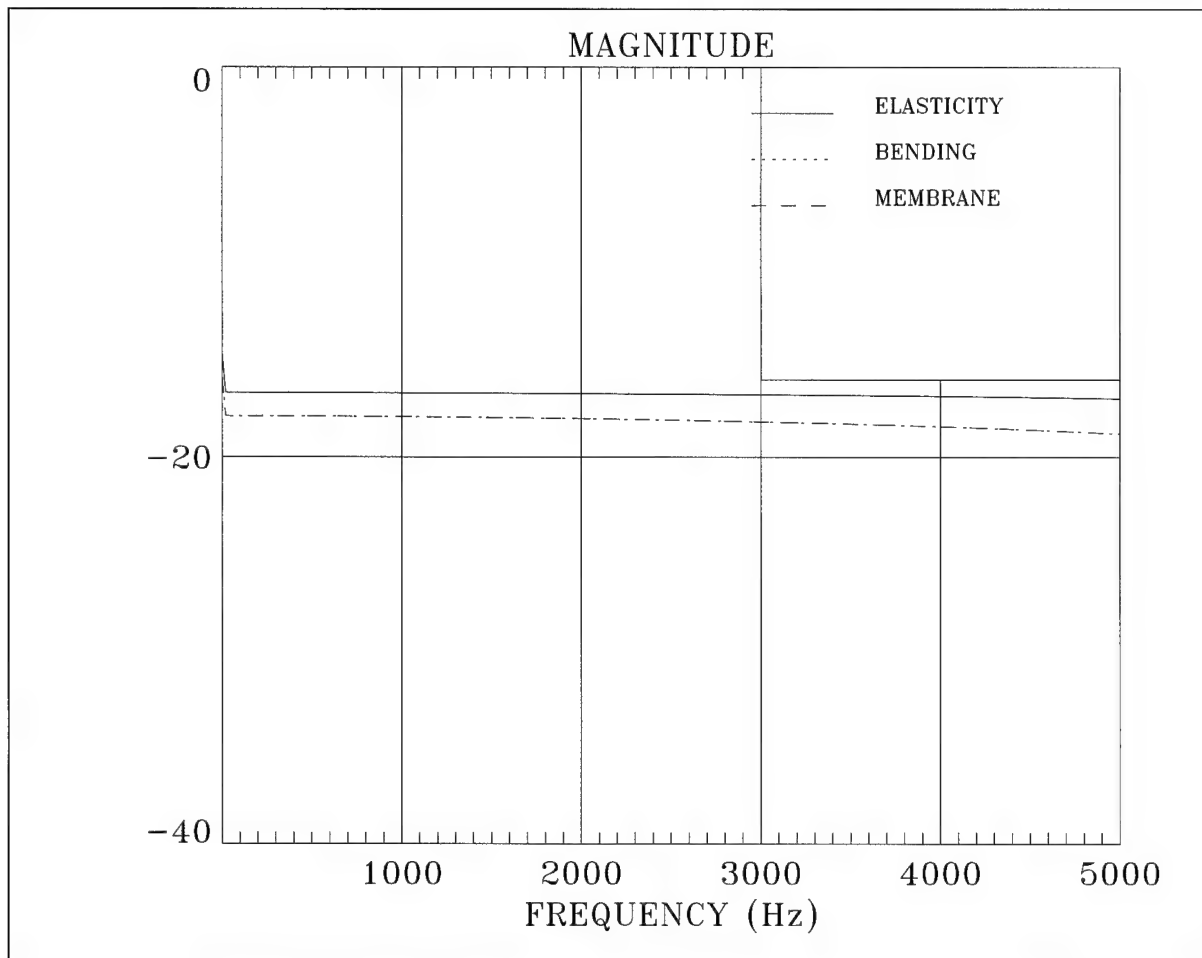
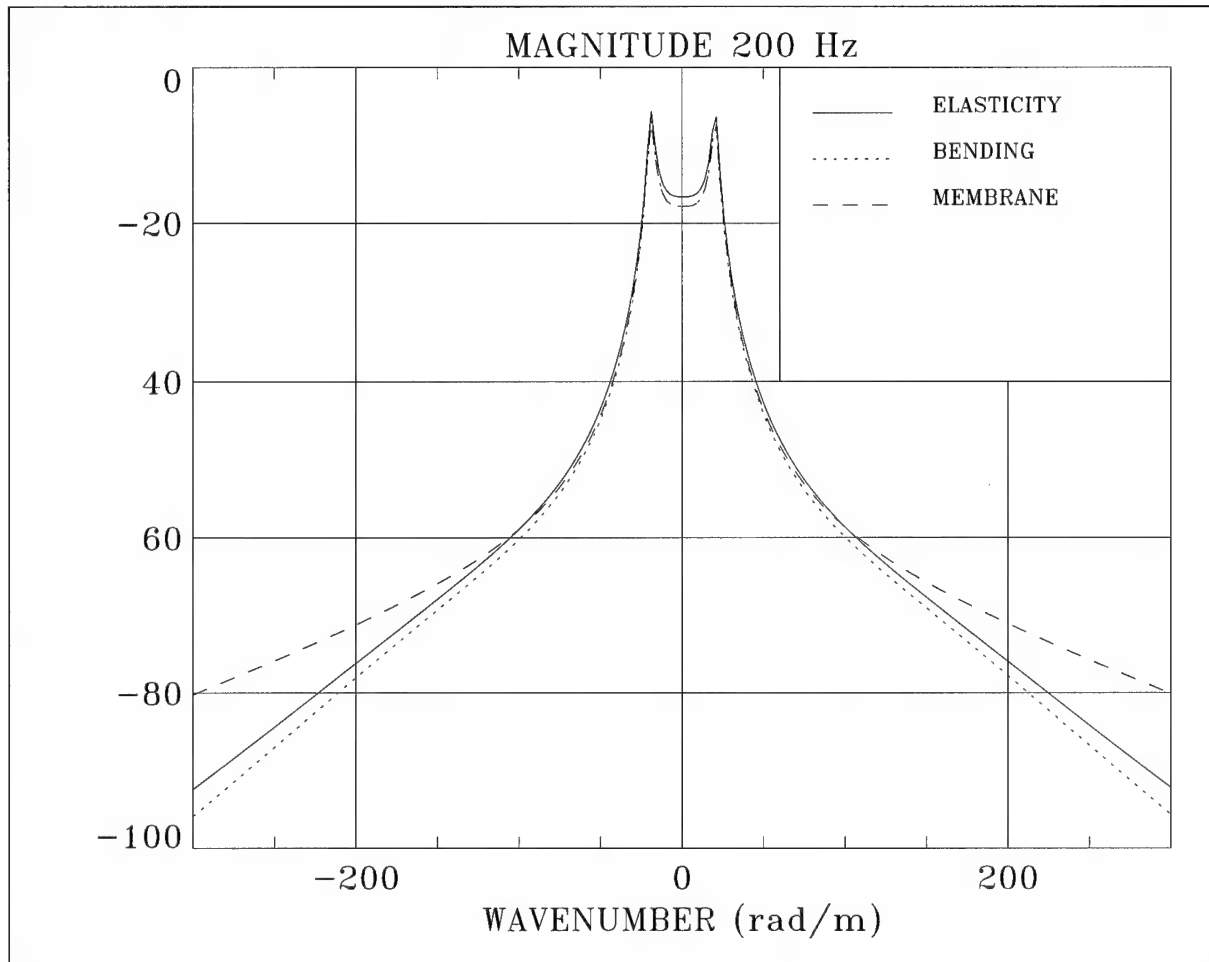


Figure 61. Pressure Transfer Surface With Magnitude = $10 \log(P_i(r_1)/P_o)^2$ at $r_1 = 0.1$ in. for Elasticity Model, Where $n = 1$ and Diameter = 0.670 in. (Wire Frame Surface)



**Figure 62. Model Comparison for Figures 56, 58, and 60 When
Magnitude = $10\text{Log}(P_i(r_1)/P_o)^2$ at $r_1 = 0.1$ in. With $n = 1$,
Diameter = 0.670 in., and $k = 0$ rad/m**



**Figure 63. Model Comparison for Figures 56, 58, and 60 When
Magnitude = $10\text{Log}(P_i(r_1)/P_o)^2$ at $r_1 = 0.1$ in. With $n = 1$,
Diameter = 0.670 in., and $f = 200$ Hz**

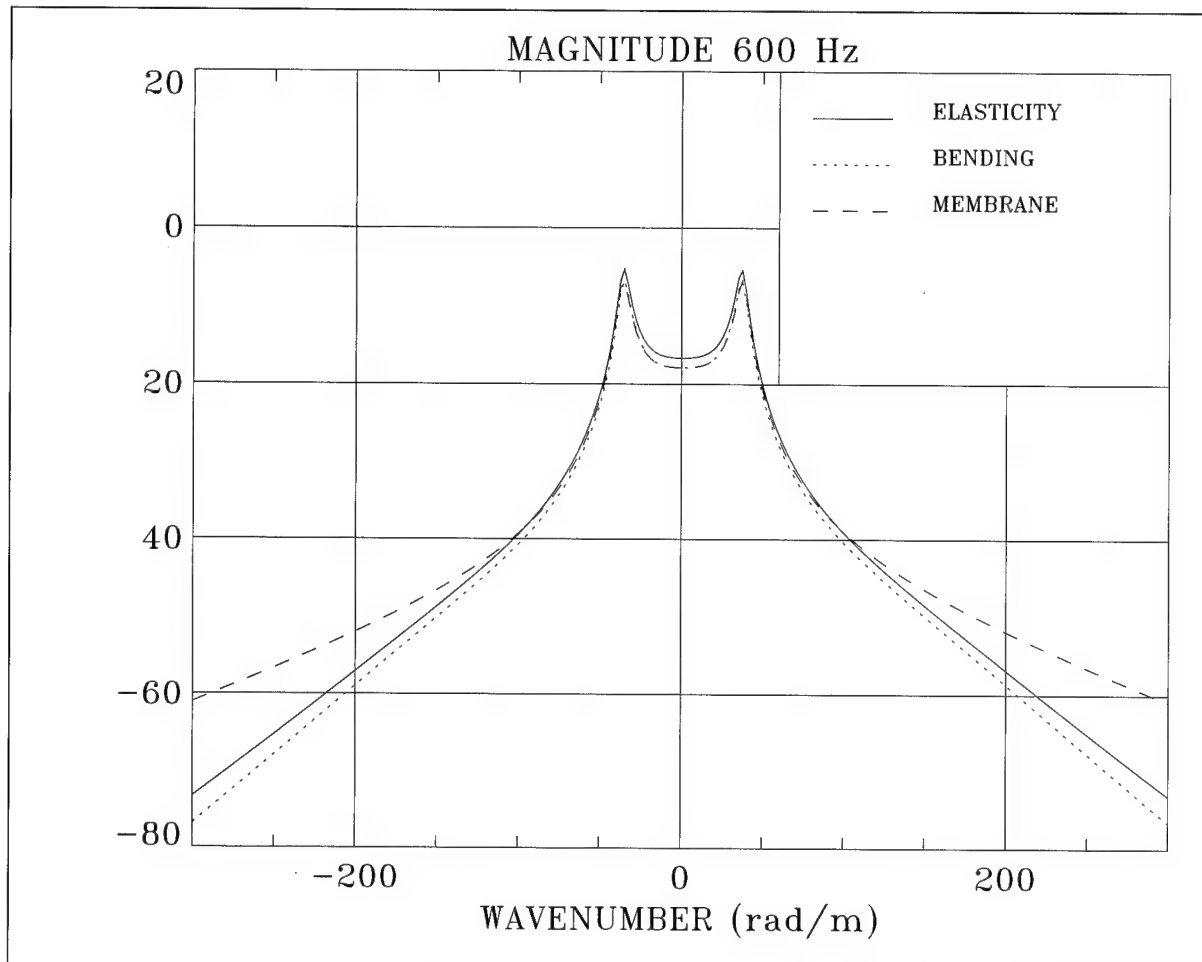


**Figure 64. Model Comparison for Figures 56, 58, and 60 When
Magnitude = $10\text{Log}(P_i(r_1)/P_o)^2$ at $r_1 = 0.1$ in. With $n = 1$,
Diameter = 0.670 in., and $f = 600$ Hz**

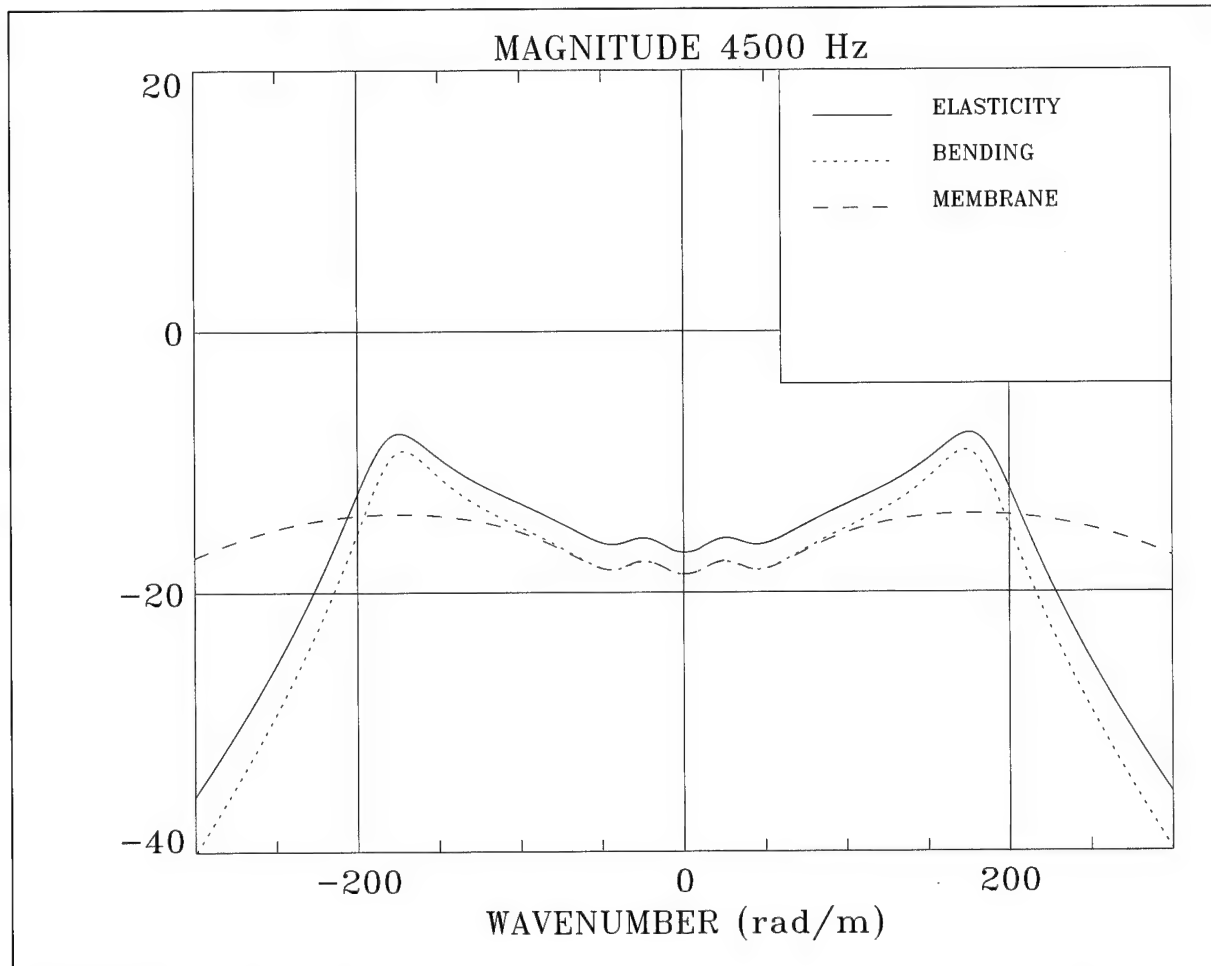


**Figure 65. Model Comparison for Figures 56, 58, and 60 When
Magnitude = $10\text{Log}(P_i(r_1)/P_o)^2$ at $r_1 = 0.1$ in. With $n = 1$,
Diameter = 0.670 in., and $f = 4500$ Hz**

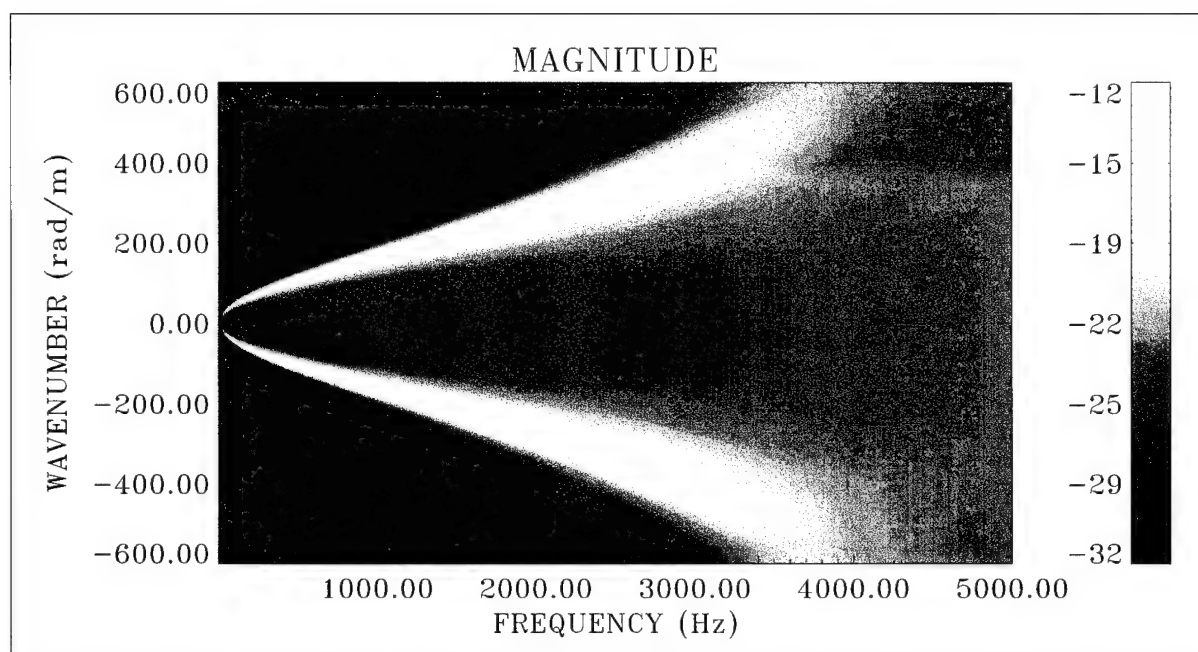


Figure 66. Pressure Transfer Surface With Magnitude = $10\text{Log}(P_i(r_1)/P_o)^2$ at $r_1 = 0.1$ in. for Membrane Shell Model, Where $n = 2$ and Diameter = 0.670 in. (Color Image)

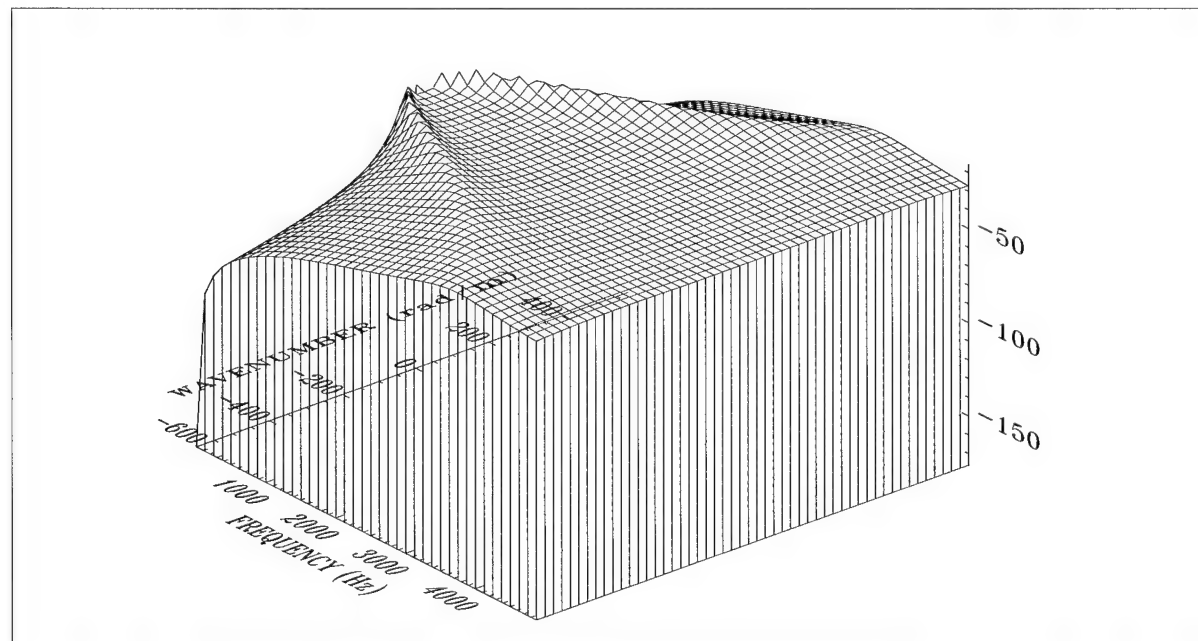


Figure 67. Pressure Transfer Surface With Magnitude = $10\text{Log}(P_i(r_1)/P_o)^2$ at $r_1 = 0.1$ in. for Membrane Shell Model, Where $n = 2$ and Diameter = 0.670 in. (Wire Frame Surface)

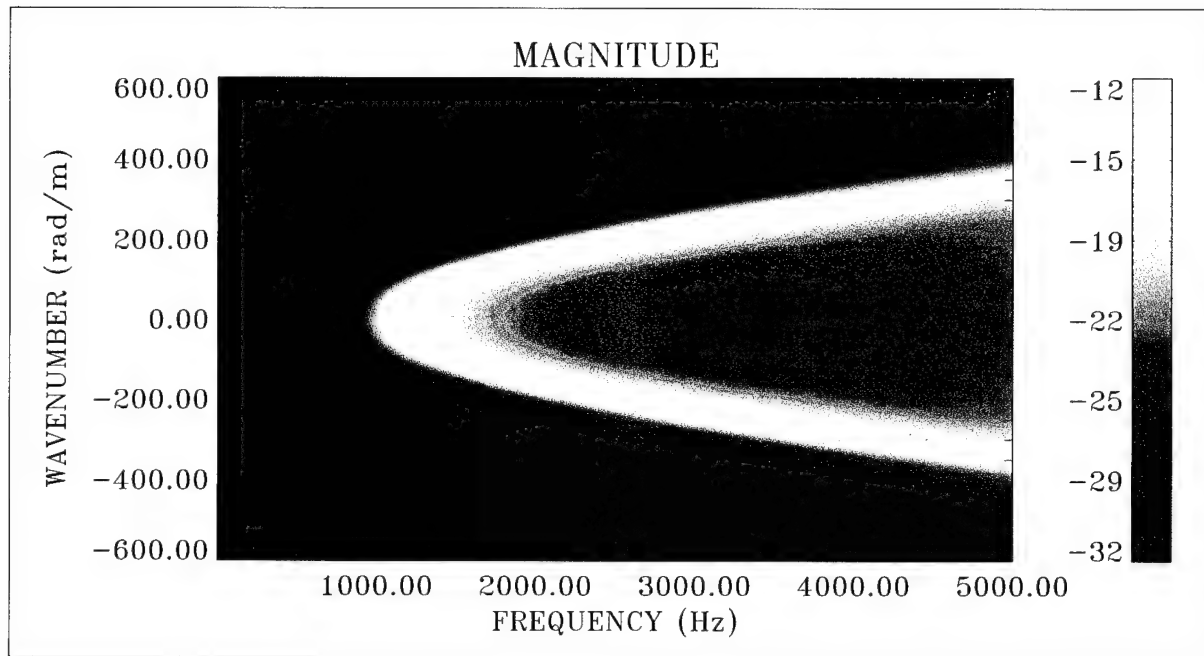


Figure 68. Pressure Transfer Surface With Magnitude = $10\text{Log}(P_i(r_1)/P_o)^2$ at $r_1 = 0.1$ in. for Bending Shell Model, Where $n = 2$ and Diameter = 0.670 in. (Color Image)

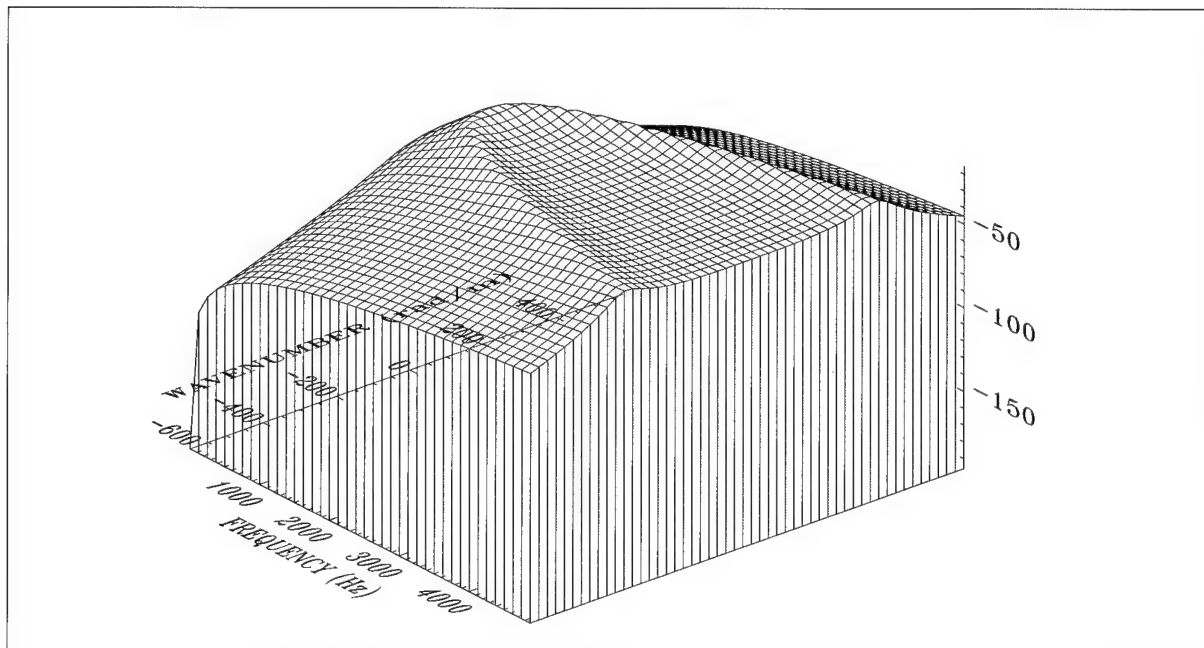


Figure 69. Pressure Transfer Surface With Magnitude = $10\text{Log}(P_i(r_1)/P_o)^2$ at $r_1 = 0.1$ in. for Bending Shell Model, Where $n = 2$ and Diameter = 0.670 in. (Wire Frame Surface)

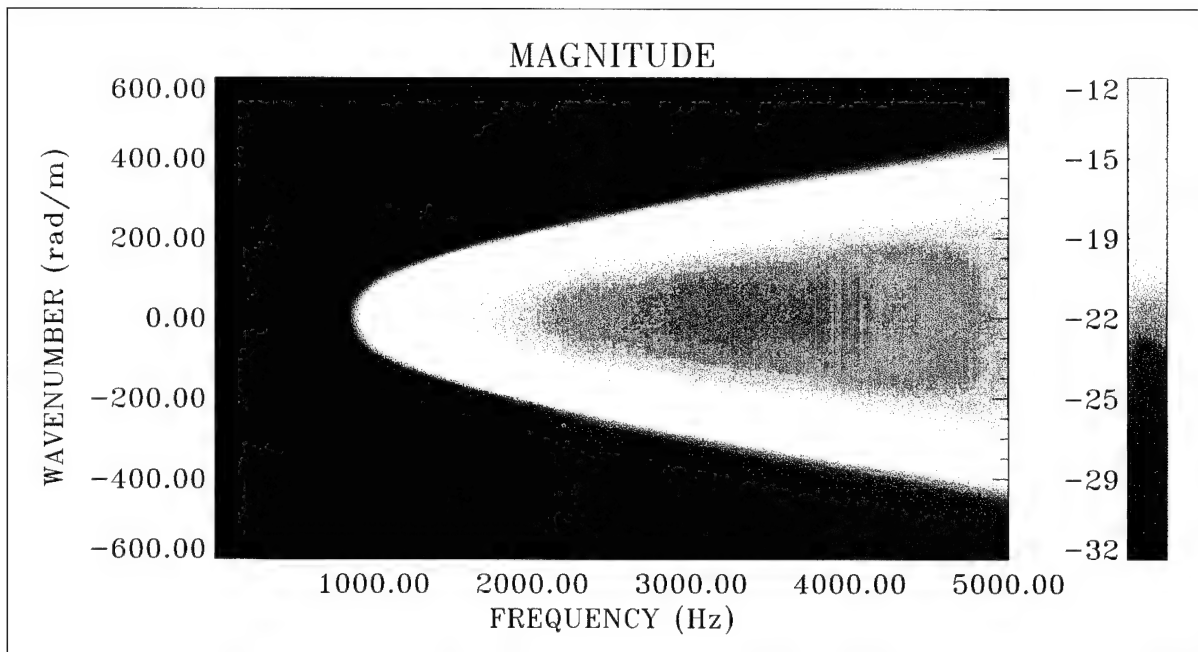


Figure 70. Pressure Transfer Surface With Magnitude = $10\text{Log}(P_i(r_1)/P_o)^2$ at $r_1 = 0.1$ in. for Elasticity Model, Where $n = 2$ and Diameter = 0.670 in. (Color Image)

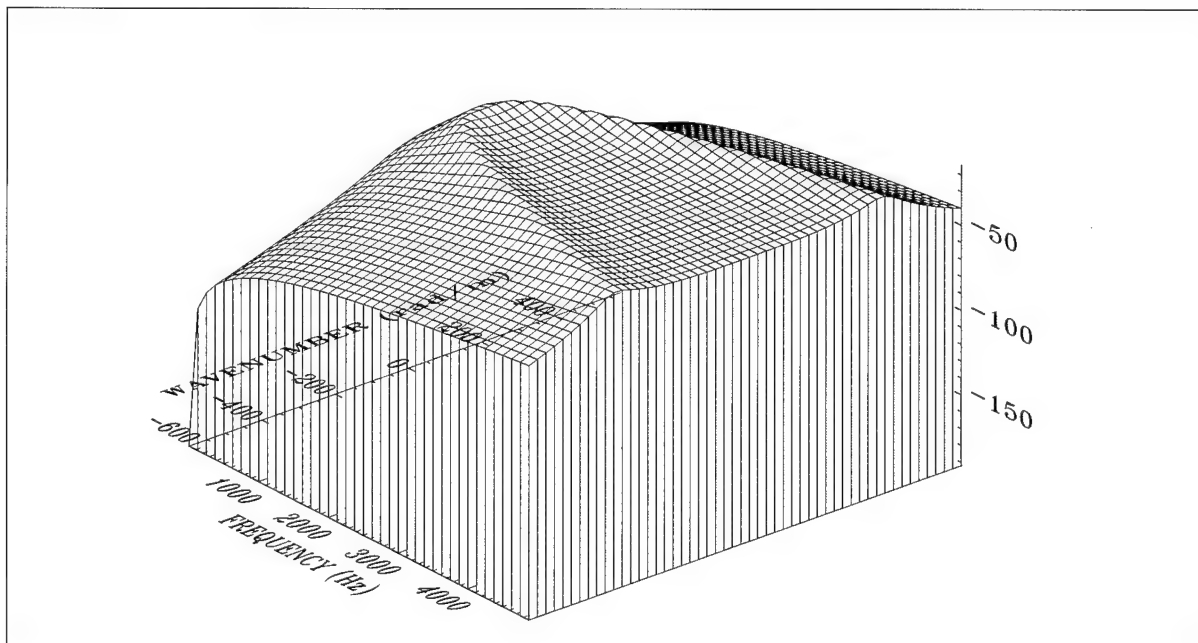
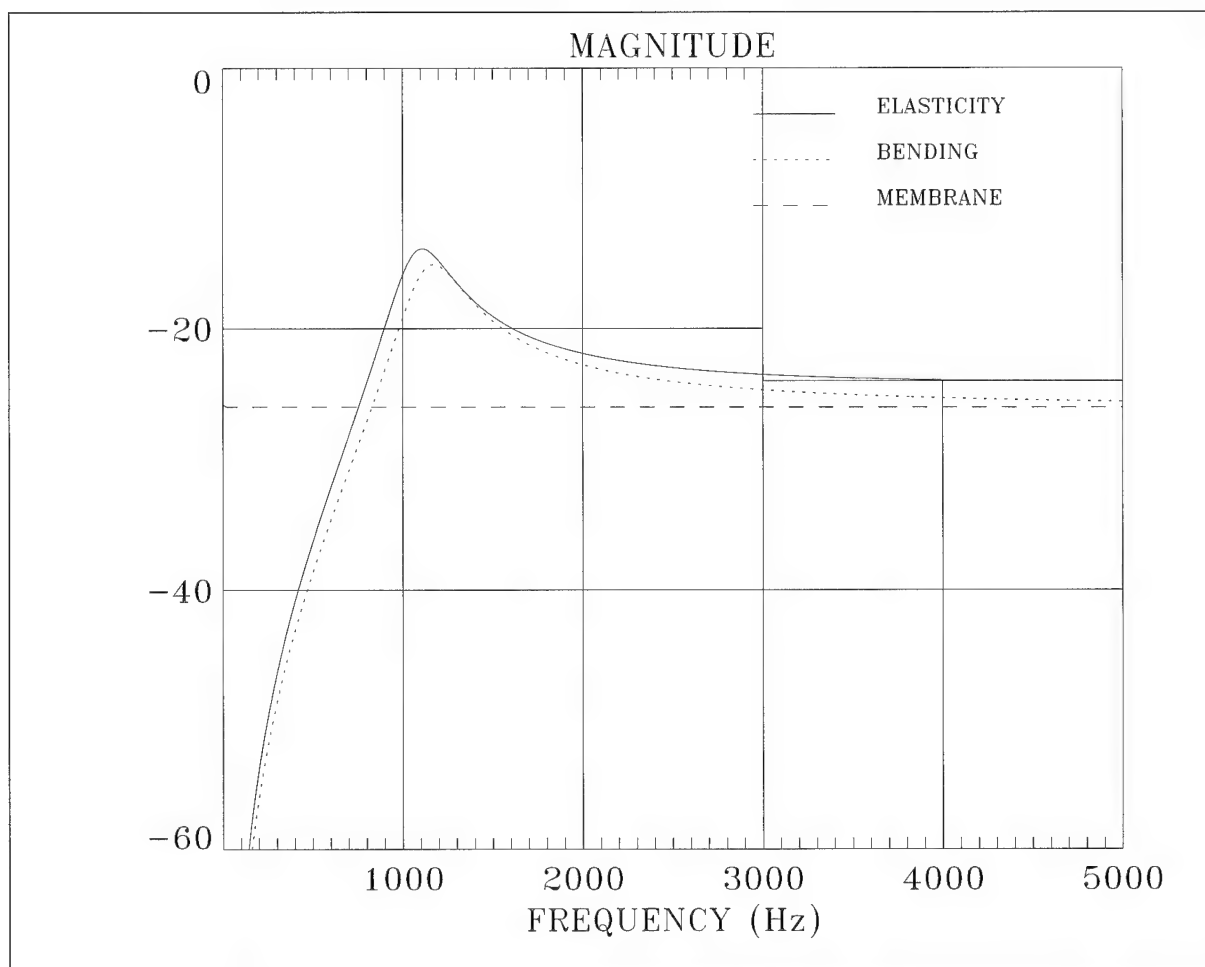
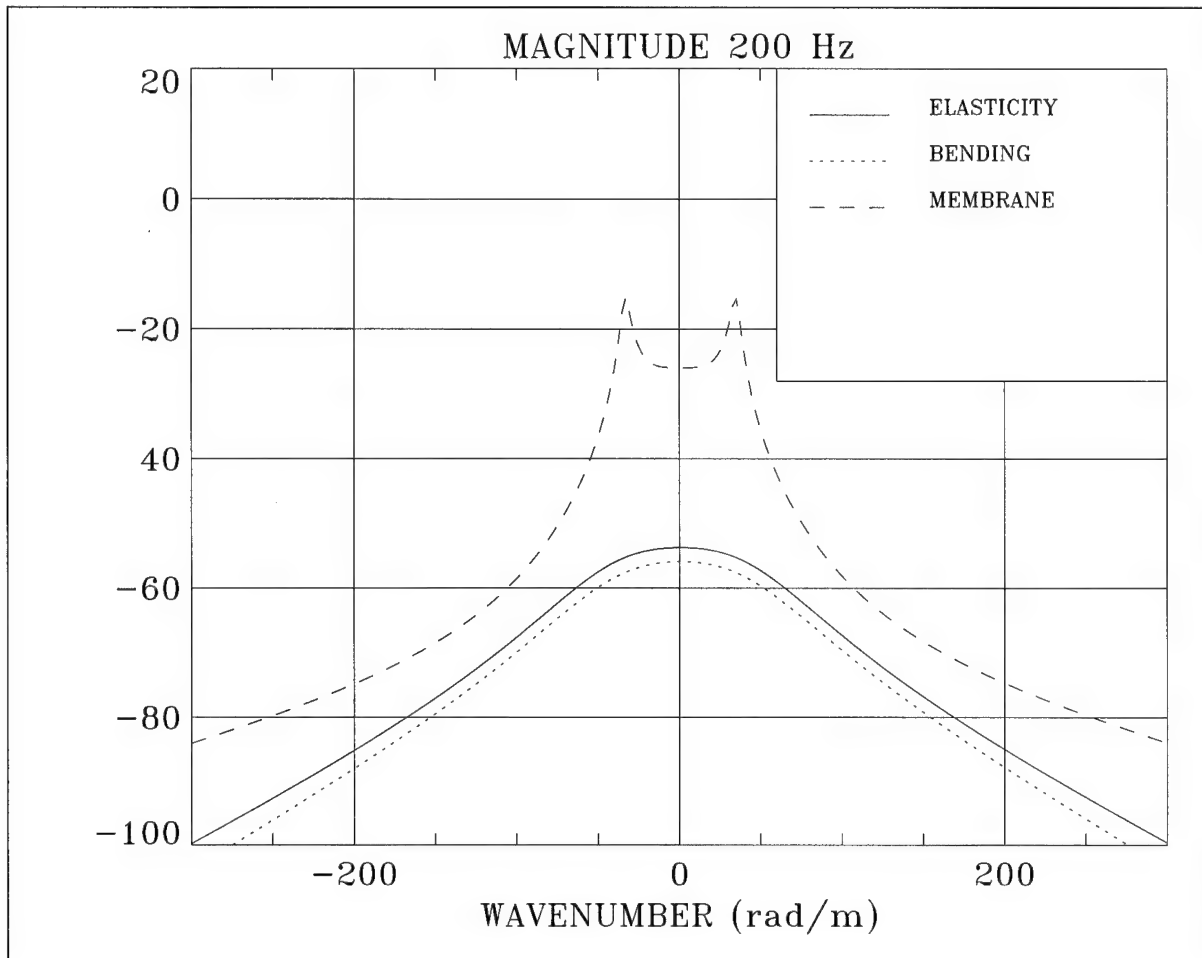


Figure 71. Pressure Transfer Surface With Magnitude = $10\text{Log}(P_i(r_1)/P_o)^2$ at $r_1 = 0.1$ in. for Elasticity Model, Where $n = 2$ and Diameter = 0.670 in. (Wire Frame Surface)



**Figure 72. Model Comparison for Figures 66, 68, and 70 When
Magnitude = $10\text{Log}(P_i(r_1)/P_o)^2$ at $r_1 = 0.1$ in. With $n = 2$,
Diameter = 0.670 in., and $k = 0$ rad/m**



**Figure 73. Model Comparison for Figures 66, 68, and 70 When
Magnitude = $10\text{Log}(P_i(r_1)/P_o)^2$ at $r_1 = 0.1$ in. With $n = 2$,
Diameter = 0.670 in., and $f = 200$ Hz**

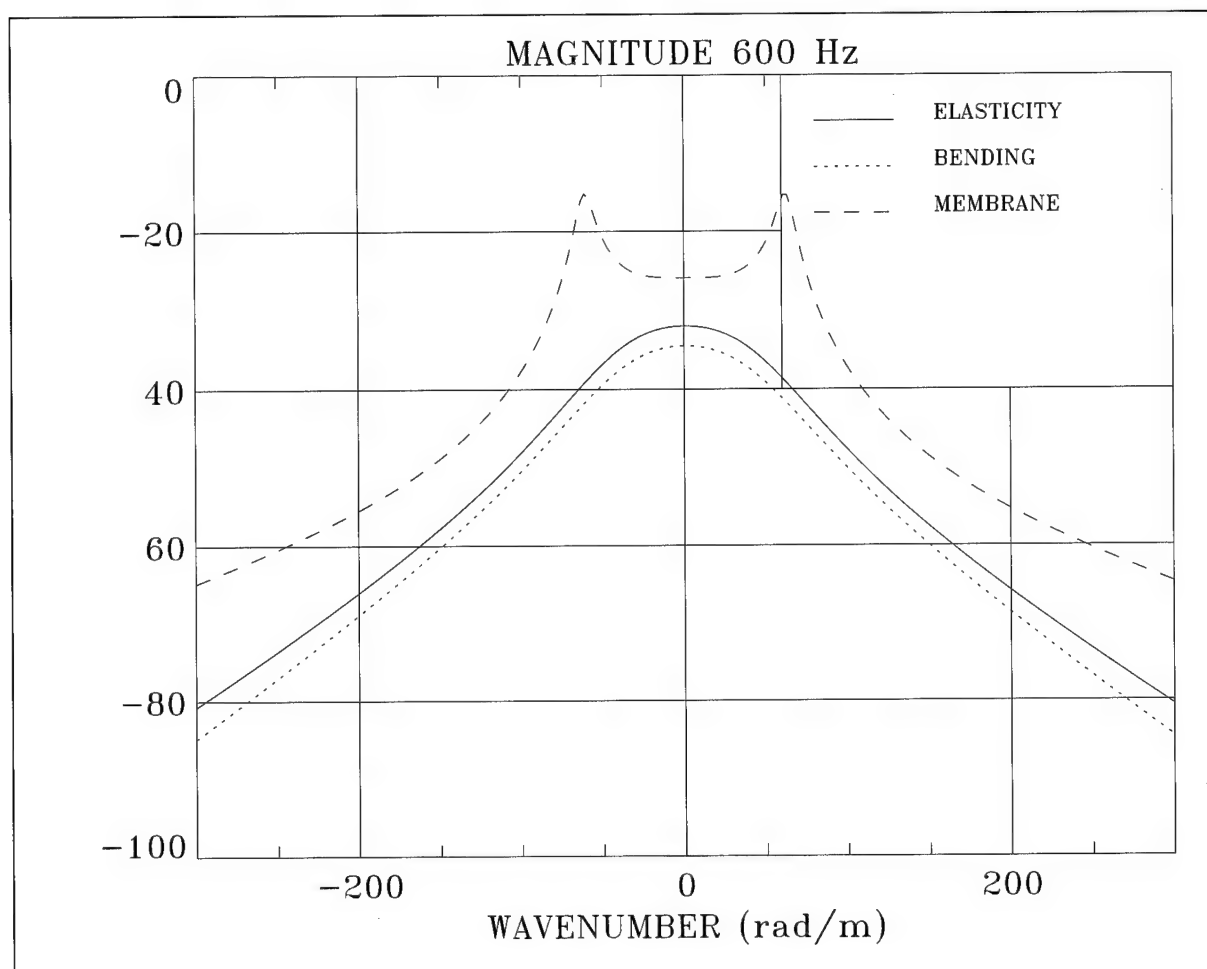


**Figure 74. Model Comparison for Figures 66, 68, and 70 When
Magnitude = $10\text{Log}(P_i(r_1)/P_o)^2$ at $r_1 = 0.1$ in. With $n = 2$,
Diameter = 0.670 in., and $f = 600$ Hz**

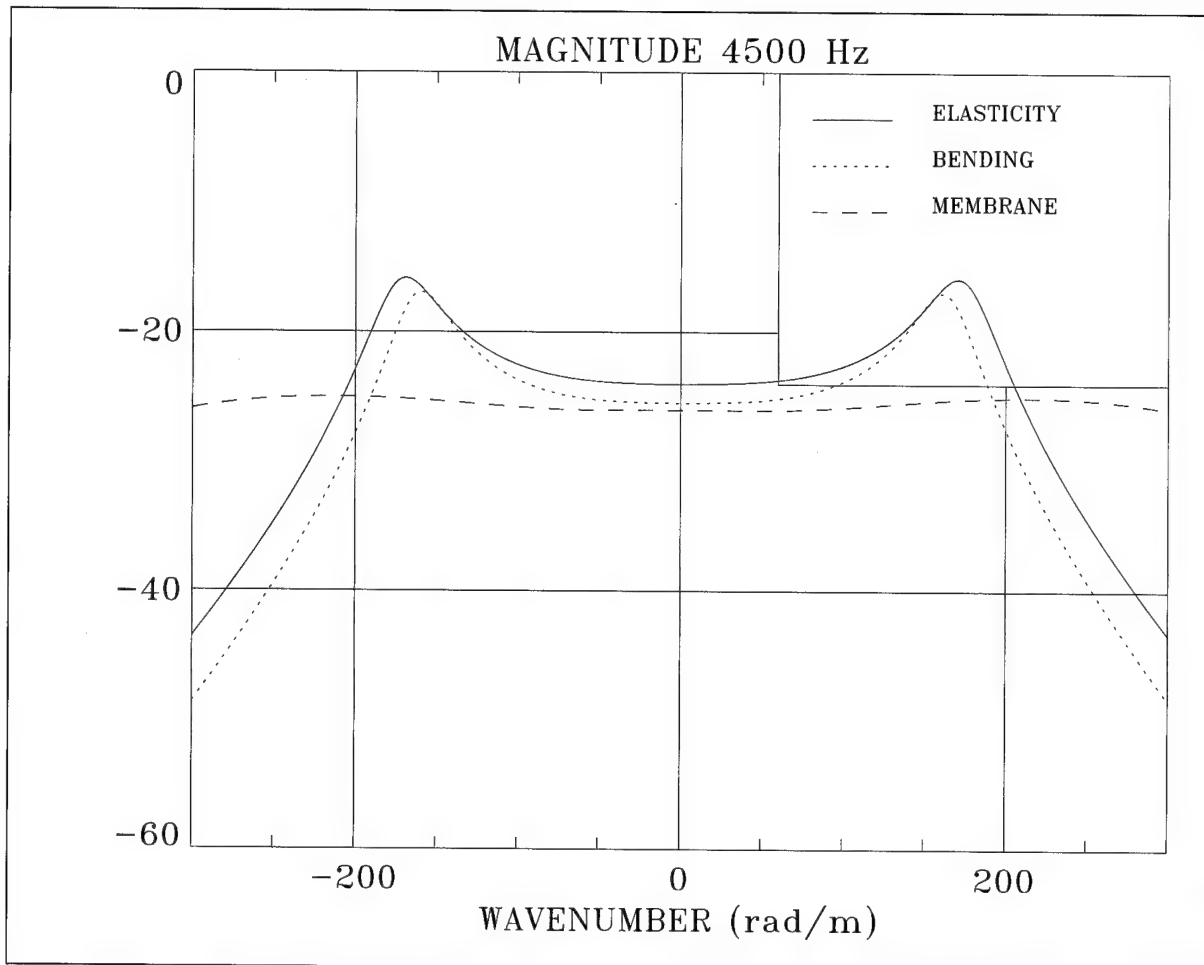


**Figure 75. Model Comparison for Figures 66, 68, and 70 When
Magnitude = $10\text{Log}(P_i(r_1)/P_o)^2$ at $r_1 = 0.1$ in. With $n = 2$,
Diameter = 0.670 in., and $f = 4500$ Hz**

Inner Fluid Pressure Field Evanescence

From this point on, unless otherwise noted, the elasticity model will be used for the simulations conducted in the exploration of the cylinder/fluid dynamic behavior.

Let us consider the effect of the propagating region and the nonpropagating region on the magnitude of the pressure field that exists in the inner fluid as a function of radial position. For wavenumbers less than ω/c_i , the pressure field propagates as shown by equation (67). For wavenumbers greater than ω/c_i , the pressure field becomes increasingly evanescent, with increasing wavenumber and decreasing radial position r , as shown by equation (71).

The simulation for the inner fluid pressure field at $r_1 = 1.1$ inches is shown in figures 76 and 77. The simulation of this pressure field at $r_1 = 0.01$ inch is shown in figures 78 and 79. In figures 80, 81, and 82, comparison of the pressure field is made for these two radial positions at three different frequencies. Attenuation of the pressure field, which is apparent in all the figures, is on the order of 12 dB at 100 rad/m.

Comparison of the images in figures 76 and 78 reveals a decrease in breathing wave resonant peak level with increasing wavenumber. The breathing wave pressure is locally generated at the cylinder/fluid boundary. Because the breathing wave phase velocity is an order of magnitude slower than the inner fluid propagation velocity, the magnitude of the pressure will suffer increasing attenuation away from the surface of generation as the breathing wave diverges in wavenumber (compare figures 80 and 81).

Similar behavior is observed with the extensional wave. However, since the phase velocity of the extensional wave is greater than the breathing wave, similar attenuation does not occur until a higher frequency is reached. In figure 82 (4500 Hz), the extensional wave has undergone approximately the same attenuation (12 dB) as the breathing wave has undergone in figure 81 (12 dB) at 900 Hz.

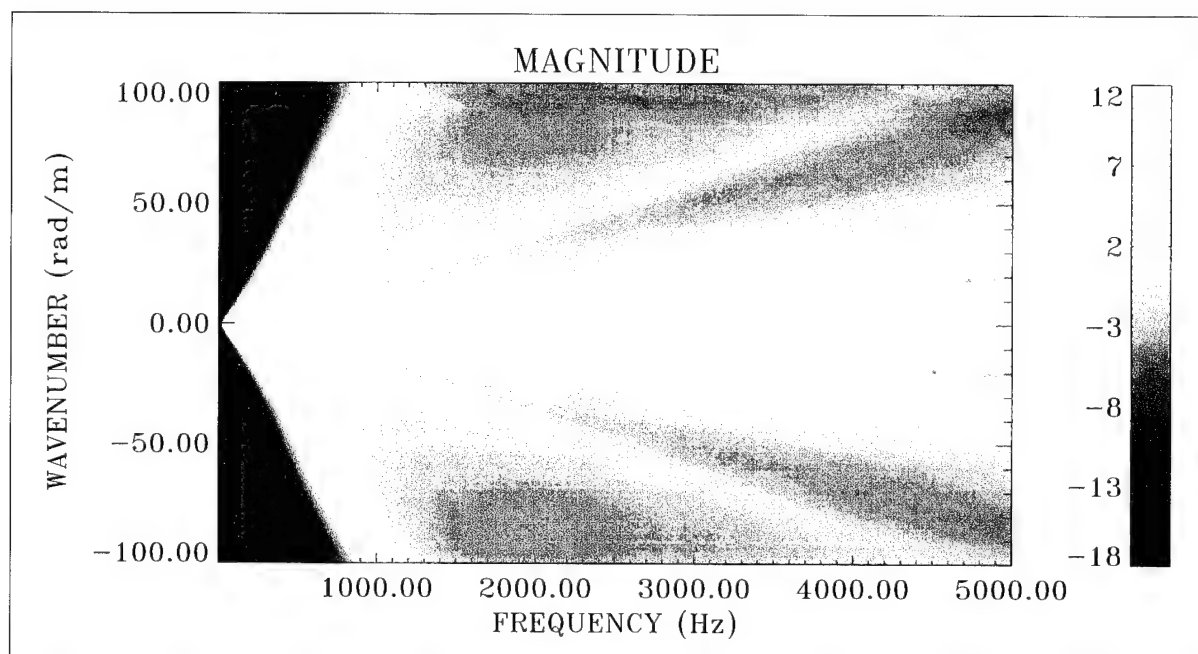


Figure 76. Pressure Transfer Surface With Magnitude = $10\text{Log}(P_i(r_1)/P_o)^2$ at $r_1 = 1.1$ in. Where $n = 0$ and Diameter = 3.00 in. for Field Decay Comparison (Color Image)

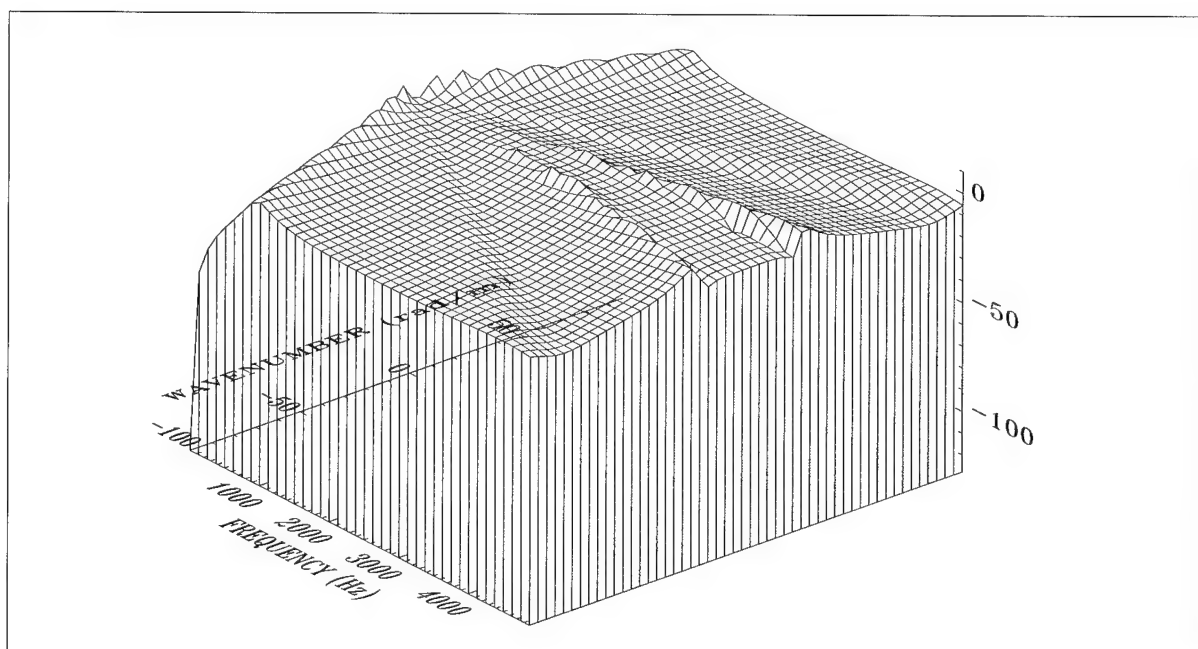


Figure 77. Pressure Transfer Surface With Magnitude = $10\text{Log}(P_i(r_1)/P_o)^2$ at $r_1 = 1.1$ in. Where $n = 0$ and Diameter = 3.00 in. for Field Decay Comparison (Wire Frame Surface)

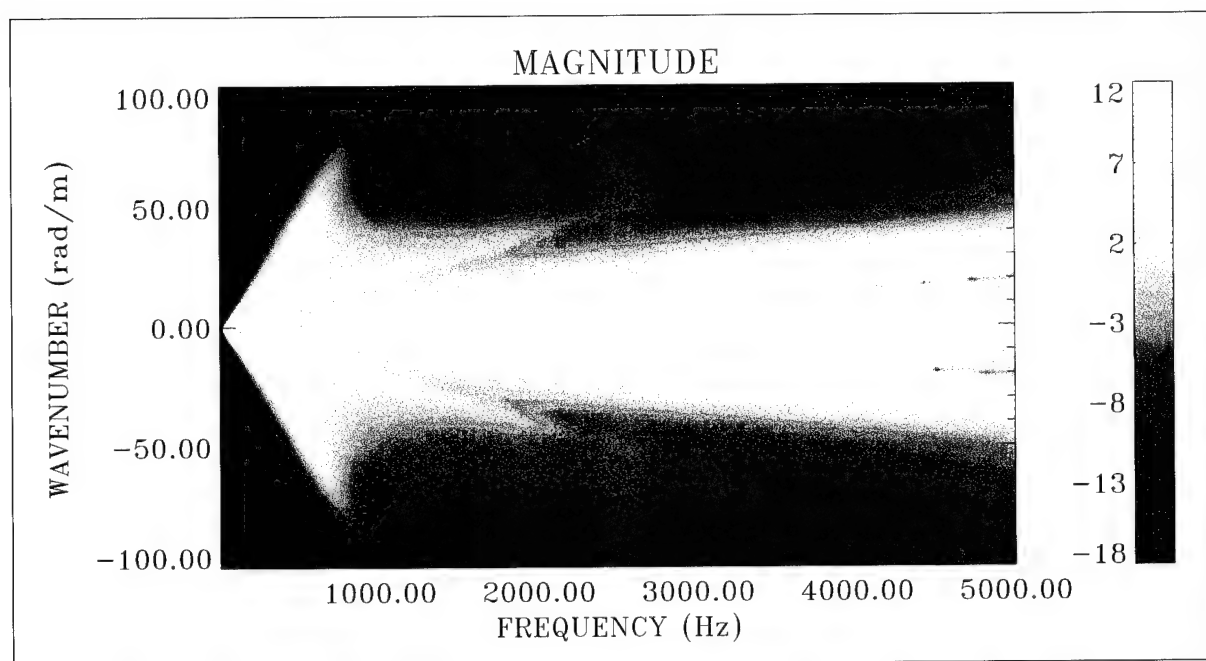


Figure 78. Pressure Transfer Surface With Magnitude = $10\text{Log}(P_i(r_1)/P_o)^2$ at $r_1 = 0.01$ in. Where $n = 0$ and Diameter = 3.00 in. for Field Decay Comparison (Color Image)

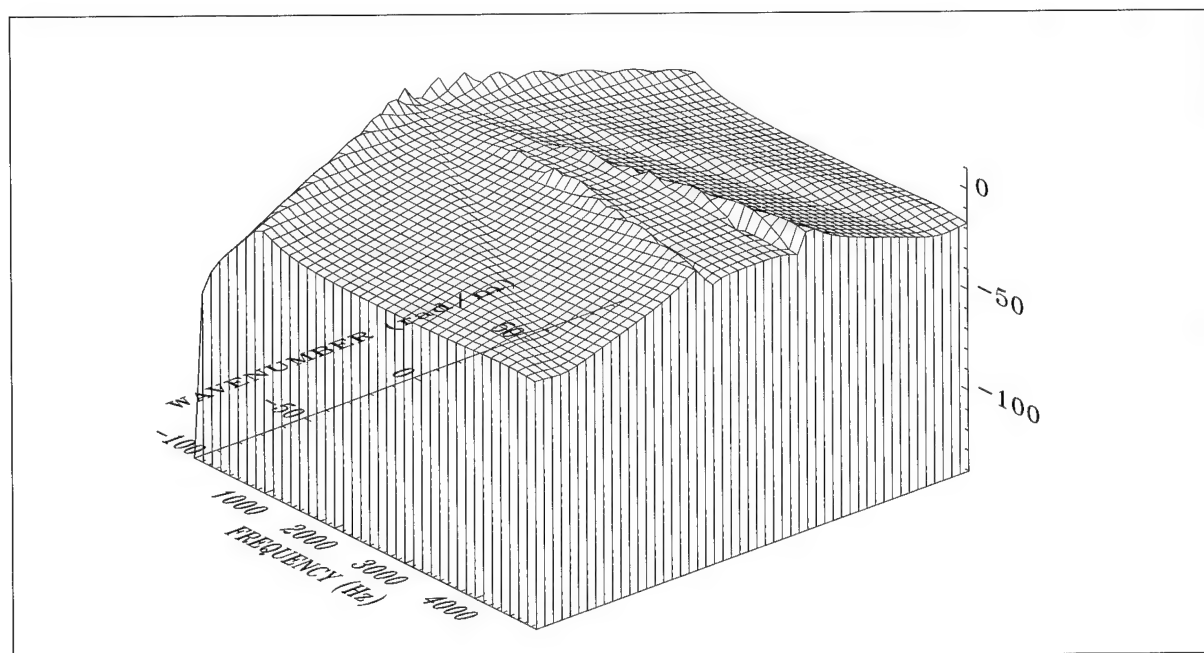
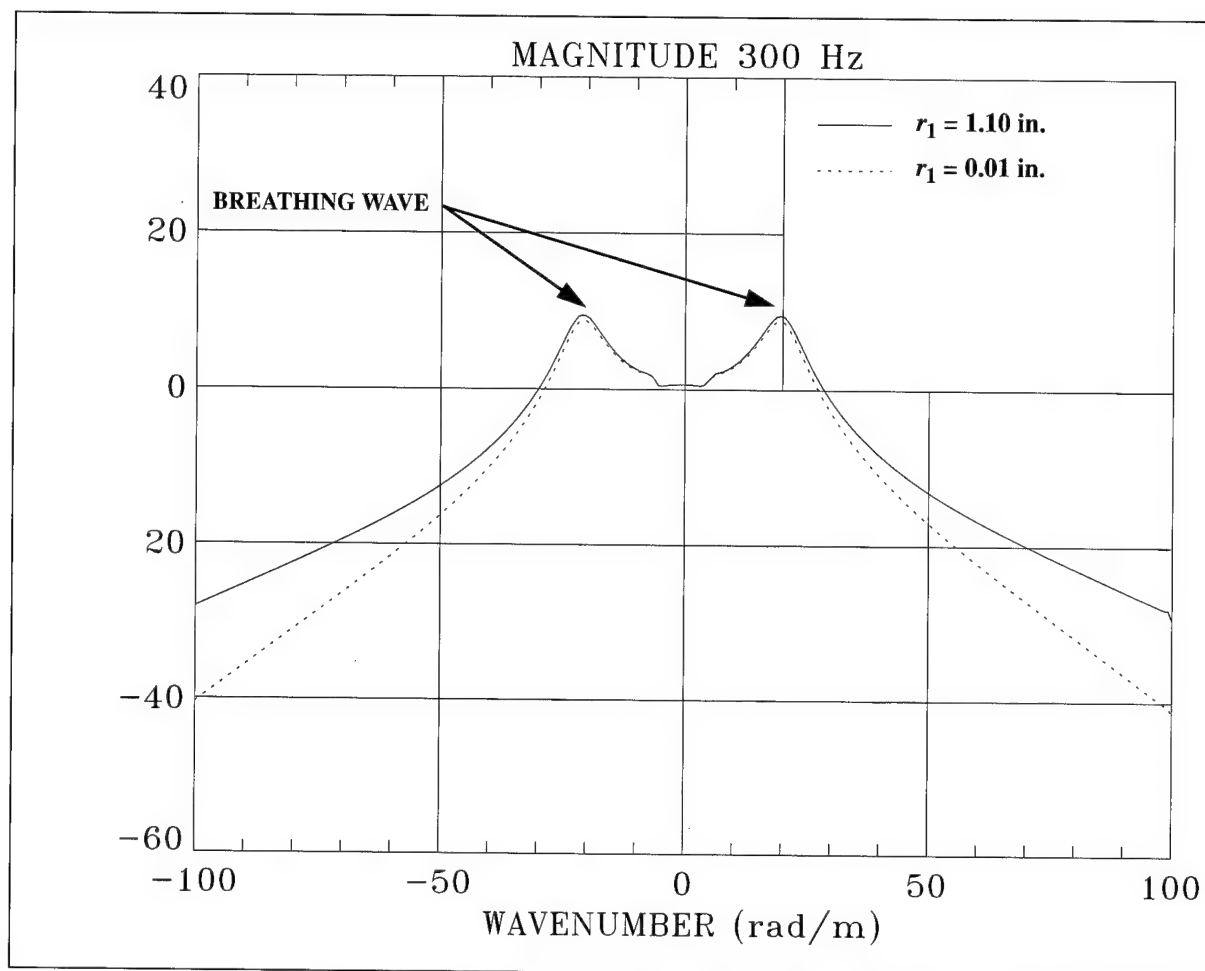
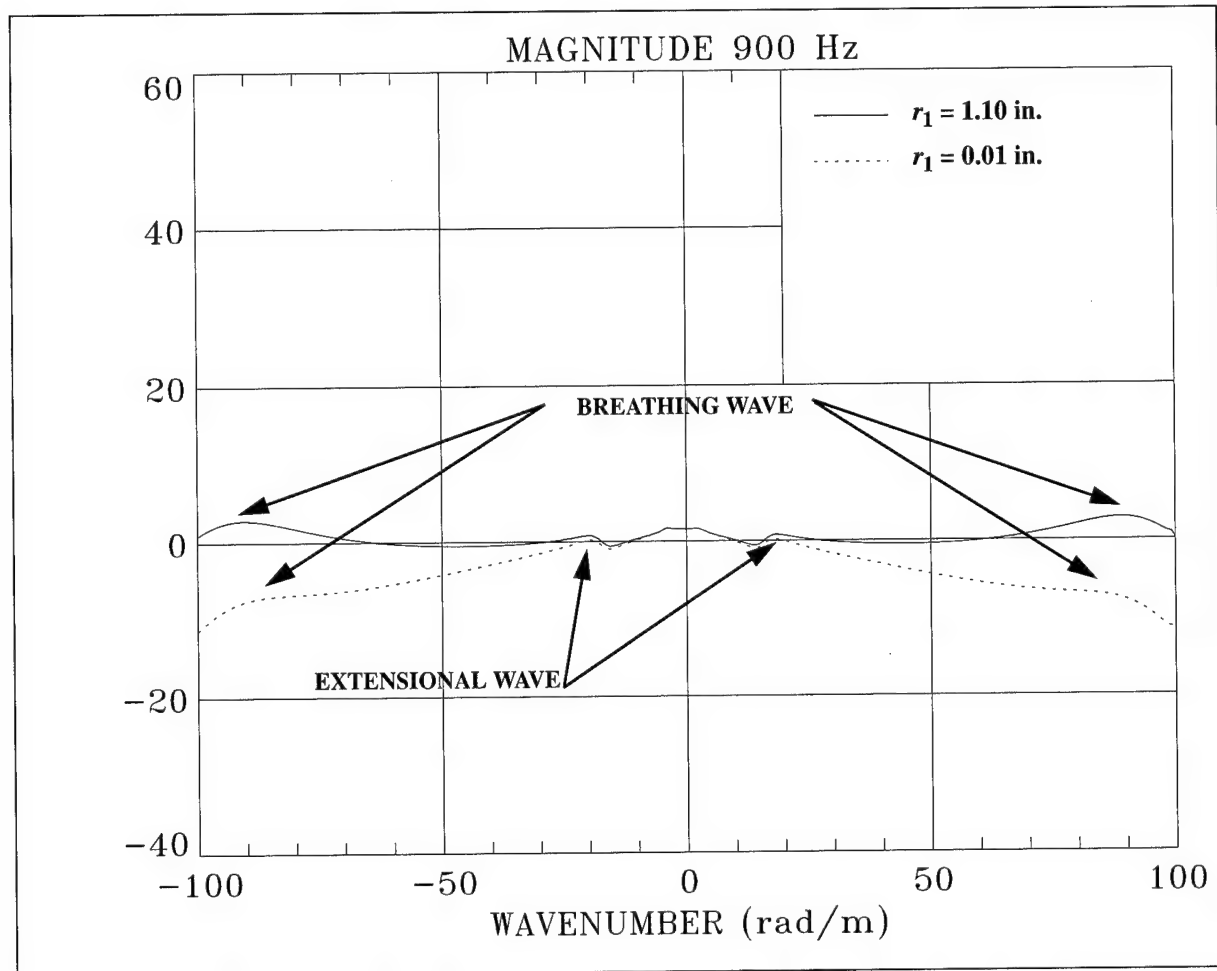


Figure 79. Pressure Transfer Surface With Magnitude = $10\text{Log}(P_i(r_1)/P_o)^2$ at $r_1 = 0.01$ in. Where $n = 0$ and Diameter = 3.00 in. for Field Decay Comparison (Wire Frame Surface)



**Figure 80. Field Decay Comparison for Figures 76 and 78 When
Magnitude = $10\text{Log}(P_i(r_1)/P_o)^2$ at Various r_1 With $n = 0$,
Diameter = 3.00 in., and $f = 300$ Hz**



**Figure 81. Field Decay Comparison for Figures 76 and 78 When
Magnitude = $10\text{Log}(P_i(r_1)/P_o)^2$ at Various r_1 With $n = 0$,
Diameter = 3.00 in., and $f = 900$ Hz**

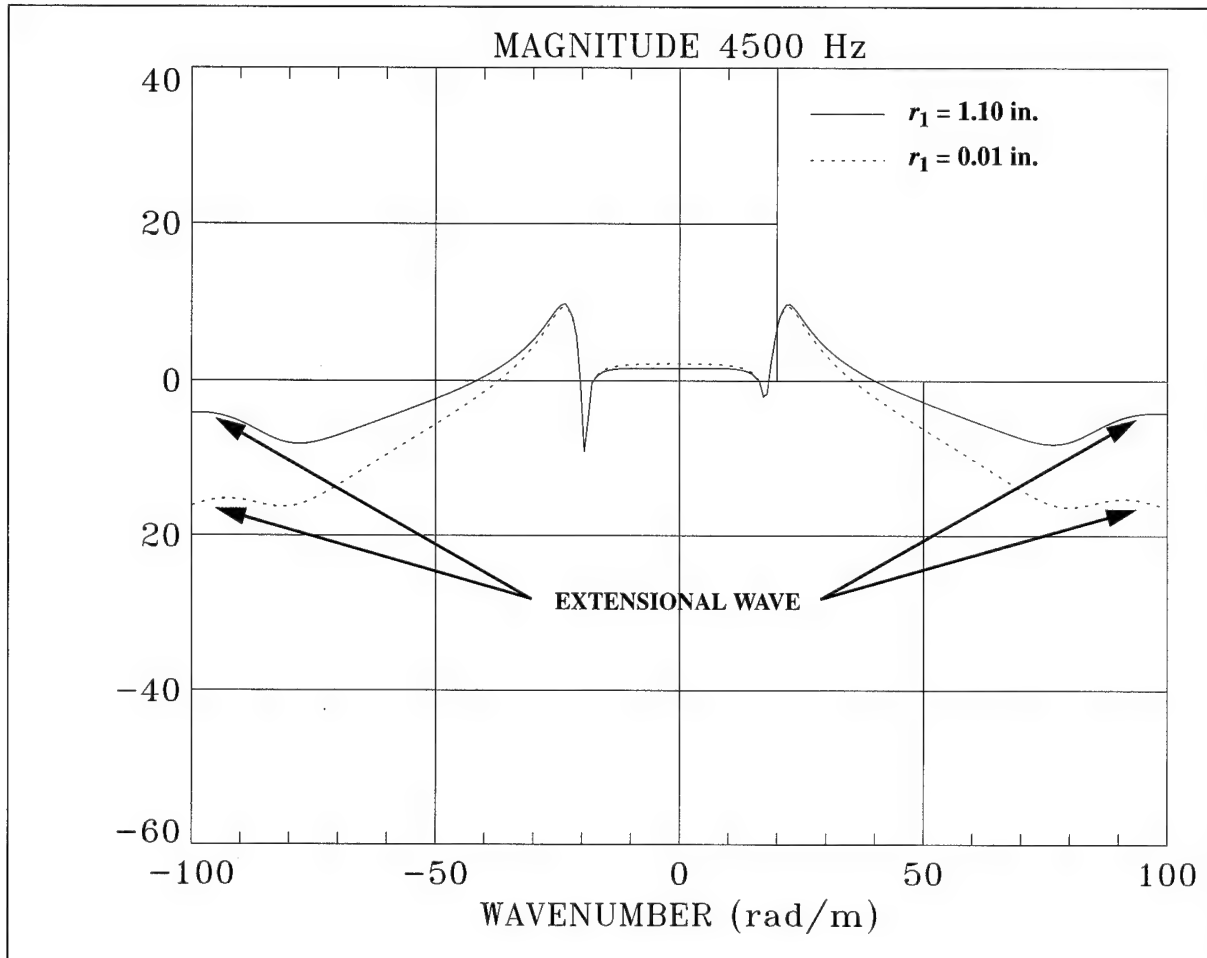


**Figure 82. Field Decay Comparison for Figures 76 and 78 When
 Magnitude = $10\text{Log}(P_i(r_1)/P_o)^2$ at Various r_1 With $n = 0$,
 Diameter = 3.00 in., and $f = 4500$ Hz**

Inner Fluid Density Variation

In this section, we shall explore the effects of a change in inner fluid density on the attenuation of the inner fluid pressure field. The plane wave velocity or dilatational velocity of the inner fluid will remain fixed at 1500 m/sec. Simulations performed with an inner fluid density of 500, 1000, and 2000 kg/m³ are displayed in figures 83, 84 and 85.

In figure 86, comparisons are made at $k = 0$ rad/m. The decrease in inner fluid density has lowered the first radial resonance of the cylinder/fluid combination. Figures 87 through 89 are comparisons of the effect of the change in density across wavenumber at three different frequencies. In figure 87, we see that a decrease of inner fluid density has increased the phase velocity of the breathing wave. Breathing wave phase velocity from figure 87 at 300 Hz is provided in table 6.

Table 6. Effect of Inner Fluid Density on Breathing Wave Phase Velocity From Figure 87

Inner Fluid Density (kg/m ³)	Breathing Wave Phase Velocity (m/sec)
500	130
1000	91
2000	66

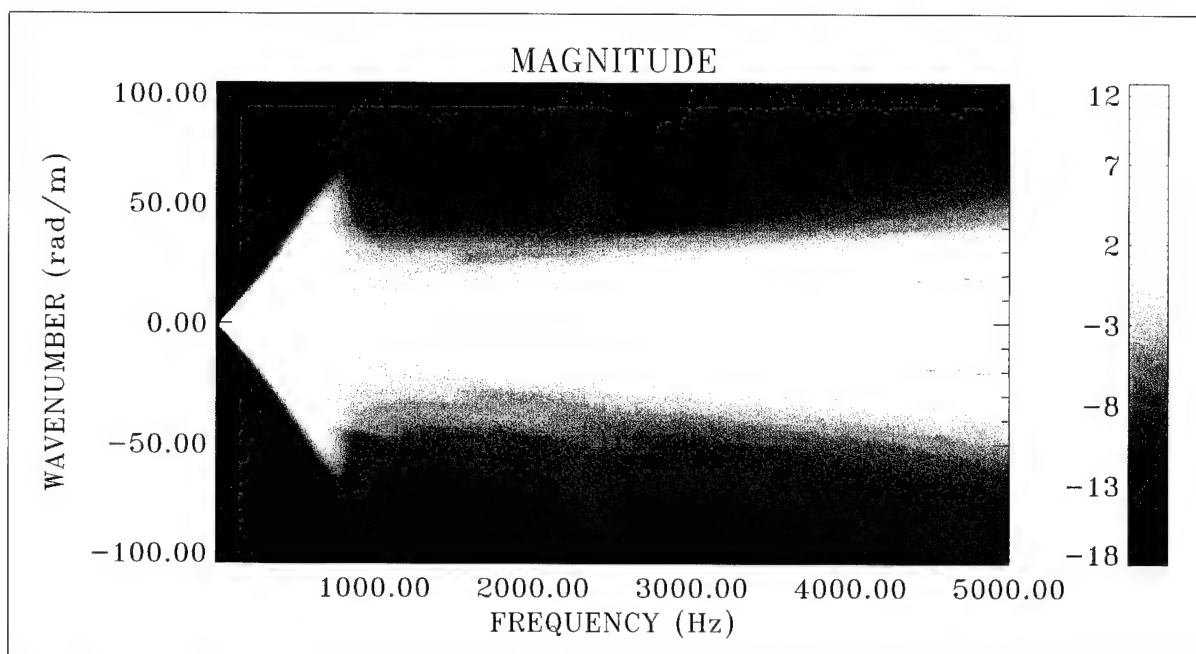


Figure 83. Pressure Transfer Surface With Magnitude = $10\text{Log}(P_i(r_1)/P_o)^2$ at $r_1 = 0.01$ in. for $\rho_i = 500 \text{ kg/m}^3$, $n = 0$, and Diameter = 3.00 in. (Color Image)

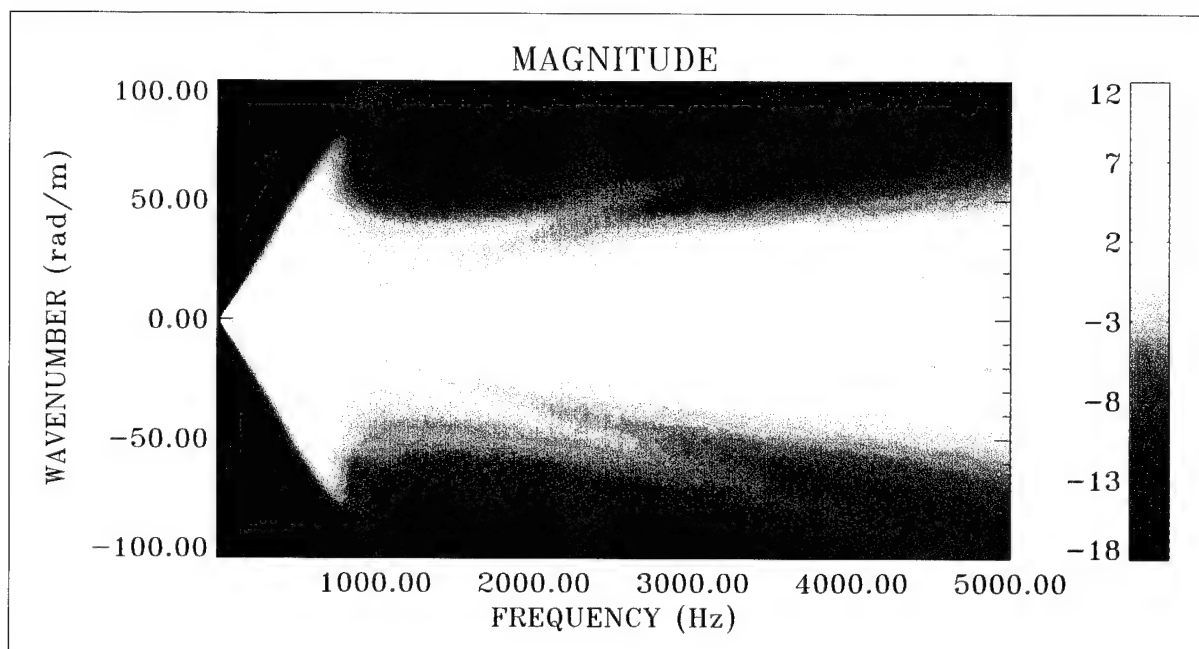


Figure 84. Pressure Transfer Surface With Magnitude = $10\text{Log}(P_i(r_1)/P_o)^2$ at $r_1 = 0.01$ in. for $\rho_i = 1000 \text{ kg/m}^3$, $n = 0$, and Diameter = 3.00 in. (Color Image)

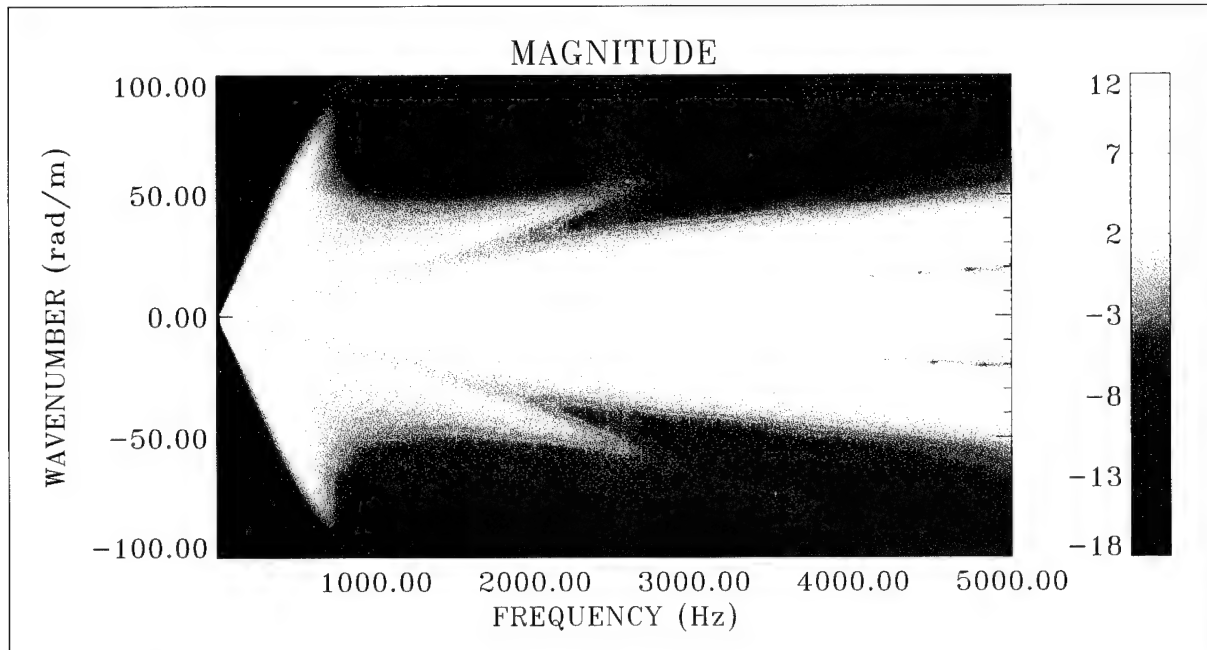


Figure 85. Pressure Transfer Surface With Magnitude = $10\text{Log}(P_i(r_1)/P_o)^2$ at $r_1 = 0.01$ in. for $\rho_i = 2000 \text{ kg/m}^3$, $n = 0$, and Diameter = 3.00 in. (Color Image)

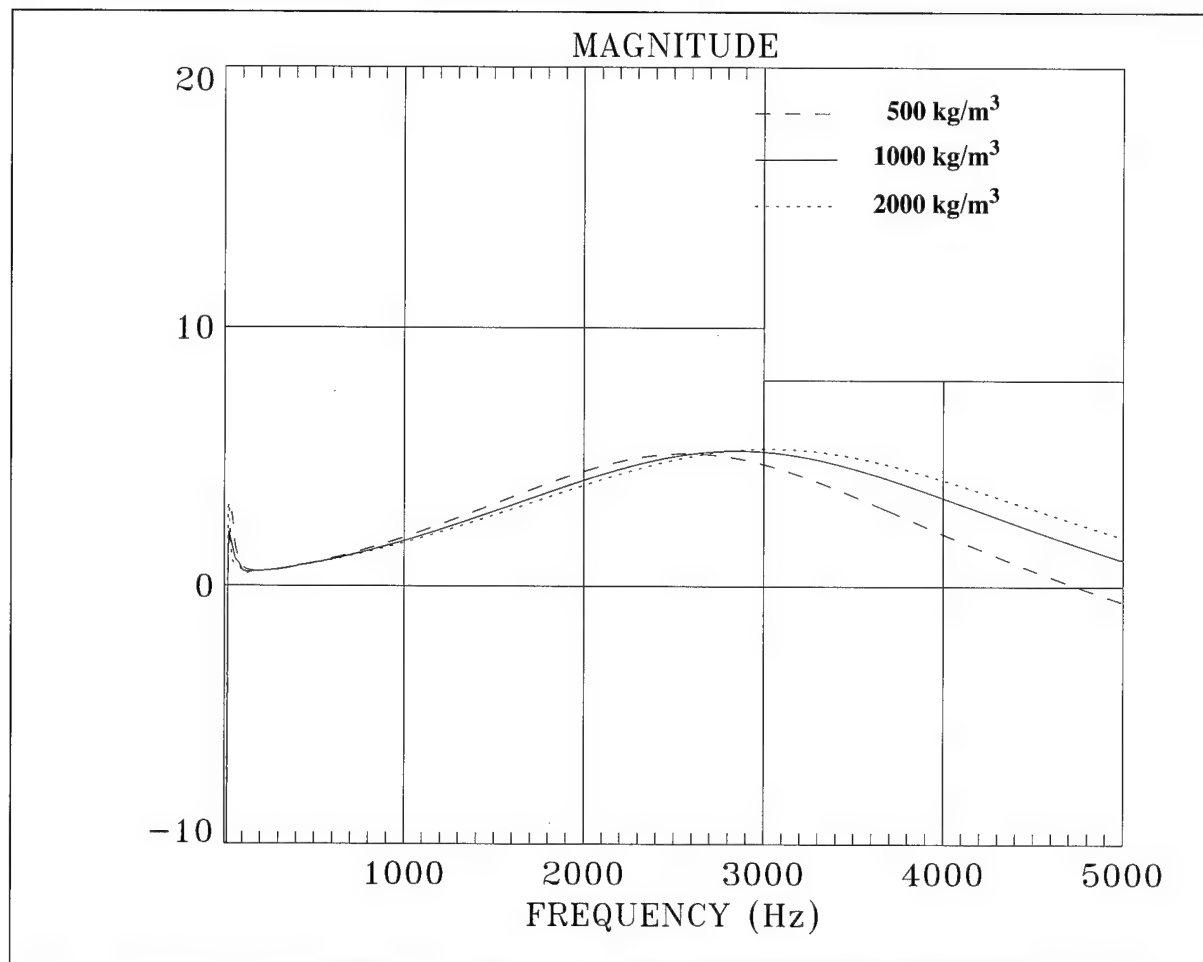


Figure 86. Effect of Inner Fluid Density When Magnitude = $10\text{Log}(P_i(r_1)/P_o)^2$ at $r_1 = 0.01$ in. for $n = 0$, Diameter = 3.00 in., and $k = 0$ rad/m

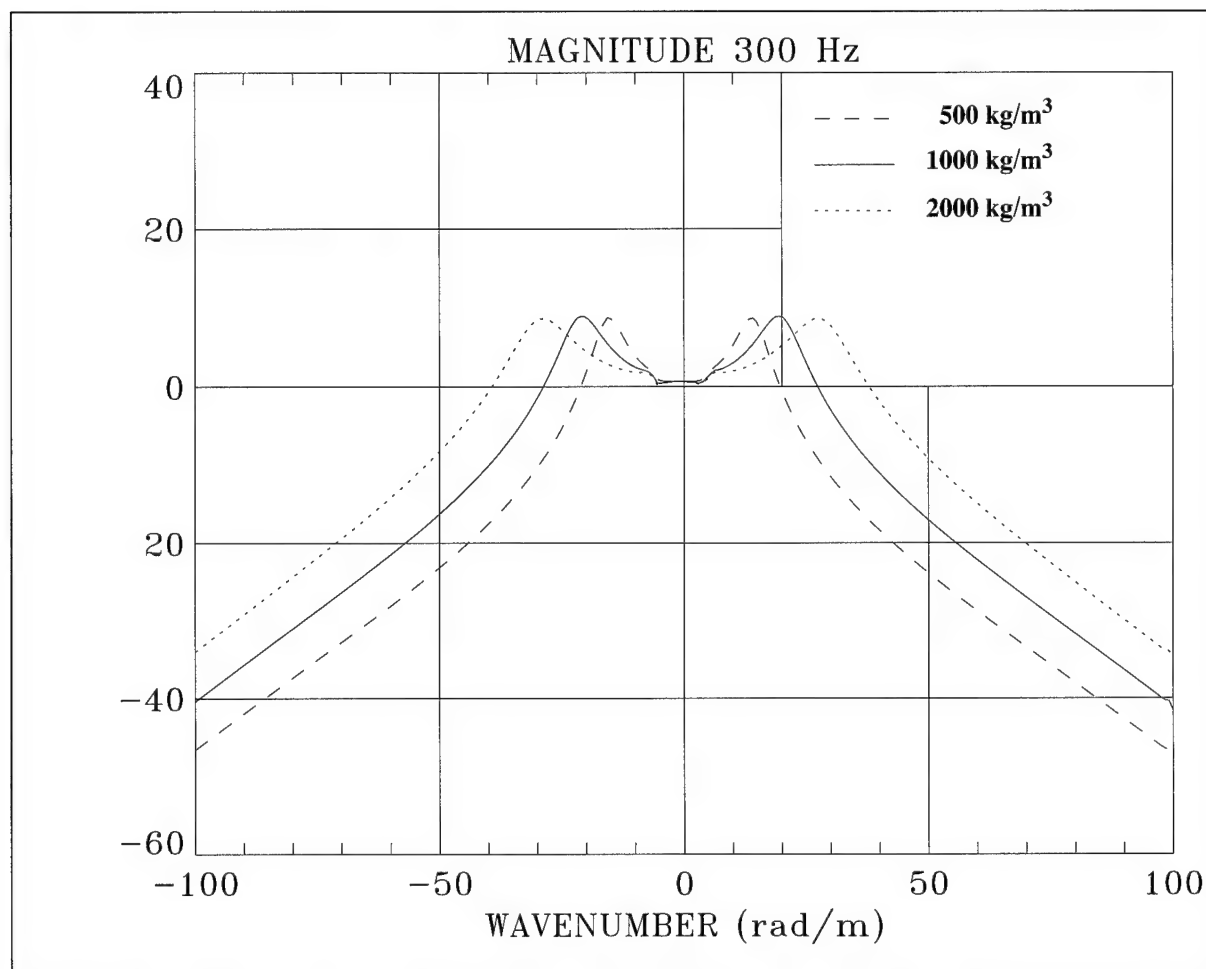


Figure 87. Effect of Inner Fluid Density When Magnitude = $10\text{Log}(P_i(r_1)/P_o)^2$ at $r_1 = 0.01$ in. for $n = 0$, Diameter = 3.00 in., and $f = 300$ Hz

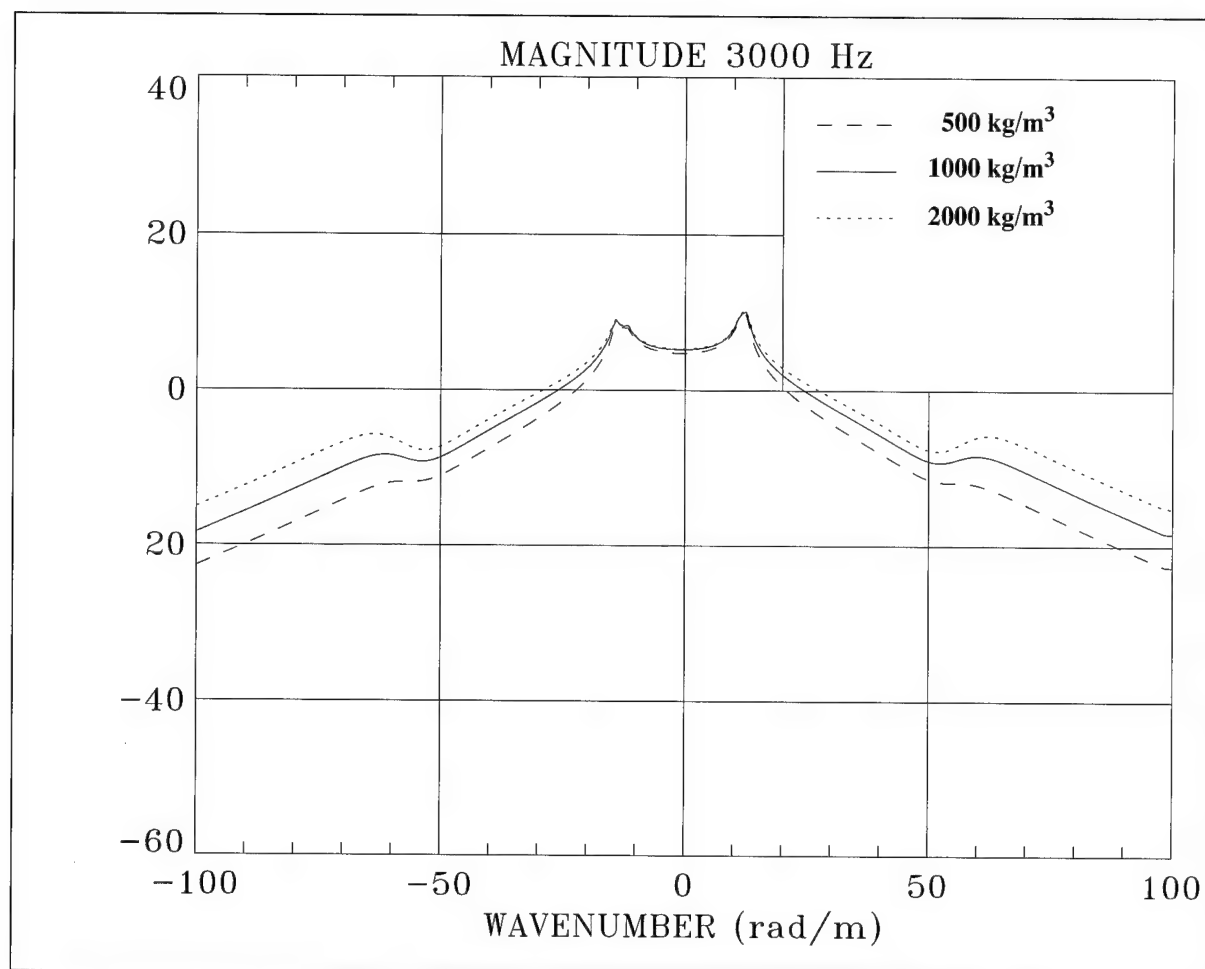


Figure 88. Effect of Inner Fluid Density When Magnitude = $10\text{Log}(P_i(r_1)/P_o)^2$ at $r_1 = 0.01$ in. for $n = 0$, Diameter = 3.00 in., and $f = 3000$ Hz

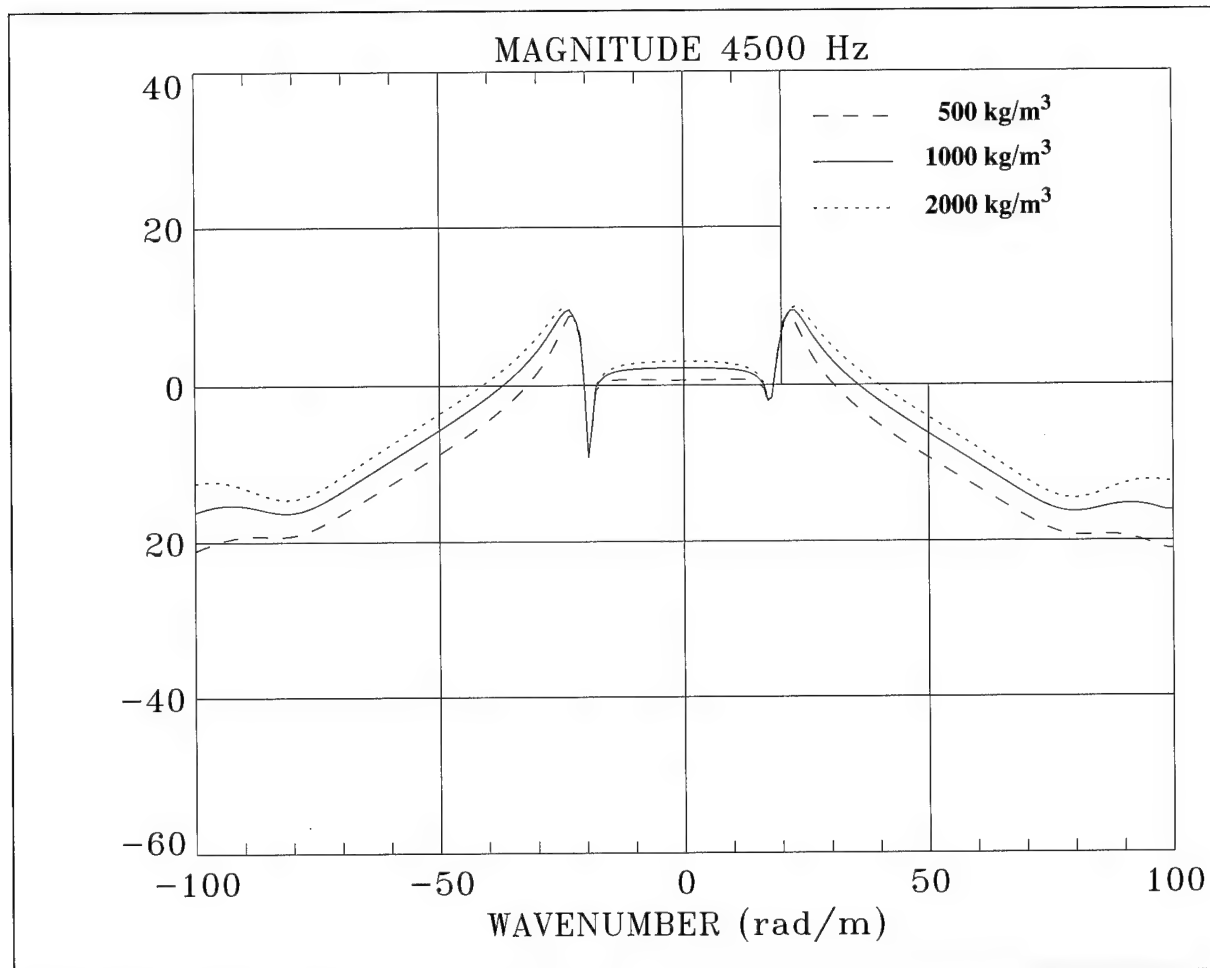


Figure 89. Effect of Inner Fluid Density When Magnitude = $10\text{Log}(P_i(r_1)/P_o)^2$ at $r_1 = 0.01$ in. for $n = 0$, Diameter = 3.00 in., and $f = 4500$ Hz

High-Frequency Response

Elasticity and Bending Shell Model Comparison. In previous sections, we have compared the shell models with the elasticity model up to 5000 Hz, accompanied by a limited comparison up to 15 kHz at $k = 0$. In this section, we will compare the bending shell model (figures 90 and 91) with the elasticity model (figures 92 and 93) over the range ± 200 rad/m and 10 to 60,000 Hz. These simulations have been performed with the data listed in tables 2, 4, and 5.

The first radial resonance can be clearly observed in the $k = 0$ cut displayed in figure 94. As was observed previously in figure 22, the bending shell model considerably overpredicts the first radial resonance of the cylinder because of the fluid loading. Both models exhibit deep nulls at 20,704 and 47,214 Hz, which are due to the J_0 nature of the inner fluid field, the propagation velocity of the inner fluid, and the dimensions of the cylinder. This behavior will be examined in the next section.

The remaining resonances seen in figure 94 (elasticity model) occur as a dilatational wave propagates through the thickness of the cylinder wall. These resonances correspond to the $1/2$, 1 , and $3/2$ wavelengths existing across the cylinder wall thickness. This will be explored in a later section for an air-loaded (rather than a water-loaded) cylinder with a variation of wall thickness and Young's modulus.

The assumptions made in shell theory result in an inadequate model for investigating the high-frequency response of the cylinder/fluid combination chosen here. For the heavy fluid loading present in this combination, it is necessary to use the elasticity formulation to properly model the dynamics of the system, even at 3000 Hz, which is only moderately high frequency.

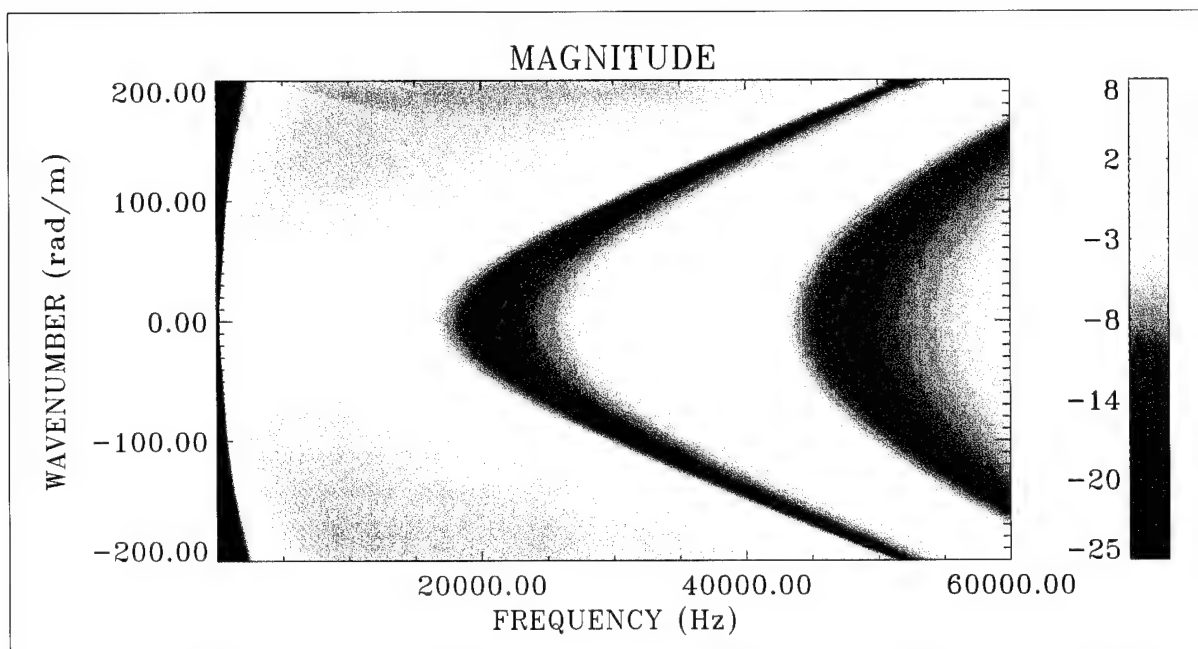


Figure 90. Pressure Transfer Surface Up to 60 kHz When Magnitude = $10\text{Log}(P_i(r_1)/P_o)^2$ at $r_1 = 1.1$ in. for Bending Shell Model, Where $n = 0$ and Diameter = 3.00 in. (Color Image)

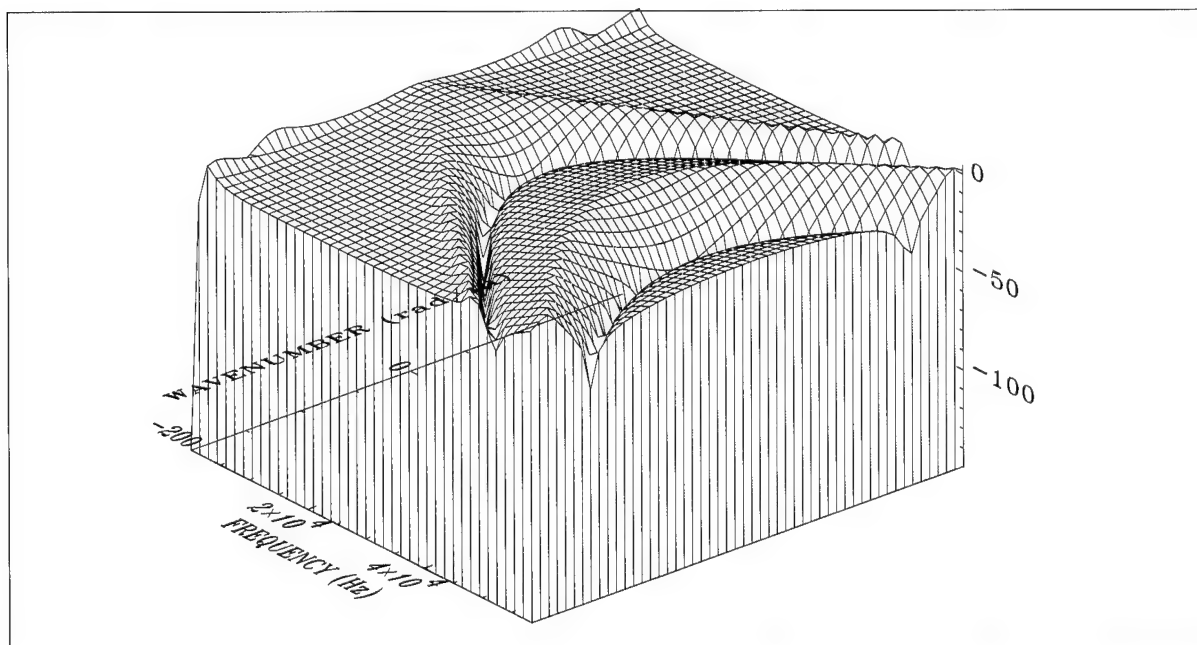


Figure 91. Pressure Transfer Surface Up to 60 kHz When Magnitude = $10\text{Log}(P_i(r_1)/P_o)^2$ at $r_1 = 1.1$ in. for Bending Shell Model, Where $n = 0$ and Diameter = 3.00 in. (Wire Frame Surface)

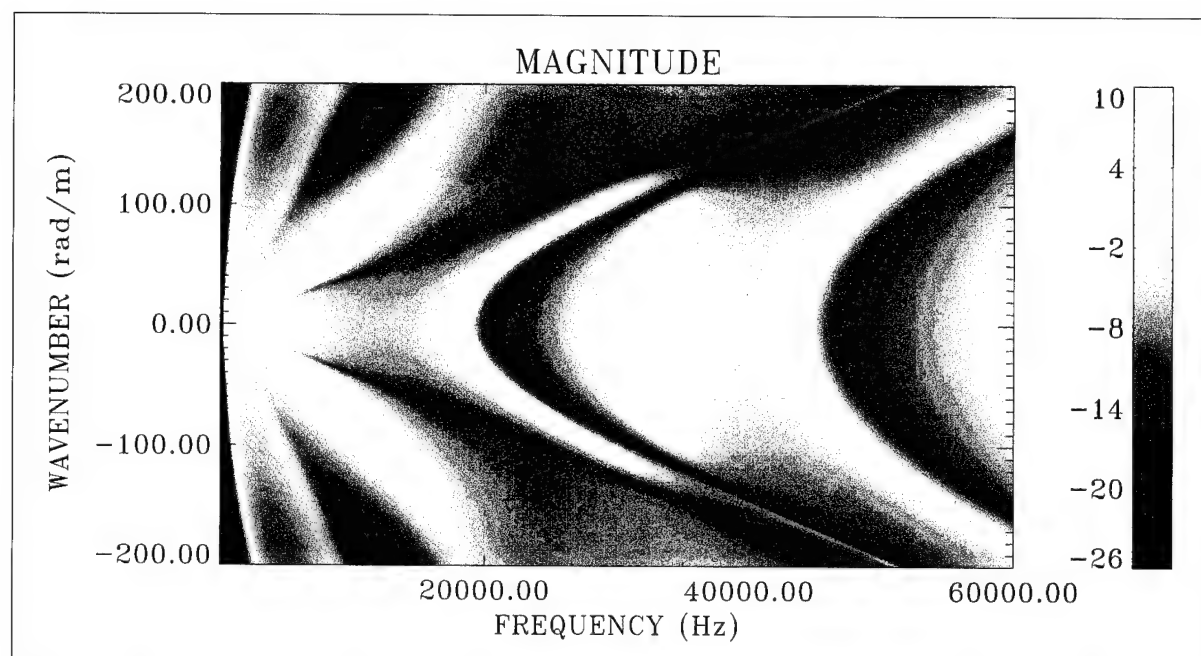


Figure 92. Pressure Transfer Surface Up to 60 kHz When Magnitude = $10\log(P_i(r_1)/P_o)^2$ at $r_1 = 1.1$ in. for Elasticity Model, Where $n = 0$ and Diameter = 3.00 in. (Color Image)

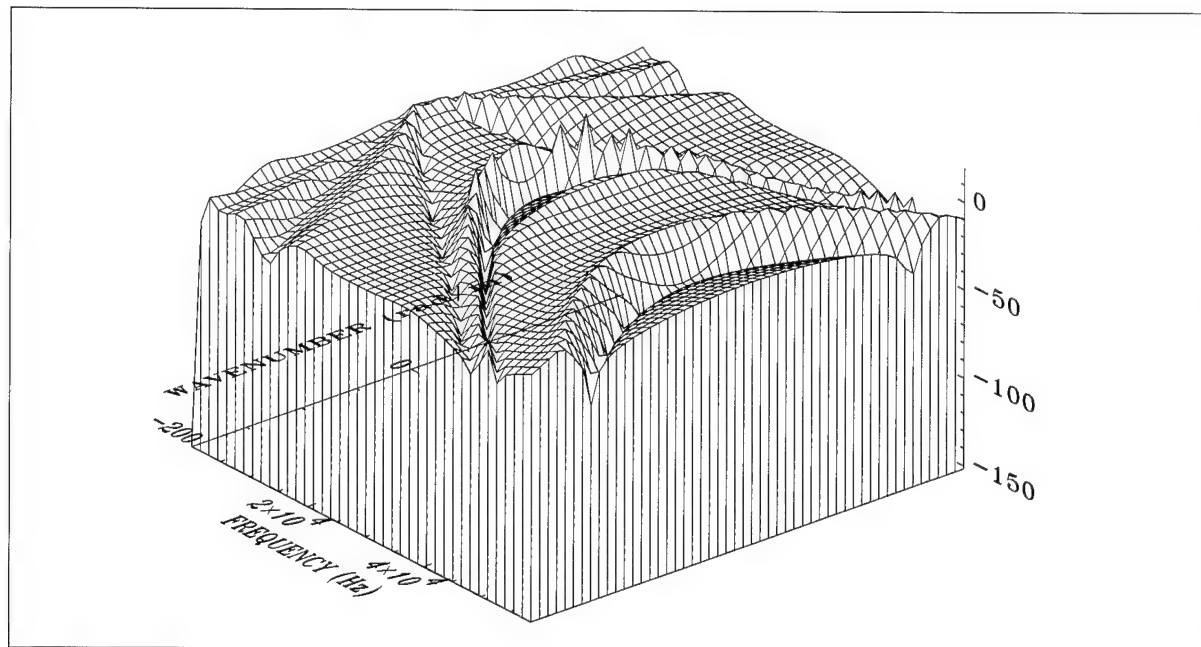


Figure 93. Pressure Transfer Surface Up to 60 kHz When Magnitude = $10\log(P_i(r_1)/P_o)^2$ at $r_1 = 1.1$ in. for Elasticity Model, Where $n = 0$ and Diameter = 3.00 in. (Wire Frame Surface)

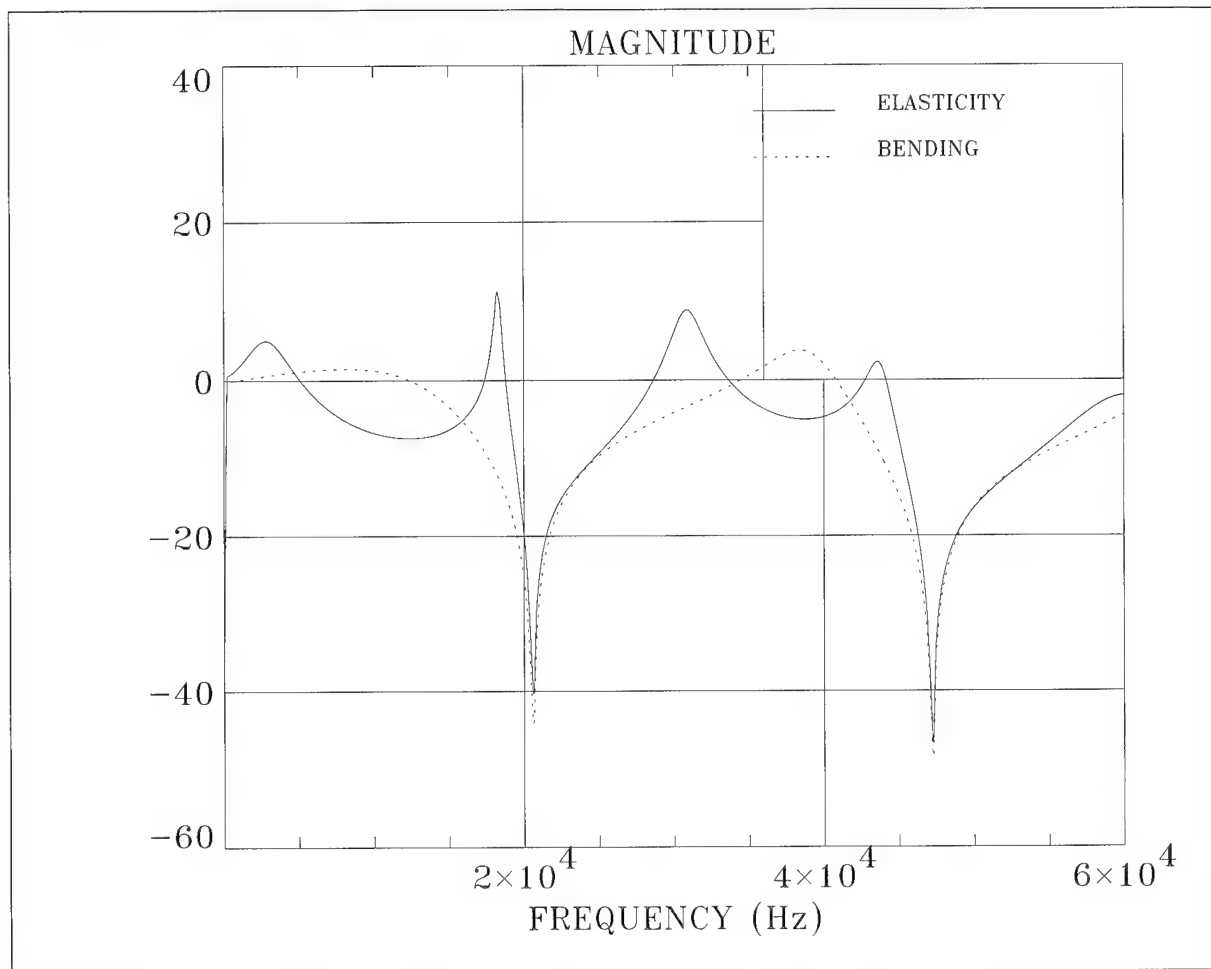


Figure 94. Model Comparison Up to 60 kHz for Figures 90 and 92
When Magnitude = $10\text{Log}(P_i(r_1)/P_o)^2$ at $r_1 = 1.1$ in. With $n = 0$,
Diameter = 3.00 in., and $k = 0$ rad/m

Inner Fluid Pressure Field Nulls. In this section, we shall consider the cause of the nulls evident in figure 94. For $n = 0$ and

$$\frac{\omega^2}{c_i^2} > k^2,$$

(the case of propagating wavenumbers), the inner fluid field is defined in terms of the J_0 Bessel function as given by equation (66). The nulls in frequency observed in figure 94 correspond to the roots of $J_0(\lambda_n)$. The argument of J_0 ,

$$r_1 \sqrt{\frac{\omega^2}{c_i^2} - k^2}, \quad (324)$$

is rearranged in order to solve for the frequency f_n corresponding to the roots λ_n of J_0 at $k = 0$ and r_1 as follows:

$$f_n = \frac{c_i}{2\pi} \sqrt{\frac{\lambda_n^2}{r_1^2} + k^2}. \quad (325)$$

Table 7 lists the frequencies f_n (calculated with equation (325)) that correspond to the first two roots of J_0 for three different values of radial position r_1 . A simulation of the inner fluid pressure

Table 7. Null Frequencies Corresponding to the First Two Roots of J_0

Root (n)	λ_n	f_n at $r_1 = 1.1$ in. (Hz)	f_n at $r_1 = 0.55$ in. (Hz)	f_n at $r_1 = 0.01$ in. (Hz)
1	2.4048	20,545 (20,704)	41,092 (41,056)	2,259,000
2	5.5201	47,161 (47,214)	94,326	5,187,000

field is shown in figures 95 and 96 evaluated at $r_1 = 0.55$ inch. In a similar manner, the pressure field in the inner fluid at $r_1 = 0.01$ inch is computed and displayed in figures 97 and 98. Comparison of the three radial positions from figures 92, 95, and 97 is made in figure 99 at $k = 0$. In figure 99, the very dramatic effect of radial location r_1 on the pressure field in the inner fluid can be observed. The nulls listed in table 7 for $r_1 = 0.01$ inch occur at frequencies that extend beyond the 60-kHz range of the figure and are therefore unobservable. The three nulls observable in figure 99 are listed in table 7 in parentheses beneath the value calculated from equation (325). The agreement is within 1 percent.

The null frequencies f_n (equation (325)) will decrease if the inner fluid propagation velocity is decreased. Such will be the case in the next section, where air is substituted for water to decrease the effect of the fluid on the structure in order to explore the second, third, and fourth resonances in figure 94.

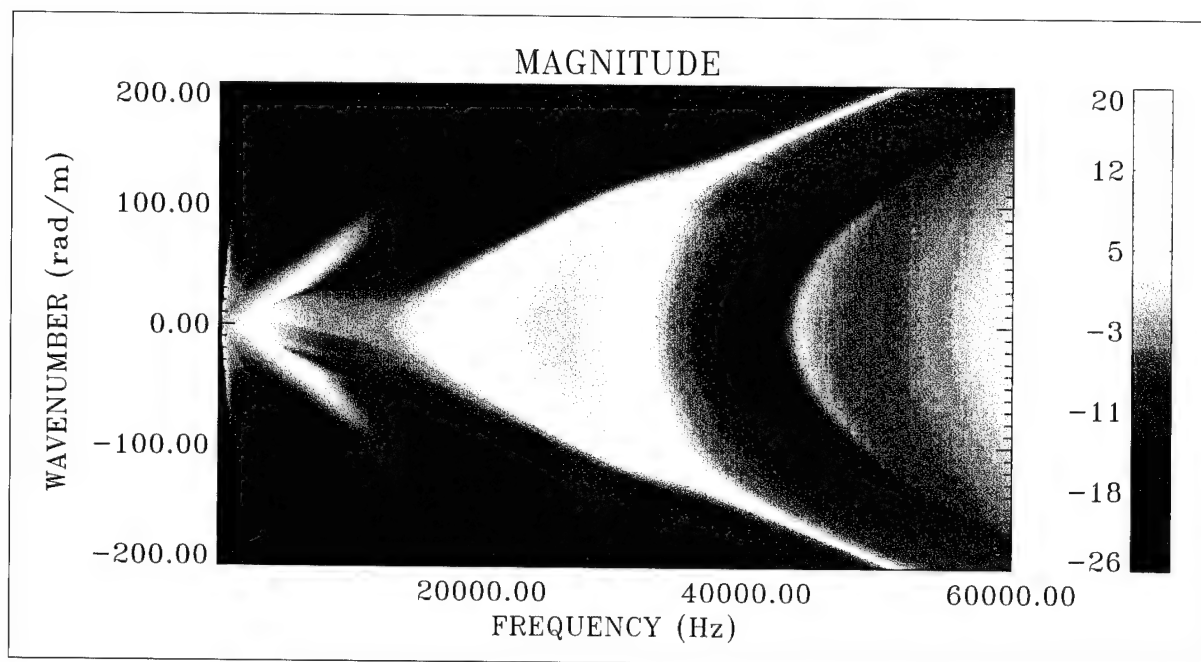


Figure 95. Pressure Transfer Surface Up to 60 kHz When Magnitude = $10\text{Log}(P_i(r_1)/P_o)^2$ at $r_1 = 0.55$ in. With $n = 0$ and Diameter = 3.00 in. (Color Image)

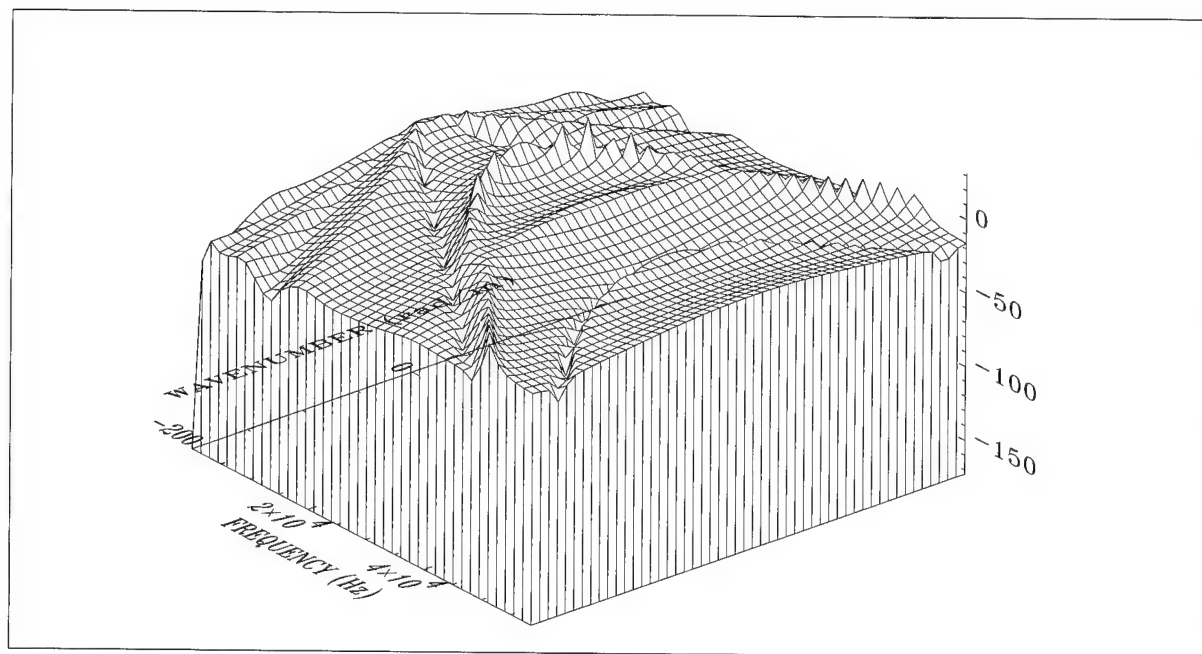


Figure 96. Pressure Transfer Surface Up to 60 kHz When Magnitude = $10\text{Log}(P_i(r_1)/P_o)^2$ at $r_1 = 0.55$ in. With $n = 0$ and Diameter = 3.00 in. (Wire Frame Surface)

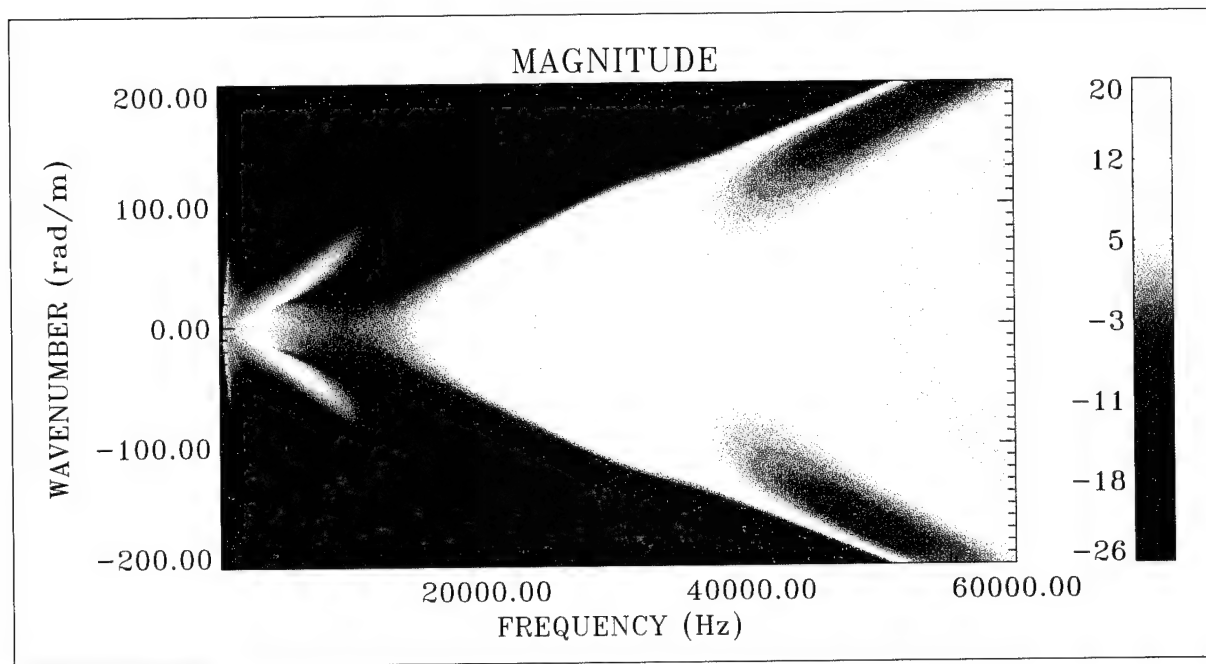


Figure 97. Pressure Transfer Surface Up to 60 kHz When Magnitude = $10\text{Log}(P_i(r_1)/P_o)^2$ at $r_1 = 0.01$ in. With $n = 0$ and Diameter = 3.00 in. (Color Image)

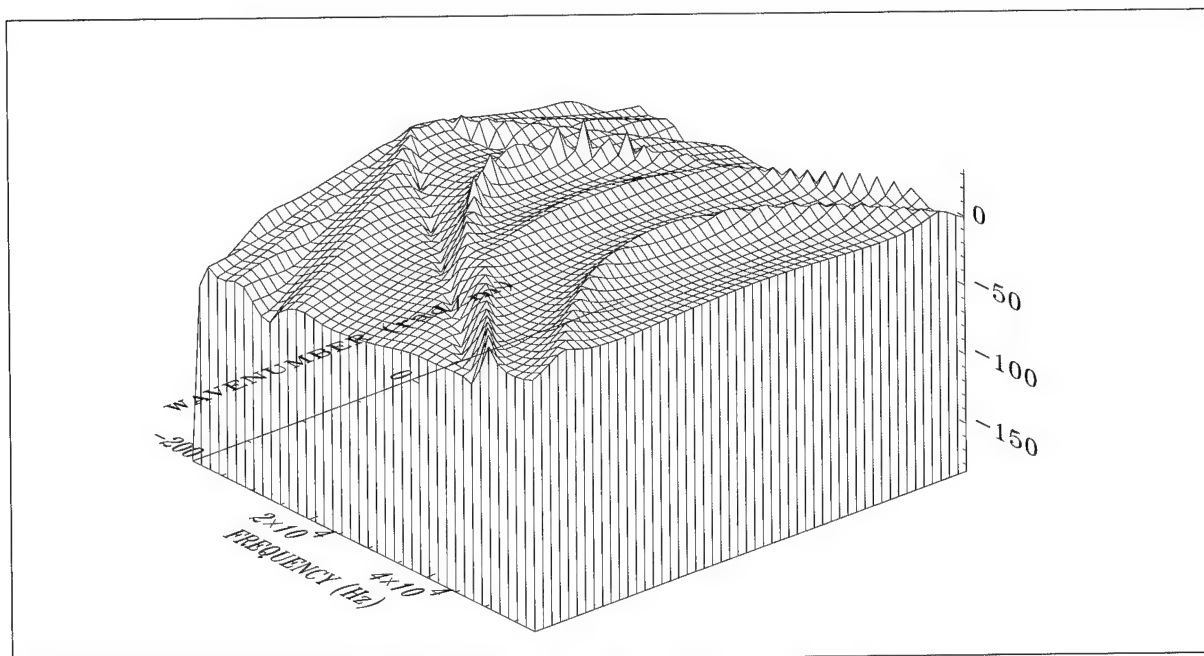
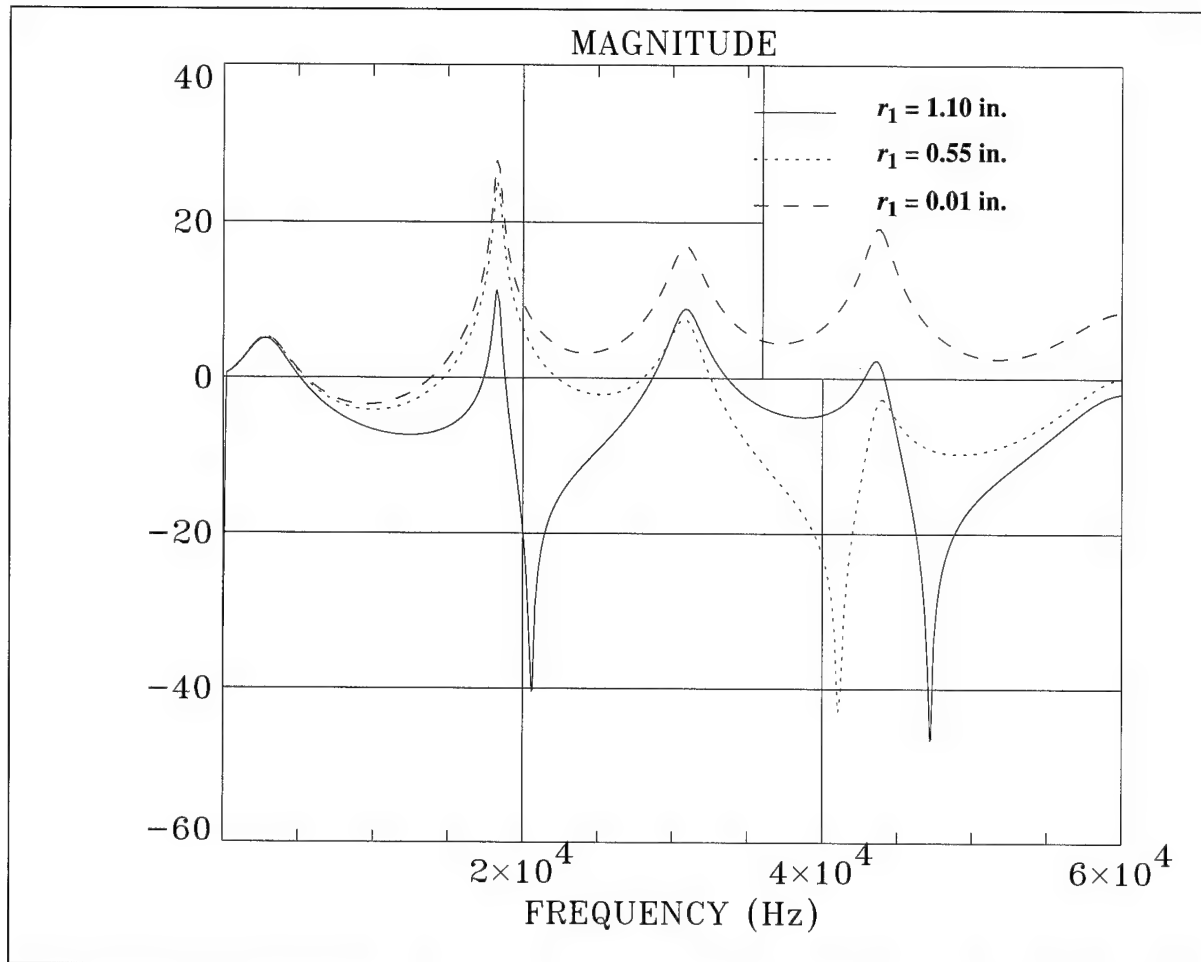


Figure 98. Pressure Transfer Surface Up to 60 kHz When Magnitude = $10\text{Log}(P_i(r_1)/P_o)^2$ at $r_1 = 0.01$ in. With $n = 0$ and Diameter = 3.00 in. (Wire Frame Surface)



**Figure 99. Comparison of Inner Fluid Pressure Field for Figures 92, 95, and 97
When Magnitude = $10\text{Log}(P_i(r_1)/P_o)^2$ at Various r_1 With $n = 0$,
Diameter = 3.00 in., and $k = 0$ rad/m**

Cylinder With Inner and Outer Fluids of Air—Wall Thickness Variation. In this section, we will examine the three resonances above the first radial resonance of the cylinder, as seen in figure 99. The wall thickness will be varied and the effect of this variation on the resonances will be examined. The simulations in this section and the one immediately following will be performed with a change in the inner and outer fluid properties from water to air, as shown in tables 8 and 9. As noted earlier, air was chosen in order to reduce the fluid's effect on the cylinder. Although sharp nulls and peaks occur at lower frequency due to the decrease in c_i (discussed in the last section), this behavior is not strong enough to affect the location of the resonances under consideration.

Table 8. Outer Fluid Properties for Wall Thickness Variation (Air)

Property	Definition
$\rho_s = 1.2 \frac{\text{kg}}{\text{m}^3}$	Density
$c_s = 343.0 \frac{\text{m}}{\text{sec}}$	Velocity of Sound

Table 9. Inner Fluid Properties for Wall Thickness Variation (Air)

Property	Definition
$\rho_i = 1.2 \frac{\text{kg}}{\text{m}^3}$	Density
$c_i = 343.0 \frac{\text{m}}{\text{sec}}$	Velocity of Sound

Simulations for the radial stress τ_{rr} are shown in figures 100 and 101 for cylinders of two different wall thicknesses. A comparison of these two figures is shown in figure 102 at $k = 0$. The wall thickness was increased from 0.3 to 0.6 inch in figure 101 so that additional

resonances would be present in the 60-kHz frequency range. From table 1, we see that the dilatational phase velocity for the cylinder material is $c_l = 447.51$ m/s. For each resonance frequency observed in figures 100 and 101, the corresponding wavelength L is calculated using

$$L = \frac{c_l}{f_{ti}},$$

and is provided in tables 10 and 11. The resonances correspond to dilatational wave propagation through the thickness of the cylinder, with standing waves existing in the thickness direction. Mode shapes of $L/2$, L , and $3L/2$ correspond to the three resonances of figure 101, while only the $L/2$ mode shape corresponds to the resonance in figure 100. Doubling the thickness of the cylinder doubles the wavelength of the first mode and halves the frequency, which is observed with the first resonance, as shown in tables 10 and 11.

Table 10. Thickness Resonance Table for $h_1 = 0.3$ in. From Figure 100

Thickness Resonance Frequency Number (i)	ft_i (Hz)	L (m)	h_1/L	h_1/L Nominal
1	30,264	0.01478	0.52	$\frac{1}{2}$

Table 11. Thickness Resonance Table for $h_1 = 0.6$ in. From Figure 101

Thickness Resonance Frequency Number (i)	ft_i (Hz)	L (m)	h_1/L	h_1/L Nominal
1	15,198	0.02940	0.52	$\frac{1}{2}$
2	30,532	0.01465	1.04	1
3	45,221	0.00989	1.54	$\frac{3}{2}$

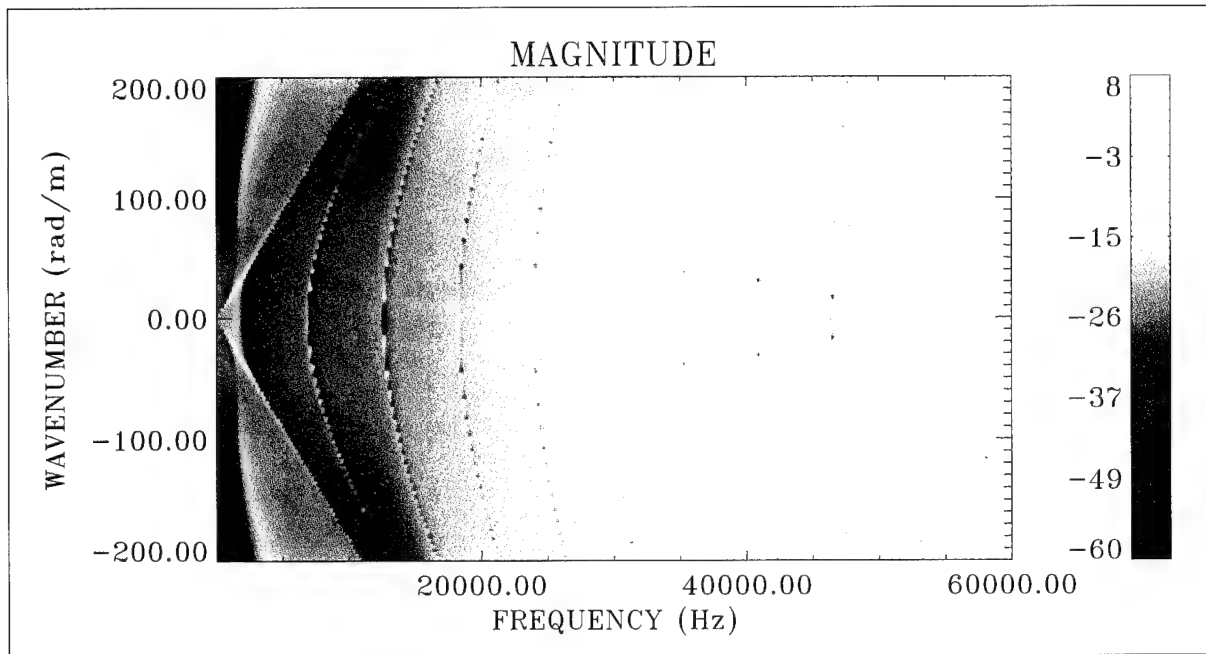


Figure 100. Radial Stress Transfer Surface Up to 60 kHz When
Magnitude = $10\text{Log}(\tau_{rr}^{C1}(r_1)/P_o)^2$ at $r_1 = 1.21$ in. With $h_1 = 0.3$ in., $n = 0$,
and Diameter = 3.00 in. (Color Image)

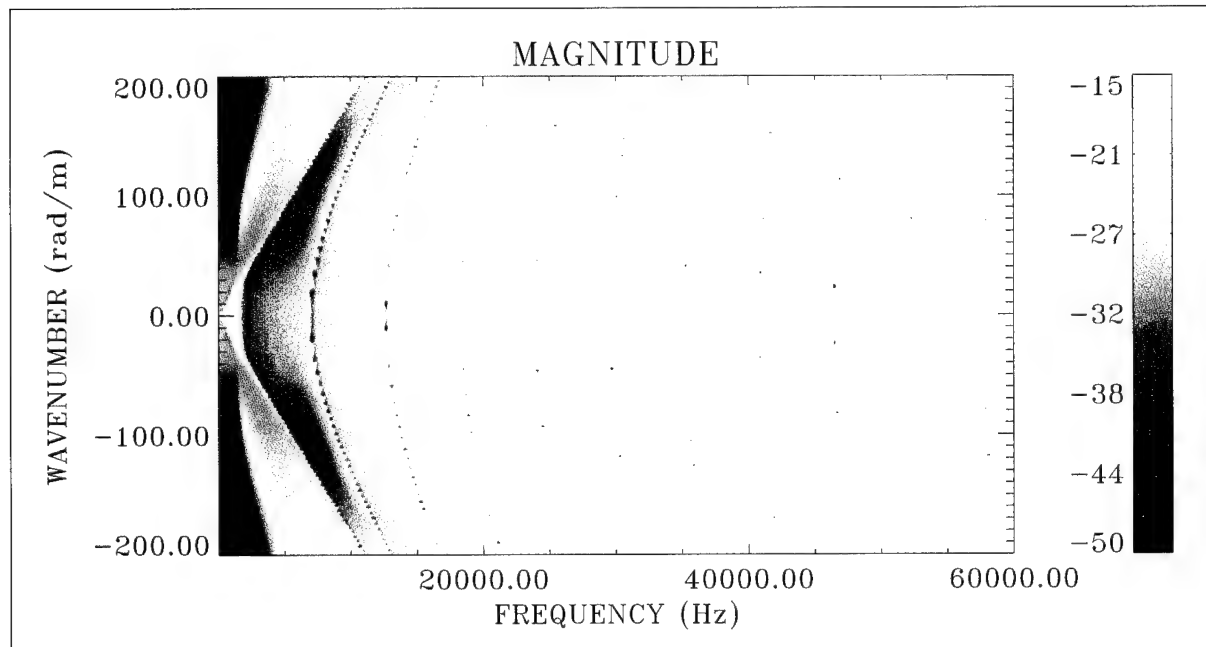


Figure 101. Radial Stress Transfer Surface Up to 60 kHz When
Magnitude = $10\text{Log}(\tau_{rr}^{C1}(r_1)/P_o)^2$ at $r_1 = 1.21$ in. With $h_1 = 0.6$ in., $n = 0$,
and Diameter = 3.00 in. (Color Image)

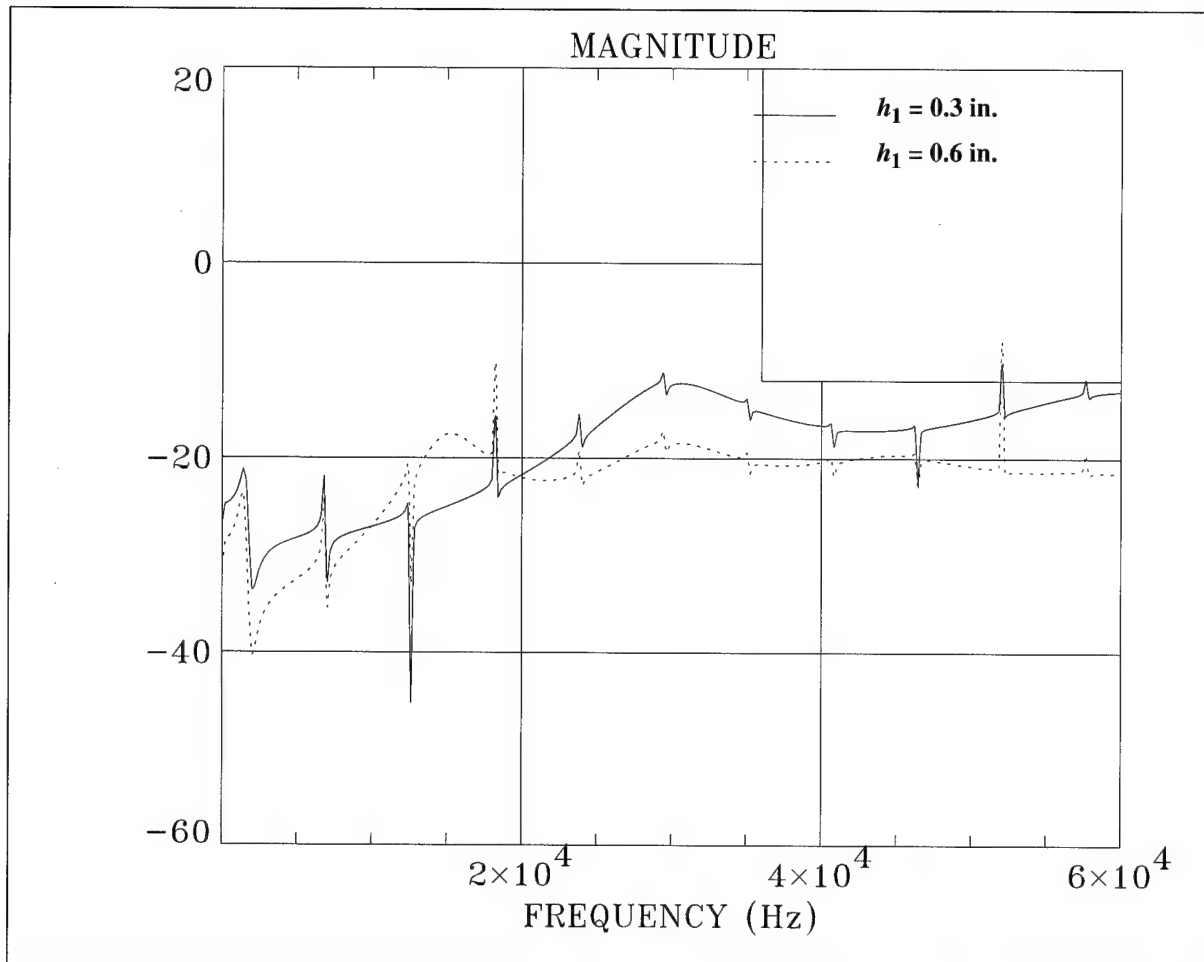


Figure 102. Effect of Variation of Wall Thickness on the Cylinder Response for Figures 100 and 101 When Magnitude = $10\text{Log}(\tau_{rr}^{C1}(r_1)/P_o)^2$ at $r_1 = 1.21$ in. With $n = 0$, Diameter = 3.00 in., and $k = 0$ rad/m

Cylinder With Inner and Outer Fluids of Air—Young's Modulus Variation. In this section, we compare the cylinder/fluid combination of the previous section to a cylinder with a factor-of-10 increase in Young's modulus. Figure 103 is a simulation for a cylinder with a Young's modulus of 1×10^9 Pa in contact with fluids of air, and figure 104 is the cylinder (with a Young's modulus of 1×10^8 Pa) that we have been studying previously.

The first thickness resonance, which was at 15,198 Hz (table 11), has increased to 48,330 Hz (figure 103). This increase in frequency corresponds to an increase in the dilatational velocity for the cylinder (table 12). The ratio of dilatational velocities for the two moduli is 3.16 ($\cong \sqrt{10}$). The corresponding ratio of the first thickness resonance frequencies is 3.18.

Table 12. Young's Modulus and Dilatational Phase Velocity

Young's Modulus (Pa)	Phase Velocity (c_l) (m/sec)
1×10^8	447.51
1×10^9	1,414.9

The first radial resonance has increased from 1,417 to 4,232 Hz, as seen in figure 105. The ratio of this frequency increase is 2.99, corresponding to a square root of modulus dependence. From shell theory, a simple approximation for the first radial resonance without fluid loading is

$$f_r = \frac{1}{2\pi\bar{a}} \sqrt{\frac{E_c}{\rho_c(1-\nu_c^2)}}, \quad (326)$$

where \bar{a} is equal to the mean radius of the cylinder. This equation portrays the basic relationship between the parameters for the first radial resonance. For the nonfluid-loaded case or the lightly fluid-loaded case under consideration here, equation (326) performs well in estimating the first radial resonance frequency. Table 13 lists the frequencies calculated from

equation (326) and the values taken from figure 105.

Table 13. Comparison of First Radial Resonance Frequency f_r

Young's Modulus (Pa)	First Radial Resonance (f_r) Equation (326) (Hz)	First Radial Resonance (f_r) Figure 105 (Hz)
1×10^8	1,393	1,417
1×10^9	4,405	4,232

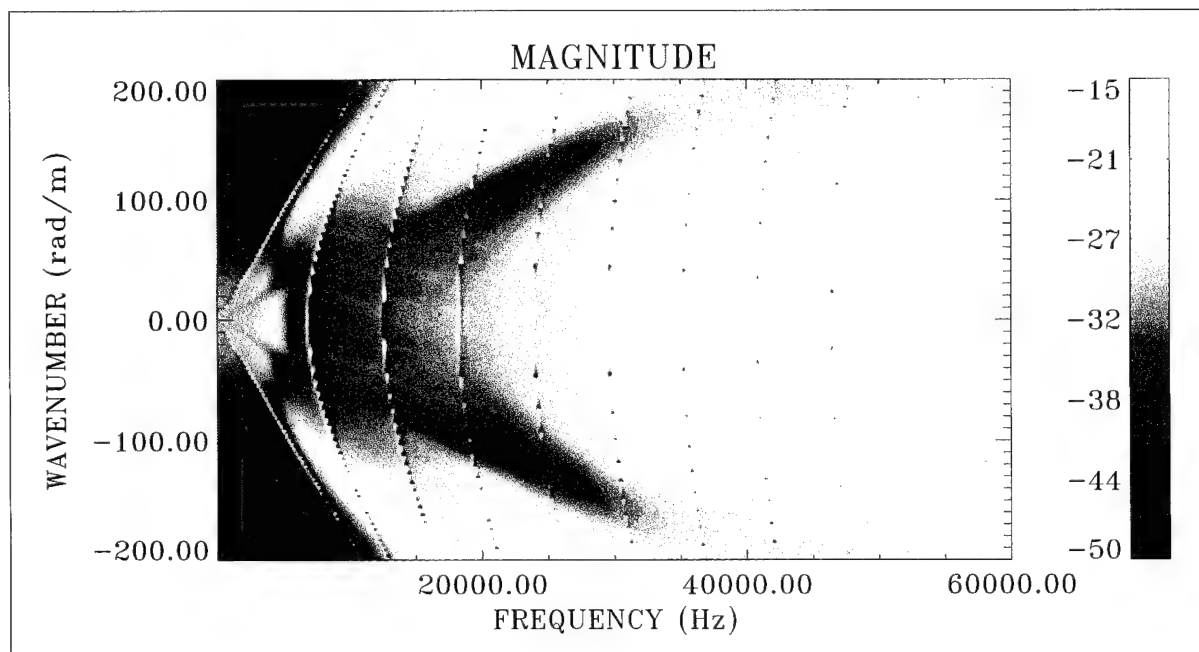


Figure 103. Radial Stress Transfer Surface Up to 60 kHz When
Magnitude = $10\text{Log}(\tau_{rr}^{C1}(r_1)/P_o)^2$ at $r_1 = 1.21$ in. With $E_1 = 1 \times 10^9$ Pa, $h_1 = 0.6$ in.,
 $n = 0$, and Diameter = 3.00 in. (Color Image)

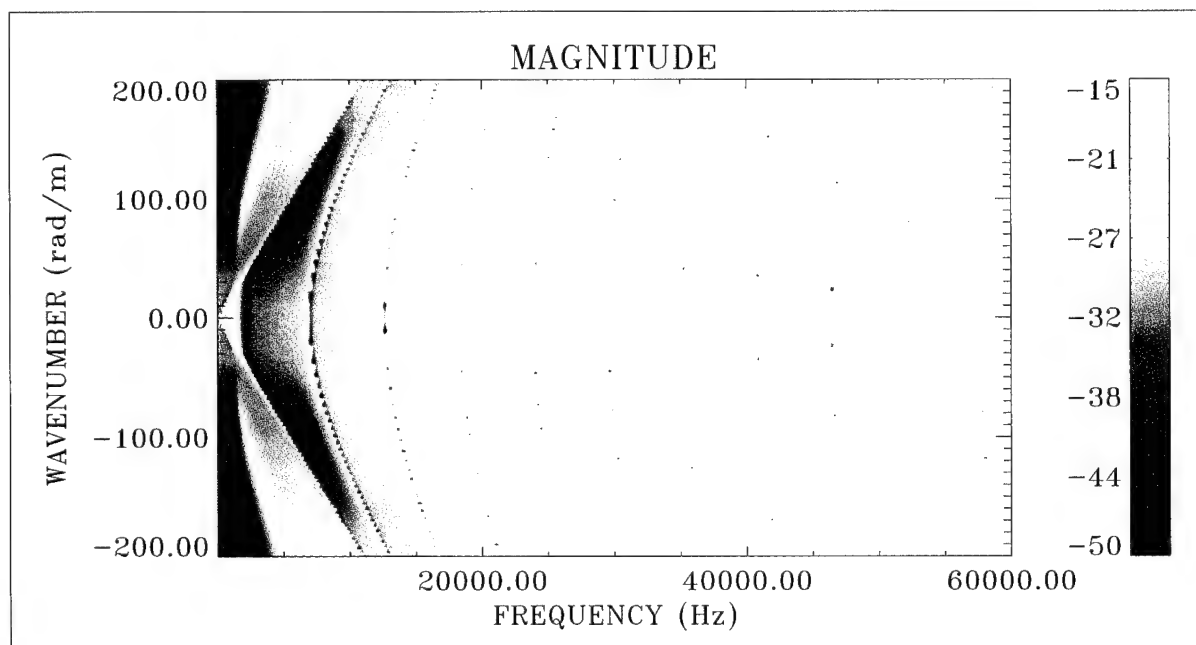


Figure 104. Radial Stress Transfer Surface Up to 60 kHz When
Magnitude = $10\text{Log}(\tau_{rr}^{C1}(r_1)/P_o)^2$ at $r_1 = 1.21$ in. With $E_1 = 1 \times 10^8$ Pa, $h_1 = 0.6$ in.,
 $n = 0$, and Diameter = 3.00 in. (Color Image)

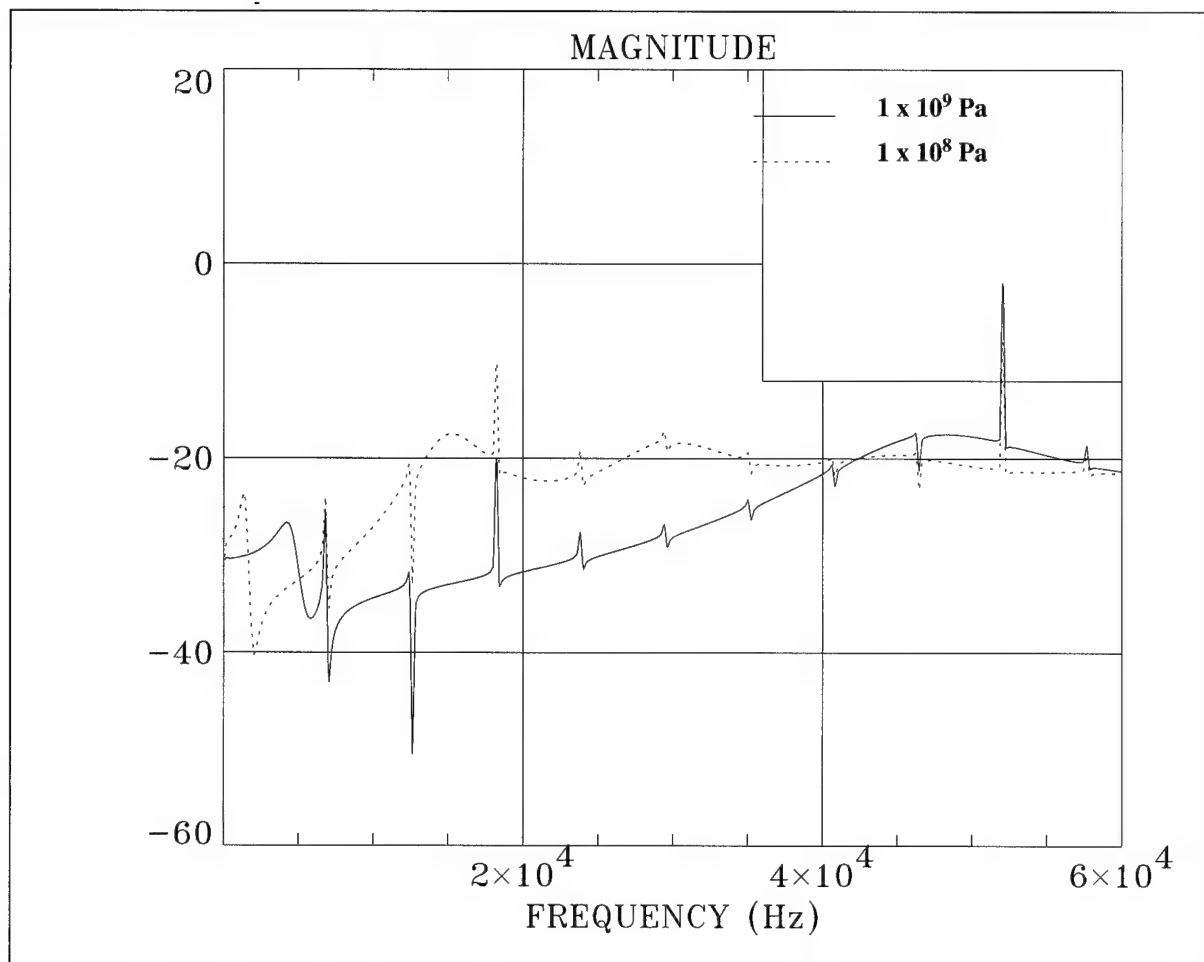


Figure 105. Effect of Variation of Young's Modulus on the Cylinder Response for Figures 103 and 104 When Magnitude = $10\text{Log}(\tau_{rr}^{C1}(r_1)/P_o)^2$ at $r_1 = 1.21$ in. With $n = 0$, Diameter = 3.00 in., and $k = 0$ rad/m

Cylinder With Inner and Outer Fluids of Water—Wall Thickness Variation. In figures 106 and 107, the pressure is calculated in the inner fluid at $r_1 = 0.01$ inch so that the simulations will be free of fluid nulls across the frequency range under consideration. The thickness resonances are clearly visible in both figures and correspond to cylinder wall thicknesses of 0.3 and 0.6 inch, respectively. Comparison of the responses is made at $k = 0$ rad/m in figure 108.

The thickness resonance frequencies are provided in table 14 for the simulations performed earlier with air (figures 100 and 101) and with water (figures 106 and 107). The first thickness resonance is severely affected by the presence of the fluid (water) in the simulation of figure 106. As the cylinder wall thickness is increased to 0.6 inch, the first and third thickness resonance frequencies are not as severely affected; however, the second thickness resonance frequency is reduced by 50 percent.

Table 14. Thickness Resonance Table for Air and Water With $h_1 = 0.3$ and 0.6 in.

Thickness Resonance Frequency Number (i)	ft_i Air $h_1 = 0.3$ in. (Hz)	ft_i Water $h_1 = 0.3$ in. (Hz)	ft_i Air $h_1 = 0.6$ in. (Hz)	ft_i Water $h_1 = 0.6$ in. (Hz)
1	30,264	18,241	15,198	13,490
2	—	30,850	30,532	20,235
3	—	43,812	45,221	41,818

Cylinder wall thickness variation also affects the first radial resonance, moving the frequency from 2816 Hz at $h_1 = 0.3$ inch to 1936 Hz at $h_1 = 0.6$ inch. The next section, which describes the last high-frequency results, will examine a branch of wave propagation occurring near this resonance.

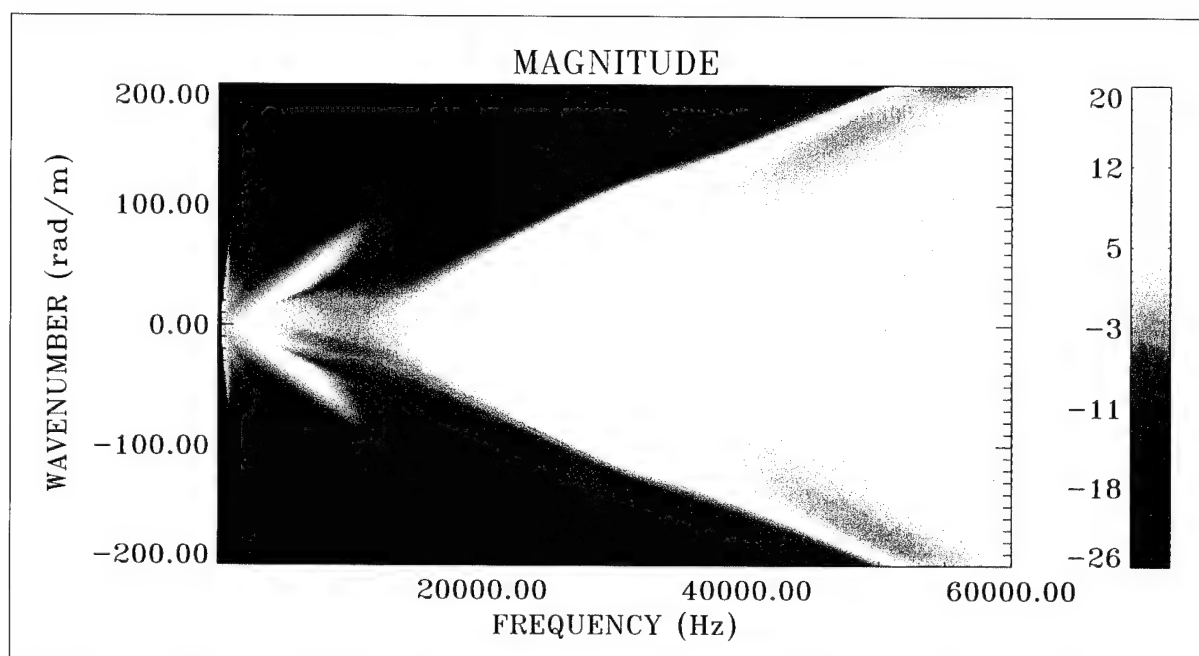


Figure 106. Pressure Transfer Surface Up to 60 kHz When Magnitude = $10\text{Log}(P_i(r_1)/P_o)^2$ at $r_1 = 0.01$ in. With $h_1 = 0.3$ in., $n = 0$, and Diameter = 3.00 in. (Color Image)

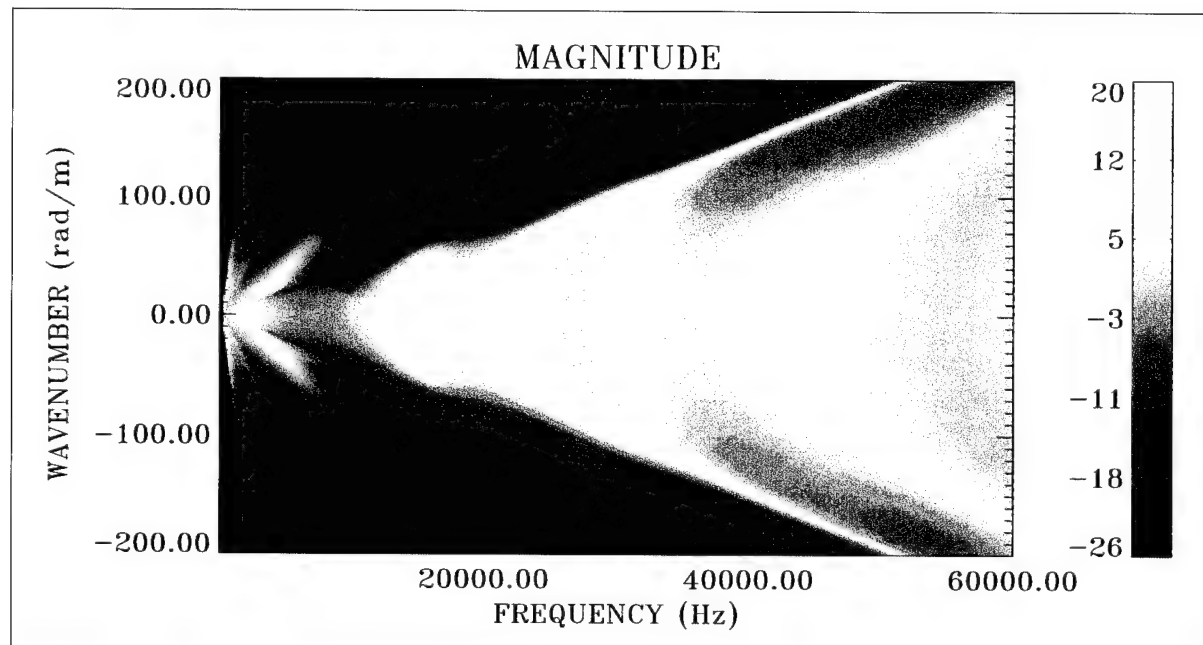


Figure 107. Pressure Transfer Surface Up to 60 kHz When Magnitude = $10\text{Log}(P_i(r_1)/P_o)^2$ at $r_1 = 0.01$ in. With $h_1 = 0.6$ in., $n = 0$, and Diameter = 3.00 in. (Color Image)

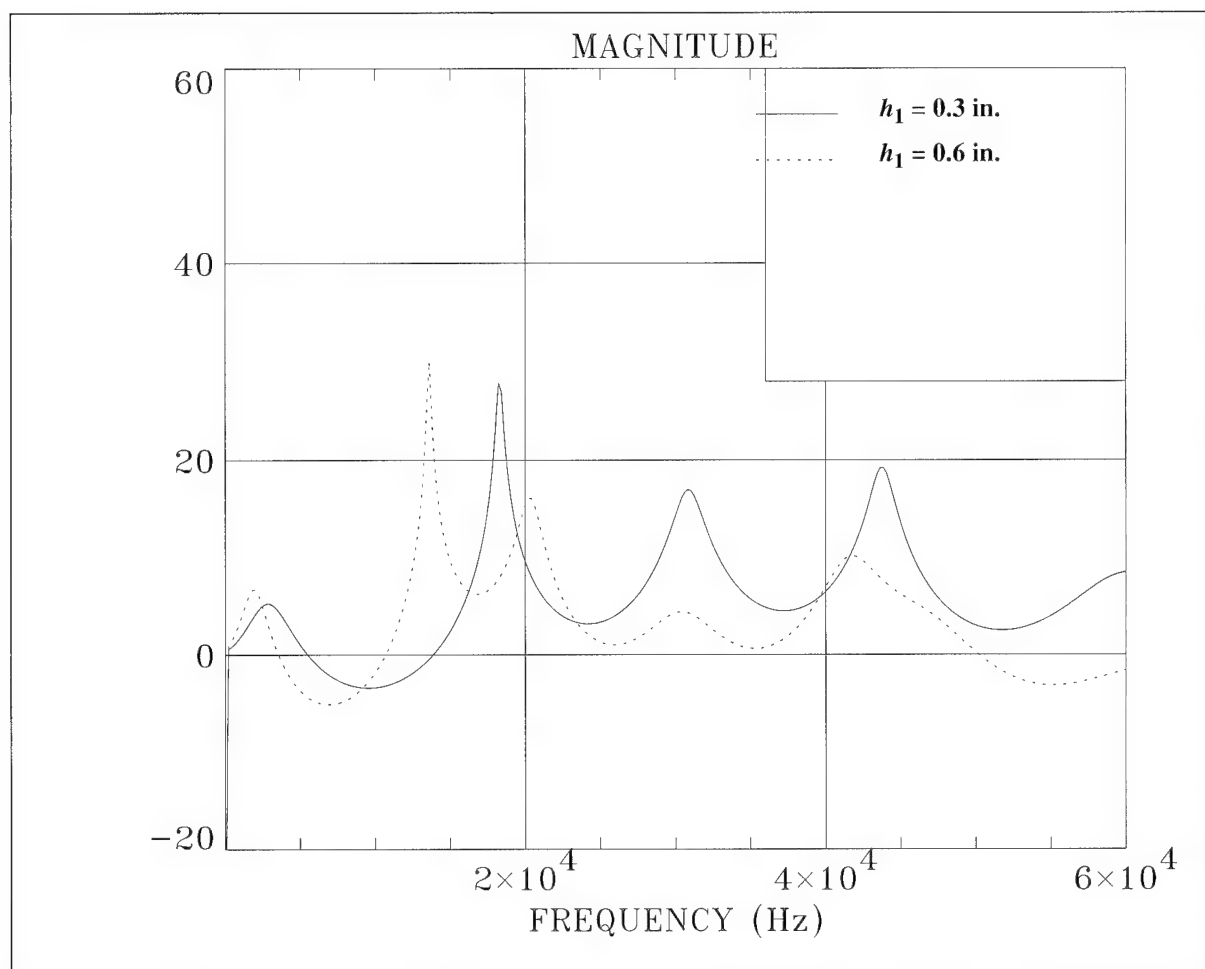


Figure 108. Effect of Variation of Wall Thickness on the Cylinder Response for Figures 106 and 107 When Magnitude = $10\text{Log}(P_i(r_1)/P_o)^2$ at $r_1 = 0.01$ in. With $n = 0$, Diameter = 3.00 in., and $k = 0$ rad/m

Cylinder With Inner and Outer Fluids of Water—Stress and Displacements. In this last and final section on high-frequency results, we shall examine the longitudinal and radial displacement fields that correspond to the radial stress field at $r_1 = 1.21$ inches. For these simulations, we return to the original data for the cylinders and fluid listed in tables 2, 4, and 5, where the fluids have the properties of water and the cylinder thickness is 0.3 inch. The radial stress is evaluated and displayed in figures 109 and 110, and the longitudinal displacement corresponding to this stress simulation is shown in figures 111 and 112. In a similar fashion, the radial displacement field is displayed in figures 113 and 114. Cuts through the displacement surfaces have been made in both wavenumber and frequency and are displayed in figures 115 through 118.

In figure 115, the longitudinal and radial displacements are compared at 2000 Hz. The predominant displacement for the breathing wave is radial, and it can be observed in the figure that the radial displacement is greater than the longitudinal displacement in the region of the breathing wave resonance peak at ± 170 rad/m. This dominance of the radial displacement at the breathing wave resonance can be observed in figures 117 and 118 at 50 and 100 rad/m, respectively.

The deformation due to the extensional wave is predominantly longitudinal. Therefore, the longitudinal displacement will be greater than the radial displacement in the region of the extensional wave resonance peak. Figures 117 and 118 illustrate the dominance of longitudinal displacement at the extensional wave resonance.

The last feature in the wavenumber-frequency plane that has not been discussed is the branch of wave propagation associated with the fluids. Figure 119 displays this region well; it is a wire frame representation of figure 13, which is a zoomed-in view of figure 110. The phase velocity of the dilatational wave (also known as the P-wave (primary or pressure wave)) for an infinite media of either inner or outer fluid is listed in table 1 as 1,500 m/sec. Close examination of the stress field indicates that there is an increase in energy associated with the fluid dilatation wave velocity. The fluid branch is sharply resonant with very narrow extent in wavenumber. The cylinder/fluid combination considered here supports this branch at the fluid P-wave phase velocity

up to the vicinity of the first radial resonance of the cylinder. At the first radial resonance (2816 Hz), this branch becomes dispersive, with the phase and group velocities slowing, as shown in table 15. The width in wavenumber of the resonant peak increases and a null in the transmitted stress field develops at the P-wave phase velocity of the fluid (1500 m/sec). Above the first radial resonance of the cylinder, the fluid P-wave is labeled as “MODIFIED FLUID P-WAVE” in the figures that follow. The effect of this fluid/structure interaction is strong longitudinal displacement in the cylinder, as evidenced by figures 115 through 118.

Table 15. Fluid P-Wave Phase and Group Velocity Versus Frequency From Figure 13

Frequency (Hz)	Phase Velocity (m/sec)	Group Velocity ± 75 (m/sec)
1,000	1,500	1,500
2,000	1,500	1,500
2,500	1,500	1,500
2,796	1,460	1,192
3,001	1,426	1,082
3,202	1,416	1,276
3,500	1,393	1,185
4,000	1,296	872
4,501	1,204	768
4,990	1,185	—

A contrast to the previous case of dense fluids (water) is shown in the simulation of figure 100, where the same cylinder was immersed in fluids of low density (air). In this case, the fluid P-wave phase velocity is unaltered by the first radial resonance of the cylinder. The P-wave phase velocity of air is 343 m/sec (tables 8 and 9) and remains nondispersive throughout the wavenumber-frequency range of the simulation (figure 100).

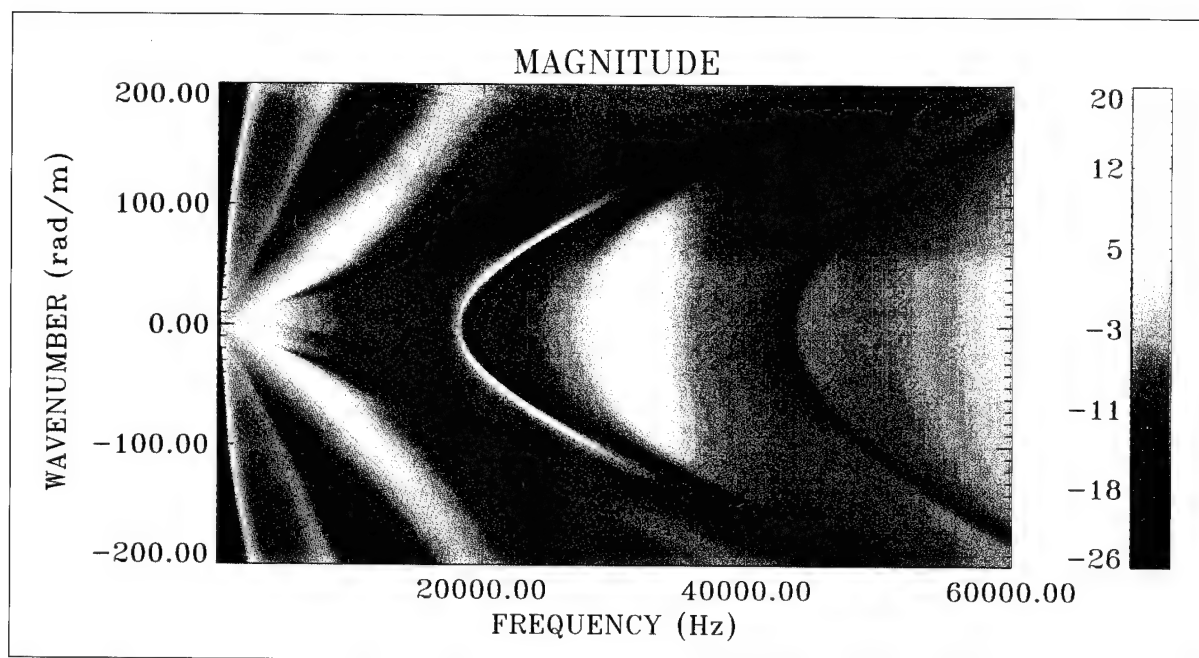


Figure 109. Radial Stress Transfer Surface Up to 60 kHz When
 Magnitude = $10\text{Log}(\tau_{rr}^{C1}(r_1)/P_o)^2$ at $r_1 = 1.21$ in. With $n = 0$ and
 Diameter = 3.00 in. (Color Image)

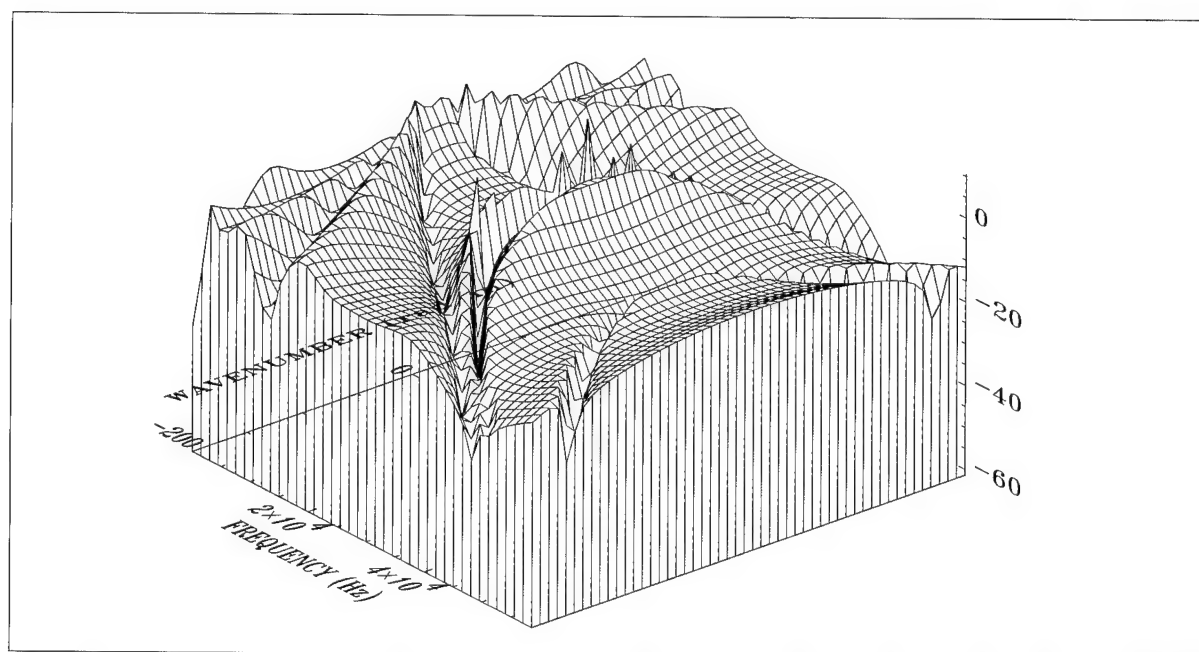


Figure 110. Radial Stress Transfer Surface Up to 60 kHz When
 Magnitude = $10\text{Log}(\tau_{rr}^{C1}(r_1)/P_o)^2$ at $r_1 = 1.21$ in. With $n = 0$ and
 Diameter = 3.00 in. (Wire Frame Surface)

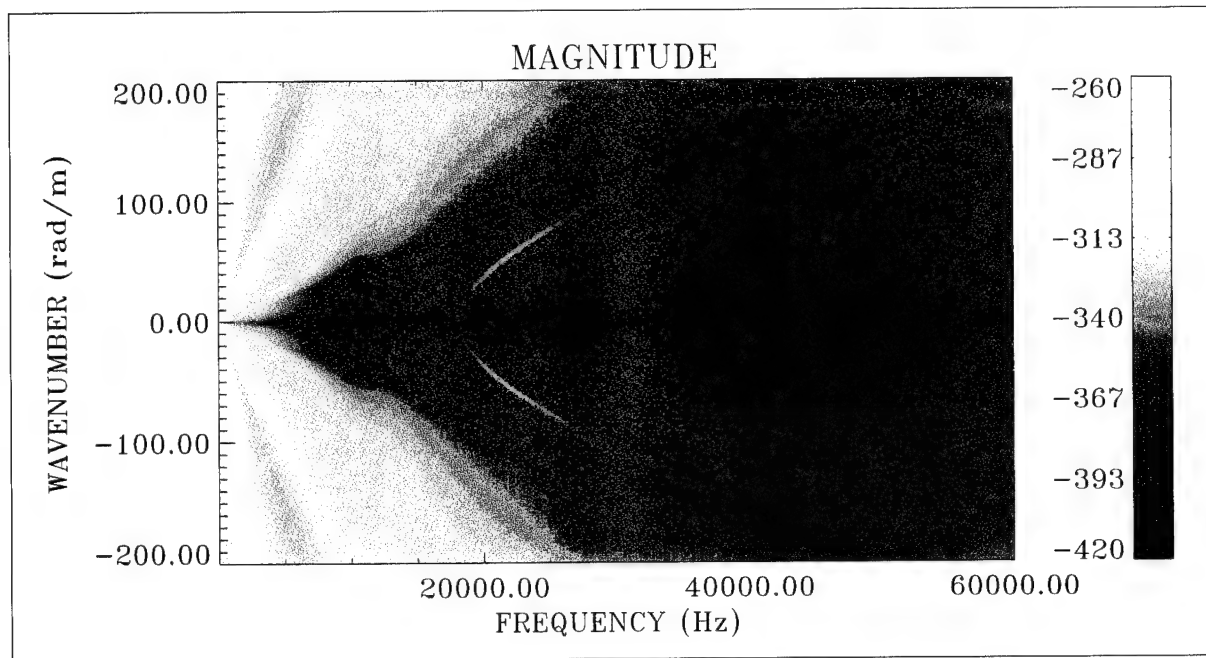


Figure 111. Longitudinal Displacement Transfer Surface Up to 60 kHz When Magnitude = $10\text{Log}(w_c^{C1}(r_1)/P_o)^2$ at $r_1 = 1.21$ in. With $n = 0$ and Diameter = 3.00 in. (Color Image)

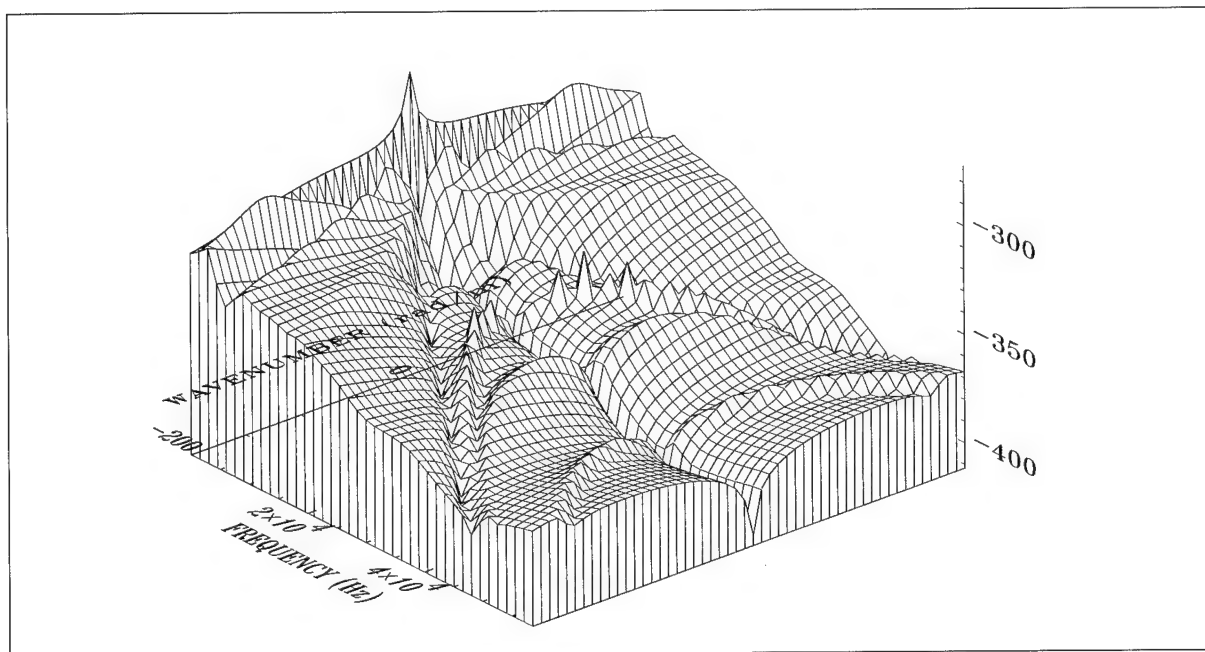


Figure 112. Longitudinal Displacement Transfer Surface Up to 60 kHz When Magnitude = $10\text{Log}(w_c^{C1}(r_1)/P_o)^2$ at $r_1 = 1.21$ in. With $n = 0$ and Diameter = 3.00 in. (Wire Frame Surface)

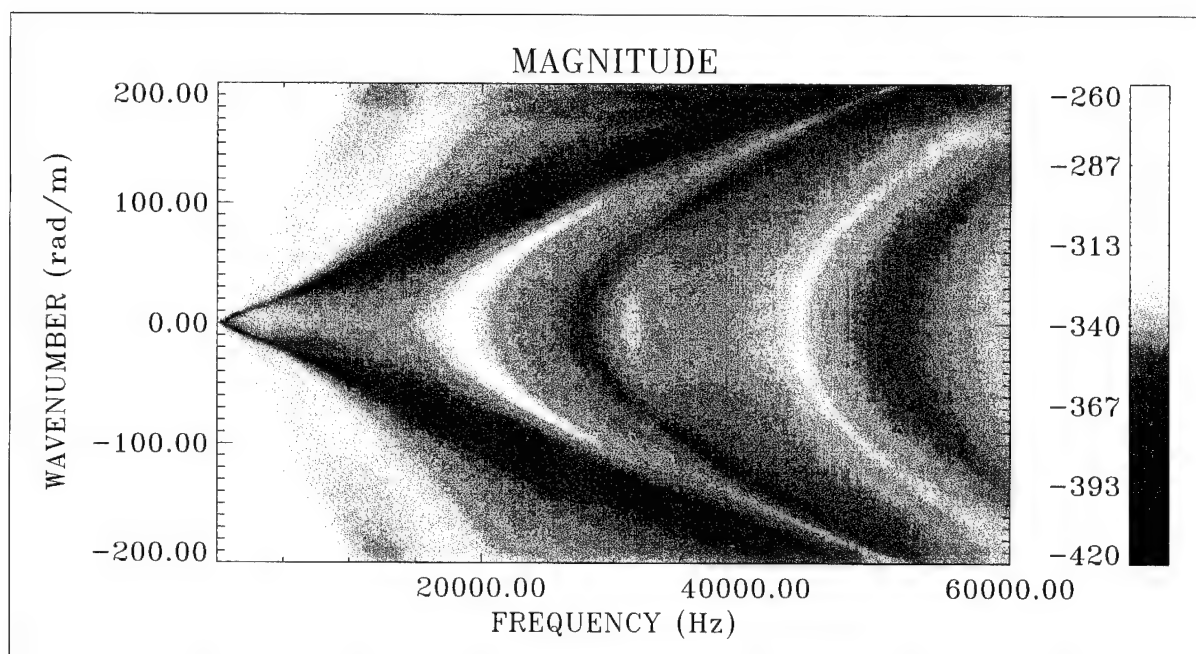


Figure 113. Radial Displacement Transfer Surface Up to 60 kHz When
Magnitude = $10\text{Log}(u_c^{C1}(r_1)/P_o)^2$ at $r_1 = 1.21$ in. With $n = 0$ and Diameter = 3.00 in.
(Color Image)

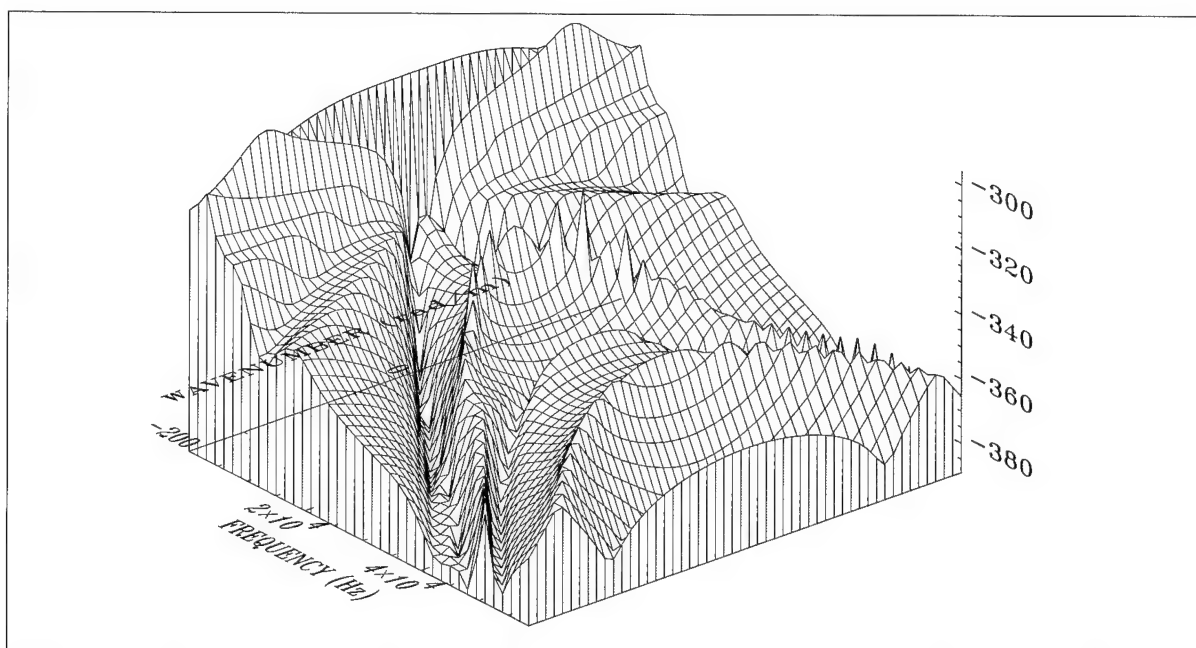


Figure 114. Radial Displacement Transfer Surface Up to 60 kHz When
Magnitude = $10\text{Log}(u_c^{C1}(r_1)/P_o)^2$ at $r_1 = 1.21$ in. With $n = 0$ and Diameter = 3.00 in.
(Wire Frame Surface)

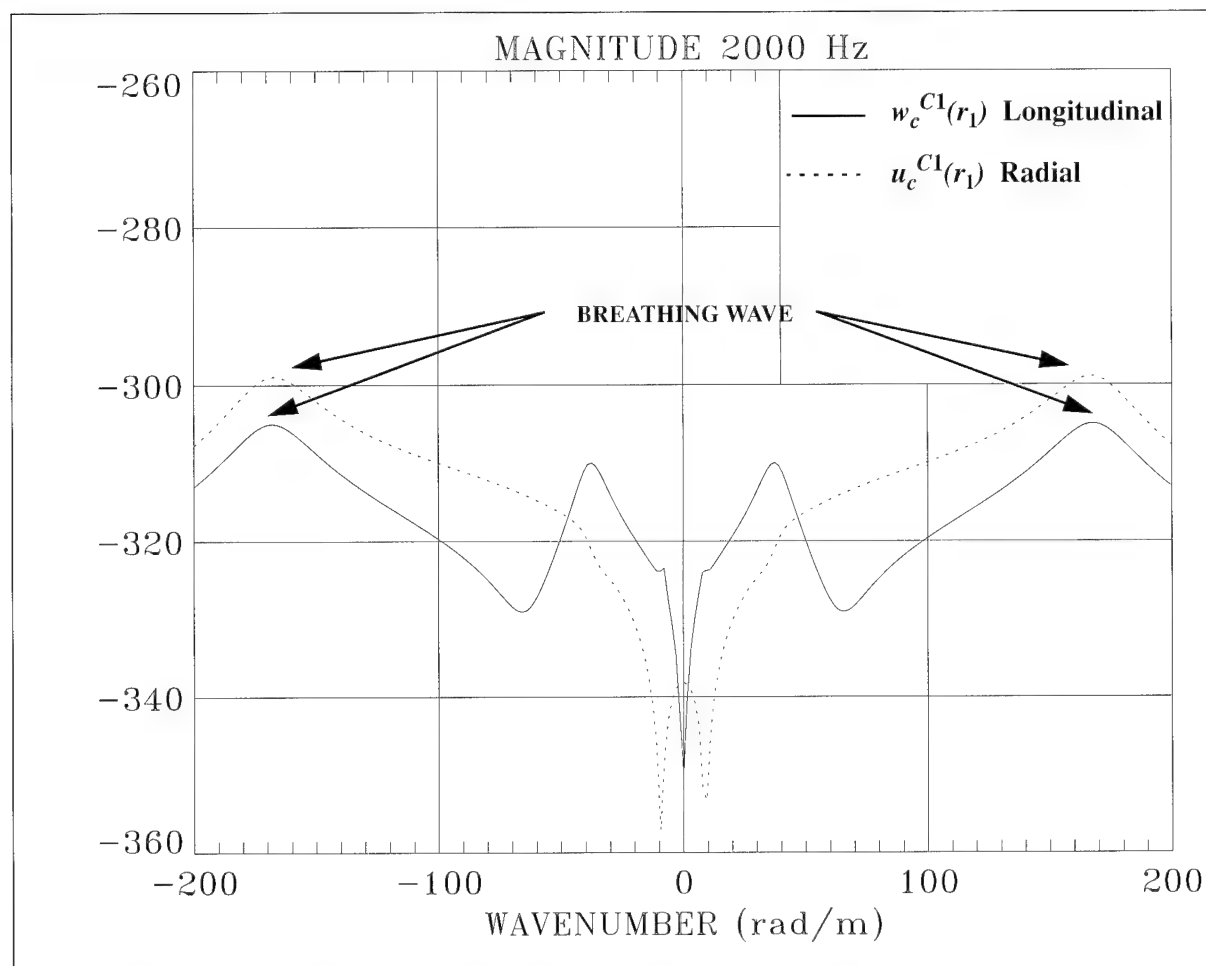


Figure 115. Cylinder Displacement Comparison for Figures 111 and 113 When Magnitude = $10\text{Log}(X/P_o)^2$ for Values of $X = w_c^{C1}(r_1)$ and $u_c^{C1}(r_1)$ at $r_1 = 1.21$ in. With $n = 0$, Diameter = 3.00 in., and $f = 2000$ Hz

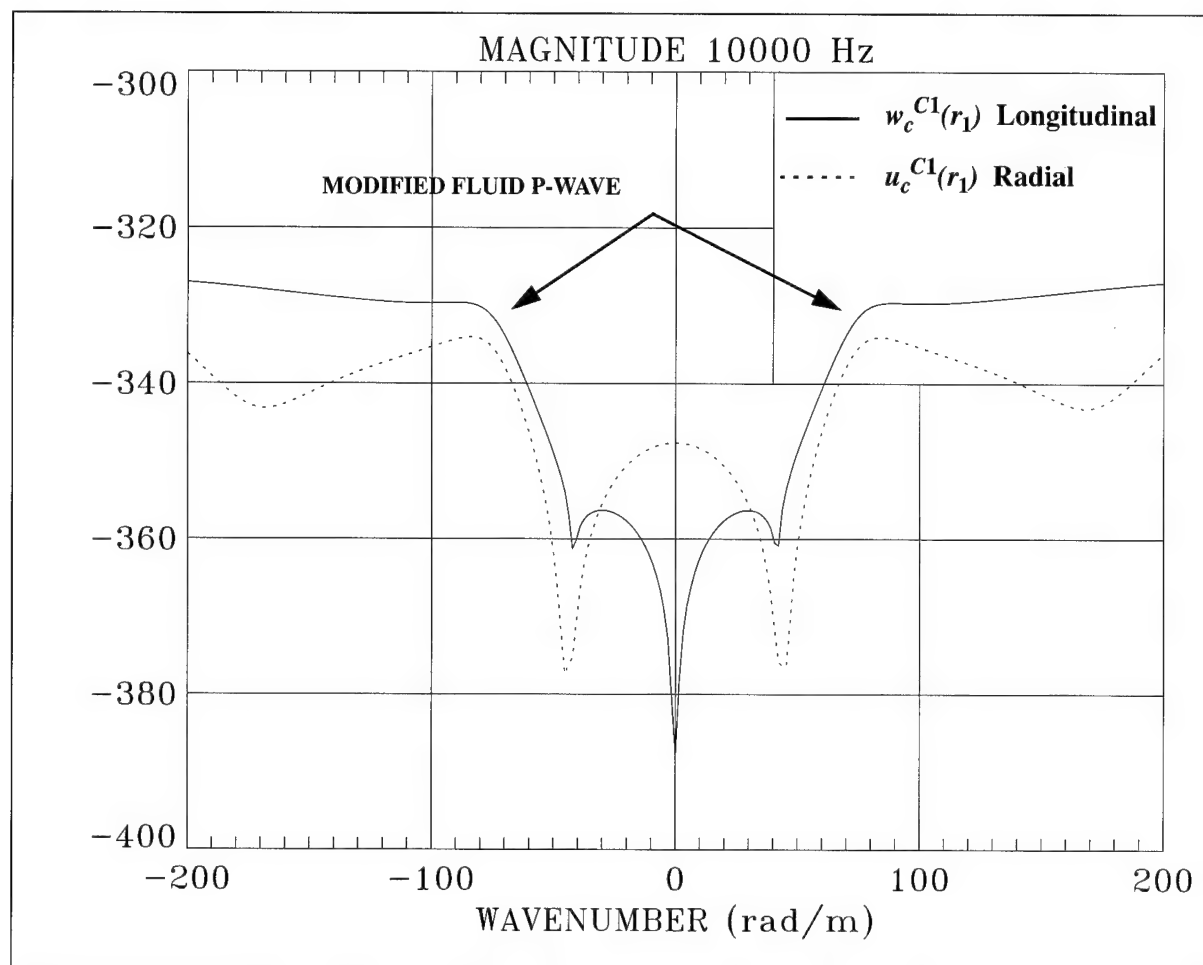


Figure 116. Cylinder Displacement Comparison for Figures 111 and 113 When Magnitude = $10\text{Log}(X/P_o)^2$ for Values of $X = w_c^{C1}(r_1)$ and $u_c^{C1}(r_1)$ at $r_1 = 1.21$ in. With $n = 0$, Diameter = 3.00 in., and $f = 10000$ Hz

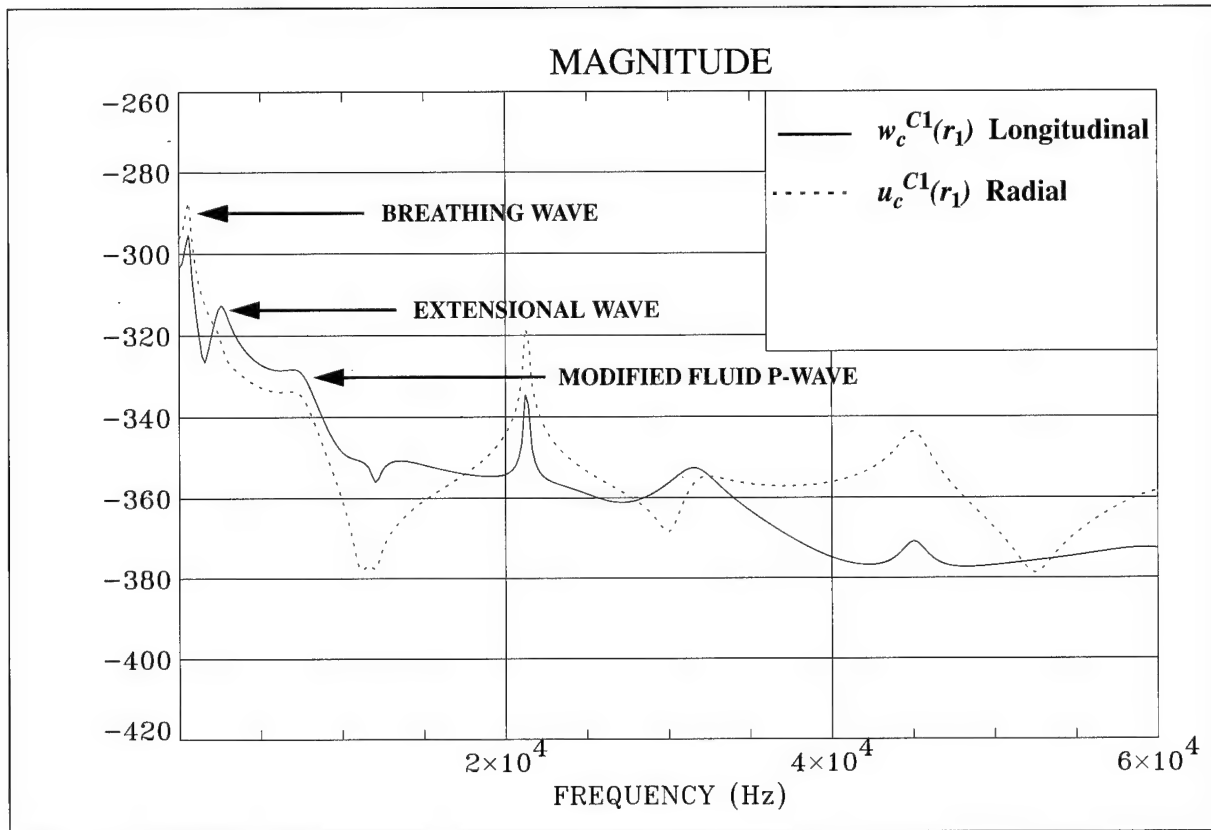


Figure 117. Cylinder Displacement Comparison for Figures 111 and 113 When Magnitude = $10\text{Log}(X/P_o)^2$ for Values of $X = w_c^{C1}(r_1)$ and $u_c^{C1}(r_1)$ at $r_1 = 1.21$ in. With $n = 0$, Diameter = 3.00 in., and $k = 50$ rad/m

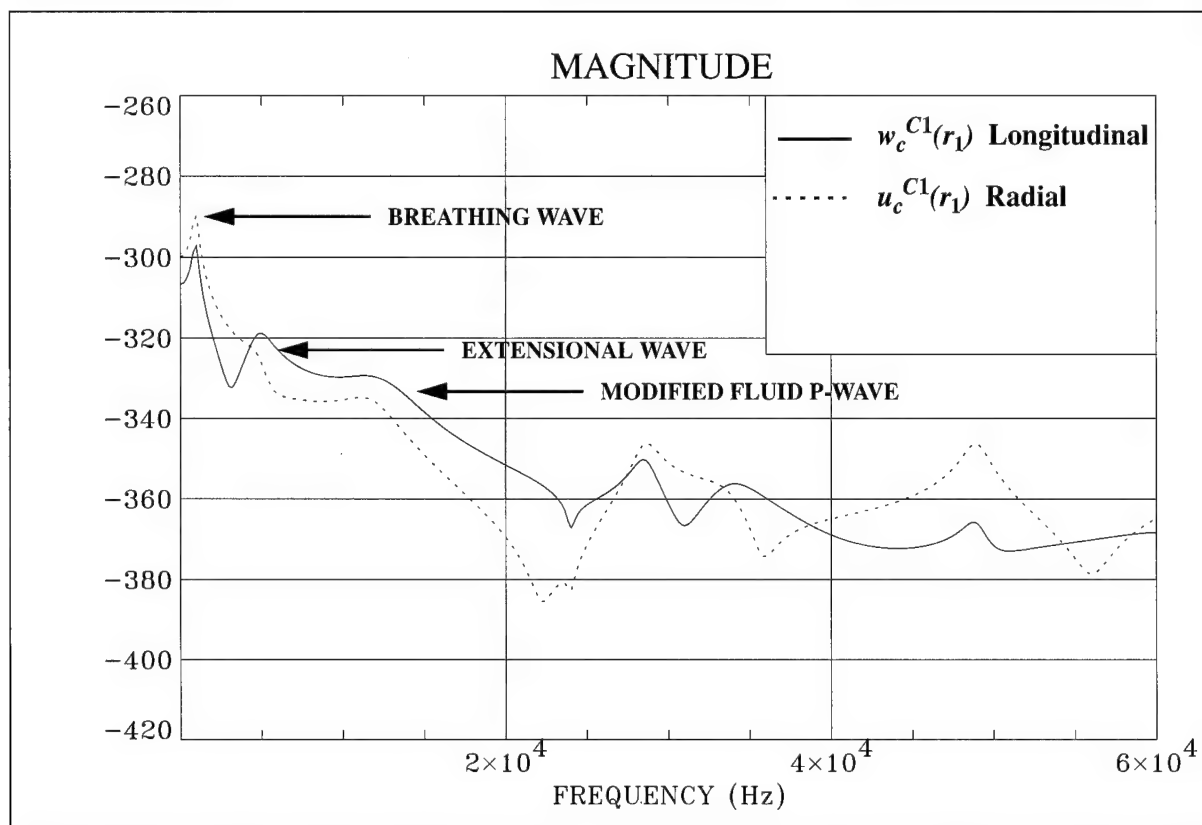
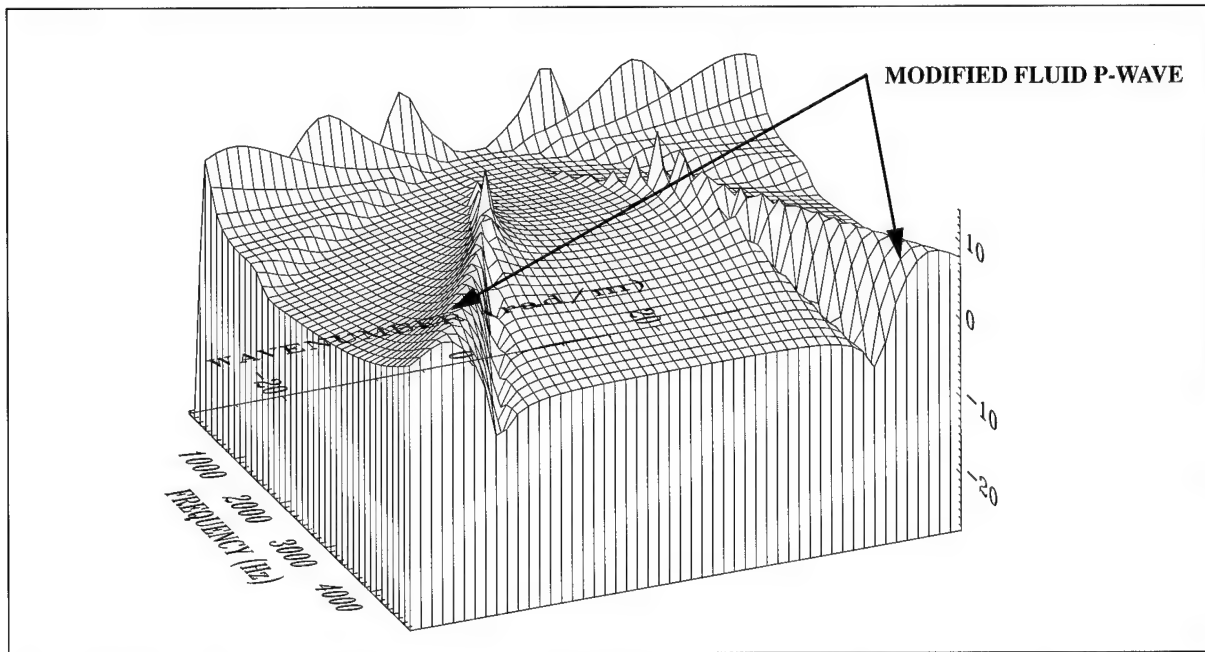


Figure 118. Cylinder Displacement Comparison for Figures 111 and 113 When Magnitude = $10\text{Log}(X/P_o)^2$ for Values of $X = w_c^{C1}(r_1)$ and $u_c^{C1}(r_1)$ at $r_1 = 1.21$ in. With $n = 0$, Diameter = 3.00 in., and $k = 100$ rad/m



**Figure 119. Radial Stress Transfer Surface With Magnitude = $10\text{Log}(\tau_{rr}^{C1}(r_1)/P_o)^2$
at $r_1 = 1.21$ in. With $n = 0$ and Diameter = 3.00 in.
(Wire Frame Surface of Figure 13)**

SINGLE-LAYER CYLINDER SIMULATIONS—LONGITUDINAL SHEAR STRESS EXCITATION

Up to this point, the type of excitation applied to the cylinder has been a pressure normal to the cylinder surface. In this section, the normal pressure excitation will be replaced with a longitudinal shear stress excitation, once again applied uniformly over the outer surface of the cylinder. The cylinder and fluid properties are taken from tables 2, 4 and 5.

Figures 120 and 121 depict the simulation for the $n = 0$ excitation. The major branch of wave propagation excited is the extensional wave. The phase velocity of the extensional wave is roughly 300 m/sec, and it is nondispersive over the range of the simulation. The breathing wave is faintly visible in figure 121. In the earlier normal pressure simulation of figure 20, we observed a high-level breathing wave and a low-level extensional wave; however, the longitudinal excitation creates a high-level extensional wave and a low-level breathing wave.

The fluid P-wave discussed in the previous section is visible in the $n = 0$ simulation. This branch has the same phase and group velocities listed in table 15.

The simulation for circumferential order number $n = 1$ is shown in figures 122 and 123, and the simulation for $n = 2$ is shown in figures 124 and 125. In both cases, the second and third branches produce higher level responses than does the first branch. The reason for this is that the longitudinal shear stress excitation imparts energy more directly into the longitudinal and circumferential motions of the cylinder than into the radial motion.

Figure 126 is a comparison of $n = 0, 1$, and 2 at 50 Hz. The major feature at $n = 0$ is the extensional wave, exhibiting sharp roll-off in wavenumber and a resonance amplitude of approximately 20 dB. At 500 Hz, in figure 127, the extensional wave amplitude has dropped to approximately 12 dB and the roll-off in wavenumber is less precipitous. The fluid P-wave is indicated on figure 128 at 2000 Hz (the extensional wave of the cylinder is also observed in this region). In figure 129 at 5000 Hz, the P-wave has become modified by the cylinder, the width of the resonant peak has increased, and the wave has become dispersive. The amplitude of the extensional wave has decreased in level.

In each of the comparisons (figures 126 through 129), the $n = 0$ excitation creates the largest amplitude pressure in the inner fluid. The $n = 1$ and 2 pressure fields will exhibit strong variation in amplitude with radial position. Simulations of this behavior have not been included in this report.

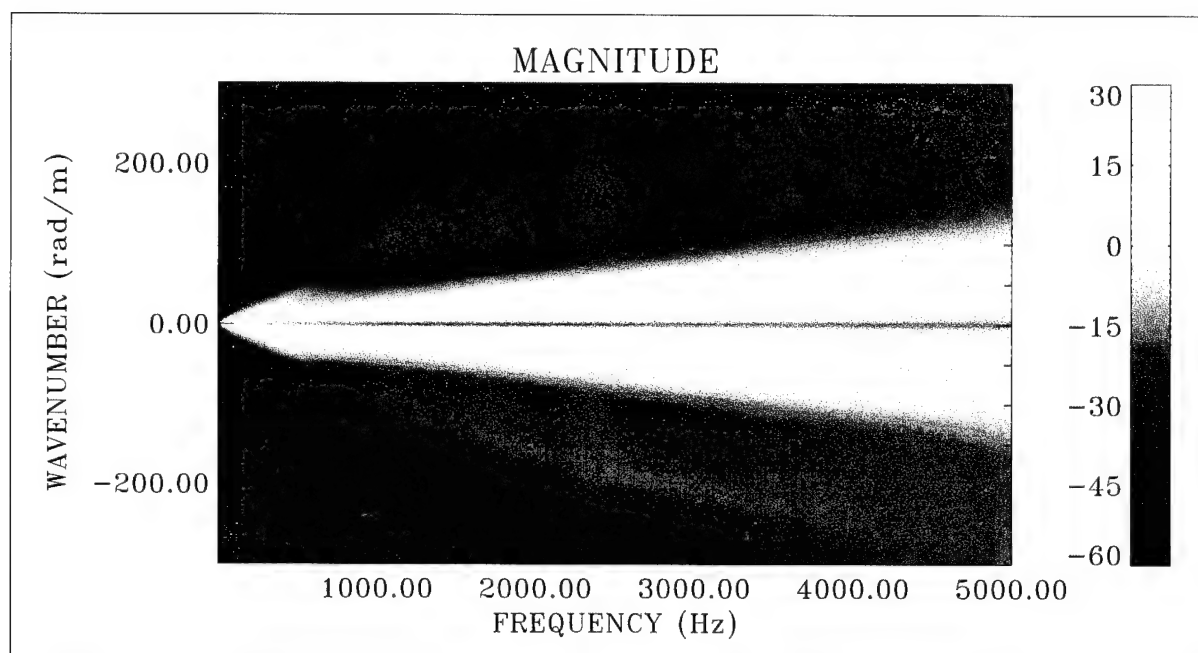


Figure 120. Pressure Transfer Surface With Magnitude = $10\text{Log}(P_i(r_1)/P_x)^2$ at $r_1 = 0.75$ in. for $n = 0$ and Diameter = 3.00 in. (Color Image)

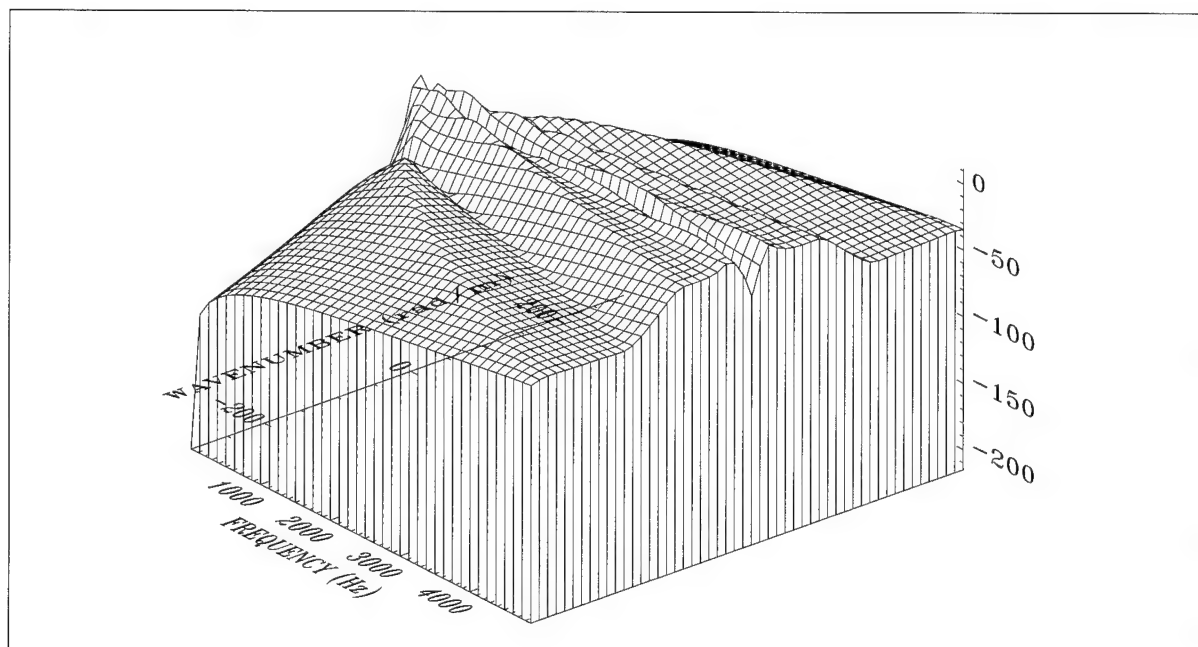


Figure 121. Pressure Transfer Surface With Magnitude = $10\text{Log}(P_i(r_1)/P_x)^2$ at $r_1 = 0.75$ in. for $n = 0$ and Diameter = 3.00 in. (Wire Frame Surface)

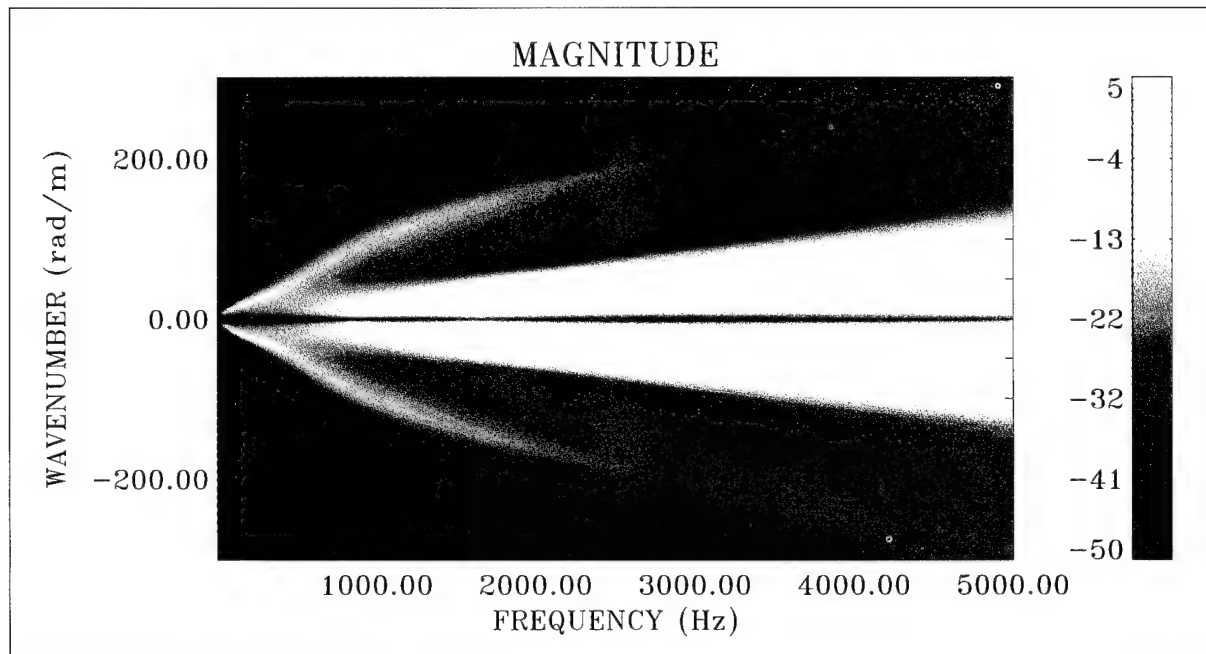


Figure 122. Pressure Transfer Surface With Magnitude = $10\text{Log}(P_i(r_1)/P_x)^2$ at $r_1 = 0.75$ in. for $n = 1$ and Diameter = 3.00 in. (Color Image)

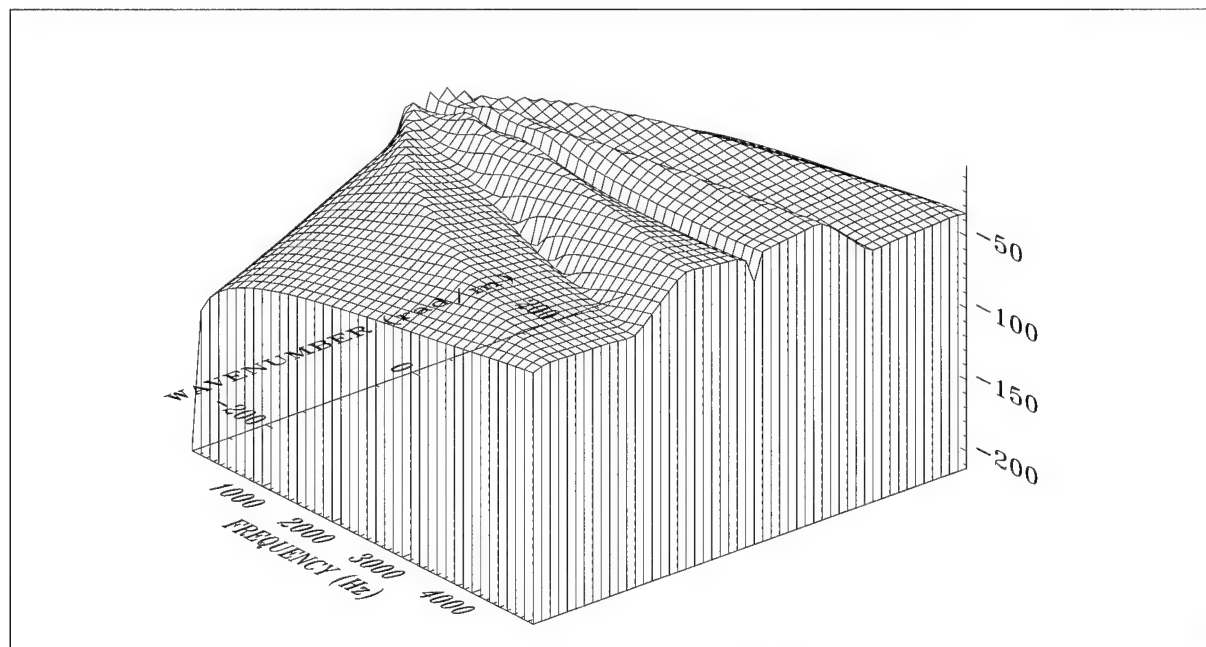


Figure 123. Pressure Transfer Surface With Magnitude = $10\text{Log}(P_i(r_1)/P_x)^2$ at $r_1 = 0.75$ in. for $n = 1$ and Diameter = 3.00 in. (Wire Frame Surface)

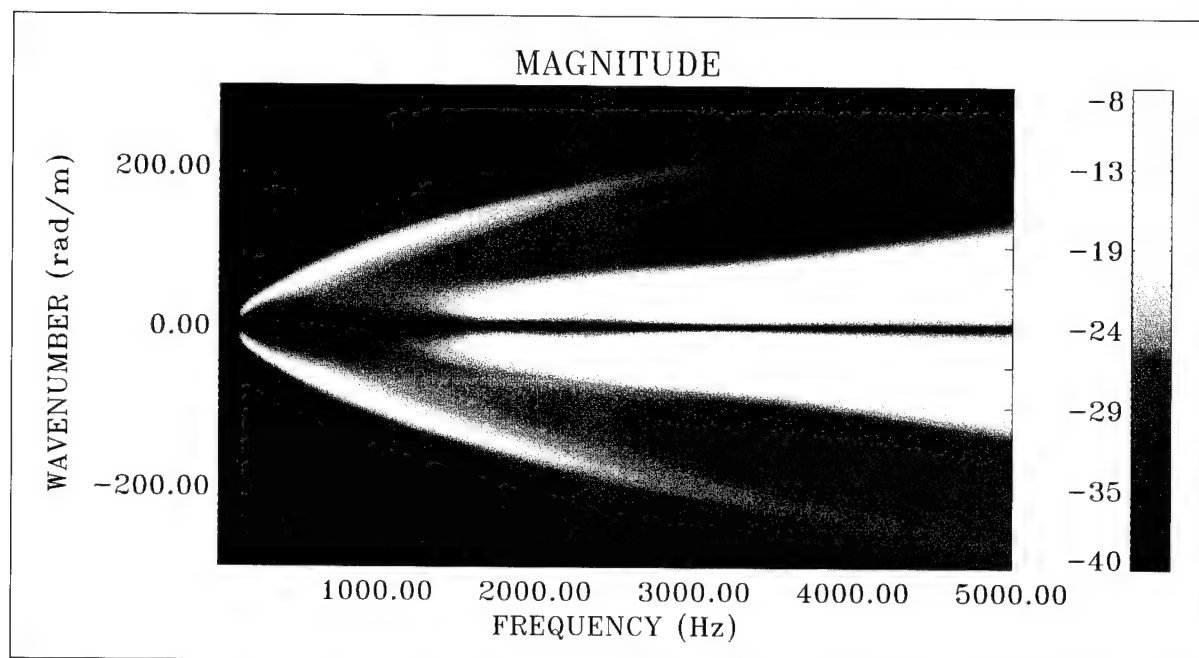


Figure 124. Pressure Transfer Surface With Magnitude = $10\text{Log}(P_i(r_1)/P_x)^2$ at $r_1 = 0.75$ in. for $n = 2$ and Diameter = 3.00 in. (Color Image)

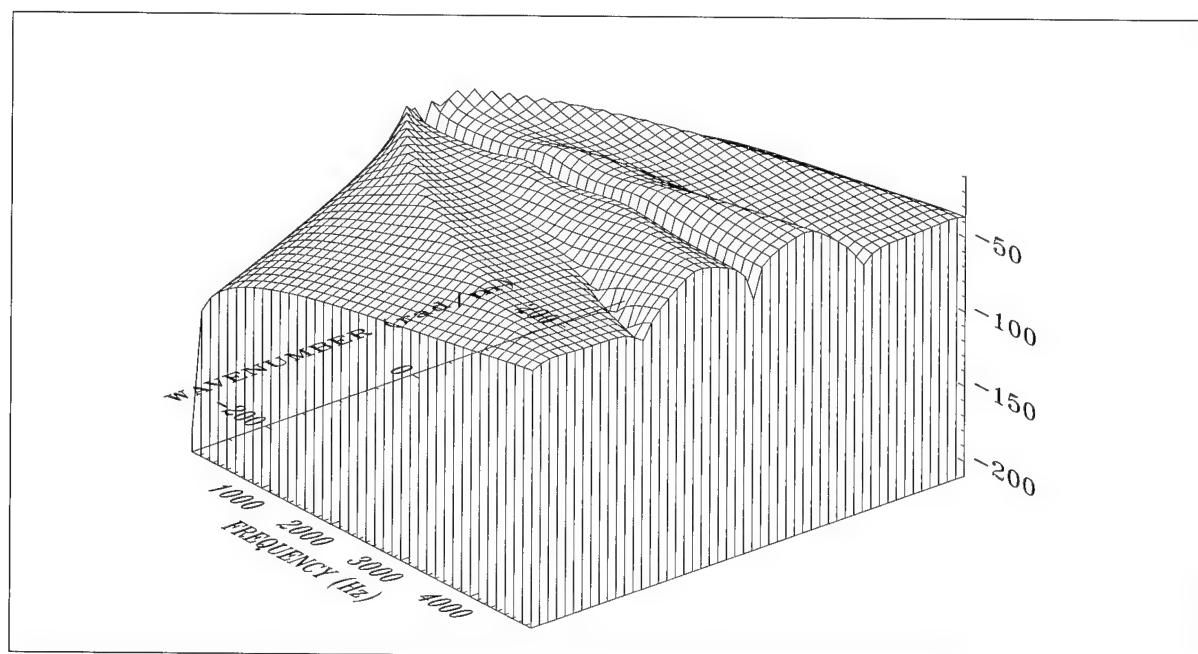


Figure 125. Pressure Transfer Surface With Magnitude = $10\text{Log}(P_i(r_1)/P_x)^2$ at $r_1 = 0.75$ in. for $n = 2$ and Diameter = 3.00 in. (Wire Frame Surface)

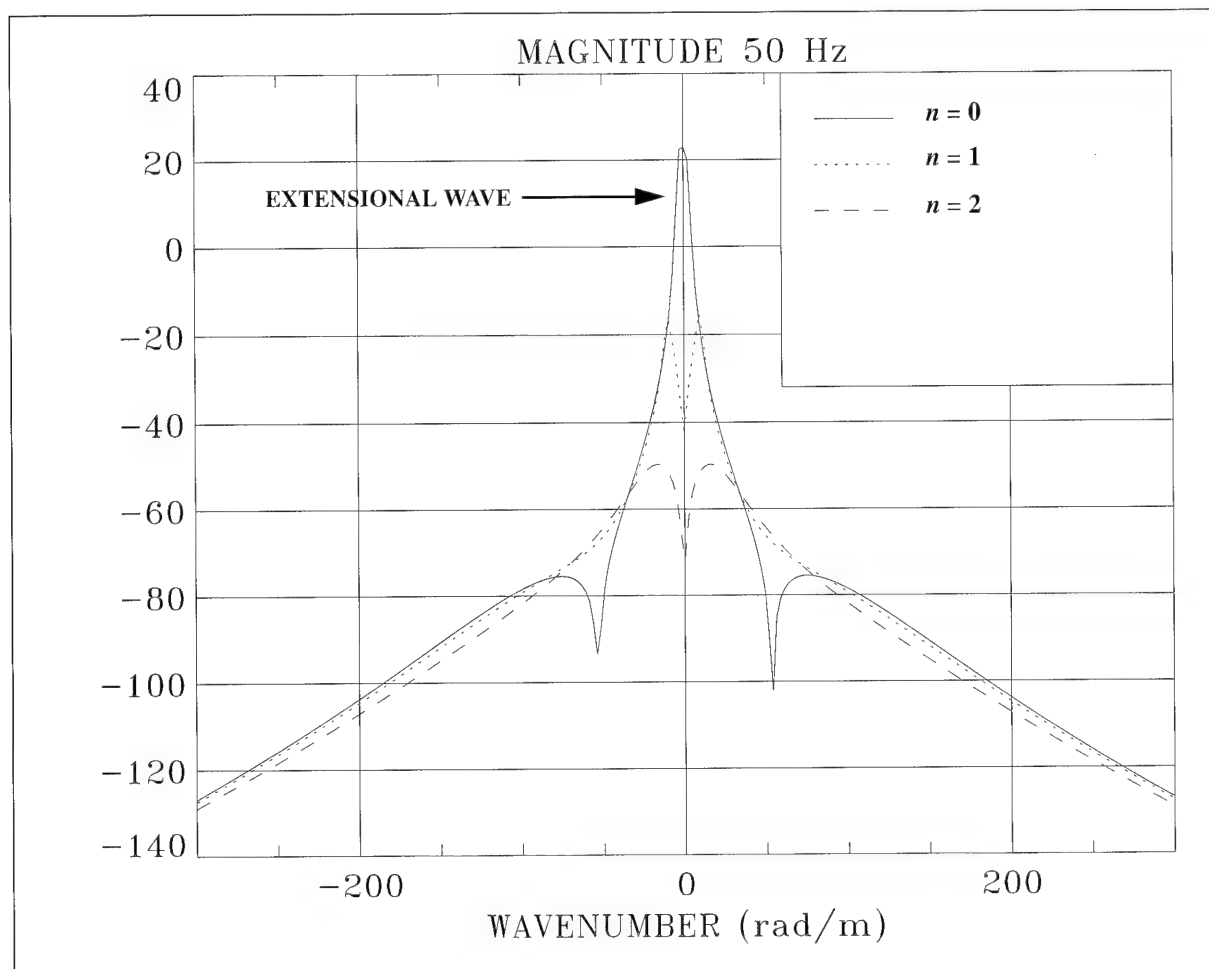


Figure 126. Comparison of Longitudinal Shear Stress Excitation for Figures 120, 122, and 124 When Magnitude = $10\text{Log}(P_i(r_1)/P_x)^2$ at $r_1 = 0.75$ in. for Various n With Diameter = 3.00 in. and $f = 50$ Hz

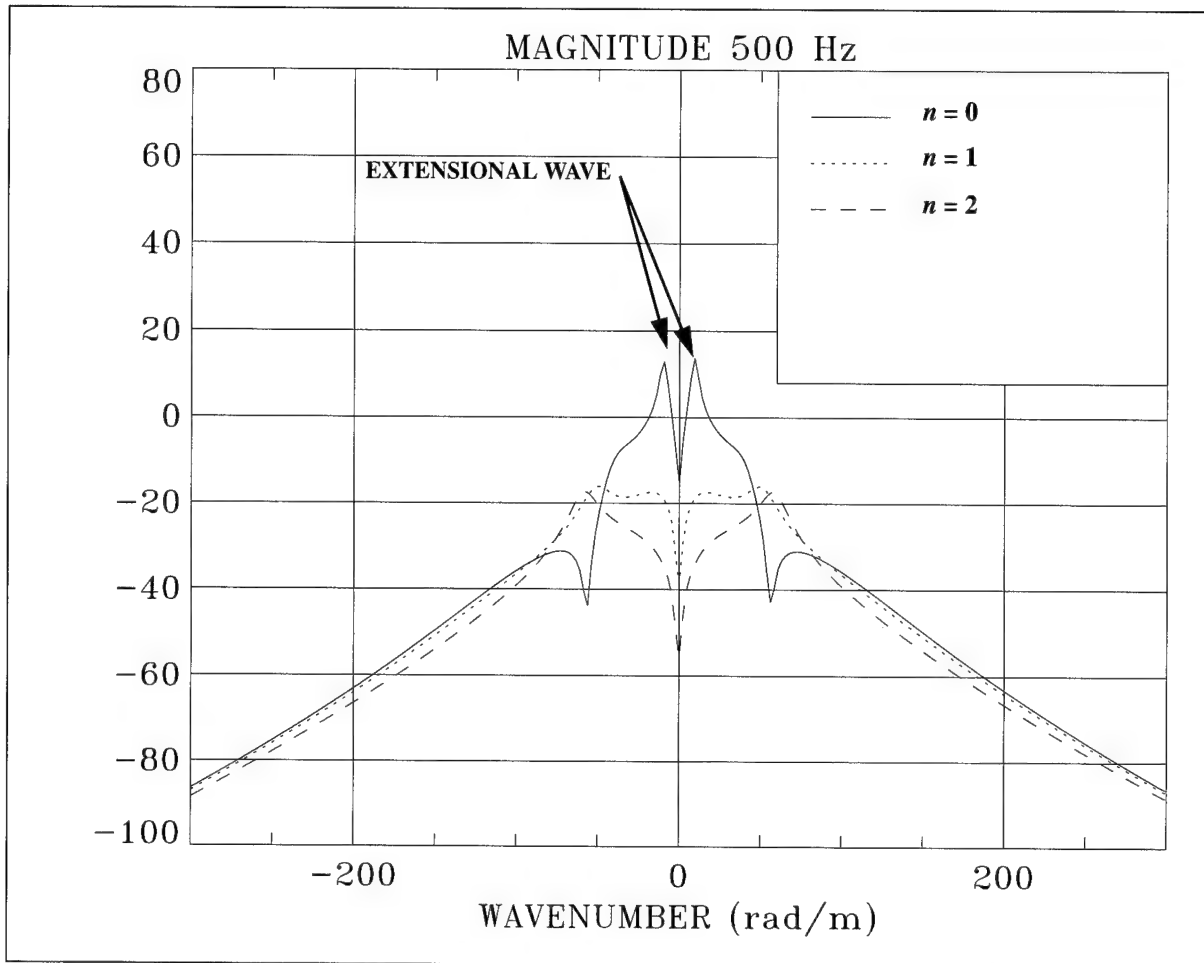


Figure 127. Comparison of Longitudinal Shear Stress Excitation for Figures 120, 122, and 124 When Magnitude = $10\text{Log}(P_i(r_1)/P_x)^2$ at $r_1 = 0.75$ in. for Various n With Diameter = 3.00 in. and $f = 500$ Hz

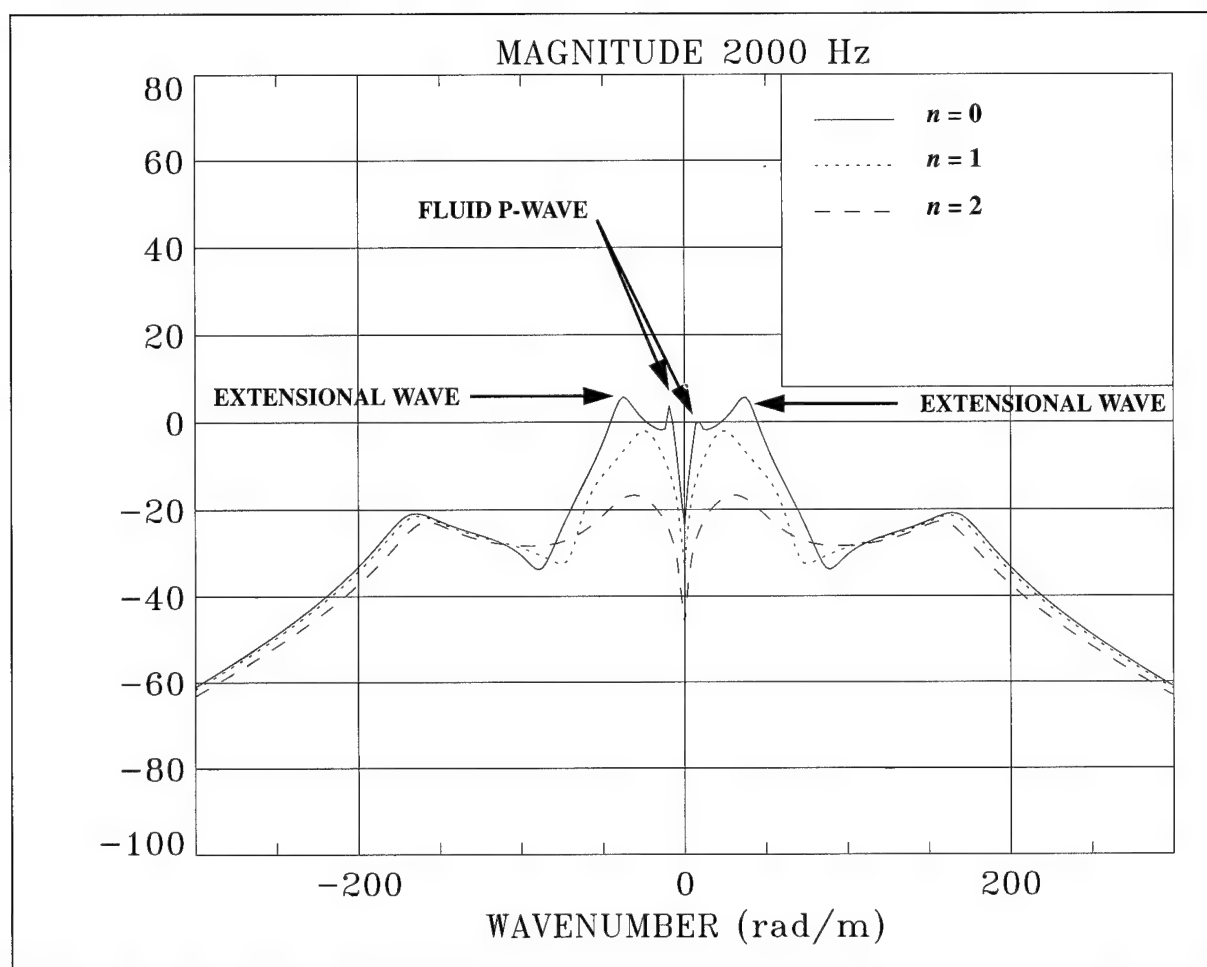


Figure 128. Comparison of Longitudinal Shear Stress Excitation for Figures 120, 122, and 124 When Magnitude = $10\text{Log}(P_i(r_1)/P_x)^2$ at $r_1 = 0.75$ in. for Various n With Diameter = 3.00 in. and $f = 2000$ Hz

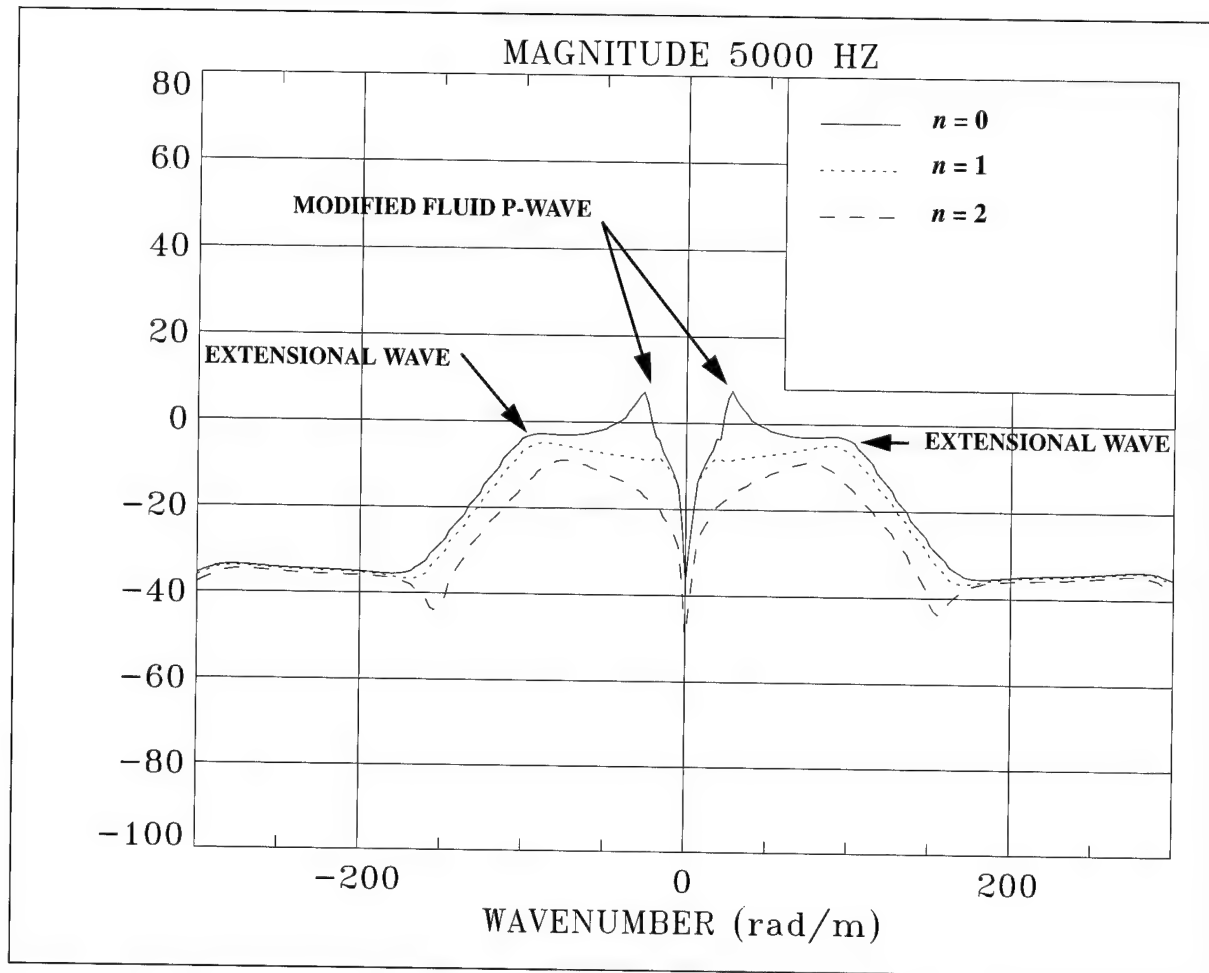


Figure 129. Comparison of Longitudinal Shear Stress Excitation for Figures 120, 122, and 124 When Magnitude = $10\text{Log}(P_i(r_1)/P_x)^2$ at $r_1 = 0.75$ in. for Various n With Diameter = 3.00 in. and $f = 5000$ Hz

SINGLE-LAYER CYLINDER SIMULATIONS—CIRCUMFERENTIAL SHEAR STRESS EXCITATION

In this section, the response of the cylinder to a circumferential shear stress excitation is considered. The properties for the cylinder and fluids are the same as those used in the previous section and are taken from tables 2, 4 and 5. Because there is no circumferential displacement in an $n = 0$ excitation, we will only consider the $n = 1$ and $n = 2$ circumferential order numbers in this section.

In figures 130 and 131, which depict the simulation for the $n = 1$ circumferential shear stress excitation, the first three branches of wave propagation are evident. The first branch gives rise to wave propagation that places the cylinder in the characteristic rx plane-bending motion. The second and third branches have cutoff frequencies associated with them. Pressure is developed in the inner fluid by Poisson coupling into a radial displacement.

Figures 132 and 133 display the $n = 2$ simulation for circumferential shear stress excitation. Two branches of wave propagation are evident in the simulation, both exhibiting cutoff frequencies.

Figures 134 through 137 are comparisons of the $n = 1$ and $n = 2$ responses at various frequencies. For all frequencies and wavenumbers, the $n = 1$ excitation produces a larger amplitude pressure field in the inner fluid. The pressure field developed by both the $n = 1$ and $n = 2$ excitations is strongly dependent on radial position.

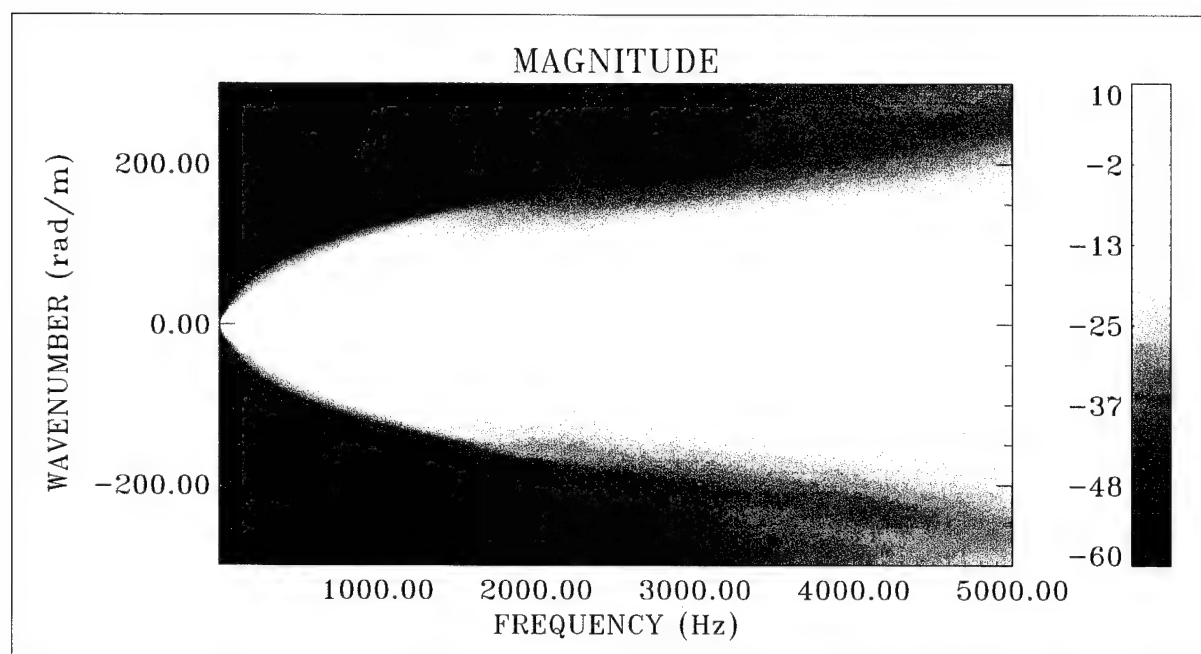


Figure 130. Pressure Transfer Surface With Magnitude = $10\text{Log}(P_i(r_1)/P_\theta)^2$ at $r_1 = 0.75$ in. for $n = 1$ and Diameter = 3.00 in. (Color Image)

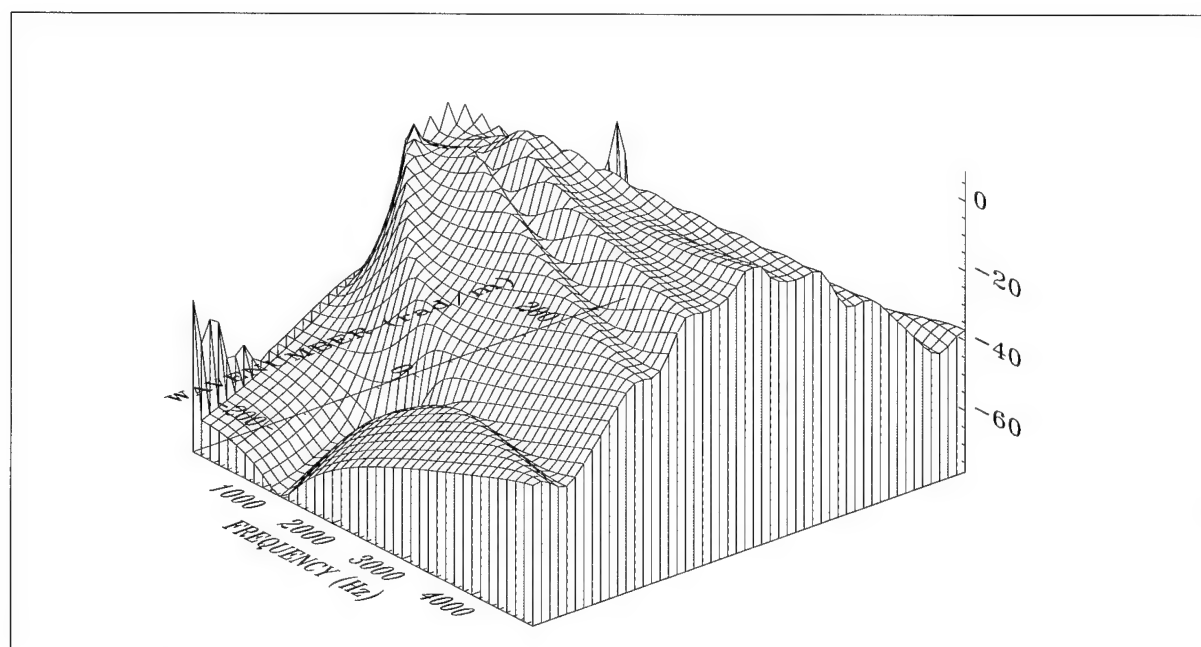


Figure 131. Pressure Transfer Surface With Magnitude = $10\text{Log}(P_i(r_1)/P_\theta)^2$ at $r_1 = 0.75$ in. for $n = 1$ and Diameter = 3.00 in. (Wire Frame Surface)

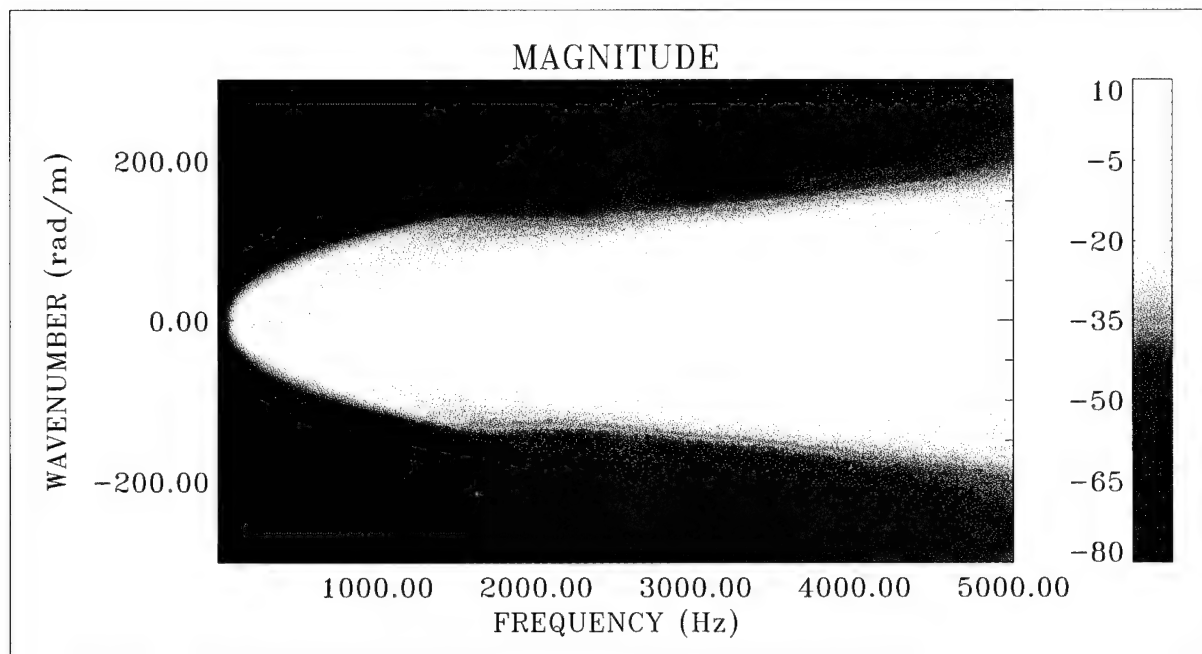


Figure 132. Pressure Transfer Surface With Magnitude = $10\text{Log}(P_i(r_1)/P_\theta)^2$ at $r_1 = 0.75$ in. for $n = 2$ and Diameter = 3.00 in. (Color Image)

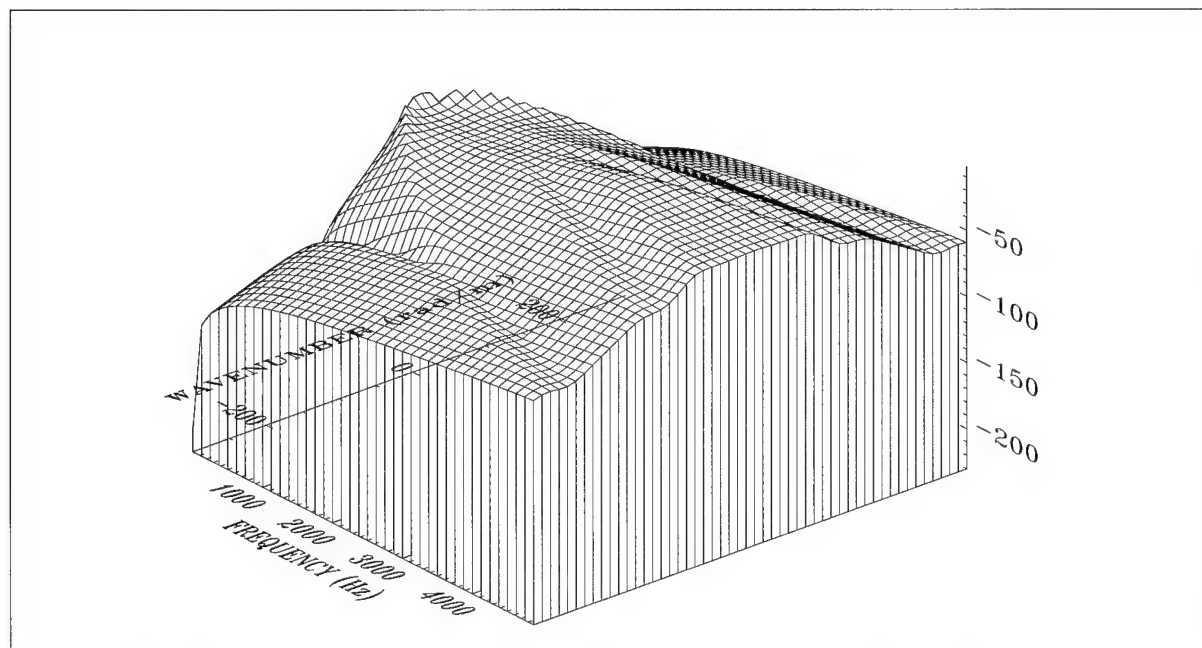


Figure 133. Pressure Transfer Surface With Magnitude = $10\text{Log}(P_i(r_1)/P_\theta)^2$ at $r_1 = 0.75$ in. for $n = 2$ and Diameter = 3.00 in. (Wire Frame Surface)

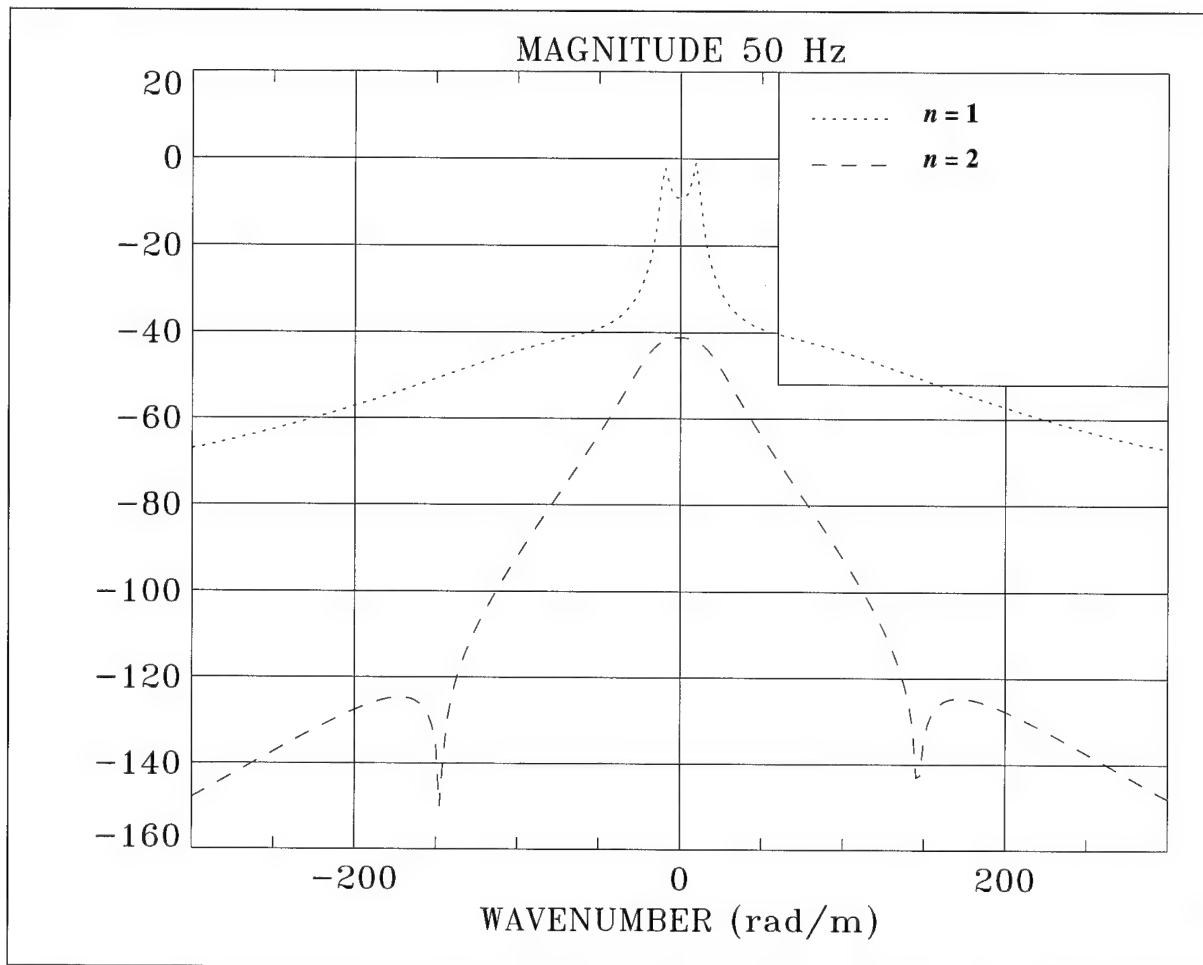


Figure 134. Comparison of Circumferential Shear Stress Excitation for Figures 130 and 132 When Magnitude = $10\text{Log}(P_f(r_1)/P_\theta)^2$ at $r_1 = 0.75$ in. for Various n With Diameter = 3.00 in. and $f = 50$ Hz

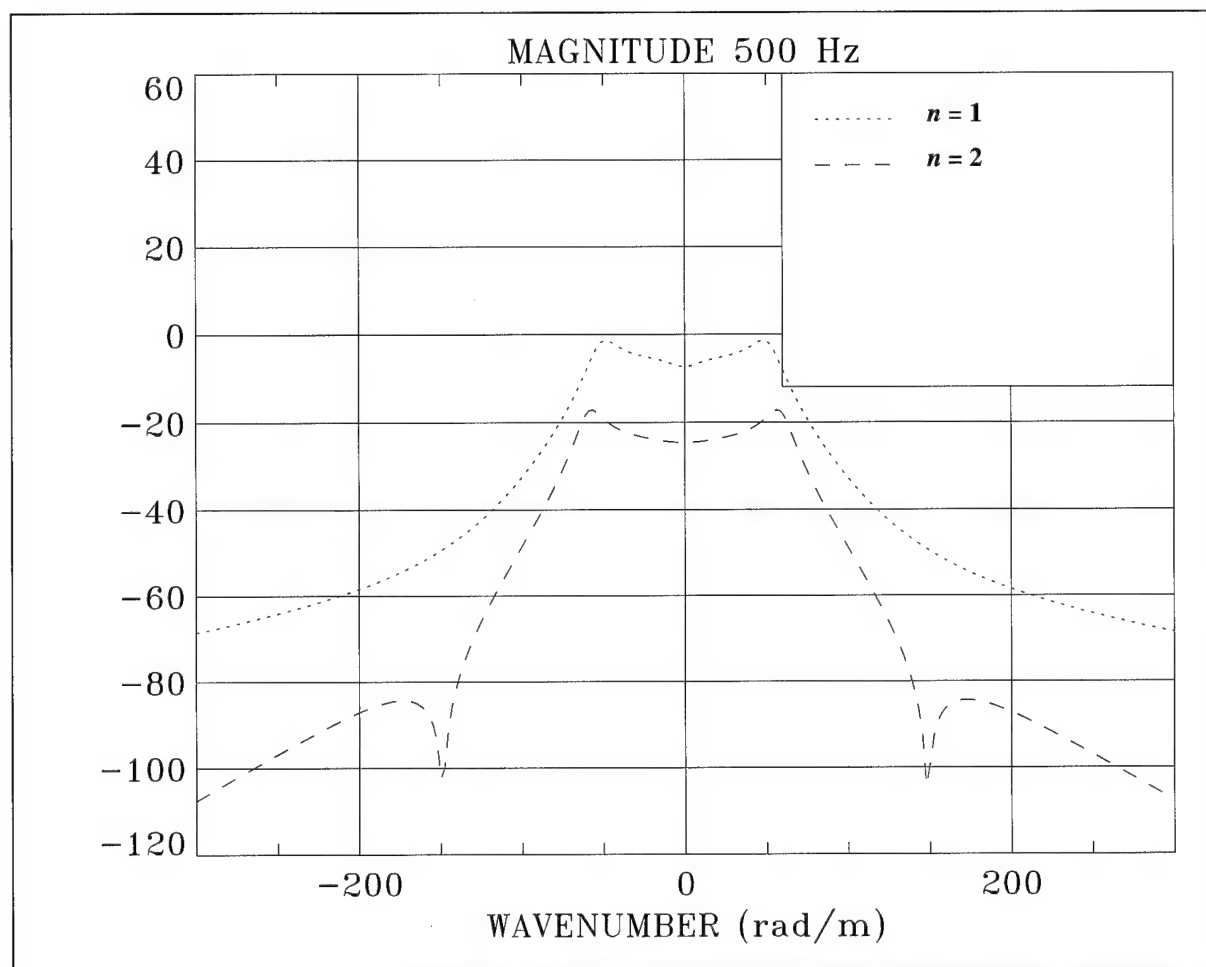


Figure 135. Comparison of Circumferential Shear Stress Excitation for Figures 130 and 132 When Magnitude = $10\text{Log}(P_i(r_1)/P_0)^2$ at $r_1 = 0.75$ in. for Various n With Diameter = 3.00 in. and $f = 500$ Hz

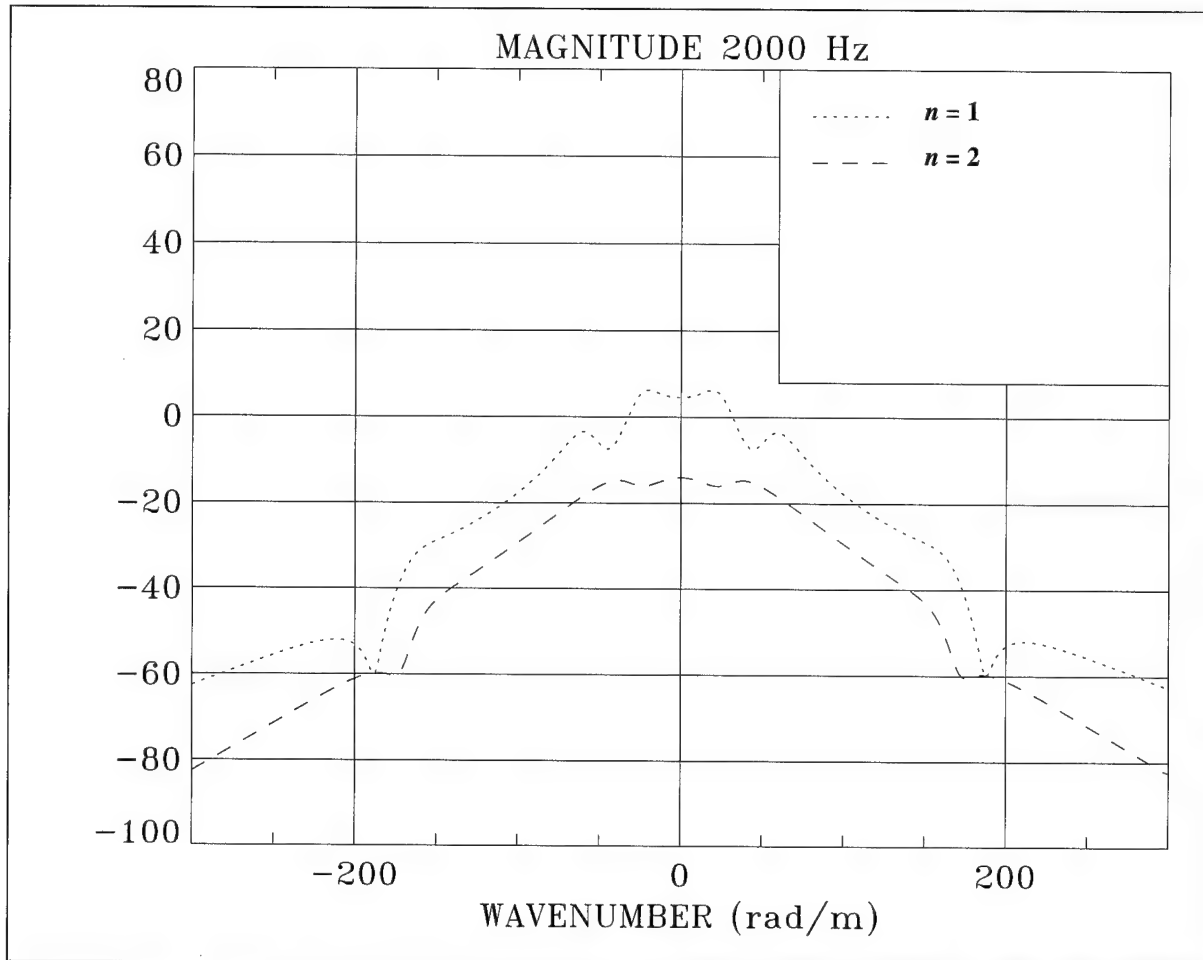


Figure 136. Comparison of Circumferential Shear Stress Excitation for Figures 130 and 132 When Magnitude = $10\text{Log}(P_i(r_1)/P_\theta)^2$ at $r_1 = 0.75$ in. for Various n With Diameter = 3.00 in. and $f = 2000$ Hz

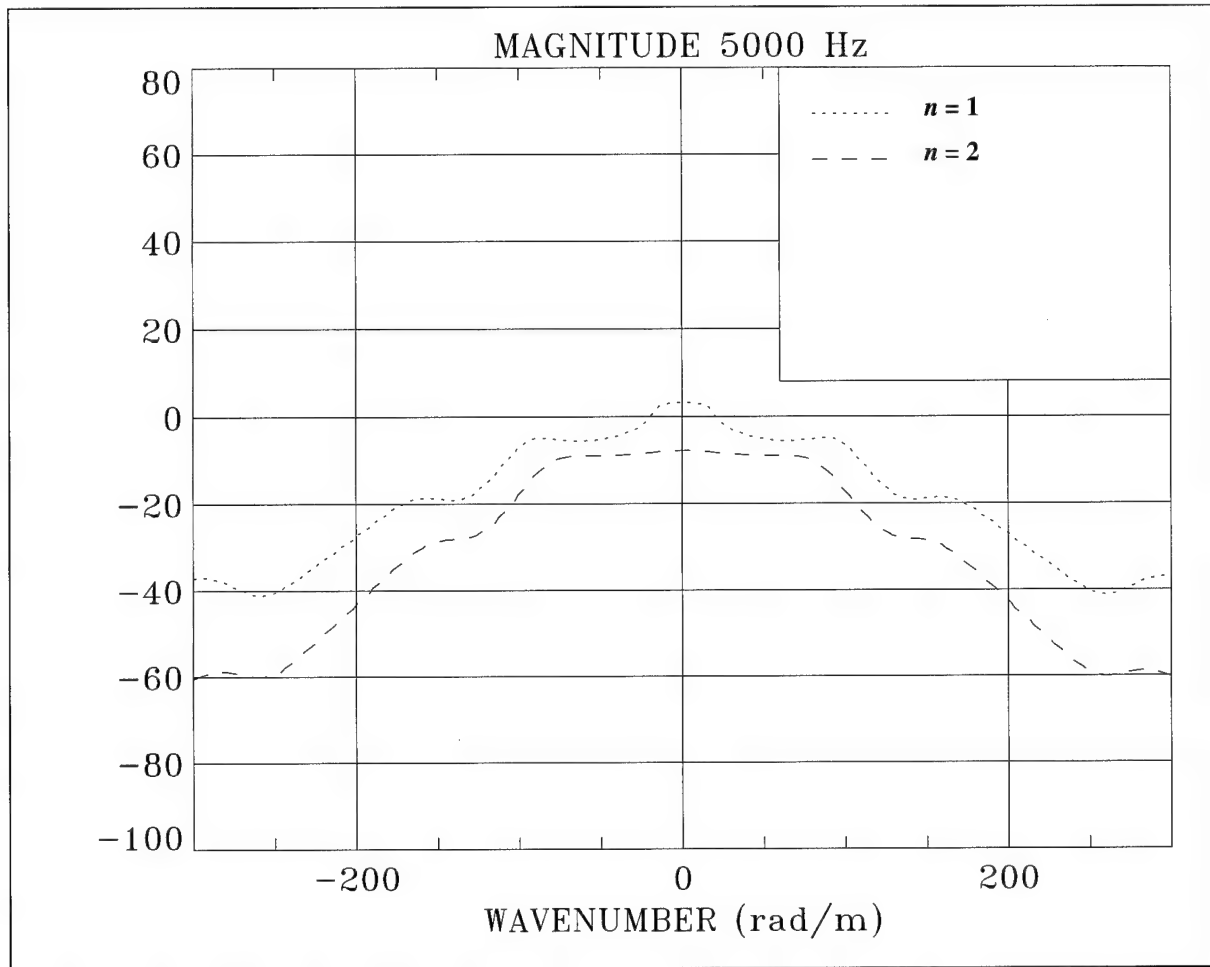


Figure 137. Comparison of Circumferential Shear Stress Excitation for Figures 130 and 132 When Magnitude = $10\text{Log}(P_i(r_1)/P_\theta)^2$ at $r_1 = 0.75$ in. for Various n With Diameter = 3.00 in. and $f = 5000$ Hz

TWO-LAYER CYLINDER SIMULATIONS

Thus far we have considered simulations of a cylinder composed of a single homogeneous layer of material in contact with fluids on the inner and outer surfaces. In this section, we will employ the full model developed in this report for the two-layer cylinder with fluids. The system matrix is given by equation (150), with elements given by equations (151) through (319). Material properties and dimensions for the two-layer cylinder are shown in table 16. The first or inner cylinder has material properties similar to hard plastic, such as polycarbonate. The outer cylinder (cylinder 2) has material properties similar to those of urethane or the rubber used for automobile tires. The inner fluid properties are consistent with air and are listed in table 17. The outer fluid material properties are those of water and are given in table 18.

Table 16. Two-Layer-Cylinder Properties—0.650-in. Diameter

Cylinder #1 Property	Cylinder #2 Property	Definition
$E_1 = 2.4 \times 10^9 \frac{\text{N}}{\text{m}^2}$	$E_2 = 1.5 \times 10^7 \frac{\text{N}}{\text{m}^2}$	Young's Modulus
$\zeta_1 = 0.14$	$\zeta_2 = 0.20$	Structural Loss Factor
$\rho_1 = 2113 \frac{\text{kg}}{\text{m}^3}$	$\rho_2 = 1000 \frac{\text{kg}}{\text{m}^3}$	Density
$\nu_1 = 0.40$	$\nu_2 = 0.45$	Poisson's Ratio
$a = 0.160 \text{ in.}$	$b = 0.260 \text{ in.}$	Inner Radius
$b = 0.260 \text{ in.}$	$c = 0.325 \text{ in.}$	Outer Radius
$h_1 = 0.100 \text{ in.}$	$h_2 = 0.065 \text{ in.}$	Thickness

The model under consideration is composed of four distinct layers. The simulations will contain contributions of wave propagation and interaction from each of the four layers. The resulting composite system will produce branches of wave propagation that are related to the

dilatational and transverse waves of the media but do not necessarily propagate at the same velocity. The velocities listed in table 19 will serve as a guide for analyzing the responses that follow. The simulations for the two-layer cylinder will be displayed as color images using the red/yellow/green/blue color map as opposed to the red temperature color map that was previously used for the single-layer cylinder.

Table 17. Two-Layer-Cylinder Inner Fluid Properties (Air)

Property	Definition
$\rho_i = 1.20 \frac{\text{kg}}{\text{m}^3}$	Density
$c_i = 343.0 \frac{\text{m}}{\text{sec}}$	Velocity of Sound

Table 18. Two-Layer-Cylinder Outer Fluid Properties (Water)

Property	Definition
$\rho_s = 1000.0 \frac{\text{kg}}{\text{m}^3}$	Density
$c_s = 1500.0 \frac{\text{m}}{\text{sec}}$	Velocity of Sound

Table 19. Two-Layer-Cylinder/Fluid Phase Velocities

	Inner Fluid Phase Velocity (m/sec)	Cylinder #1 Phase Velocity (m/sec)	Cylinder #2 Phase Velocity (m/sec)	Outer Fluid Phase Velocity (m/sec)
c_l	—	1,560.0	238.5	—
c_t	—	636.9	71.9	—
c_e	—	1,065.8	122.5	—
c_i	343.0	—	—	—
c_s	—	—	—	1,500.0

Radial Pressure Excitation

The first series of simulations are for a radial pressure excitation applied to the outer surface of the cylinder, as shown in figure 1. The circumferential strain is the quantity calculated just below the outer surface at $r_1 = 0.324$ inch, and it is displayed as a color image using the red/yellow/green/blue color map in figure 138 and as a wire frame surface in figure 139. Comparison of the amplitude in frequency is made in figure 140.

The first radial resonance frequency occurs at 6210 Hz for this system. The P-wave in the inner fluid is faintly visible as a series of dots at a phase velocity of 343 m/sec in figure 138. This wave is unaffected by the structure, which is consistent with the previous observation of what occurred when air was used as the fluid with the single-layer cylinder. The P-wave of the outer fluid experiences dispersion due to interaction with the cylinder above the radial resonance frequency. The other major branch of wave propagation evident in the simulation is an extensional wave for the composite cylinder. The phase velocity of this wave is shown in table 20; its value falls between those listed in table 19 for the individual layers.

Table 20. Extensional Wave Phase Velocity From Figure 138

Frequency (Hz)	Phase Velocity (m/sec)
1,000	800
2,000	800
3,000	800
4,000	800
5,000	800
6,000	800
7,000	700
7,500	663
7,800	610

Figures 141 through 143 are simulations of the circumferential strain at $r_1 = 0.259$ inch, which is just below the outer radius of the inner cylinder. The effect of the inner fluid P-wave on the strain field is captured in the 6000-Hz curve in figure 143 (note the small bump at approximately 100 rad/m). This P-wave produces a very narrow spike in wavenumber. The wavenumber interval chosen for the simulations is not small enough to capture the P-wave continuously, which is why it appears as a series of dots in the color images. Decreasing the wavenumber interval would lead to a corresponding increase in calculation time and was not considered important enough for the purposes of this report.

The circumferential strain field is evaluated at $r_1 = 0.250$ inch (which is within the confines of the thickness of the inner cylinder), as shown in figures 144 through 146. In figures 147 through 149, the circumferential strain field is evaluated at $r_1 = 0.161$ inch, which is just inside the inner radius of the inner cylinder. Comparison at $k = 0$ is made in figure 150 for the four radial locations previously mentioned, and the radial resonance can be clearly observed in all the curves. Figures 151 through 154 are comparisons at various frequencies for each of the four radial locations. Although the extensional wave in the cylinder and the P-wave in the outer fluid have been labeled only once in figures 153 and 154 (at $r_1 = 0.32$ inch) to prevent cluttering of the plots, they can also be seen at the radial locations shown on the other curves. The P-wave in the inner fluid is evident in figure 153. This wave produces a narrow spike in wavenumber, which was not captured by the calculation in the negative wavenumber region because the algorithms do not necessarily evaluate the equations at precisely the same wavenumber on both sides of zero.

The attenuation of circumferential strain sensitivity is displayed in figure 155. The magnitude plotted in this figure is the difference in level between $r_1 = 0.259$ inch and $r_1 = 0.324$ inch. The curves indicate the wavenumber-filtering property of the structure due to normal pressure excitation from just beneath the outer radius of the outer cylinder to just beneath the outer radius of the inner cylinder.

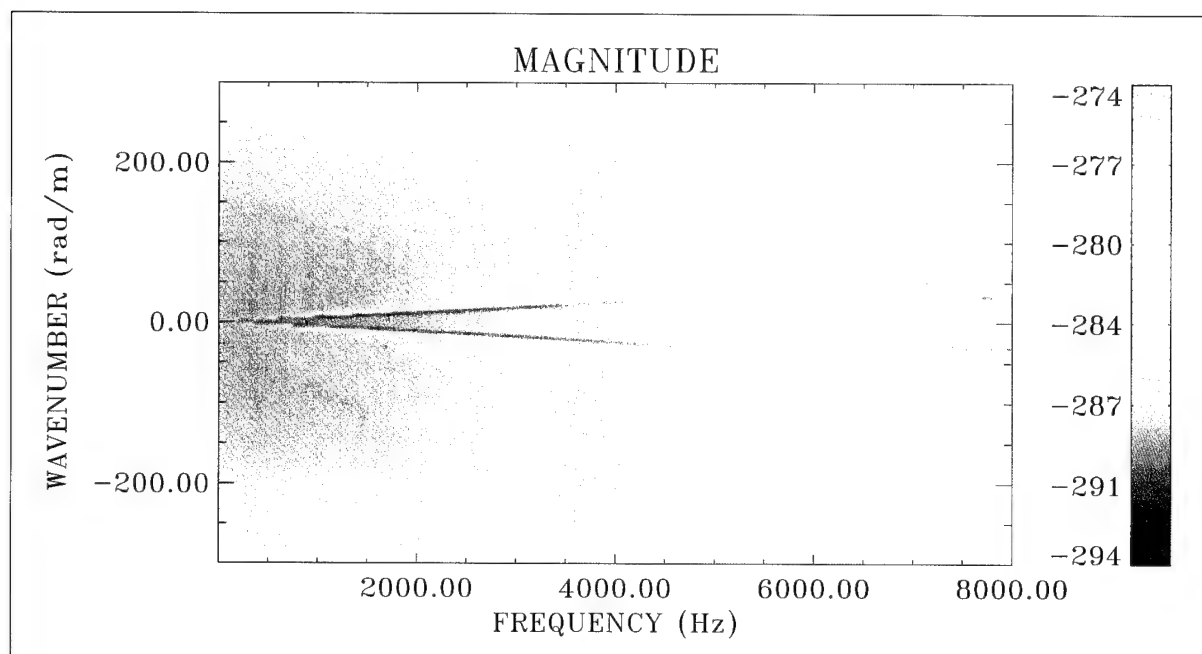


Figure 138. Circumferential Strain Transfer Surface With
Magnitude = $10\text{Log}(\epsilon_{\theta\theta}^{C2}(r_1)/P_o)^2$ at $r_1 = 0.324$ in. With $n = 0$ and
Diameter = 0.650 in. (Color Image)

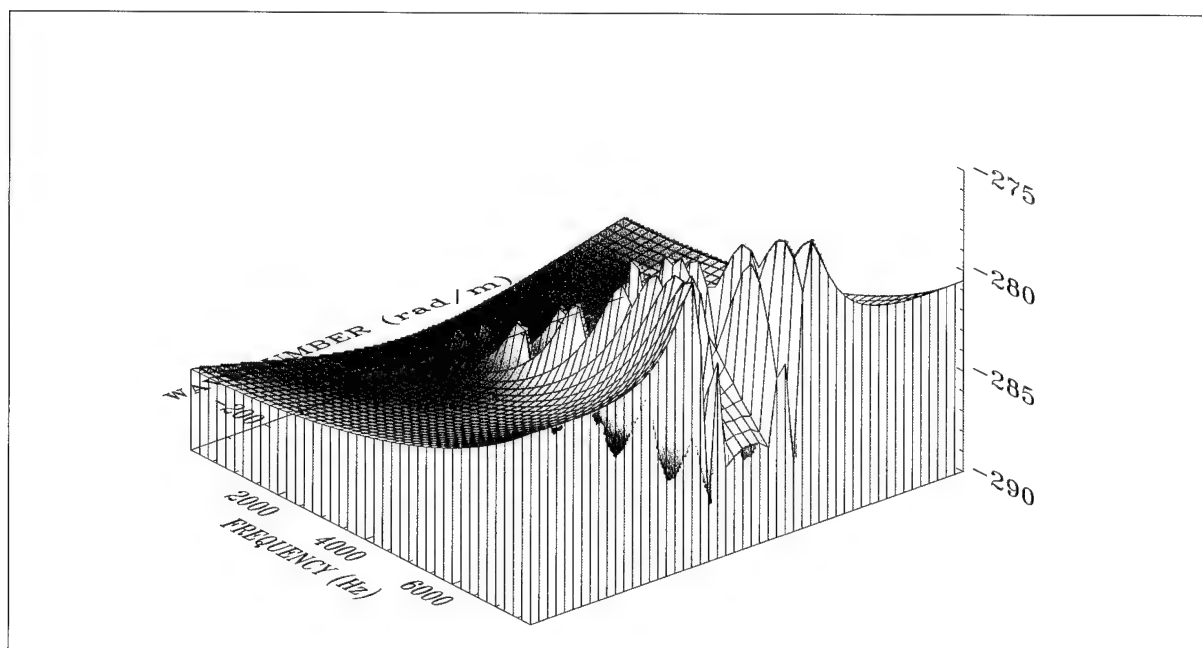


Figure 139. Circumferential Strain Transfer Surface With
Magnitude = $10\text{Log}(\epsilon_{\theta\theta}^{C2}(r_1)/P_o)^2$ at $r_1 = 0.324$ in. With $n = 0$ and
Diameter = 0.650 in. (Wire Frame Surface)

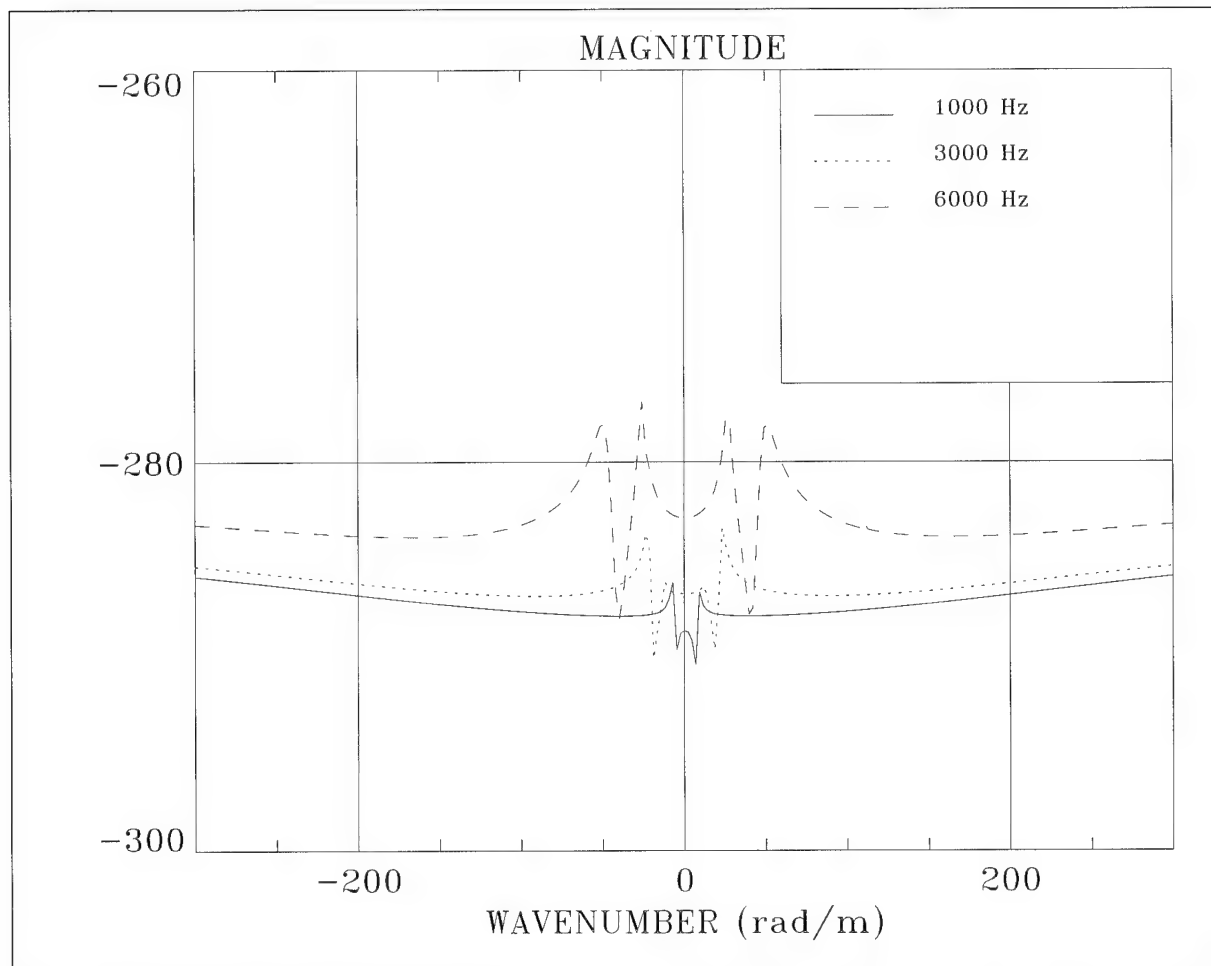


Figure 140. Comparison of Circumferential Strain Distribution for Figure 138
 When Magnitude = $10\text{Log}(\epsilon_{\theta\theta}^{C^2}(r_1)/P_o)^2$ at $r_1 = 0.324$ in. With $n = 0$ and Diameter = 0.650 in.

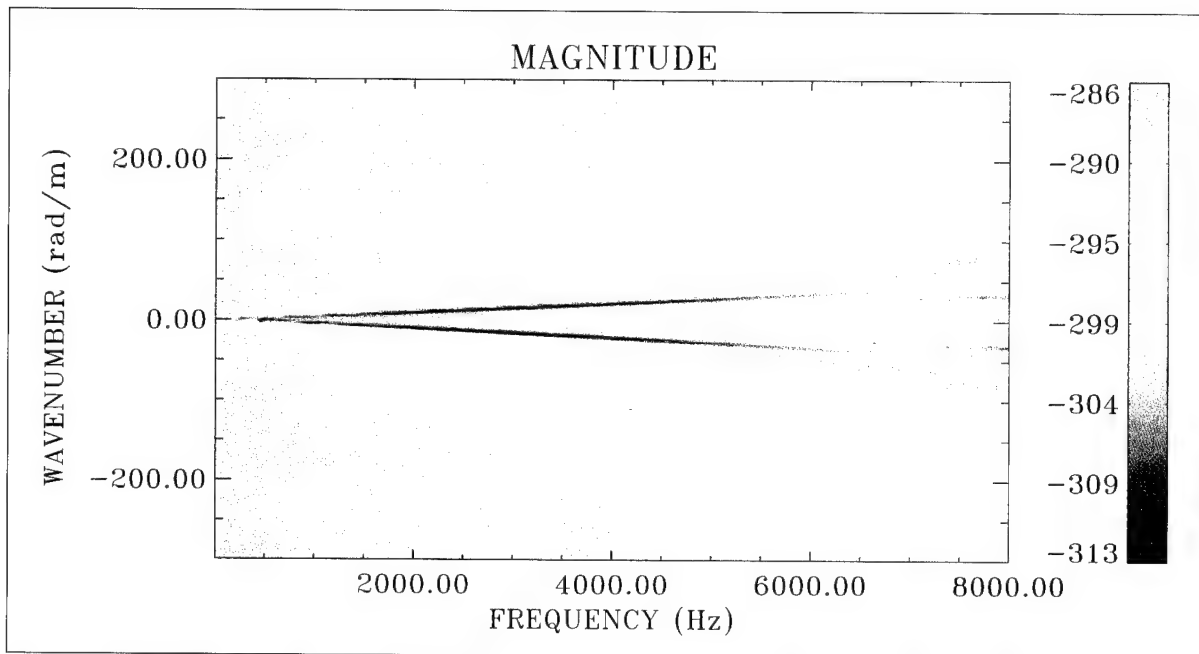


Figure 141. Circumferential Strain Transfer Surface With
Magnitude = $10\text{Log}(\epsilon_{\theta\theta}^{C1}(r_1)/P_o)^2$ at $r_1 = 0.259$ in. With $n = 0$ and
Diameter = 0.650 in. (Color Image)

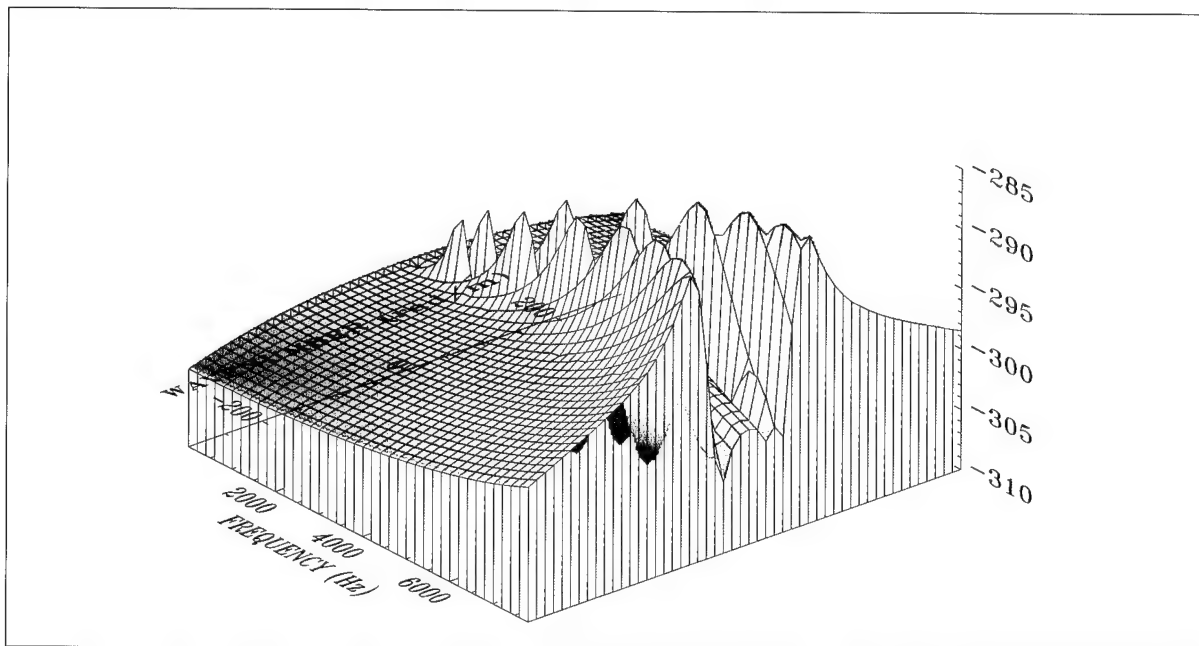


Figure 142. Circumferential Strain Transfer Surface With
Magnitude = $10\text{Log}(\epsilon_{\theta\theta}^{C1}(r_1)/P_o)^2$ at $r_1 = 0.259$ in. With $n = 0$ and
Diameter = 0.650 in. (Wire Frame Surface)

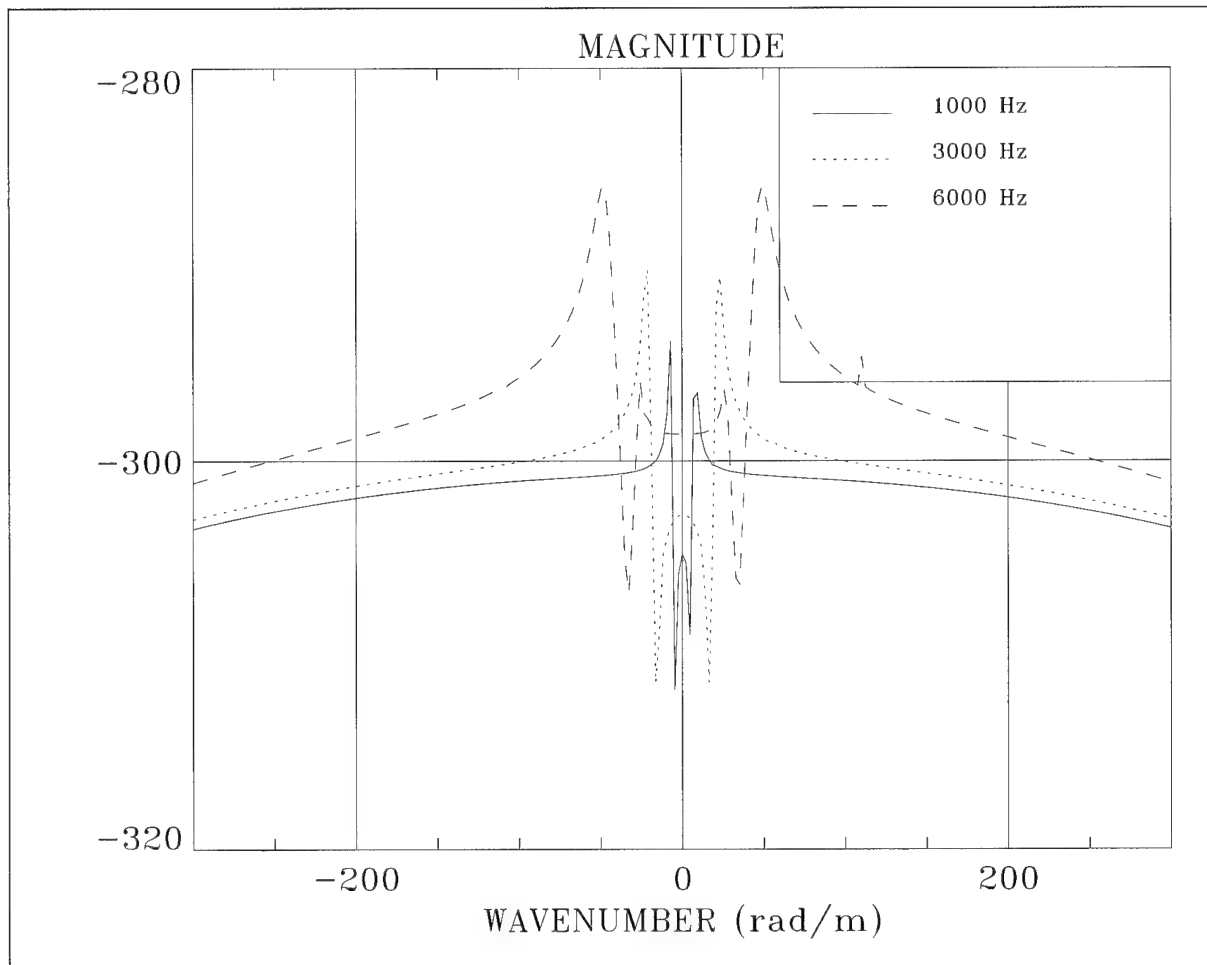


Figure 143. Comparison of Circumferential Strain Distribution for Figure 141
When Magnitude = $10\text{Log}(\epsilon_{\theta\theta}^{C1}(r_1)/P_o)^2$ at $r_1 = 0.259$ in. With $n = 0$ and Diameter = 0.650 in.

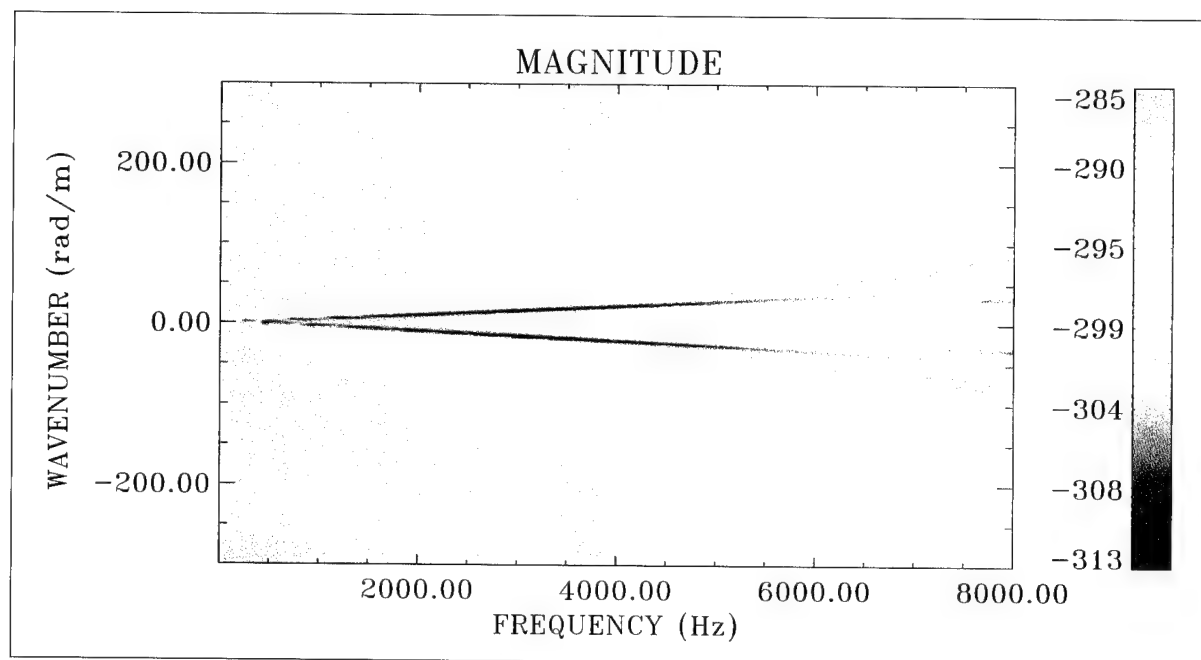


Figure 144. Circumferential Strain Transfer Surface With Magnitude = $10\text{Log}(\epsilon_{\theta\theta}^{C1}(r_1)/P_o)^2$ at $r_1 = 0.250$ in. With $n = 0$ and Diameter = 0.650 in. (Color Image)

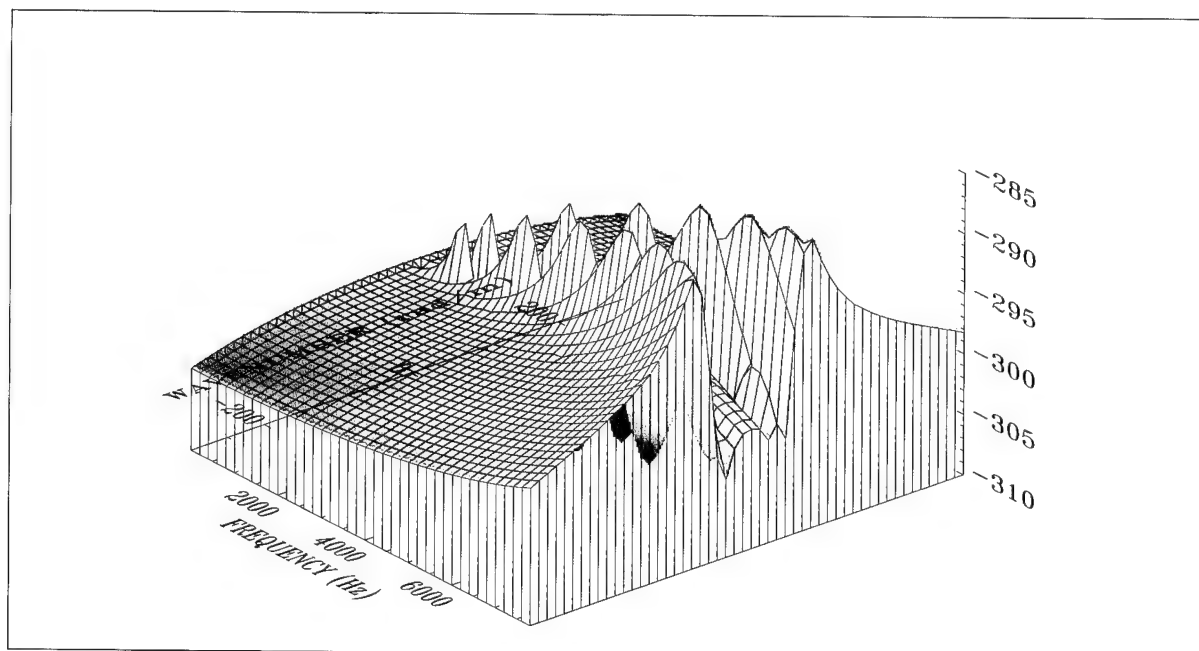


Figure 145. Circumferential Strain Transfer Surface With Magnitude = $10\text{Log}(\epsilon_{\theta\theta}^{C1}(r_1)/P_o)^2$ at $r_1 = 0.250$ in. With $n = 0$ and Diameter = 0.650 in. (Wire Frame Surface)

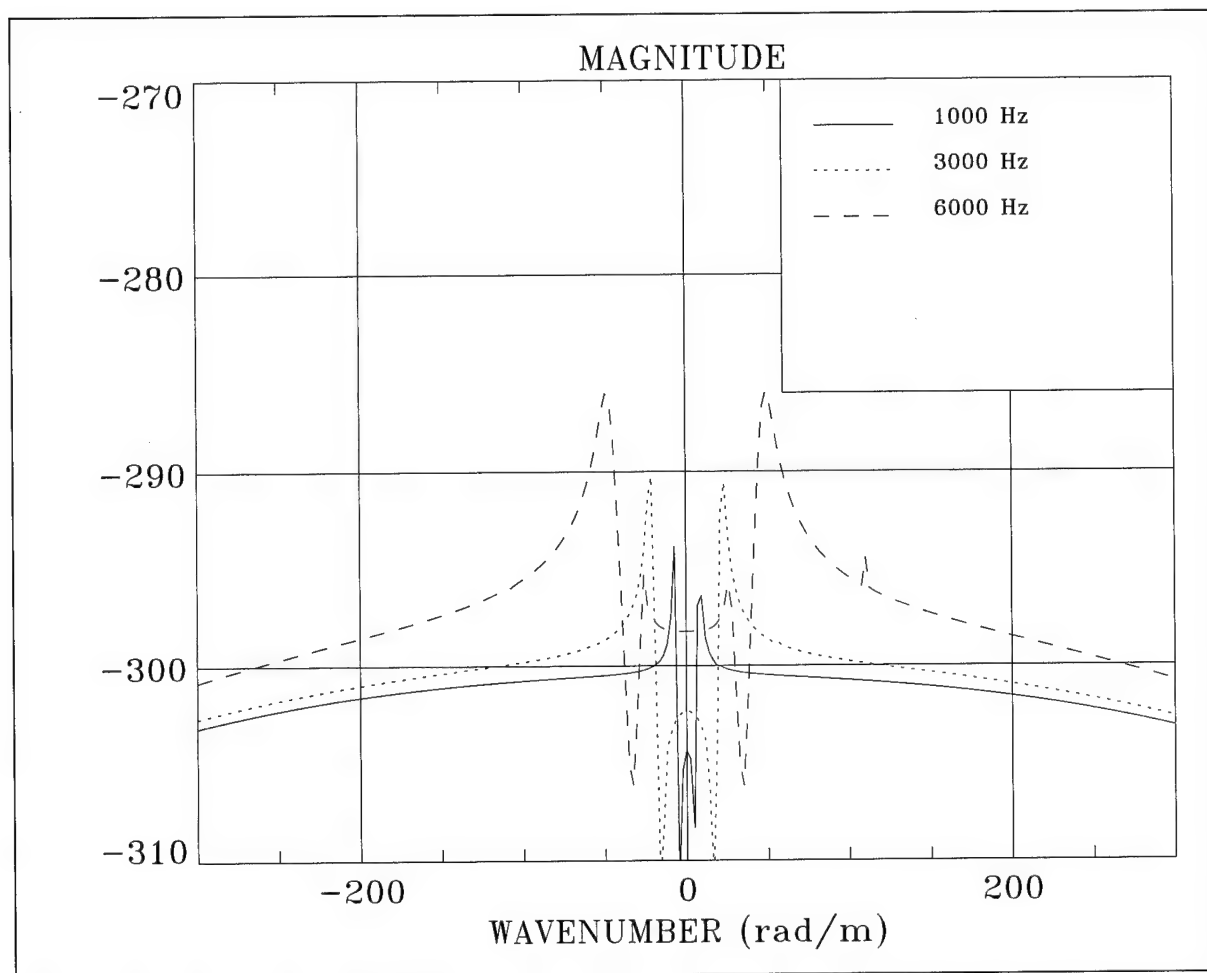


Figure 146. Comparison of Circumferential Strain Distribution for Figure 144
When Magnitude = $10\text{Log}(\epsilon_{\theta\theta}^{C1}(r_1)/P_o)^2$ at $r_1 = 0.250$ in. With $n = 0$ and Diameter = 0.650 in.

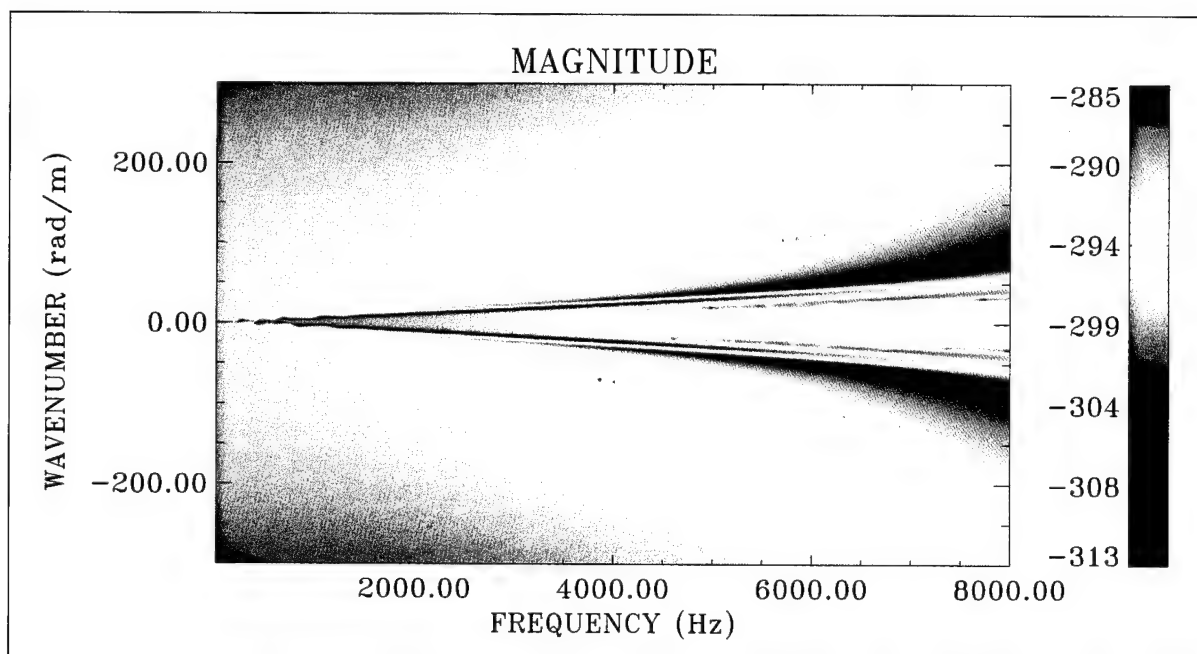


Figure 147. Circumferential Strain Transfer Surface With Magnitude = $10\text{Log}(\epsilon_{\theta\theta}^{C1}(r_1)/P_o)^2$ at $r_1 = 0.161$ in. With $n = 0$ and Diameter = 0.650 in. (Color Image)

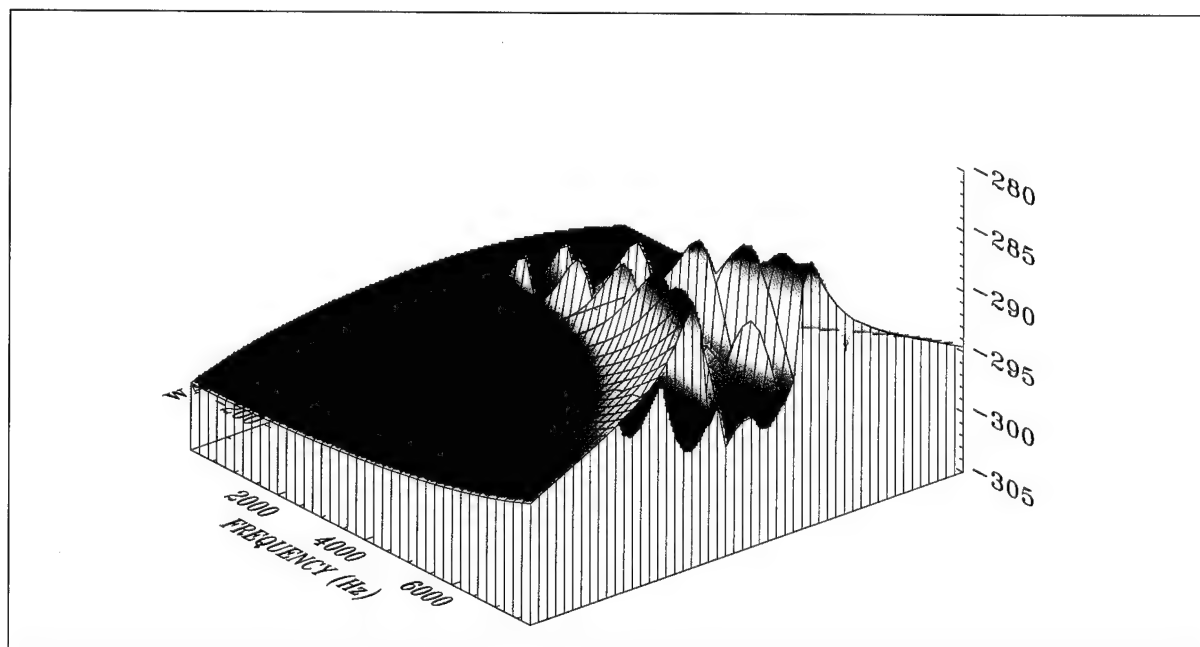


Figure 148. Circumferential Strain Transfer Surface With Magnitude = $10\text{Log}(\epsilon_{\theta\theta}^{C1}(r_1)/P_o)^2$ at $r_1 = 0.161$ in. With $n = 0$ and Diameter = 0.650 in. (Wire Frame Surface)

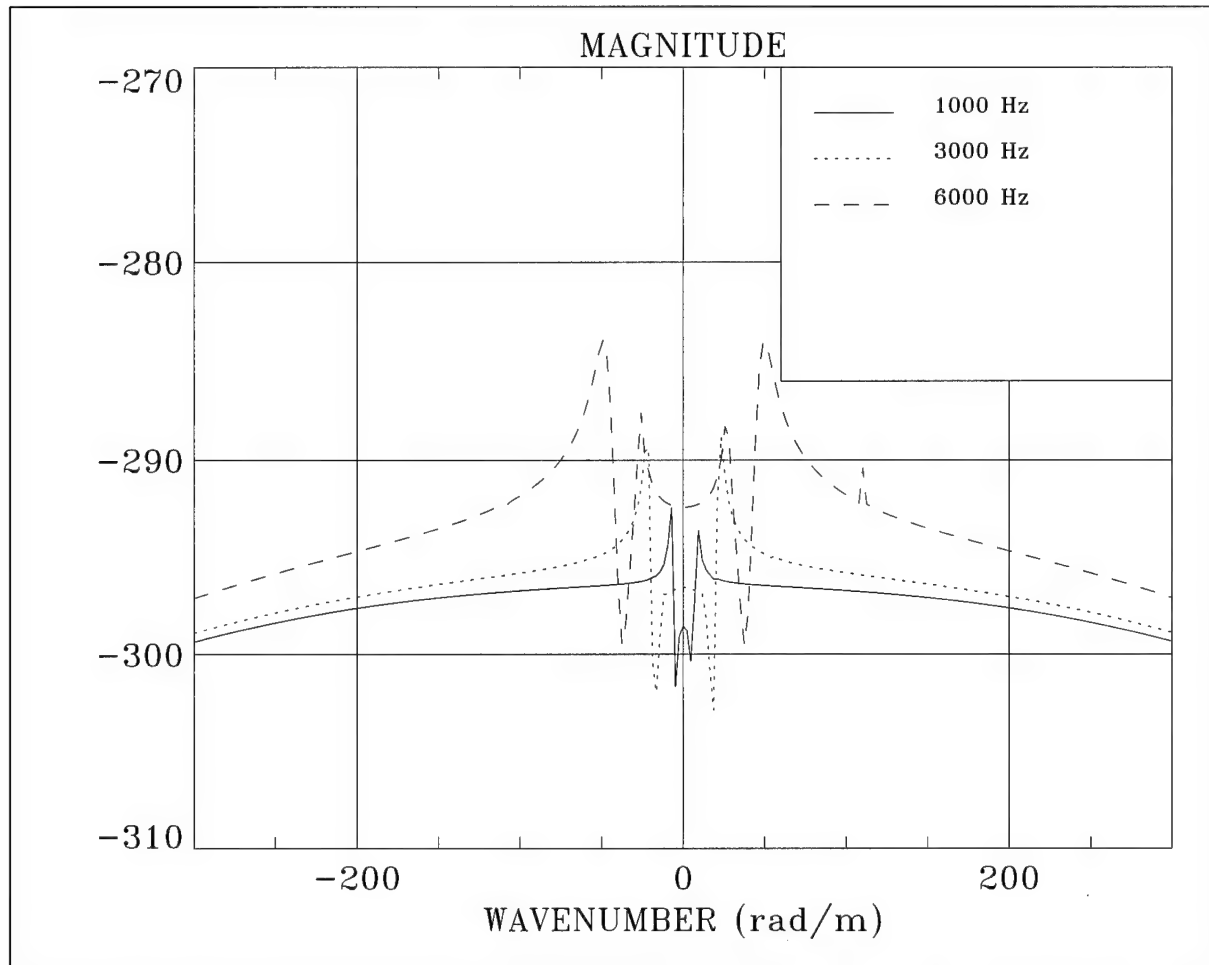


Figure 149. Comparison of Circumferential Strain Distribution for Figure 147
When Magnitude = $10\text{Log}(\epsilon_{\theta\theta}^{C1}(r_1)/P_o)^2$ at $r_1 = 0.161$ in. With $n = 0$ and Diameter = 0.650 in.

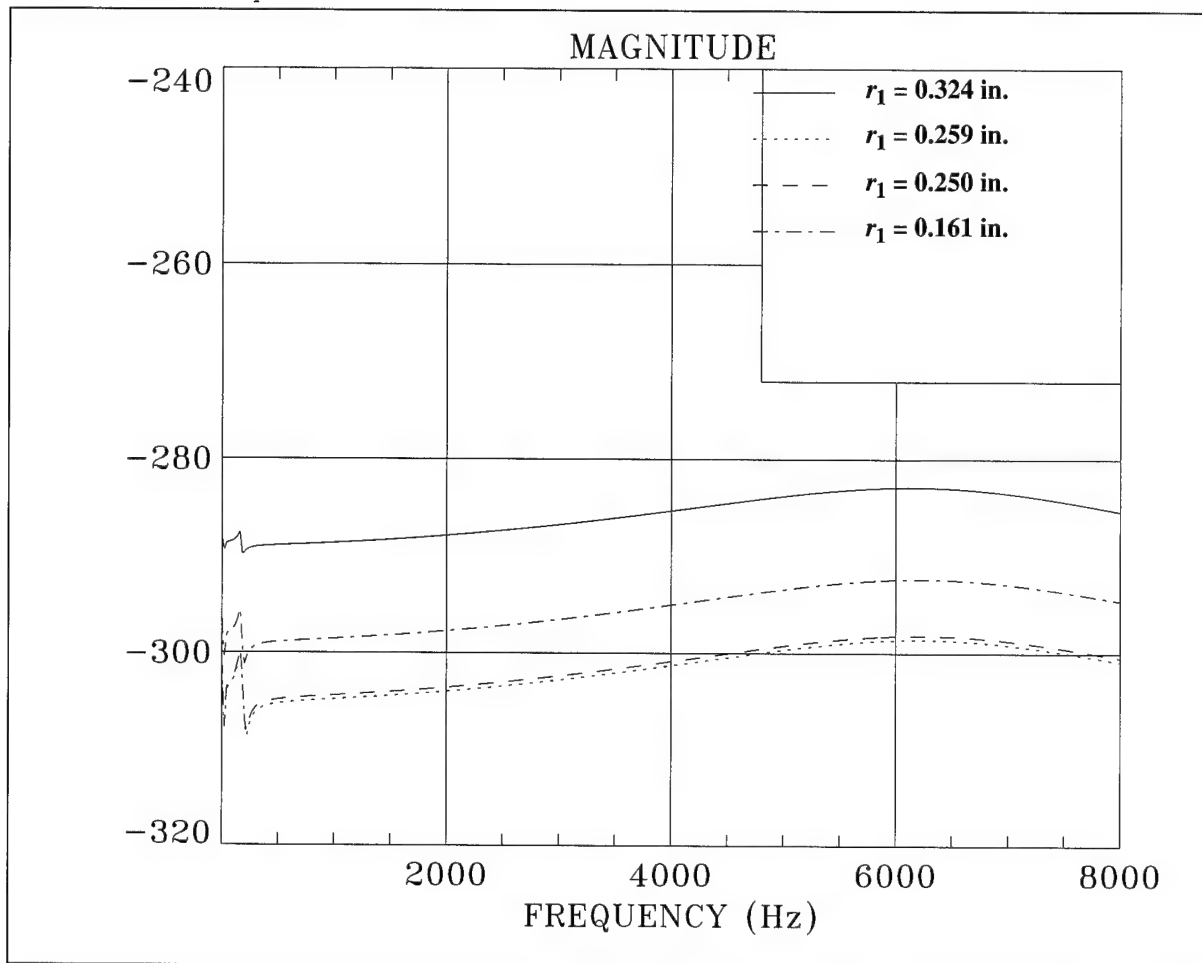


Figure 150. Comparison of Circumferential Strain Distribution for Figures 138, 141, 144, and 147 When Magnitude = $10\text{Log}(\varepsilon_{\theta\theta}^{Ci}(r_1)/P_o)^2$ at Various r_1 With $i = 1$ or 2 , $n = 0$, Diameter = 0.650 in., and $k = 0$ rad/m

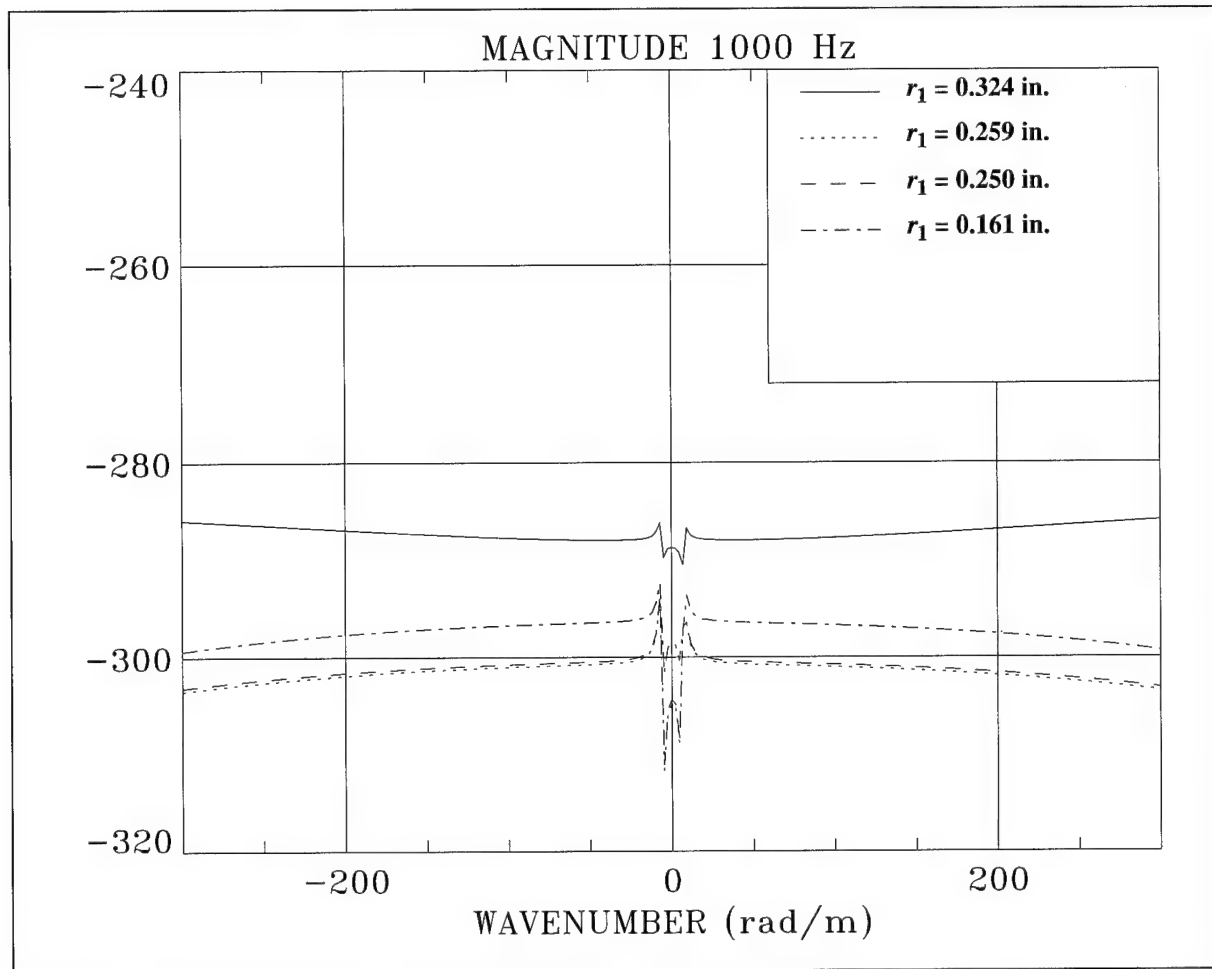


Figure 151. Comparison of Circumferential Strain Distribution for Figures 138, 141, 144, and 147 When Magnitude = $10\text{Log}(\epsilon_{\theta\theta}^{Ci}(r_1)/P_o)^2$ at Various r_1 With $i = 1$ or 2 , $n = 0$, Diameter = 0.650 in., and $f = 1000$ Hz

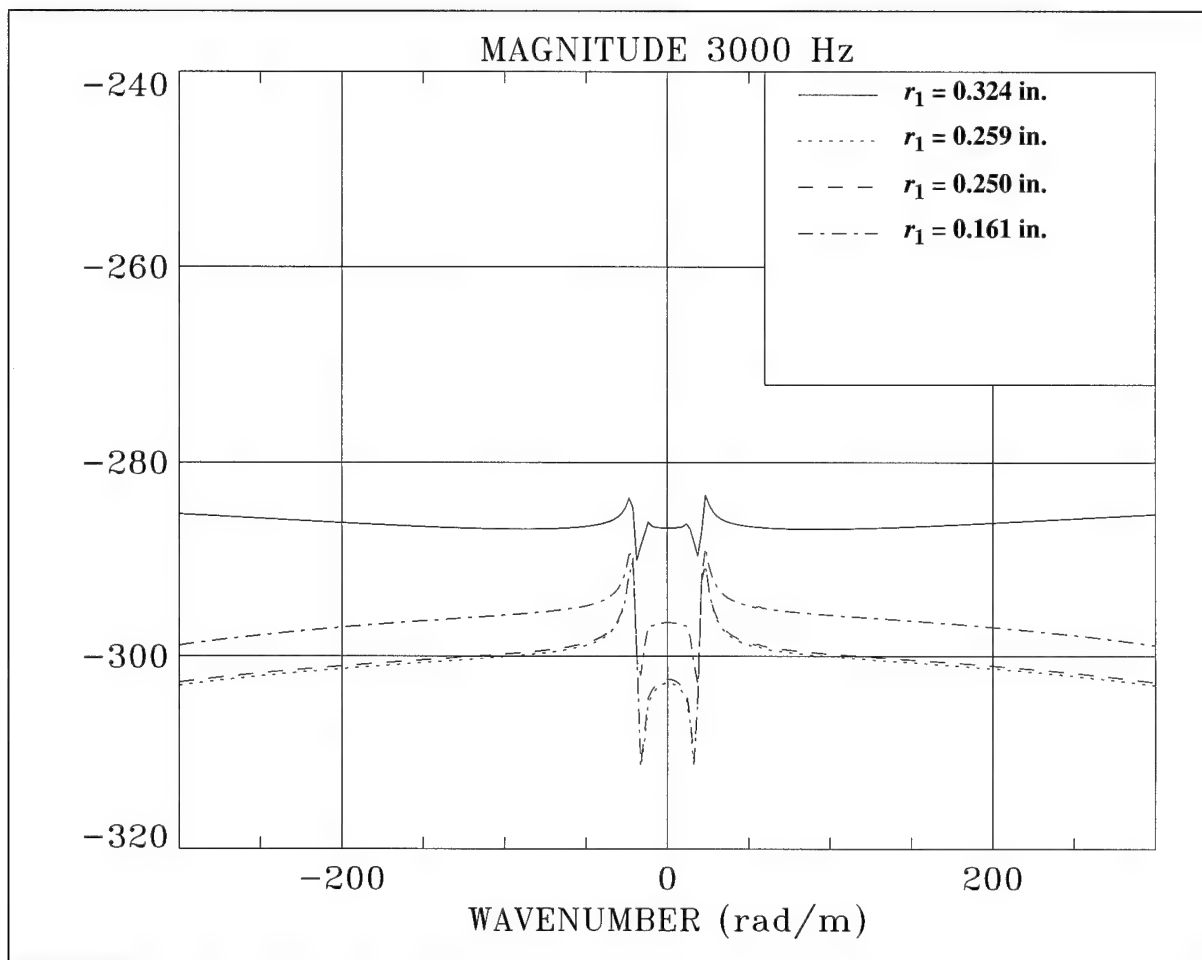


Figure 152. Comparison of Circumferential Strain Distribution for Figures 138, 141, 144, and 147 When Magnitude = $10\text{Log}(\epsilon_{\theta\theta}^{Ci}(r_1)/P_o)^2$ at Various r_1 With $i = 1$ or 2 , $n = 0$, Diameter = 0.650 in., and $f = 3000$ Hz

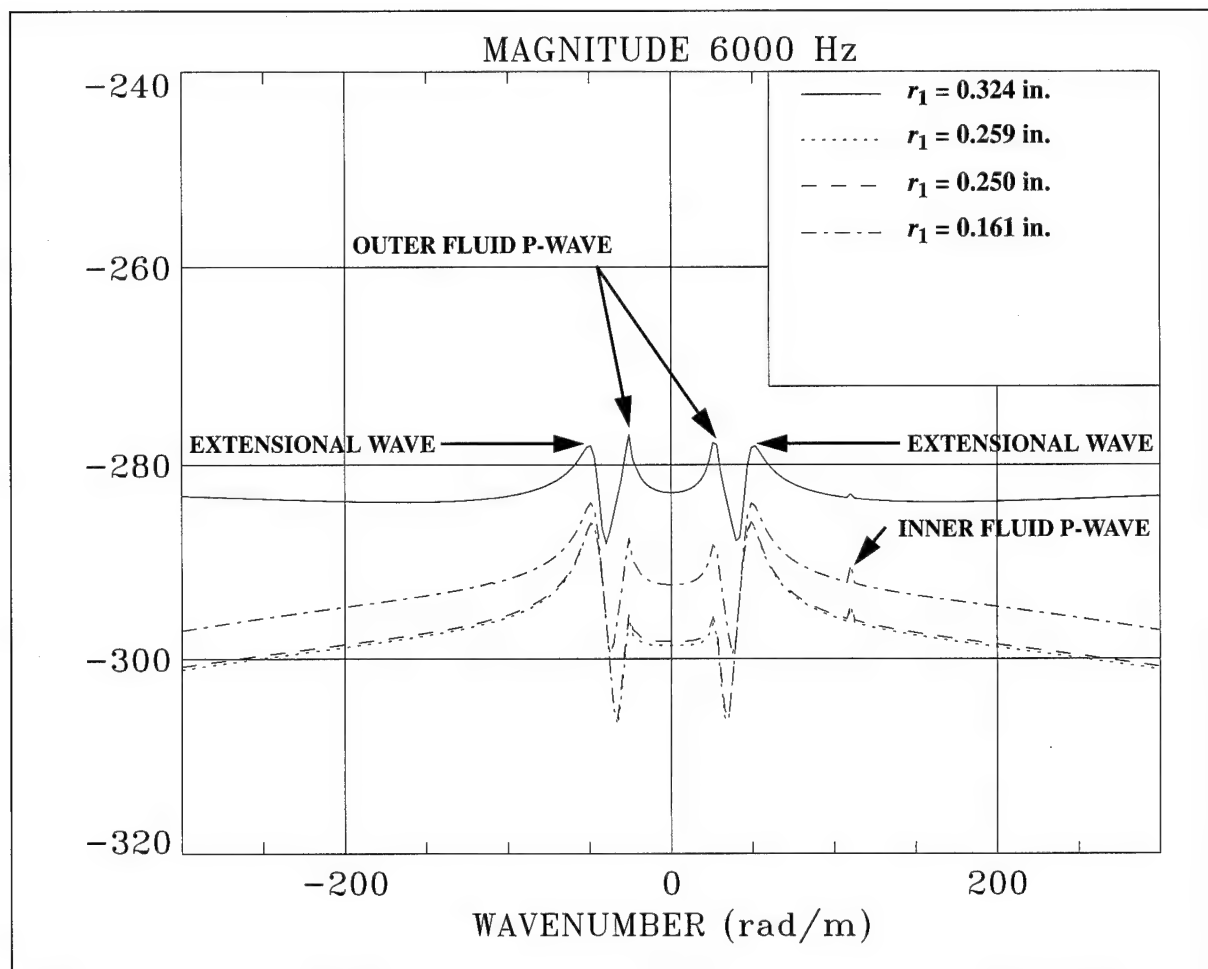


Figure 153. Comparison of Circumferential Strain Distribution for Figures 138, 141, 144, and 147 When Magnitude = $10\text{Log}(\epsilon_{\theta\theta}^{Ci}(r_1)/P_o)^2$ at Various r_1 With $i = 1$ or 2 , $n = 0$, Diameter = 0.650 in., and $f = 6000$ Hz

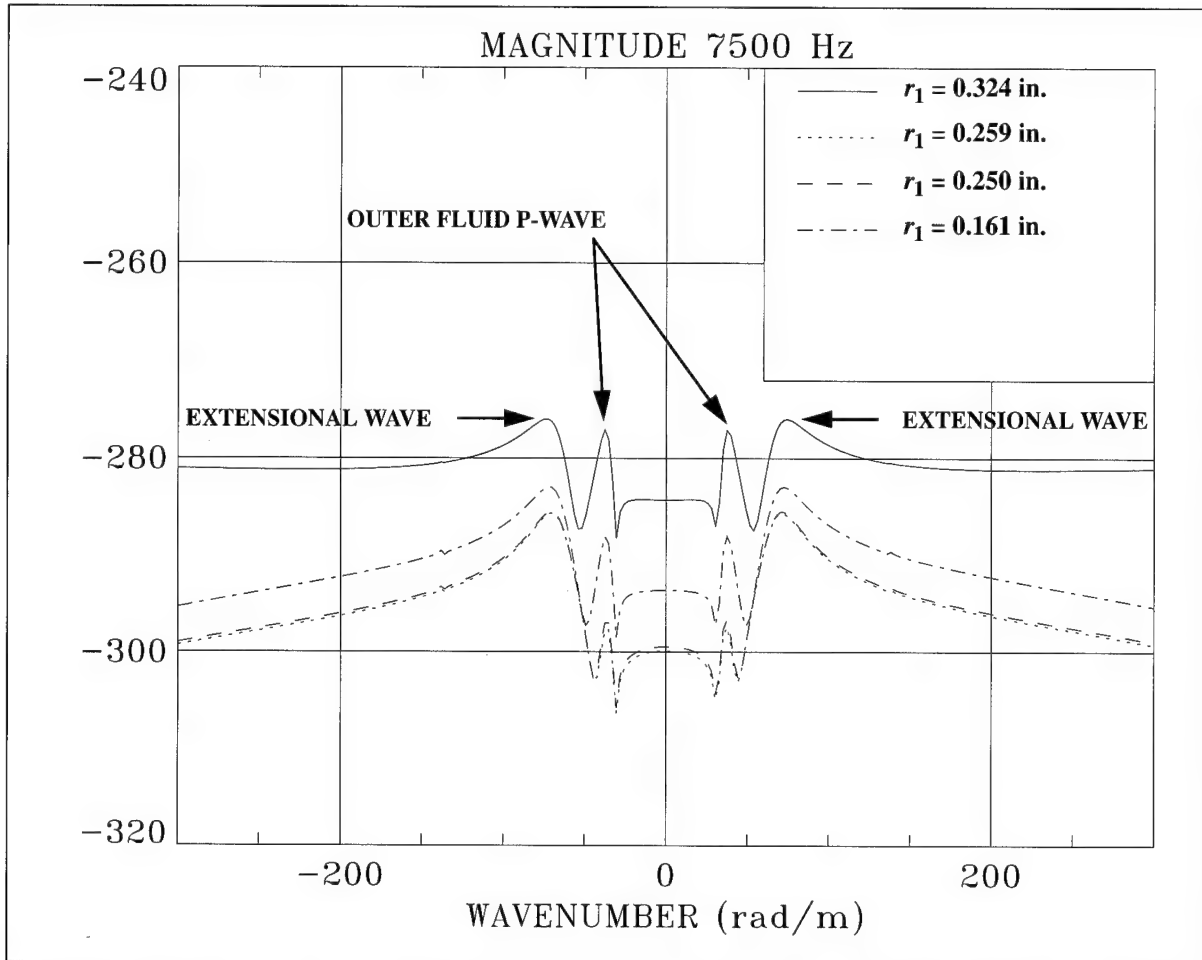
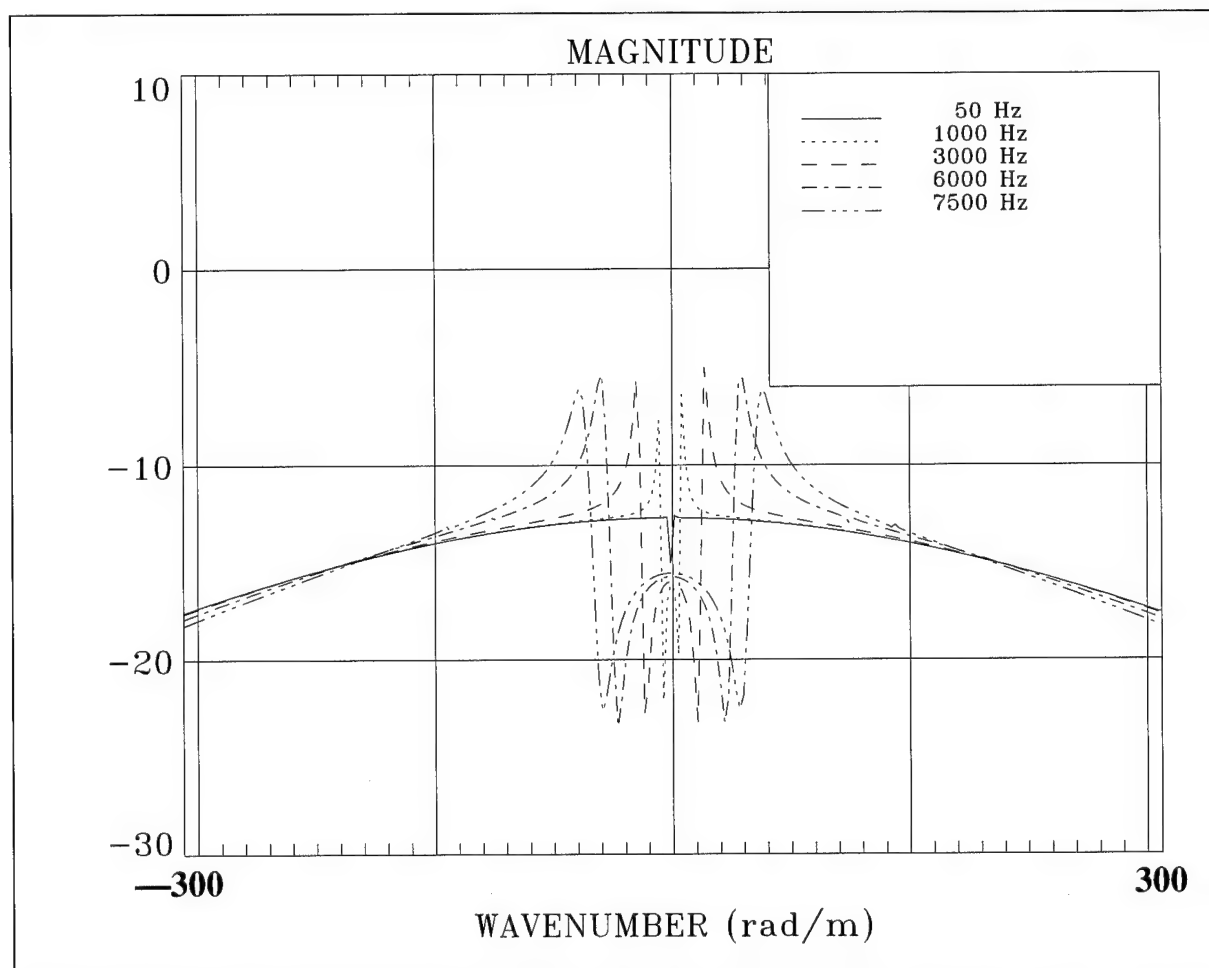


Figure 154. Comparison of Circumferential Strain Distribution for Figures 138, 141, 144, and 147 When Magnitude = $10\text{Log}(\epsilon_{\theta\theta}^{Ci}(r_1)/P_o)^2$ at Various r_1 With $i = 1$ or 2 , $n = 0$, Diameter = 0.650 in., and $f = 7500$ Hz



**Figure 155. Attenuation of Circumferential Strain From Figures 138 and 141
When Magnitude = $(10\text{Log}(\epsilon_{\theta\theta}^{C1}(0.259)/P_o)^2 - 10\text{Log}(\epsilon_{\theta\theta}^{C2}(0.324)/P_o)^2)$ at Various f
With $n = 0$ and Diameter = 0.650 in.**

Longitudinal and Radial Displacements. The longitudinal and radial displacements that correspond to the location $r_1 = 0.259$ inch (as discussed in the previous section) are now calculated. The simulation for longitudinal displacement is shown in figures 156 and 157; the simulation for radial displacement is presented in figures 158 and 159. Comparisons of these two surfaces are made at selected frequencies in figures 160 through 163.

At 1000 Hz in figure 160 and 3000 Hz in figure 161, the extensional wave is the major branch of wave propagation. Moving up to 6000 Hz in figure 162 and 7500 Hz in figure 163, the inner and outer fluid P-waves become evident. Because the wavenumber increment used for the simulation is larger than the width in wavenumber of the inner fluid P-wave resonance, the inner fluid P-wave shows up intermittently in the simulations.

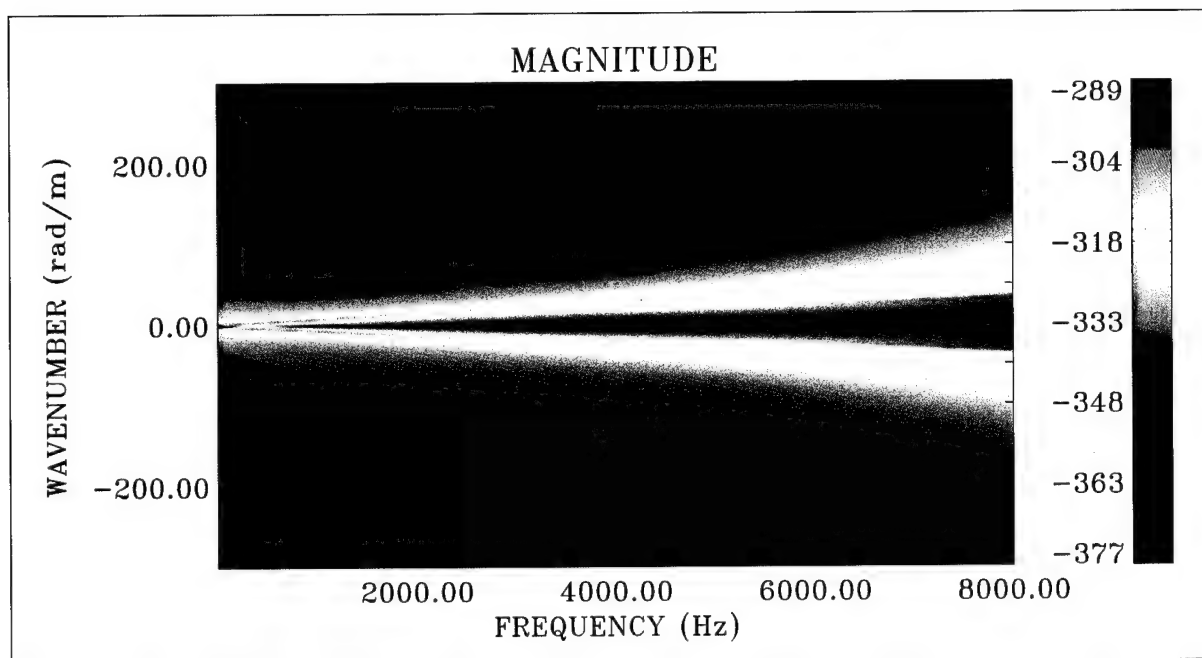


Figure 156. Longitudinal Displacement Transfer Surface With Magnitude = $10\text{Log}(w_c^{C1}(r_1)/P_o)^2$ at $r_1 = 0.259$ in. With $n = 0$ and Diameter = 0.650 in. (Color Image)

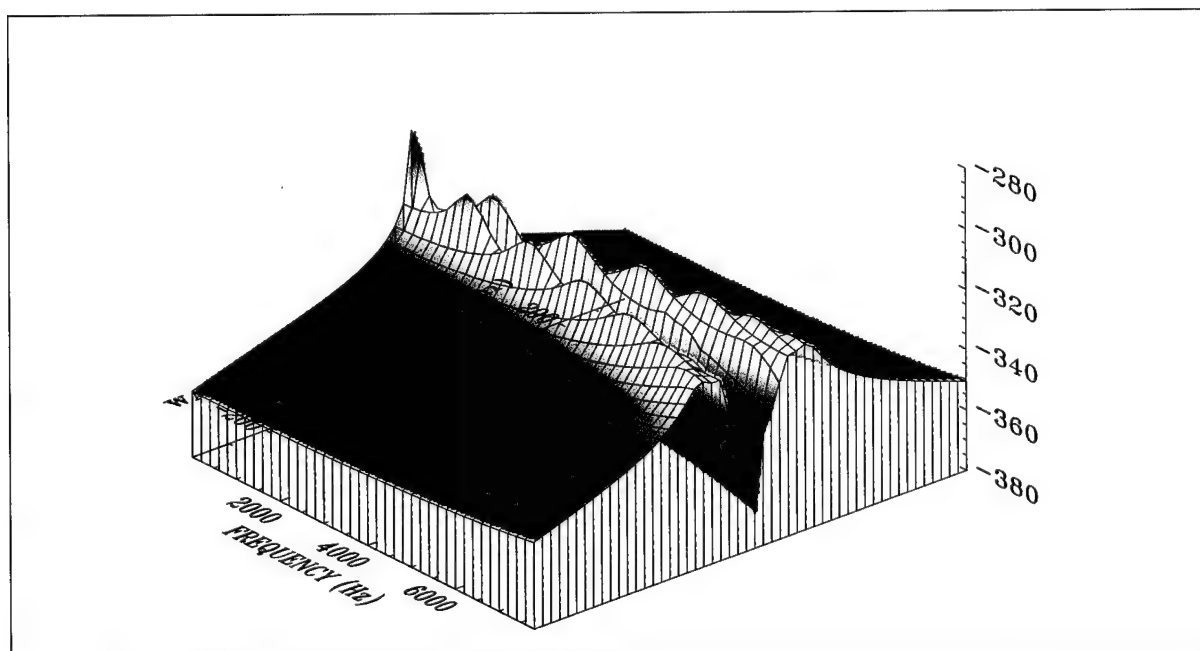


Figure 157. Longitudinal Displacement Transfer Surface With Magnitude = $10\text{Log}(w_c^{C1}(r_1)/P_o)^2$ at $r_1 = 0.259$ in. With $n = 0$ and Diameter = 0.650 in. (Wire Frame Surface)

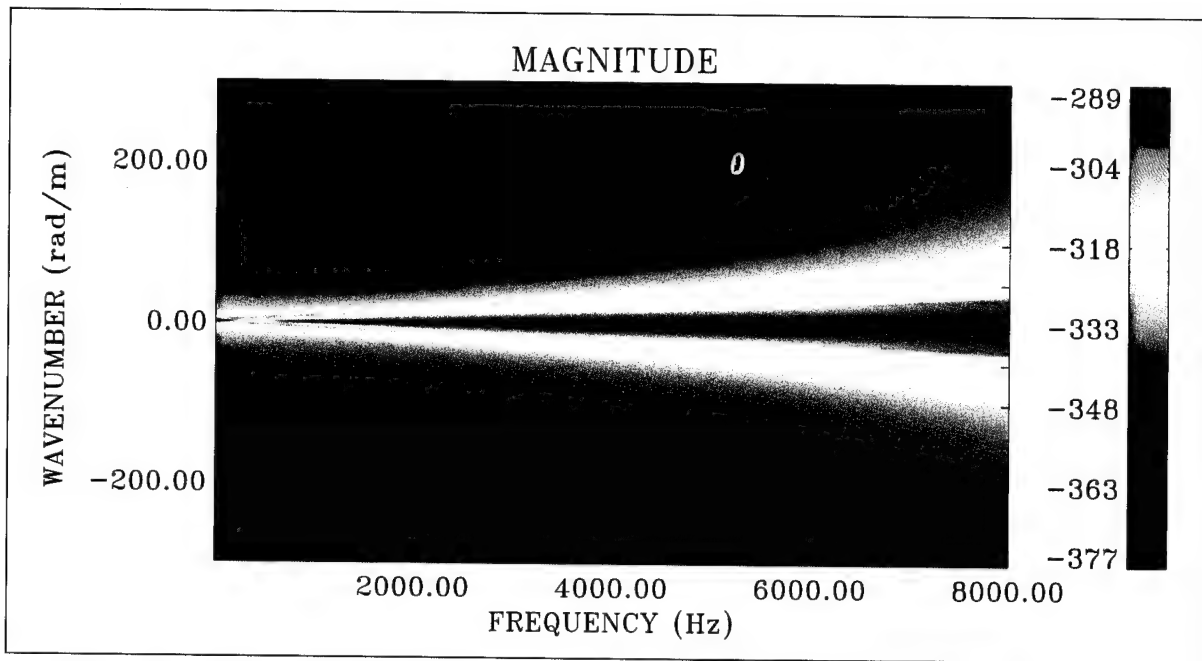


Figure 158. Radial Displacement Transfer Surface With Magnitude = $10\text{Log}(u_c^{C1}(r_1)/P_o)^2$ at $r_1 = 0.259$ in. With $n = 0$ and Diameter = 0.650 in. (Color Image)

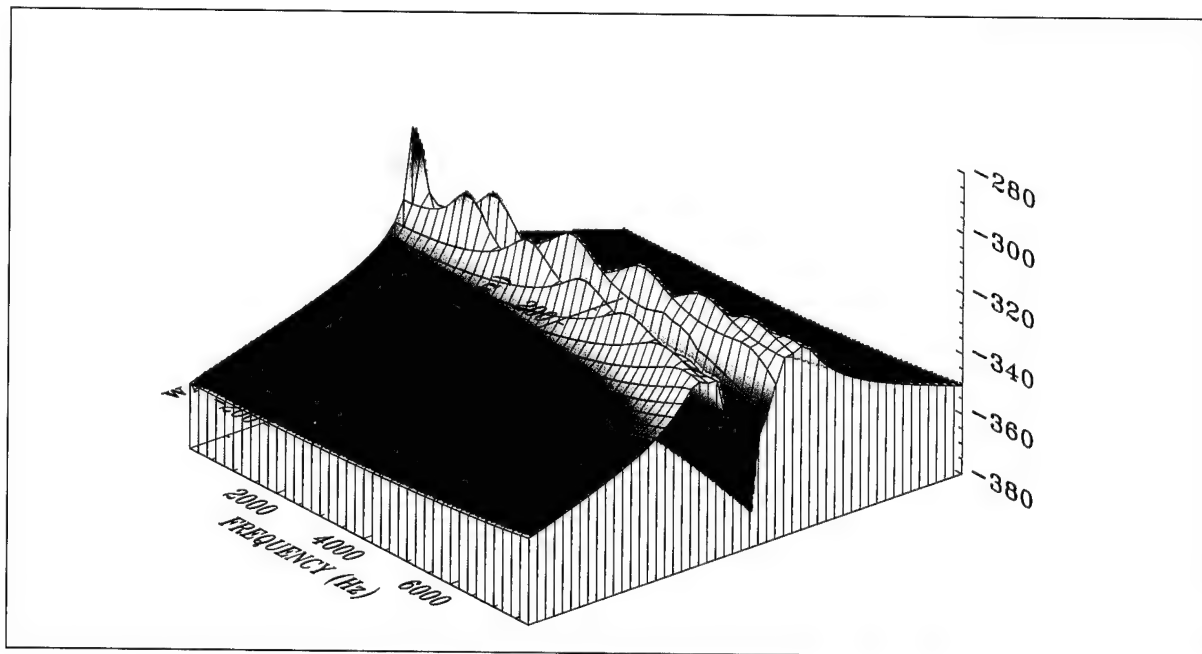


Figure 159. Radial Displacement Transfer Surface With Magnitude = $10\text{Log}(u_c^{C1}(r_1)/P_o)^2$ at $r_1 = 0.259$ in. With $n = 0$ and Diameter = 0.650 in. (Wire Frame Surface)

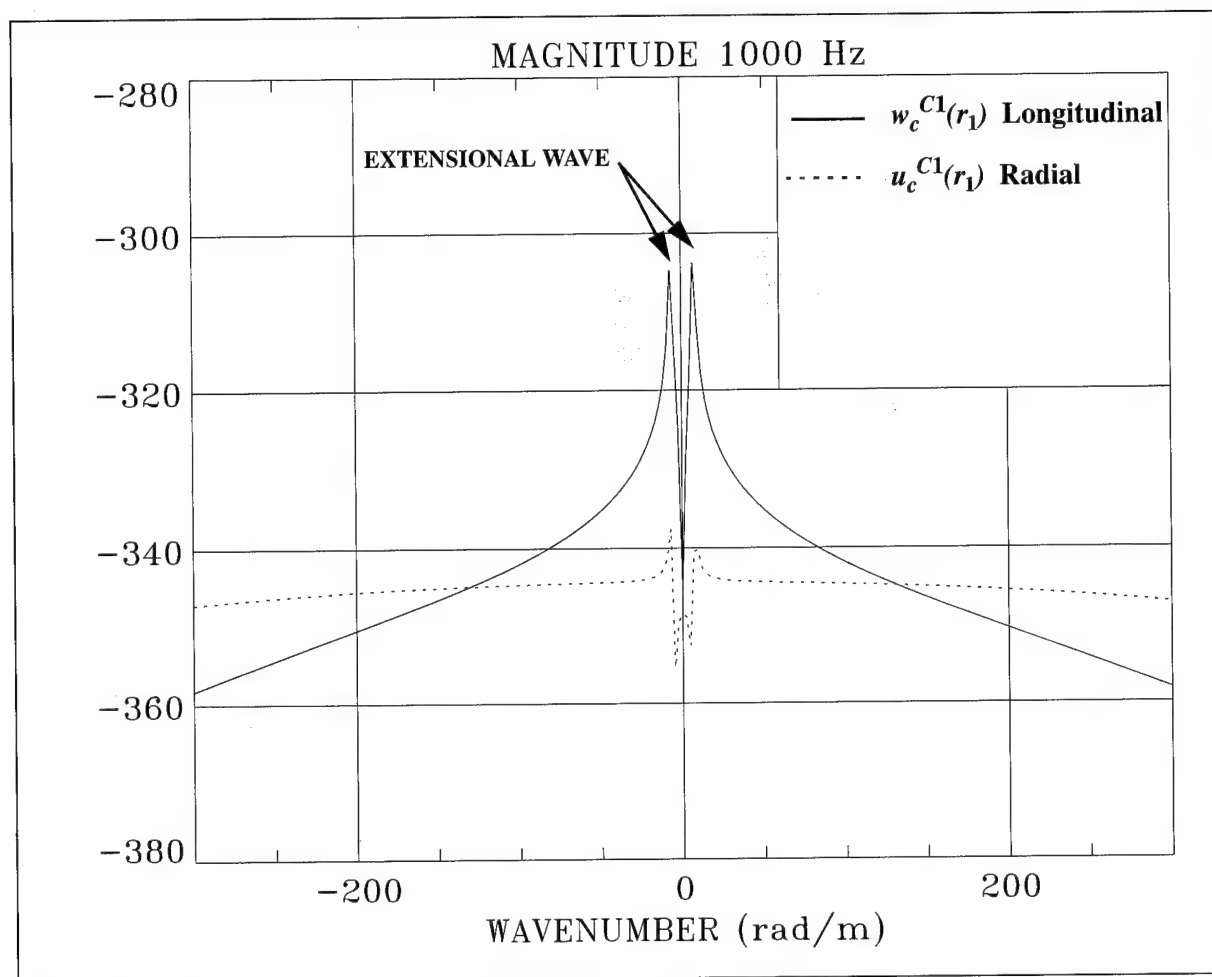


Figure 160. Comparison of Displacement Distribution for Figures 156 and 158 When Magnitude = $10\text{Log}(X/P_o)^2$ for Values of $X = w_c^{C1}(r_1)$ and $u_c^{C1}(r_1)$ at $r_1 = 0.259$ in. With $n = 0$, Diameter = 0.650 in., and $f = 1000$ Hz

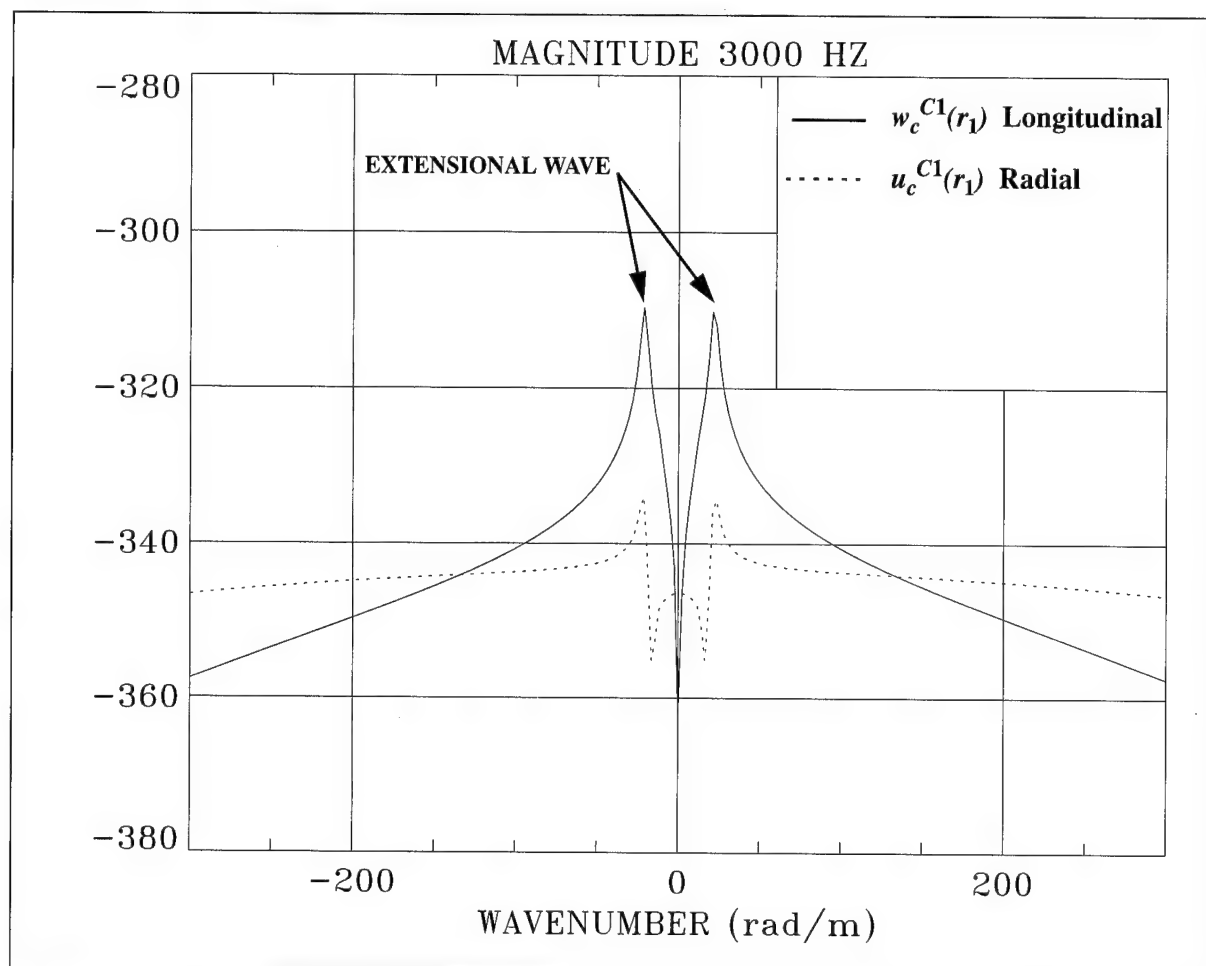


Figure 161. Comparison of Displacement Distribution for Figures 156 and 158 When Magnitude = $10\text{Log}(X/P_o)^2$ for Values of $X = w_c^{C1}(r_1)$ and $u_c^{C1}(r_1)$ at $r_1 = 0.259$ in. With $n = 0$, Diameter = 0.650 in., and $f = 3000$ Hz

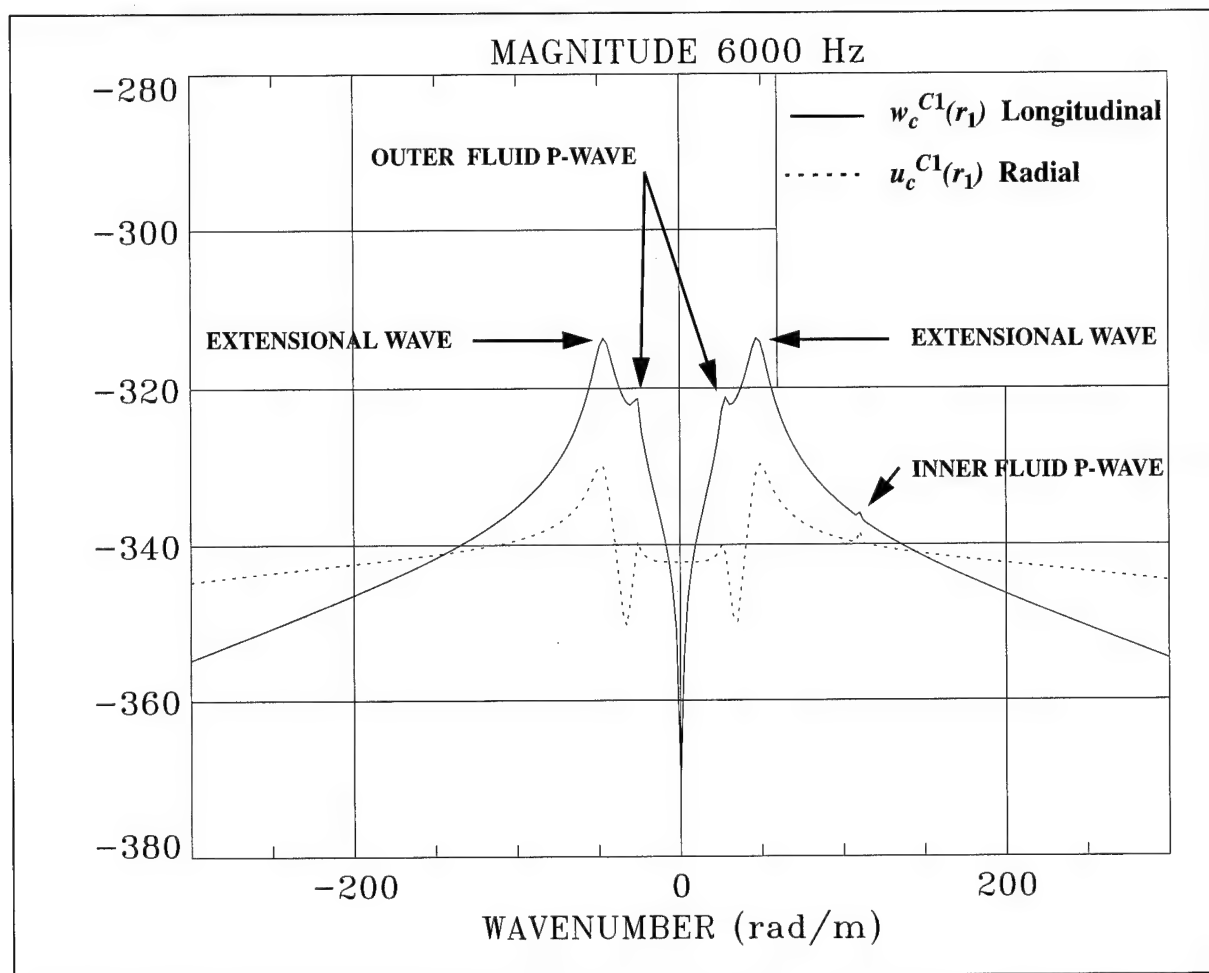


Figure 162. Comparison of Displacement Distribution for Figures 156 and 158 When Magnitude = $10\text{Log}(X/P_o)^2$ for Values of $X = w_c^{C1}(r_1)$ and $u_c^{C1}(r_1)$ at $r_1 = 0.259$ in. With $n = 0$, Diameter = 0.650 in., and $f = 6000$ Hz

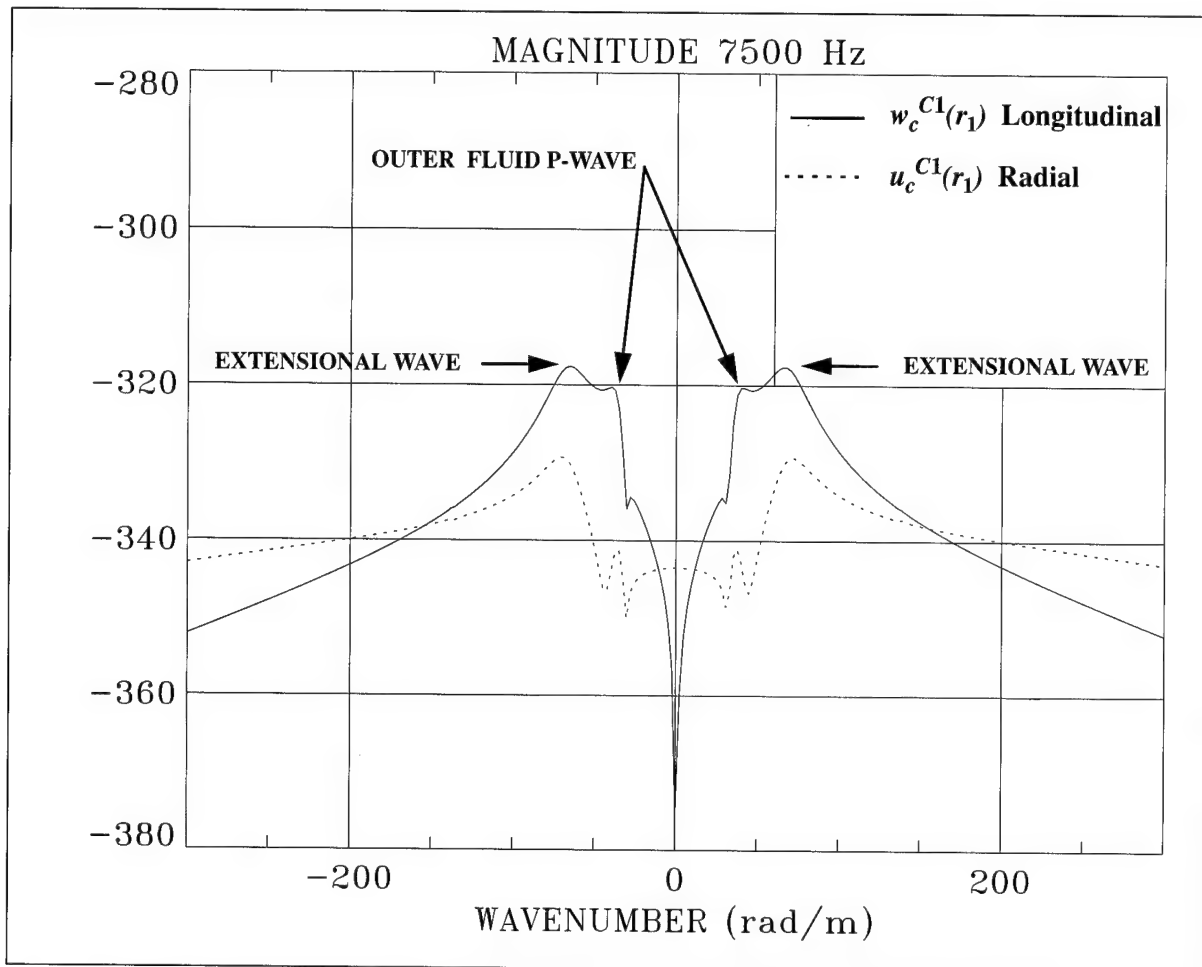


Figure 163. Comparison of Displacement Distribution for Figures 156 and 158 When Magnitude = $10\text{Log}(X/P_o)^2$ for Values of $X = w_c^{C1}(r_1)$ and $u_c^{C1}(r_1)$ at $r_1 = 0.259$ in. With $n = 0$, Diameter = 0.650 in., and $f = 7500$ Hz

Longitudinal Shear Stress Excitation

In this section, the two-layer cylinder is excited with a longitudinal shear stress excitation. The fluids are the same as those defined previously in tables 17 and 18. The circumferential strain sensitivity is evaluated at $r_1 = 0.324$ inch in figures 164 and 165. This radial location is just below the outer surface of the second cylinder. Cuts through the surface are made in figure 166 at various frequencies. The major branch of wave propagation in this simulation for the composite cylinder is the extensional wave whose amplitude decreases as frequency increases (see figure 166).

At a depth of $r_1 = 0.259$ inch, just below the outer radius of the inner cylinder, the simulation for circumferential strain is presented in figures 167 and 168. Cuts through this surface at various frequencies are presented in figure 169. As was the case at $r_1 = 0.324$ inch, the extensional wave is the dominant branch of wave propagation, although the decrease in its amplitude with frequency is greater at $r_1 = 0.259$ inch than at $r_1 = 0.324$ inch.

Comparisons of the circumferential strain at the two radial locations are made in figures 170 through 174. Above the extensional wavenumber, there is significant attenuation of circumferential strain sensitivity. At ± 300 rad/m, this sensitivity has been reduced by approximately 30 dB. The extensional wave resonance peak level, which decreases as r_1 decreases from 0.324 to 0.259 inch, can be observed in figures 171 through 174.

The attenuation of circumferential strain sensitivity is displayed in figure 175. The magnitude plotted in this figure shows the difference in level between $r_1 = 0.259$ inch and $r_1 = 0.324$ inch. The curves reveal the wavenumber-filtering property of the structure due to longitudinal shear stress excitation from just beneath the outer radius of the outer cylinder to just beneath the outer radius of the inner cylinder.

A comparison of figure 175 with figure 155 reveals the different amounts of filtering that the structure presents to the two forms of excitation (i.e., longitudinal shear stress and normal pressure excitation).

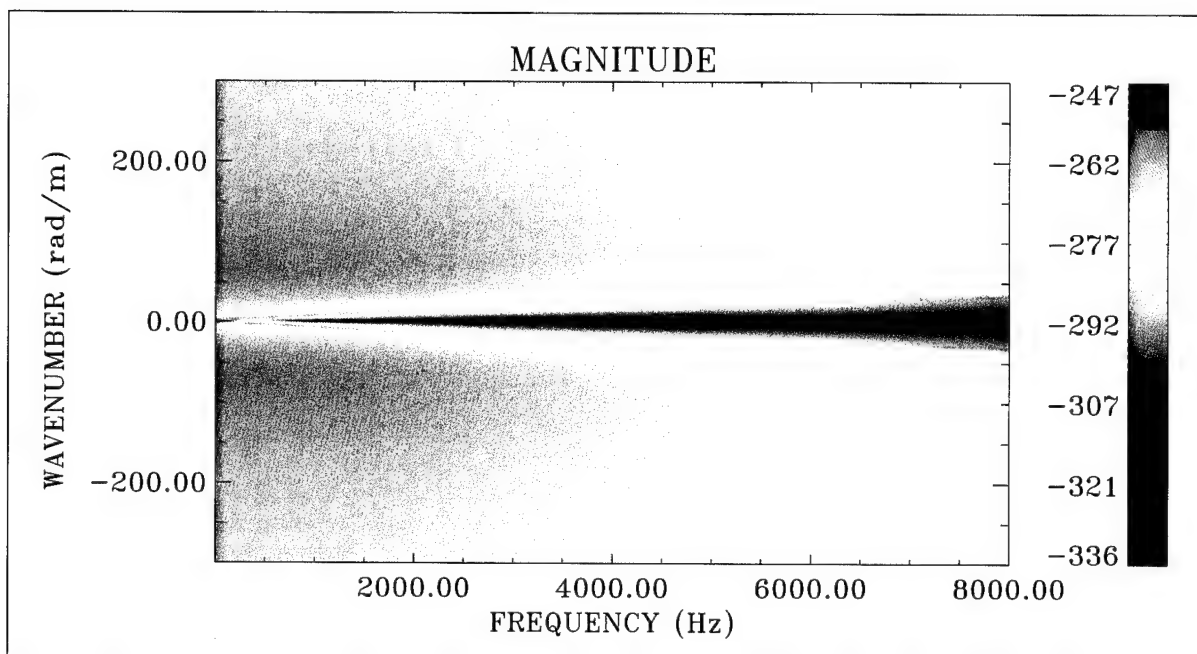


Figure 164. Circumferential Strain Transfer Surface With Magnitude = $10\text{Log}(\epsilon_{\theta\theta}^{C2}(r_1)/P_x)^2$ at $r_1 = 0.324$ in. With $n = 0$ and Diameter = 0.650 in. (Color Image)

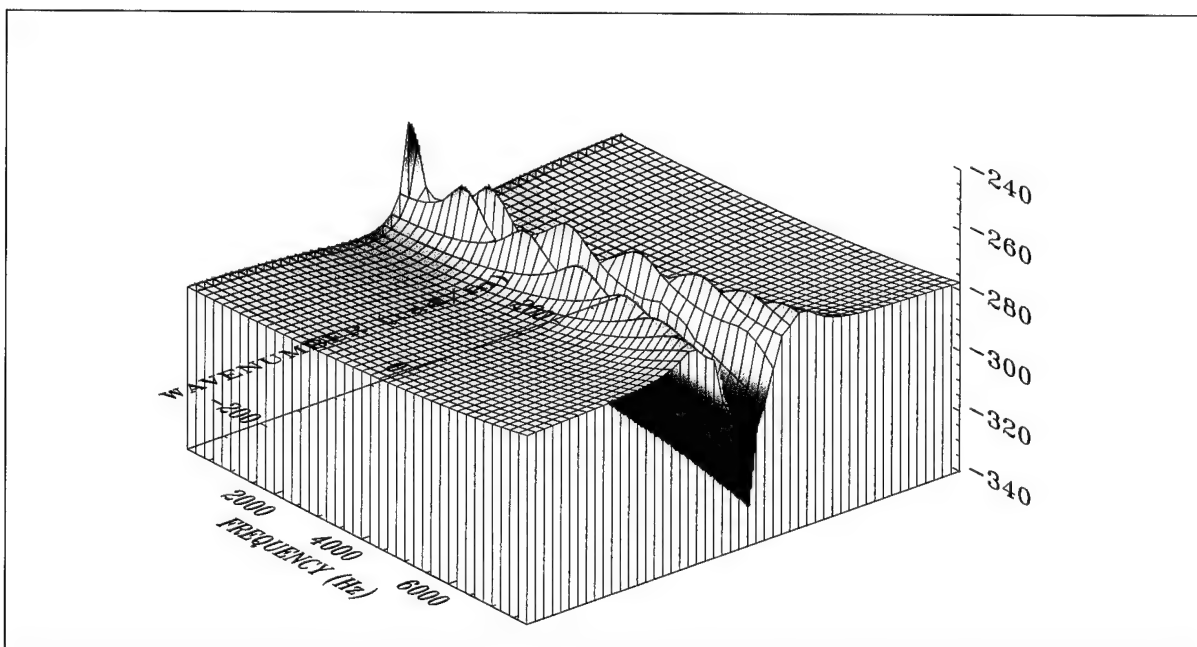


Figure 165. Circumferential Strain Transfer Surface With Magnitude = $10\text{Log}(\epsilon_{\theta\theta}^{C2}(r_1)/P_x)^2$ at $r_1 = 0.324$ in. With $n = 0$ and Diameter = 0.650 in. (Wire Frame Surface)

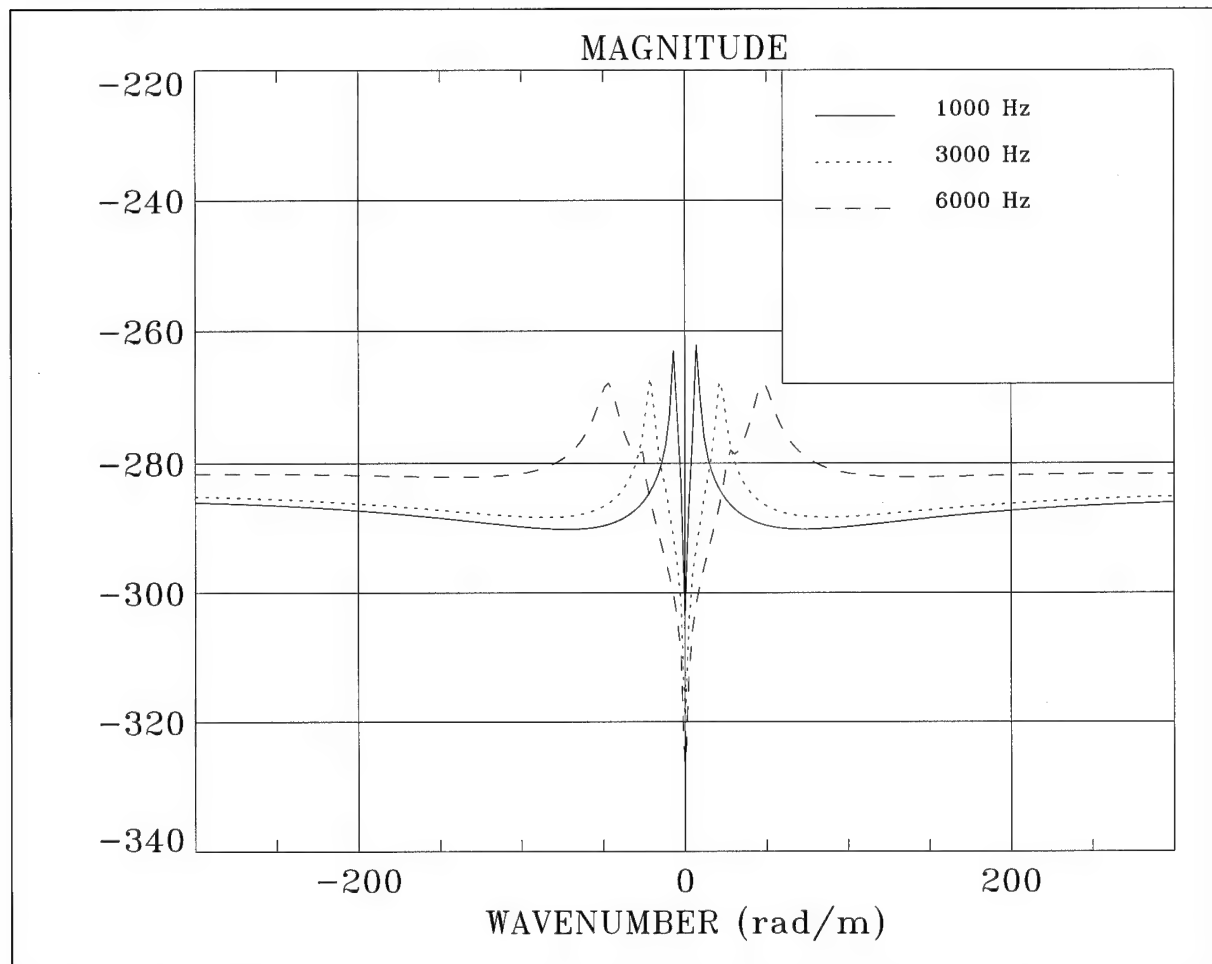


Figure 166. Comparison of Circumferential Strain Distribution for Figure 164
 When Magnitude = $10\text{Log}(\epsilon_{\theta\theta}^{C^2}(r_1)/P_x)^2$ at $r_1 = 0.324$ in. With $n = 0$ and Diameter = 0.650 in.

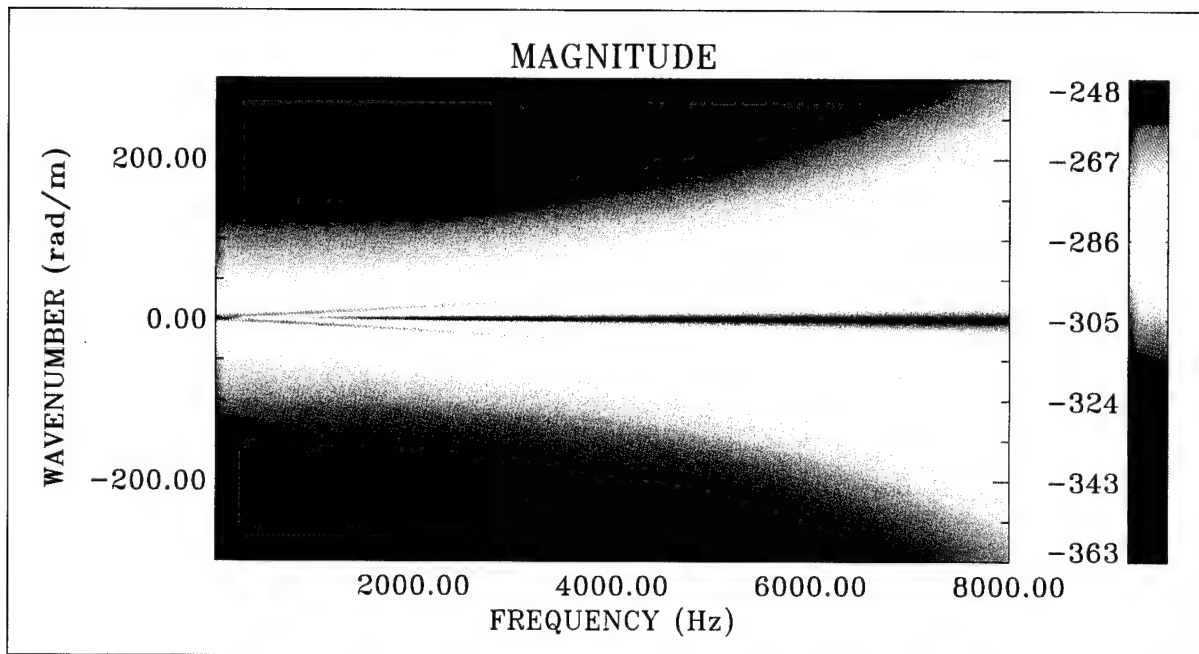


Figure 167. Circumferential Strain Transfer Surface With Magnitude = $10\text{Log}(\epsilon_{\theta\theta}^{C1}(r_1)/P_x)^2$ at $r_1 = 0.259$ in. With $n = 0$ and Diameter = 0.650 in. (Color Image)

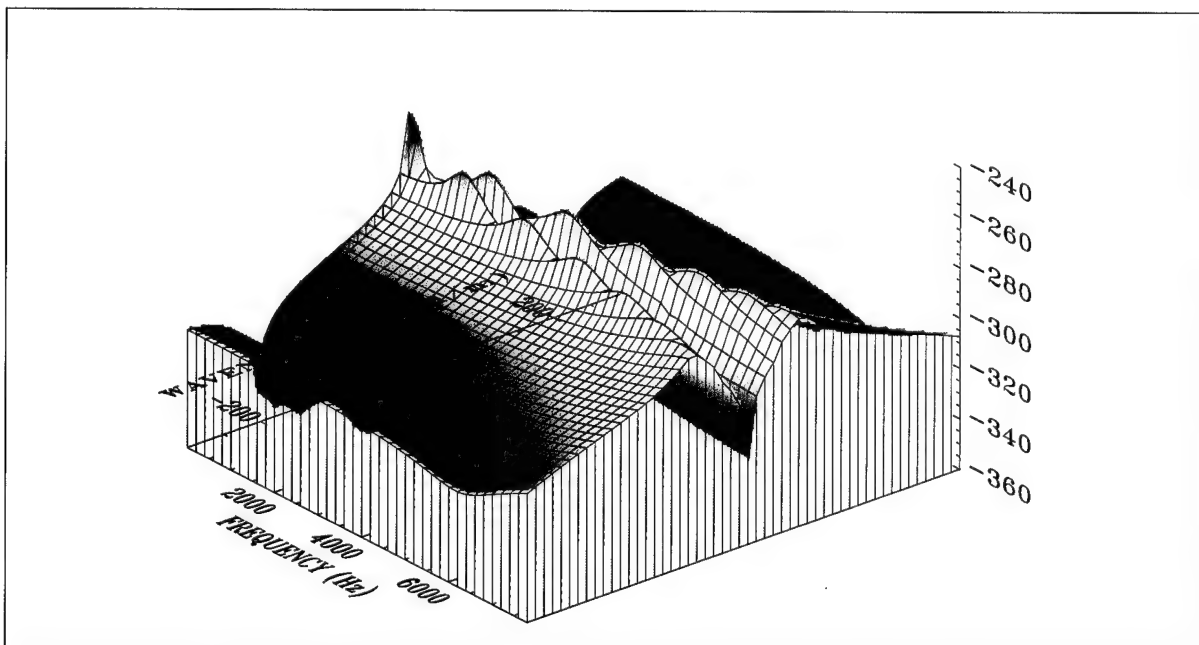


Figure 168. Circumferential Strain Transfer Surface With Magnitude = $10\text{Log}(\epsilon_{\theta\theta}^{C1}(r_1)/P_x)^2$ at $r_1 = 0.259$ in. With $n = 0$ and Diameter = 0.650 in. (Wire Frame Surface)

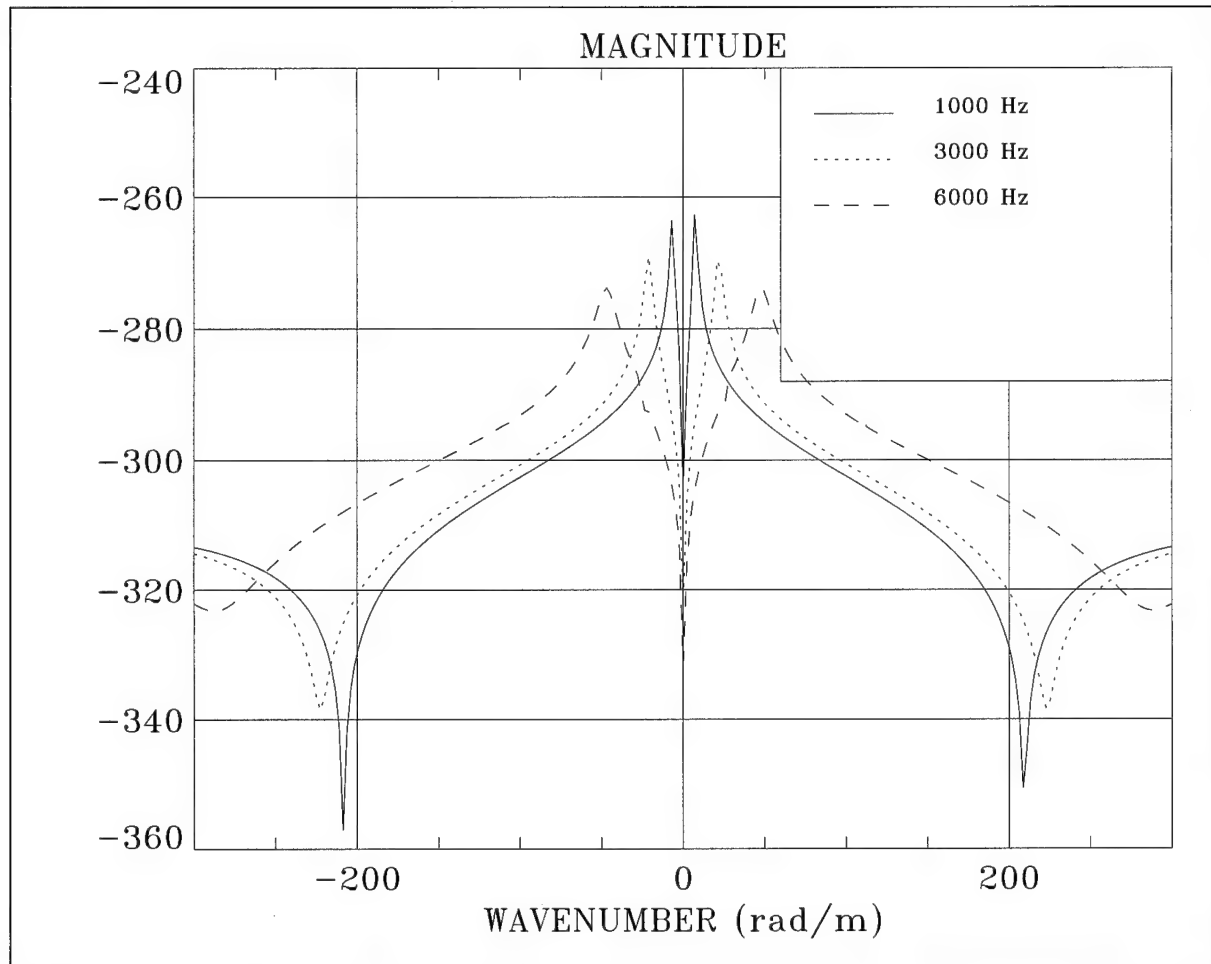


Figure 169. Comparison of Circumferential Strain Distribution for Figure 167
When Magnitude = $10\text{Log}(\epsilon_{\theta\theta}^{C1}(r_1)/P_x)^2$ at $r_1 = 0.259$ in. With $n = 0$ and Diameter = 0.650 in.

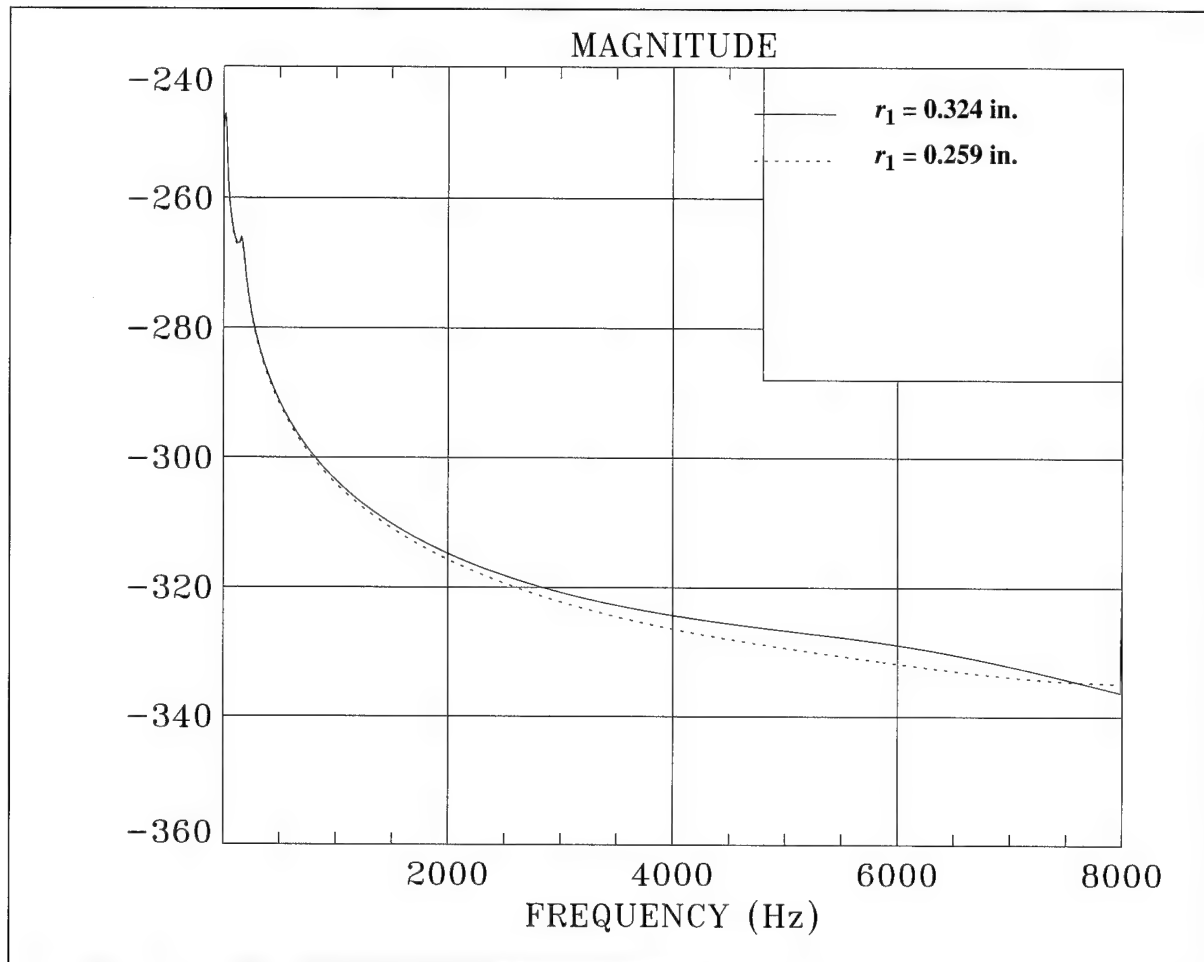


Figure 170. Comparison of Circumferential Strain Distribution for Figures 164 and 167
When Magnitude = $10\text{Log}(\epsilon_{\theta\theta}^{Ci}(r_1)/P_x)^2$ at Various r_1 With $i = 1$ or 2 , $n = 0$,
Diameter = 0.650 in., and $k = 0$ rad/m

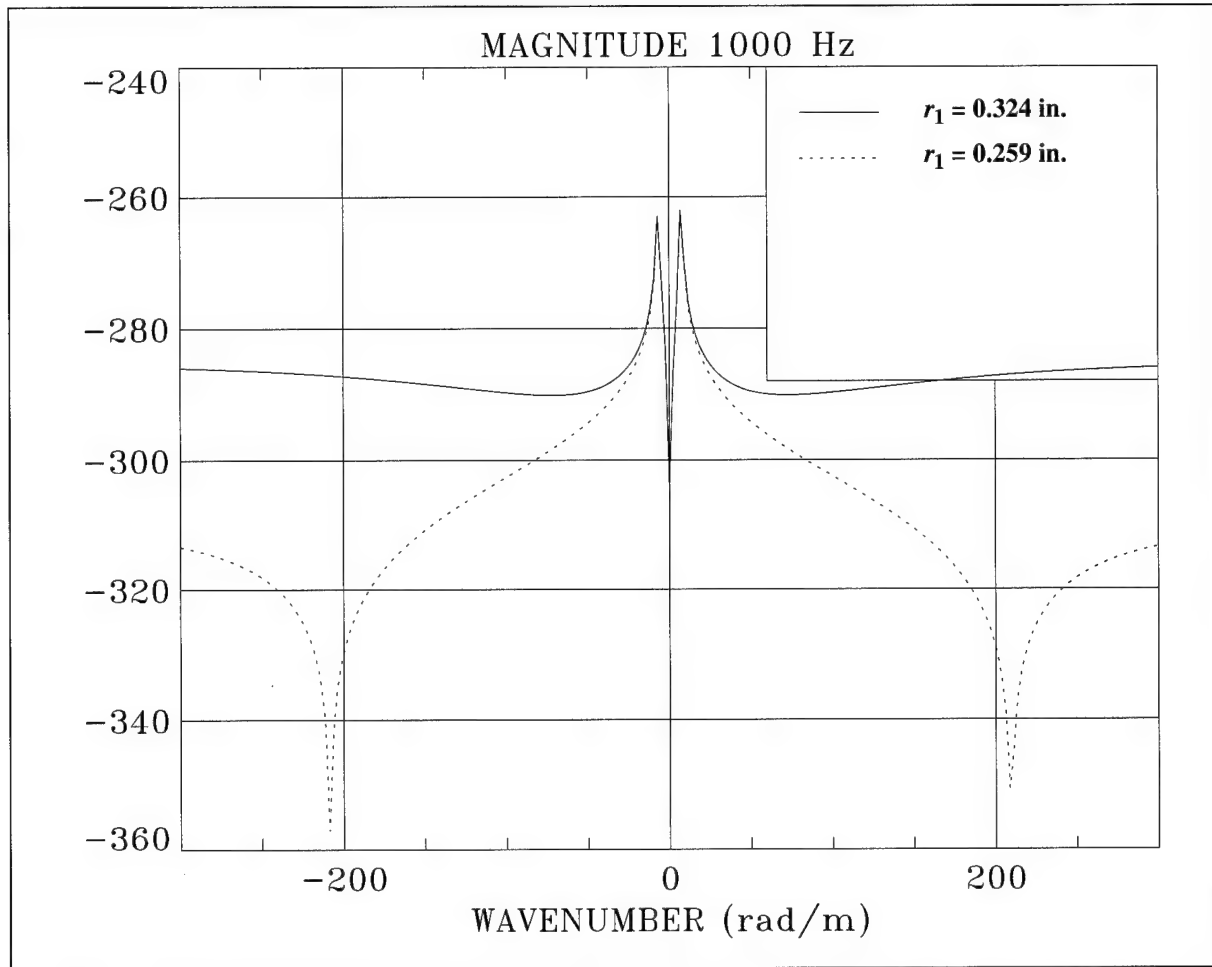


Figure 171. Comparison of Circumferential Strain Distribution for Figures 164 and 167
When Magnitude = $10\text{Log}(\epsilon_{\theta\theta}^{Ci}(r_1)/P_x)^2$ at Various r_1 With $i = 1$ or 2 , $n = 0$,
Diameter = 0.650 in., and $f = 1000$ Hz

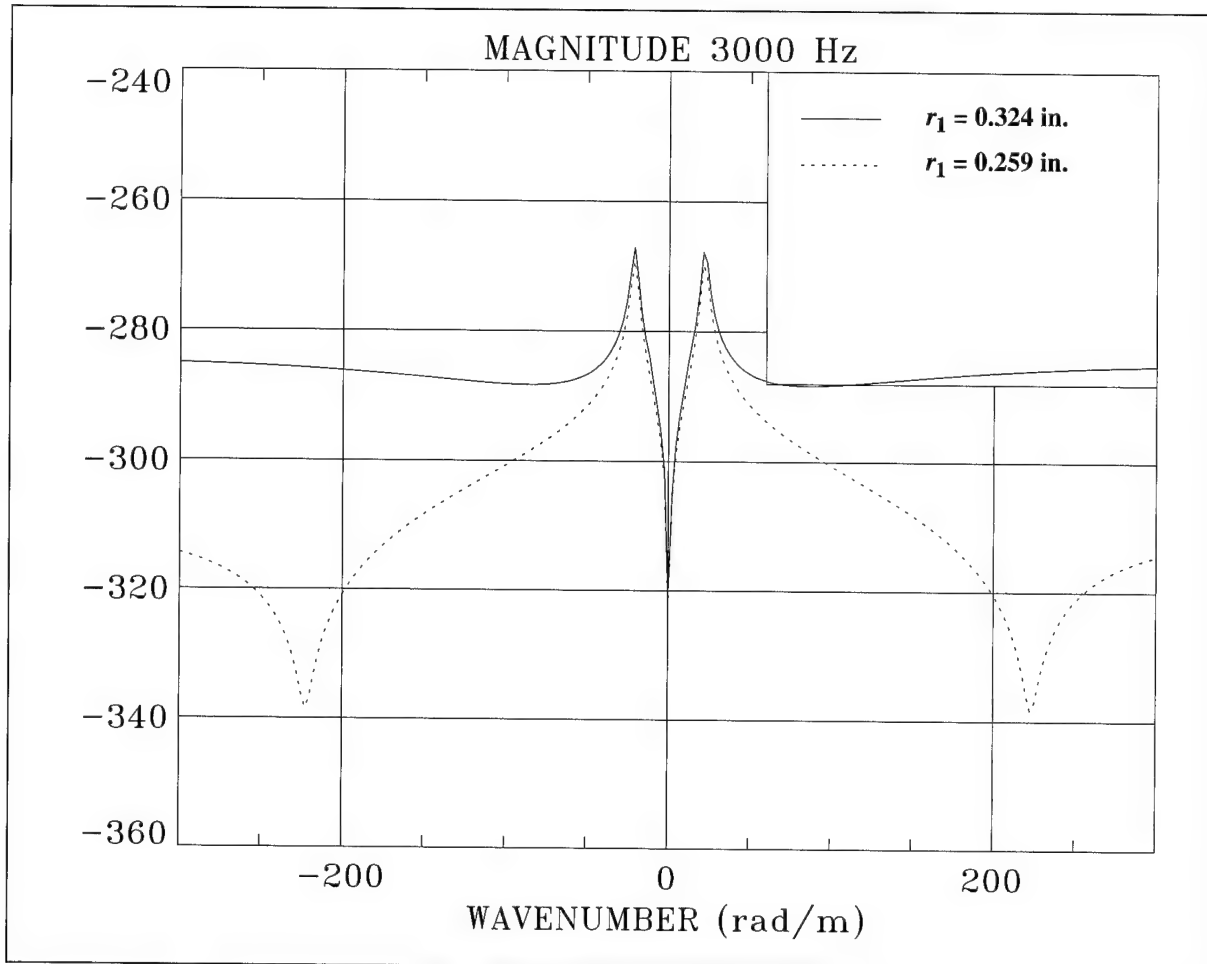


Figure 172. Comparison of Circumferential Strain Distribution for Figures 164 and 167
When Magnitude = $10\text{Log}(\epsilon_{\theta\theta}^{Ci}(r_1)/P_x)^2$ at Various r_1 With $i = 1$ or 2 , $n = 0$,
Diameter = 0.650 in., and $f = 3000$ Hz

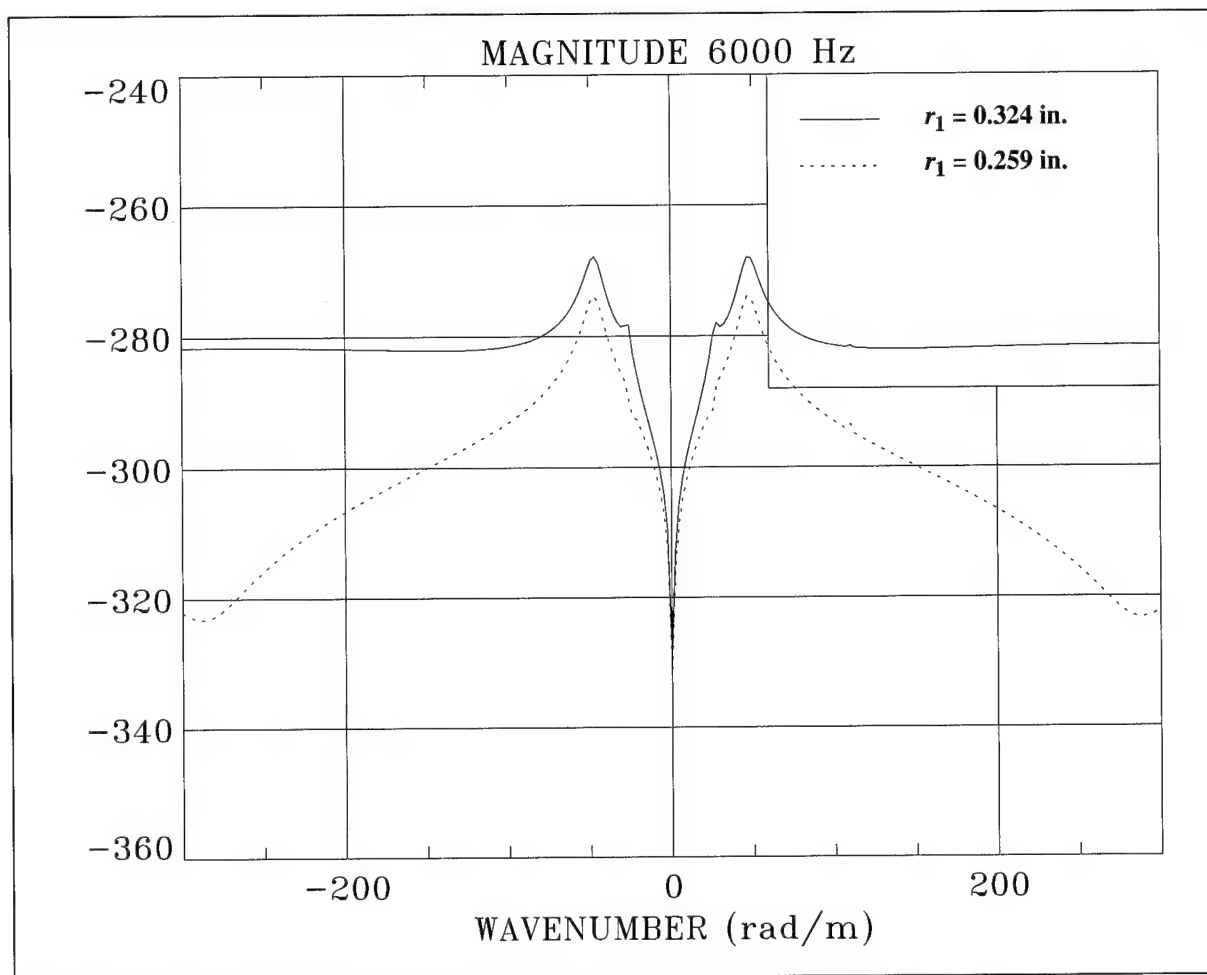


Figure 173. Comparison of Circumferential Strain Distribution for Figures 164 and 167
When Magnitude = $10\text{Log}(\epsilon_{\theta\theta}^{Ci}(r_1)/P_x)^2$ at Various r_1 With $i = 1$ or 2 , $n = 0$,
Diameter = 0.650 in., and $f = 6000$ Hz

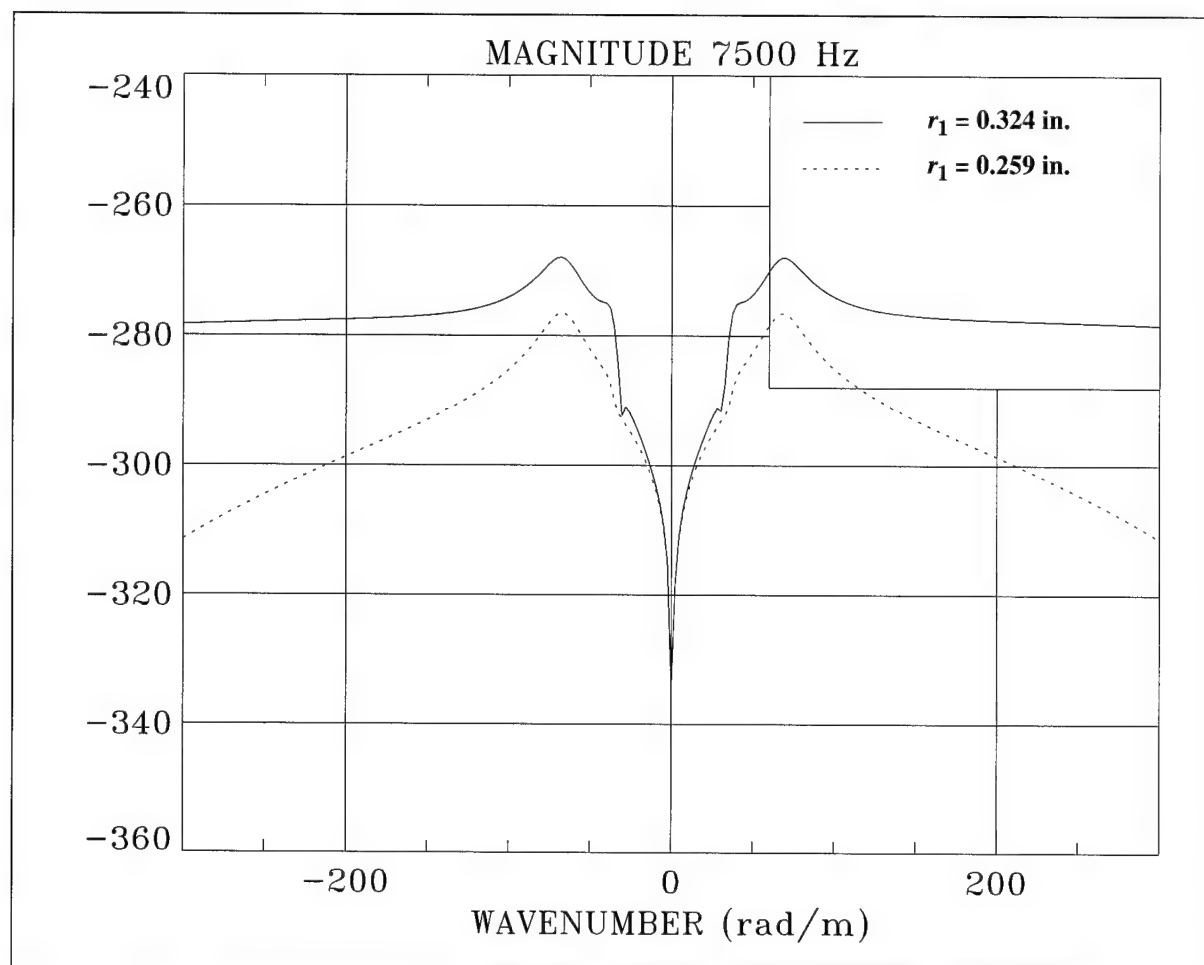


Figure 174. Comparison of Circumferential Strain Distribution for Figures 164 and 167
When Magnitude = $10\text{Log}(\epsilon_{\theta\theta}^{Ci}(r_1)/P_x)^2$ at Various r_1 With $i = 1$ or 2 , $n = 0$,
Diameter = 0.650 in., and $f = 7500$ Hz

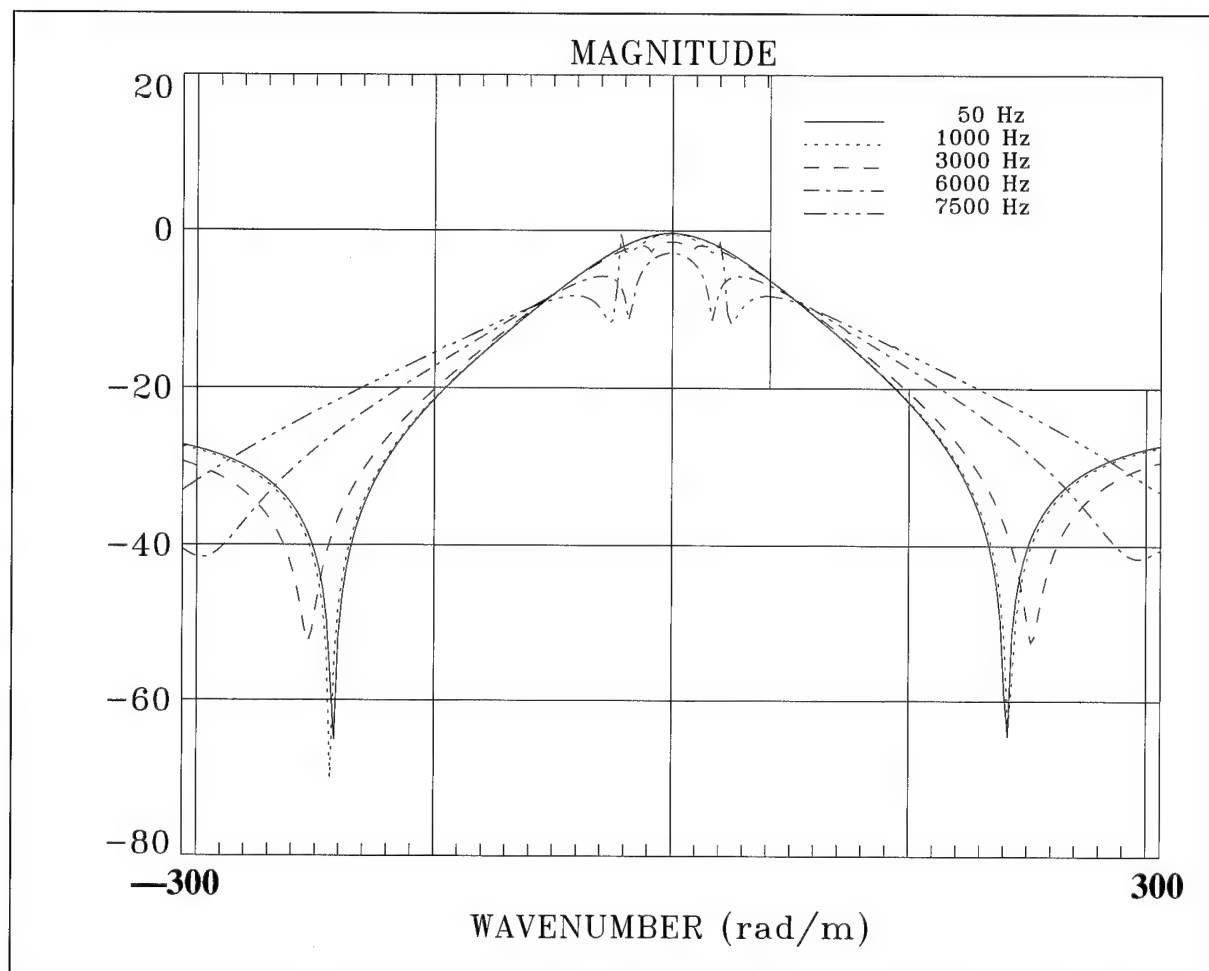


Figure 175. Attenuation of Circumferential Strain From Figures 164 and 167
When Magnitude = $(10\text{Log}(\epsilon_{\theta\theta}^{C1}(0.259)/P_x)^2 - 10\text{Log}(\epsilon_{\theta\theta}^{C2}(0.324)/P_x)^2)$ at Various f
With $n = 0$ and Diameter = 0.650 in.

Comparison of Radial Pressure and Longitudinal Shear Stress Excitations. Previously, we have examined the circumferential strain sensitivity to normal pressure, P_o , and to longitudinal shear stress, P_x . In this section, we will compare this sensitivity to P_o (figure 141) and P_x (figure 167) at various frequencies. Figures 176 through 181 are cuts in frequency for this comparison.

At 40 Hz (figure 176), the extensional wave, at low wavenumber, shows the circumferential strain sensitivity to longitudinal shear stress to be above the sensitivity to normal pressure by 40 dB. As frequency increases, the magnitude of the extensional wave generated by the longitudinal shear stress excitation decreases, and at 6000 Hz the difference between the two responses in the region of the extensional wave is approximately 13 dB.

In general, the figures show that the circumferential strain sensitivity to longitudinal shear stress is lower than the normal pressure sensitivity above 100 rad/m. The circumferential strain sensitivity to normal pressure, unlike longitudinal shear stress, is relatively flat, with increasing wavenumber above the cylinders extensional wave region.

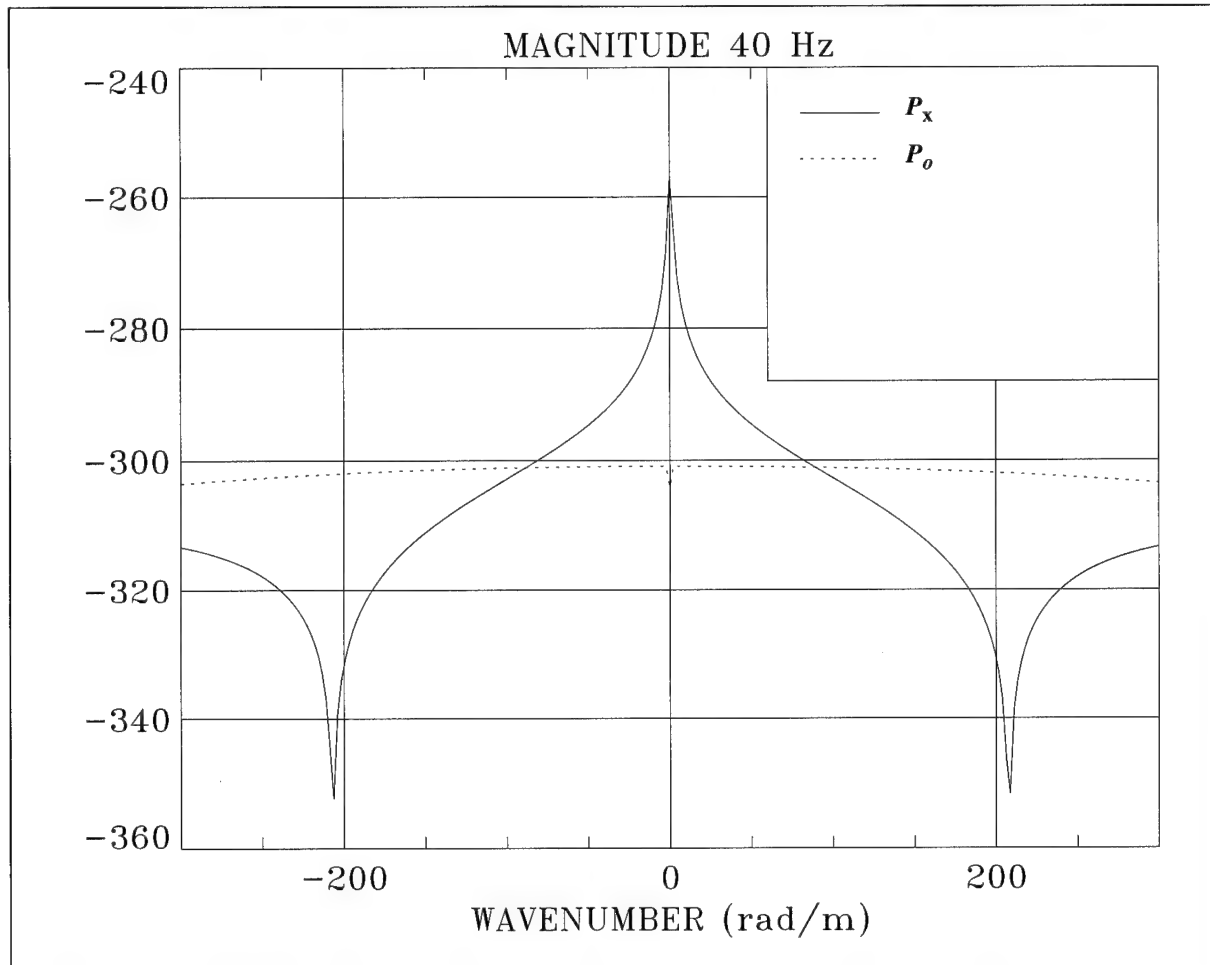


Figure 176. Comparison of Circumferential Strain Distribution for Figures 141 and 167
When Magnitude = $10\text{Log}(\epsilon_{\theta\theta}^{C1}(r_1)/P_i)^2$ With $i = o$ or x , $n = 0$,
Diameter = 0.650 in., and $f = 40$ Hz

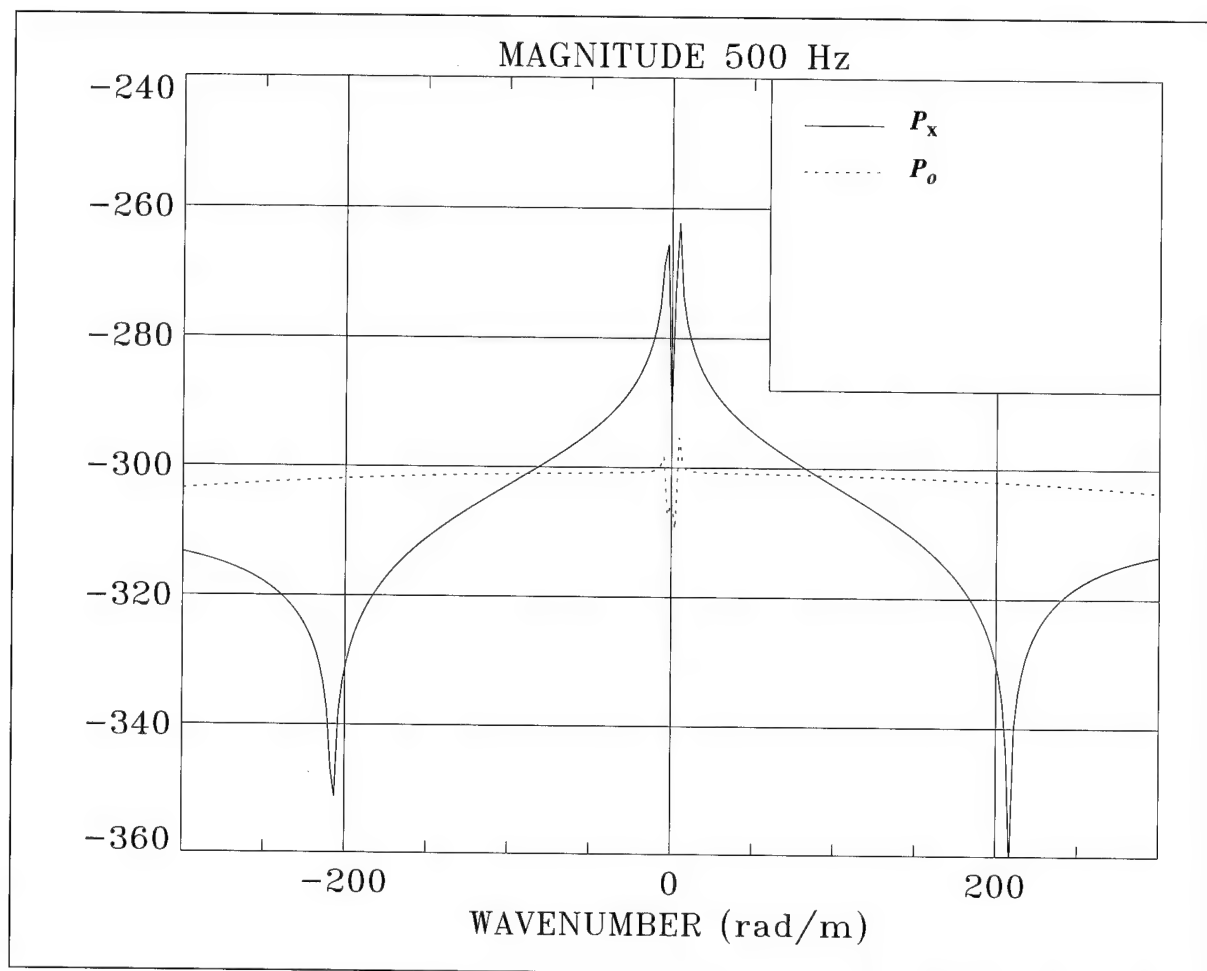


Figure 177. Comparison of Circumferential Strain Distribution for Figures 141 and 167
When Magnitude = $10\text{Log}(\epsilon_{\theta\theta}^{C1}(r_1)/P_i)^2$ With $i = o$ or x , $n = 0$,
Diameter = 0.650 in., and $f = 500$ Hz

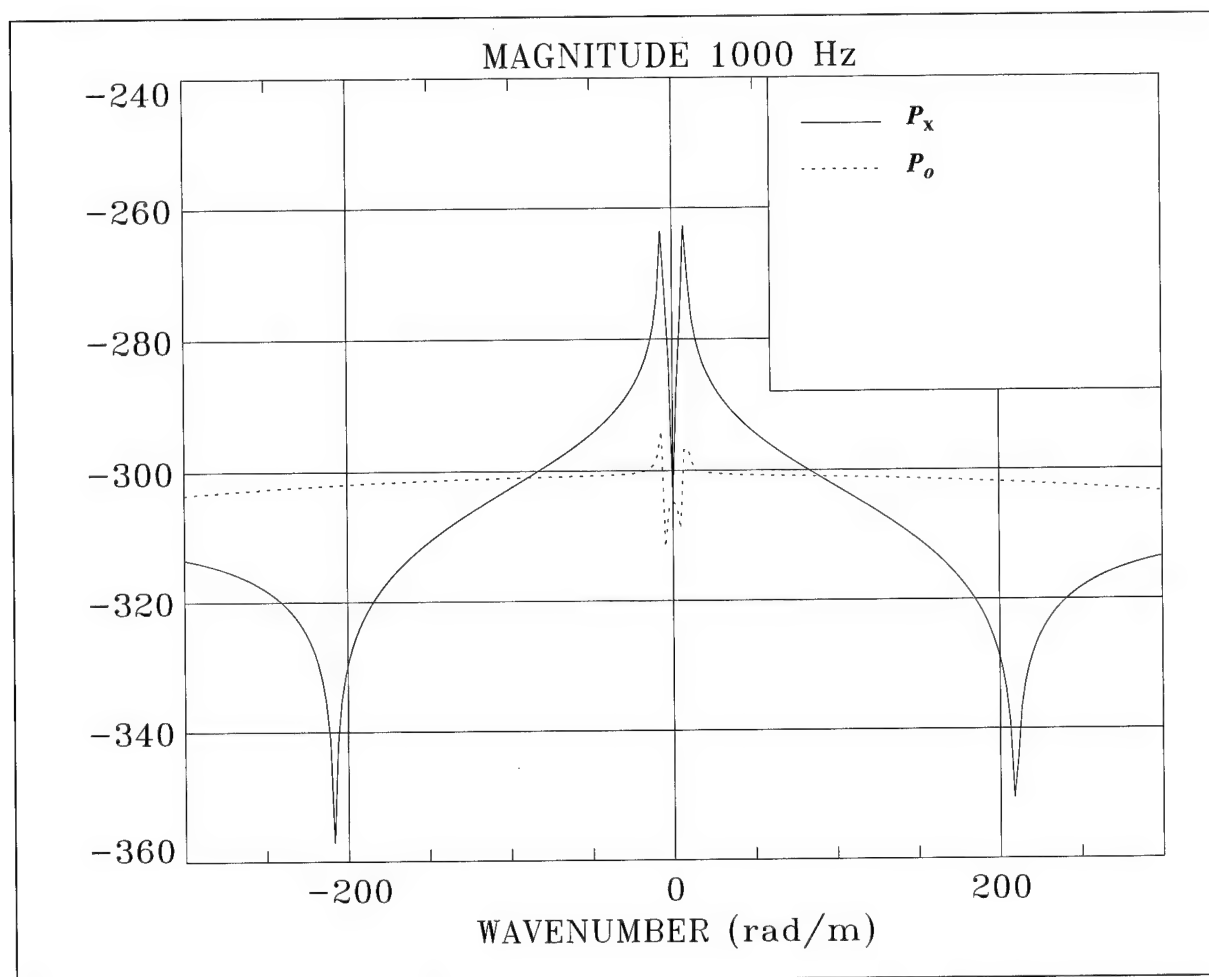


Figure 178. Comparison of Circumferential Strain Distribution for Figures 141 and 167
When Magnitude = $10\text{Log}(\epsilon_{\theta\theta}^{C1}(r_1)/P_i)^2$ With $i = o$ or x , $n = 0$,
Diameter = 0.650 in., and $f = 1000$ Hz

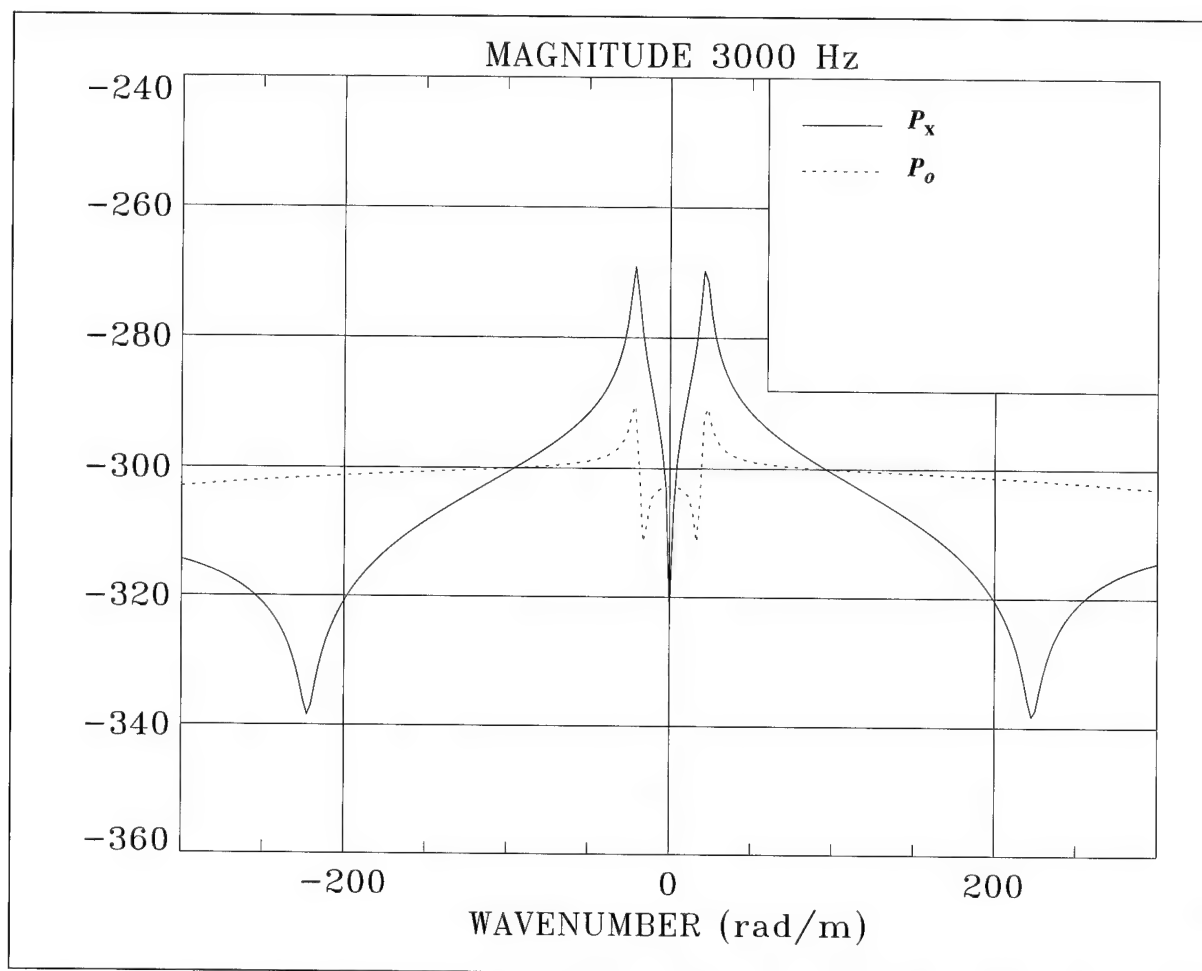


Figure 179. Comparison of Circumferential Strain Distribution for Figures 141 and 167
When Magnitude = $10\text{Log}(\epsilon_{\theta\theta}^{C1}(r_1)/P_i)^2$ With $i = o$ or x , $n = 0$,
Diameter = 0.650 in., and $f = 3000$ Hz

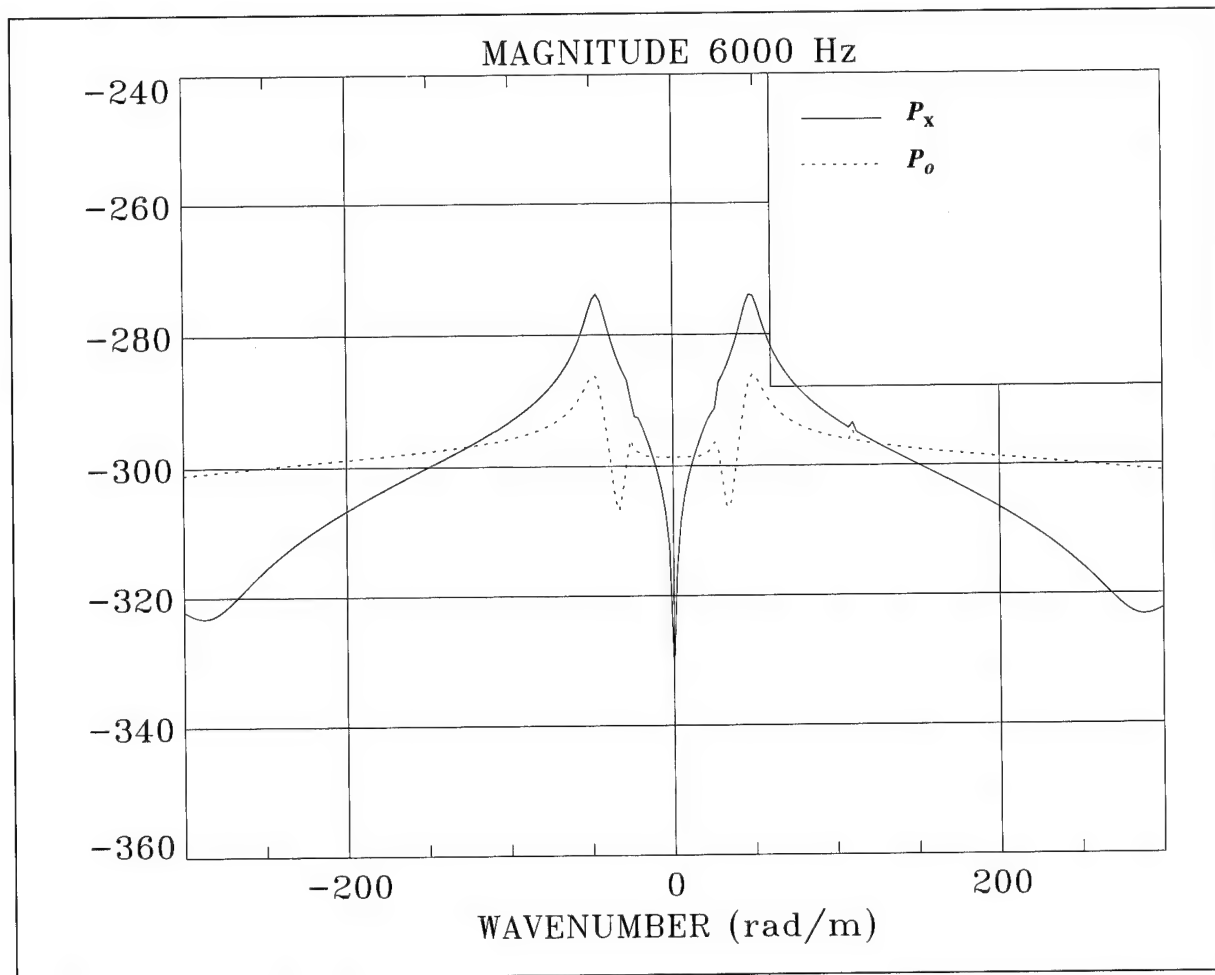


Figure 180. Comparison of Circumferential Strain Distribution for Figures 141 and 167
When Magnitude = $10\text{Log}(\epsilon_{\theta\theta}^{C1}(r_1)/P_i)^2$ With $i = o$ or x , $n = 0$,
Diameter = 0.650 in., and $f = 6000$ Hz

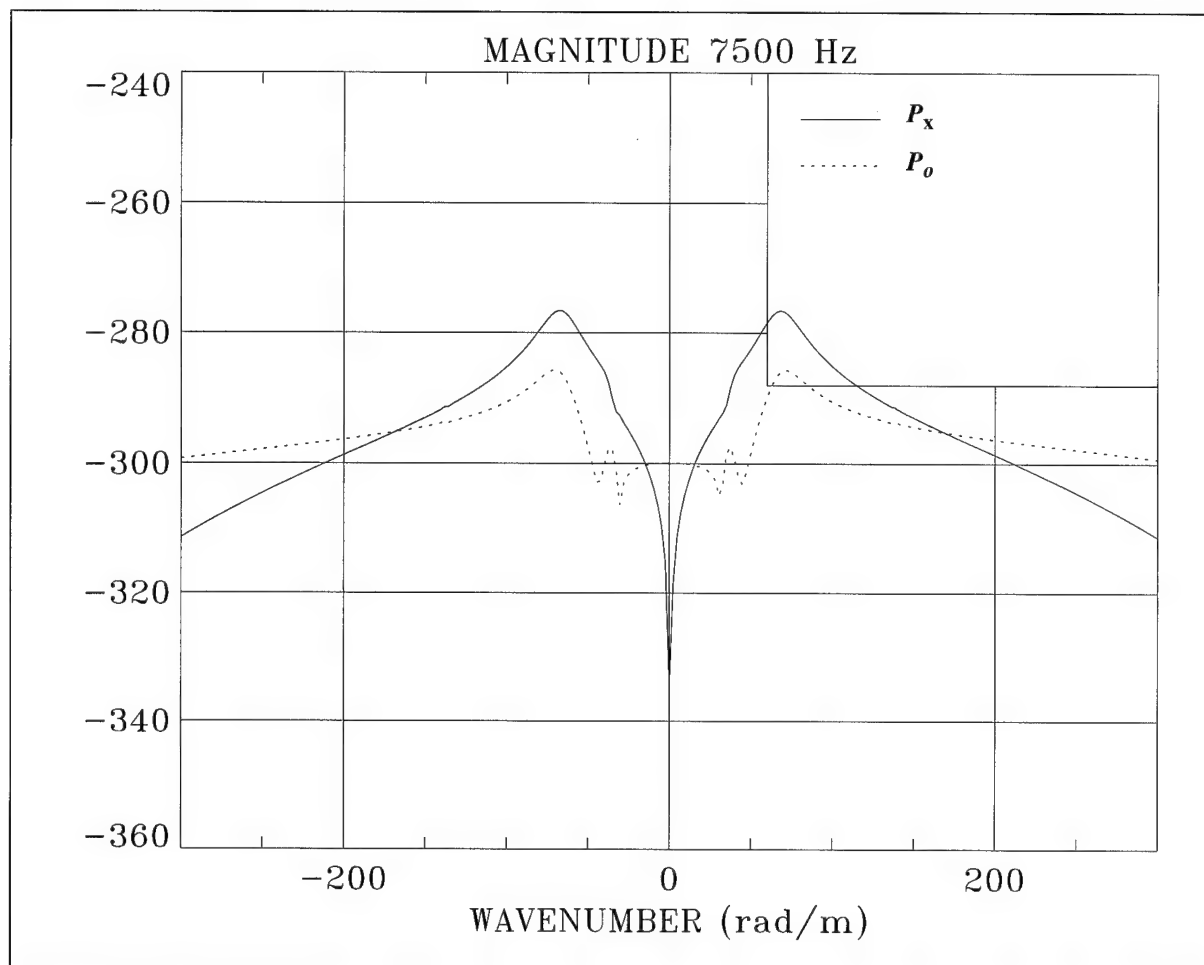


Figure 181. Comparison of Circumferential Strain Distribution for Figures 141 and 167
When Magnitude = $10\text{Log}(\epsilon_{\theta\theta}^{C1}(r_1)/P_i)^2$ With $i = o$ or x , $n = 0$,
Diameter = 0.650 in., and $f = 7500$ Hz

CONCLUSIONS AND RECOMMENDATIONS

An exact closed-form solution to the problem of forced harmonic excitation of a two-layer cylinder with inner and outer fluids has been derived. Results are presented for the dynamic response of a single-layer cylinder with inner and outer fluids of water and for a two-layer cylinder with air as the inner fluid and water as the outer fluid.

Single-Layer Summary

The elasticity model is compared to membrane and bending shell models developed previously. Comparisons among the models are made for a 3.00-inch-diameter cylinder and a 0.670-inch-diameter cylinder. To summarize the results, for the 3.00-inch-diameter cylinder, the shell models are in good agreement with the elasticity model for the region extending to 1000 Hz and ± 75 rad/m. Outside of this region, the difference increases beyond 5 dB, and the elasticity solution should be used. For the $n = 0$ case, the fluid loading influences the first radial natural frequency of the shell models so dramatically that the error (relative to the elasticity solution) is greater than a factor of three as evidenced by figure 22. For the $n = 2$ case, the membrane model should not be used at all because it misrepresents the behavior of the first branch (i.e., lack of cutoff frequency and appropriate branch structure). Although not shown in this report, similar behavior will occur with the membrane shell model for $n > 2$.

For the 0.670-inch-diameter cylinder, the membrane shell models are generally within 4 dB of the elasticity model for the $n = 0$ circumferential order number in the region ± 150 rad/m and 0 to 5000 Hz. If it is necessary to obtain a simulation with an error of less than 4 dB, the elasticity model should be used. The shell models should not be used for the determination of the first radial natural frequency of this cylinder/fluid combination; the elasticity model should be used. For the higher circumferential order numbers, it should be remembered that although the membrane model will not support a cutoff frequency for the first branch of wave propagation, the bending shell model will be within 4 dB of the elasticity solution. If an error of less than 4 dB is required, the elasticity model should be used.

The pressure field in the inner fluid consists of propagating and nonpropagating regions. Below the wavenumber w/c_i , the pressure field propagates and is given by the J_0 Bessel function of equation (67). Above w/c_i the pressure field becomes increasingly evanescent, with increasing wavenumber and decreasing radial position r , and is given by equation (71). This behavior serves to attenuate breathing wave and extensional wave pressure levels (which are locally generated at the cylinder/fluid surface) as the measurement point moves toward the center of the cylinder ($r = 0$) or to a higher wavenumber.

Decreasing the density of the inner fluid lowers the first radial resonance of the cylinder fluid combination. Decreasing the density also increases the phase velocity of the breathing wave. A factor of four decrease in inner fluid density almost doubles the breathing wave phase velocity from 66 to 130 m/sec.

A comparison of shell and elasticity models at high frequencies (up to 60 kHz) shows that the shell models do not accurately resolve the behavior of the cylinder. For the cases considered here (which represent heavy fluid loading), the elasticity model accurately predicts the first radial natural frequency of the system (the shell models do not). Furthermore, in contrast to the shell model, the elasticity model reveals the specific dynamics associated with the thickness of the cylinder. Dilatation wave propagation creates standing waves across the thickness of the cylinder at frequencies (f_{ti}) corresponding to an integer number of half wavelengths for light fluid loading (air). Doubling the cylinder wall thickness halves the frequencies (tables 10 and 11), and increasing the Young's modulus increases the resonant frequencies, as expected (table 13). For heavy fluid loading (water), the frequencies that result deviate from the integer-number-of-half-wavelength relationship observed when air is used as the inner and outer fluids (table 14). Nulls occur in the inner fluid pressure field due to the J_0 nature of the field (the null frequency is given by equation (325) and is a function of the dilatational phase velocity of the inner fluid, the radial position r_1 , and the wavenumber k). The first two null frequencies are tabulated in table 7 for the 3.00-inch cylinder with water as the internal fluid.

The dilatational or P-wave phase velocity of the inner and outer fluids interacts with the cylinder. For the 3.00-inch-diameter cylinder with fluids of water (figures 109 and 119), close

examination of the stress field indicates that there is an increase in energy associated with the fluid dilatation wave velocity; that is, the fluid branch becomes sharply resonant with a very narrow extent in wavenumber. The combination of cylinder and fluids considered here supports this branch at the fluid P-wave phase velocity up to the vicinity of the first radial resonance of the cylinder. At the radial resonance (2816 Hz), this branch becomes dispersive, with the phase and group velocities slowing, as shown in table 15. The width in wavenumber of the resonant peak increases and a null in the transmitted stress field develops at the P-wave phase velocity of the fluid (1,500 m/sec). Above the first radial resonance of the cylinder, the fluid P-wave is modified by the presence of the cylinder and becomes dispersive.

In contrast to the previously discussed case of dense fluids (water) is the simulation shown in figure 100, where the 3.00-inch cylinder was immersed in fluids of low density (air). In this case, the fluid P-wave phase velocity is unaltered by the first radial resonance of the cylinder. The P-wave phase velocity of air is 343 m/sec (tables 8 and 9) and remains nondispersive throughout the wavenumber-frequency range of the simulation (figure 100).

Normal pressure excitation ($n = 0$) applied to the cylinder creates a high-amplitude breathing wave and a low-amplitude extensional wave; however, the longitudinal shear stress excitation creates a high-amplitude extensional wave and a low-amplitude breathing wave. The amplitude of the extensional wave generated by the longitudinal shear stress excitation decreases with increasing frequency. The interaction of the fluid P-wave and the cylinder during longitudinal shear stress excitation ($n = 0$) parallels that of the radial pressure excitation (i.e., nondispersive behavior up to the first radial resonance frequency of the cylinder and dispersive behavior above the resonance frequency).

The $n = 1$ circumferential order number excitation (normal pressure, longitudinal shear stress, and circumferential shear stress) generates a branch of wave propagation that causes the cylinder to undergo an rx plane-bending deformation, as depicted in figure 9. Cutoff frequencies are associated with the second and third branches of wave propagation for $n = 1$ and $n = 2$ for both longitudinal and circumferential shear stress excitations.

Two-Layer Summary

The two-layer cylinder simulations (circumferential strain with normal pressure excitation) are performed with air as the inner fluid and water as the outer fluid. The first radial resonance frequency for the composite cylinder and fluids occurs at 6210 Hz. The P-wave of the inner fluid is nondispersive throughout the range of the simulations. The P-wave of the outer fluid is nondispersive up to the first radial resonance of the cylinder and then becomes dispersive. The extensional wave phase velocity for the two-layer cylinder is 800 m/sec, becoming dispersive above the cylinder radial resonance frequency of 6210 Hz. Figure 155 displays the attenuation of circumferential strain across the outer layer of the composite cylinder.

A circumferential strain excitation ($n = 0$) applied to the composite cylinder produces an extensional wave whose amplitude is 20 dB larger at 1000 Hz and 5 dB larger at 7500 Hz than the extensional wave generated by the normal pressure excitation. The outer fluid P-wave is evident in the simulations using the circumferential shear stress excitation at approximately the same amplitude as for the normal pressure excitation.

These results provide a small sampling of the problems that can be analyzed with the mathematical models developed in this report. It should be emphasized that the elasticity models represent the "truth" for the structures (subjected to harmonic forcing functions in space and time) presented here. There are no simplifying assumptions that discard information as in shell analysis. The elasticity models can be used for analyzing structures that range from the dimensions of a human hair to the largest cylinder that would be practical to manufacture or would occur in nature. Furthermore, the frequency range allowed by these models is exceedingly broad. In other words, the simulations presented here could be said to explore only the lower limit of what is possible to study with the elasticity models. The primary challenge becomes a numerical one, where the limitations occur in the ability to compute the Bessel functions, invert the system matrix, and maintain enough precision throughout the entire calculation to ensure a valid solution to the equations.

REFERENCES

1. A. N. Holden, "Longitudinal Modes of Elastic Waves in Isotropic Cylinders and Slabs," *Bell Systems Technical Journal*, vol. 30, 1951, pp. 956-969.
2. R. K. Kaul and J. J. McCoy, "Propagation of Axisymmetric Waves in a Circular Semi-Infinite Elastic Rod," *Journal of the Acoustical Society of America*, vol. 36, 1964, pp. 653-660.
3. J. D. Achenbach, *Wave Propagation in Elastic Solids*, Elsevier Publishing Company, Inc., New York, 1990, pp. 55-56.
4. J. D. Achenbach, p. 65.
5. J. D. Achenbach, p. 54.
6. J. D. Achenbach, pp. 238-239.
7. J. D. Achenbach, pp. 239-240.
8. J. D. Achenbach, pp. 73-75.
9. J. D. Achenbach, p. 78.
10. W. M. Ewing, W. S. Jardetzky, and F. Press, *Elastic Waves in Layered Media*, McGraw-Hill Book Company, Inc., New York, 1957, p. 317.
11. M. C. Junger and D. Feit, *Sound, Structures and Their Interaction*, The MIT Press, Cambridge, MA, 1986, p. 167.
12. M. S. Peloquin, "FORTRAN Algorithms for the Three-Dimensional Solution of Two-Layer Solid and Hollow Cylinder Dynamic Elasticity Problems With and Without Fluids," NUWC-NPT Technical Document 11,065, Naval Undersea Warfare Center Detachment, New London, CT, November 1995.
13. M. S. Peloquin, "Forced Harmonic Vibration of the Generally Orthotropic Cylindrical Shell With Inner and Outer Fluid Loading," NUWC-NPT Technical Report 10,199, Naval Undersea Warfare Center Detachment, New London, CT, November 1992, p. 4.

APPENDIX A

BESSEL FUNCTIONS OF COMPLEX ARGUMENT, SERIES REPRESENTATION

The inclusion of structural damping in the cylinder necessitates the evaluation of Bessel functions of complex argument. The series representation of these functions is then required. From Abramowitz and Stegun,¹ equations (A-1) through (A-6) are used for complex argument z , where z ranges from $0 \leq z \leq 3$. The circumferential order number n appears in the equations as well.

The Gamma² function is given by

$$\Gamma(n + K + 1) = (n + K)! \quad (\text{A-1})$$

The Psi³ or Digamma function is

$$\psi(1) = -\gamma, \quad \psi(n) = -\gamma + \sum_{k=1}^{n-1} k^{-1}, \quad n \geq 2 \quad (\text{A-2})$$

The value used for Euler's constant is $\gamma = 0.577215664901532860606512$.

The Bessel function of the first⁴ kind is

$$J_n(z) = \left(\frac{z}{2}\right)^n \sum_{k=0}^{\infty} \frac{\left(\left(-\frac{1}{4}\right)z^2\right)^k}{k! \Gamma(n + k + 1)} \quad (\text{A-3})$$

-
1. M. Abramowitz and I. A. Stegun, *Handbook of Mathematical Functions*, U.S. Government Printing Office, Washington, DC, June 1964.
 2. M. Abramowitz and I. A. Stegun, p. 255, equation (6.1.6).
 3. M. Abramowitz and I. A. Stegun, p. 258, equation (6.3.2).
 4. M. Abramowitz and I. A. Stegun, p. 360, equation (9.1.10).

The Bessel function of the second⁵ kind over the range $0 < z \leq 3$ is

$$Y_n(z) = \left(-\frac{\left(\frac{z}{2}\right)^n}{\pi} \right) \left(\sum_{k=0}^{n-1} \frac{(n-k-1)!}{k!} \right) \left(\frac{1}{4} z^2 \right)^k + \frac{2}{\pi} \ln\left(\frac{z}{2}\right) J_n(z) - \frac{\left(\frac{z}{2}\right)^n}{\pi} \sum_{k=0}^{\infty} (\psi(k+1) + \psi(n+k+1)) \frac{\left(\left(-\frac{1}{4}\right) z^2\right)^k}{k! (n+k)!} . \quad (\text{A-4})$$

The Hankel function⁶ of the first kind is given by

$$H_n^{(1)}(z) = J_n(z) + iY_n(z) . \quad (\text{A-5})$$

The expression⁷ used for the modified Bessel function I_n over the range $0 \leq z \leq 3$ is

$$I_n(z) = \left(\frac{z}{2}\right)^n \sum_{k=0}^{\infty} \frac{\left(\left(\frac{1}{4}\right) z^2\right)^k}{k! \Gamma(n+k+1)} . \quad (\text{A-6})$$

The expression⁸ used for the modified Bessel function K_n over the range $0 < z \leq 3$ is

$$K_n(z) = \frac{1}{2} \left(\frac{1}{2} z\right)^{-n} \left(\sum_{k=0}^{n-1} \frac{(n-k-1)!}{k!} \right) \left(\left(-\frac{1}{4}\right) z^2 \right)^k + (-1)^{n+1} \ln\left(\frac{z}{2}\right) I_n(z) + (-1)^n \left(\frac{z}{2}\right)^n \left(\sum_{k=0}^{\infty} (\psi(k+1) + \psi(n+k+1)) \right) \frac{\left(\frac{1}{4} z^2\right)^k}{k! (n+k)!} . \quad (\text{A-7})$$

5. M. Abramowitz and I. A. Stegun, p. 360, equation (9.1.11).

6. M. Abramowitz and I. A. Stegun, p. 358, equation (9.1.3).

7. M. Abramowitz and I. A. Stegun, p. 375, equation (9.6.10).

8. M. Abramowitz and I. A. Stegun, p. 375, equation (9.6.11).

For the argument range $3 < z < \infty$, asymptotic expansions are used from Korn and Korn:⁹

$$J_n(z) = \sqrt{\frac{2}{\pi z}} \left(A_n(z) \cos\left(z - \frac{n\pi}{2} - \frac{\pi}{4}\right) - B_n(z) \sin\left(z - \frac{n\pi}{2} - \frac{\pi}{4}\right) \right) \quad (\text{A-8})$$

and

$$Y_n(z) = \sqrt{\frac{2}{\pi z}} \left(A_n(z) \sin\left(z - \frac{n\pi}{2} - \frac{\pi}{4}\right) + B_n(z) \cos\left(z - \frac{n\pi}{2} - \frac{\pi}{4}\right) \right), \quad (\text{A-9})$$

where

$$A_n(z) = 1 - \frac{(4n^2 - 1)(4n^2 - 9)}{2!(8z)^2} + \frac{(4n^2 - 1)(4n^2 - 9)(4n^2 - 25)(4n^2 - 49)}{4!(8z)^4} \mp \dots,$$

and

$$B_n(z) = \frac{4n^2 - 1}{8z} - \frac{(4n^2 - 1)(4n^2 - 9)(4n^2 - 25)}{3!(8z)^3} \pm \dots \quad (\text{A-10})$$

9. G. A. Korn and T. M. Korn, *Mathematical Handbook for Scientists and Engineers*, McGraw-Hill Book Company, New York, pp. 868-869, equations (21.8-44) and (21.8.45).

APPENDIX B

DERIVATIVES OF BESSEL FUNCTIONS

An expression for the first derivative of the Bessel functions needed for the evaluation of the displacement potentials is taken from Arpaci,¹ and is seen here in equations (B-1) and (B-2):

$$\frac{d}{dx}(Z_n(\alpha x)) = -\alpha Z_{n+1}(\alpha x) + \frac{n}{x}Z_n(\alpha x), \quad Z = J, Y, K, H^{(1)}, H^{(2)} \quad (\text{B-1})$$

and

$$\frac{d}{dx}(I_n(\alpha x)) = \alpha I_{n+1}(\alpha x) + \frac{n}{x}I_n(\alpha x). \quad (\text{B-2})$$

The argument of the Bessel functions is composed of α (a constant) and x (a complex number).

An expression for the second derivative of the Bessel functions listed in equation (B-1) is derived by differentiating this equation again with respect to x , which requires the use of the product rule on the second term of the right-hand side of equation (B-1) and the following effect of the recursion relationships for Bessel functions:

$$\frac{d}{dx}(Z_{n+1}(\alpha x)) = -\alpha Z_{n+2}(\alpha x) + \frac{n+1}{x}Z_{n+1}(\alpha x), \quad Z = J, Y, K, H^{(1)}, H^{(2)} \quad (\text{B-3})$$

The final expression for the second derivative is

$$\frac{\partial^2}{\partial x^2}Z_n(\alpha x) = \frac{\alpha^2}{4}(Z_{n-2}(\alpha x) - (2Z_n(\alpha x) + Z_{n+2}(\alpha x)))$$

$$Z = J, Y, K, H^{(1)}, H^{(2)} \quad (\text{B-4})$$

1. V. S. Arpaci, *Conduction Heat Transfer*, Addison-Wesley Publishing Company, Reading, MA, p. 139, equation (3-139).

APPENDIX C

OUTPUT QUANTITY EQUATIONS

The equations necessary to compute the quantities chosen for the simulations are listed in this appendix. The system matrices, equations (85) and (150), are inverted for one excitation at a time (i.e., P_o , P_x , or P_θ). The fluid displacement potential constant D is used with equations (67) and (71) to compute the magnitude of the pressure field in the inner fluid as

$$\frac{P_i(r_1)}{P_o} = \omega^2 \rho_i D J_n(g_1 r_1) \quad (C-1)$$

and

$$\frac{P_i(r_1)}{P_o} = \omega^2 \rho_i G I_n(g_1 r_1) . \quad (C-2)$$

The circumferential, longitudinal, and time dependence term $\cos(n\theta) e^{i(kx - \omega t)}$ has been dropped from the equations given here. The values calculated are at a maximum amplitude; therefore $\cos(n\theta) e^{i(kx - \omega t)}$ is equal to 1.

The following equations are used to compute displacements, stresses, and strains in cylinder 2 of the two-layer cylinder. If the cylinder of interest was the first-layer (rather than the second layer shown here), coefficients $A_1^{C1}, A_2^{C1}, B_1^{C1}, B_2^{C1}, C_1^{C1}$ and C_2^{C1} would be substituted for $A_1^{C2}, A_2^{C2}, B_1^{C2}, B_2^{C2}, C_1^{C2}$ and C_2^{C2} in the equations. Quantities from the single-layer model are obtained by using coefficients $A_1^{C1}, A_2^{C1}, B_1^{C1}, B_2^{C1}, C_1^{C1}$ and C_2^{C1} resulting from system matrix (85).

The magnitude of the radial displacement of a particle of cylinder material is given by equation (C-3) as

$$\frac{u_c^{C2}(r_1)}{P_o} = \left(A_1^{C2} \frac{\partial}{\partial r} J_n(p_2 r_1) + A_2^{C2} \frac{\partial}{\partial r} Y_n(p_2 r_1) + B_1^{C2} \frac{n}{c} J_n(q_2 r_1) + B_2^{C2} \frac{n}{c} Y_n(q_2 r_1) + \right. \\ \left. C_1^{C2} i k J_{n+1}(q_2 r_1) + C_2^{C2} i k Y_{n+1}(q_2 r_1) \right). \quad (C-3)$$

The magnitude of the longitudinal displacement of a particle of cylinder material is given by

$$\frac{w_c^{C2}(r_1)}{P_o} = A_1^{C2} (i k J_n(p_2 r_1)) + A_2^{C2} (i k Y_n(p_2 r_1)) + \\ C_1^{C2} \left(-\frac{\partial}{\partial r} J_{n+1}(q_2 r_1) - \left(\frac{n+1}{r} \right) J_{n+1}(q_2 r_1) \right) + \\ C_2^{C2} \left(-\frac{\partial}{\partial r} Y_{n+1}(q_2 r_1) - \left(\frac{n+1}{r} \right) Y_{n+1}(q_2 r_1) \right). \quad (C-4)$$

The radial stress in the cylinder is given by

$$\frac{\tau_{rr}^{C2}(r_1)}{P_o} = \left(A_1^{C2} \left[(\lambda_2 + 2\mu_2) \frac{\partial^2}{\partial r^2} J_n(p_2 r_1) + \frac{\lambda_2}{r_1} \frac{\partial}{\partial r} J_n(p_2 r_1) - \lambda_2 J_n(p_2 r_1) \left(\frac{n^2}{r_1^2} + k^2 \right) \right] + \right. \\ A_2^{C2} \left[(\lambda_2 + 2\mu_2) \frac{\partial^2}{\partial r^2} Y_n(p_2 r_1) + \frac{\lambda_2}{r_1} \frac{\partial}{\partial r} Y_n(p_2 r_1) - \lambda_2 Y_n(p_2 r_1) \left(\frac{n^2}{r_1^2} + k^2 \right) \right] - \\ B_1^{C2} \left[\frac{2\mu_2 n}{r_1^2} \left(J_n(q_2 r_1) - r_1 \frac{\partial}{\partial r} J_n(q_2 r_1) \right) \right] - B_2^{C2} \left[\frac{2\mu_2 n}{r_1^2} \left(Y_n(q_2 r_1) - r_1 \frac{\partial}{\partial r} Y_n(q_2 r_1) \right) \right] + \\ \left. C_1^{C2} 2\mu_2 i k \frac{\partial}{\partial r} J_{n+1}(q_2 r_1) + C_2^{C2} 2\mu_2 i k \frac{\partial}{\partial r} Y_{n+1}(q_2 r_1) \right). \quad (C-5)$$

The magnitude of the circumferential strain in the cylinder is given by

$$\begin{aligned} \frac{\epsilon_{\theta\theta}^{C2}(r_1)}{P_o} = & A_1^{C2} \left(\frac{1}{r_1} \frac{\partial}{\partial r} J_n(p_2 r_1) - \frac{n^2}{r_1^2} J_n(p_2 r_1) \right) + A_2^{C2} \left(\frac{1}{r_1} \frac{\partial}{\partial r} Y_n(p_2 r_1) - \frac{n^2}{r_1^2} Y_n(p_2 r_1) \right) + \\ & B_1^{C2} \left(\left(-\frac{n}{r_1} \right) \frac{\partial}{\partial r} J_n(q_2 r_1) + \frac{n}{r_1^2} J_n(q_2 r_1) \right) + B_2^{C2} \left(\left(-\frac{n}{r_1} \right) \frac{\partial}{\partial r} Y_n(q_2 r_1) + \frac{n}{r_1^2} Y_n(q_2 r_1) \right) + \\ & C_1^{C2} \left(\frac{ik(n+1)}{r_1} J_{n+1}(q_2 r_1) \right) + C_2^{C2} \left(\frac{ik(n+1)}{r_1} Y_{n+1}(q_2 r_1) \right). \end{aligned} \quad (C-6)$$

Equations (C-1) through (C-6) have been normalized by P_o . If a different excitation was chosen (i.e., P_x or P_θ), the coefficients $A_1^{C1}, A_2^{C1}, B_1^{C1}, B_2^{C1}, C_1^{C1}$ and C_2^{C1} or $A_1^{C2}, A_2^{C2}, B_1^{C2}, B_2^{C2}, C_1^{C2}$ and C_2^{C2} resulting from the system matrix inversion would be different, and the appropriate excitation would be substituted for P_o in equations (C-1) through (C-6).

APPENDIX D

TWO-LAYER MODEL VERIFICATION

In this section, a verification of the two-layer elasticity model relative to the single-layer model is undertaken. The objective is to produce the same result for both models. First, let us consider the single-layer cylinder and fluids, whose material properties and dimensions are given in tables 2, 4, and 5 of the main text. The evaluation then amounts to the use of the two-layer model to analyze a cylinder that is physically identical to the single-layer cylinder. In reality, the two-layer cylinder is homogeneous; however, it is treated mathematically as a two-layer composite. The material properties and dimensions of the two-layer cylinder used for the comparison are listed in table D-1. The inner and outer fluids (tables D-2 and D-3) have properties consistent with those of tables 4 and 5.

Table D-1. Two-Layer-Cylinder Properties—3.00-in. Diameter for Model Comparison

Cylinder #1 Property	Cylinder #2 Property	Definition
$E_1 = 1.0 \times 10^8 \frac{\text{N}}{\text{m}^2}$	$E_1 = 1.0 \times 10^8 \frac{\text{N}}{\text{m}^2}$	Young's Modulus
$\zeta_1 = 0.3$	$\zeta_1 = 0.3$	Structural Loss Factor
$\rho_1 = 1070 \frac{\text{kg}}{\text{m}^3}$	$\rho_1 = 1070 \frac{\text{kg}}{\text{m}^3}$	Density
$\nu_1 = 0.4$	$\nu_1 = 0.4$	Poisson's Ratio
$a = 1.200 \text{ in.}$	$b = 1.350 \text{ in.}$	Inner Radius
$b = 1.350 \text{ in.}$	$c = 1.500 \text{ in.}$	Outer Radius
$h_1 = 0.15 \text{ in.}$	$h_2 = 0.15 \text{ in.}$	Thickness

Table D-2. Two-Layer-Cylinder Outer Fluid Properties (Water) for Model Comparison

Property	Definition
$\rho_s = 1000.0 \frac{\text{kg}}{\text{m}^3}$	Density
$c_s = 1500.0 \frac{\text{m}}{\text{sec}}$	Speed of Sound

Table D-3. Two-Layer-Cylinder Inner Fluid Properties (Water) for Model Comparison

Property	Definition
$\rho_i = 1000.0 \frac{\text{kg}}{\text{m}^3}$	Density
$c_i = 1500.0 \frac{\text{m}}{\text{sec}}$	Speed of Sound

Simulations are performed for the single- and two-layer models with a normal pressure excitation ($n = 0$). Figure D-1 is the simulation for the two-layer model and figure D-2 is the simulation for the single-layer model. In figure D-3, a comparison of the two models is made at $k = 0$ rad/m. The curves in this figure overlay each other, which indicates agreement between the solutions. Figure D-1 is subtracted from figure D-2 and the result is displayed in figure D-4, where the superscripts $M2$ and $M1$ correspond to the two-layer and single-layer models, respectively. The agreement between solutions is less than 0.05 dB everywhere on the surface, except at very low frequencies and very high wavenumbers. These results confirm the validity of the two-layer cylinder model relative to the single-layer cylinder model. Figure D-1 is also used on the cover of this report.

Figures D-5 through D-8 compare the two models (as previously described) for circumferential order number $n = 1$, and figures D-9 through D-12 compare the two models for circumferential order number $n = 2$. In both cases, the agreement between the models is extremely close; no measurable difference results until the low-frequency/high-wavenumber region is reached.

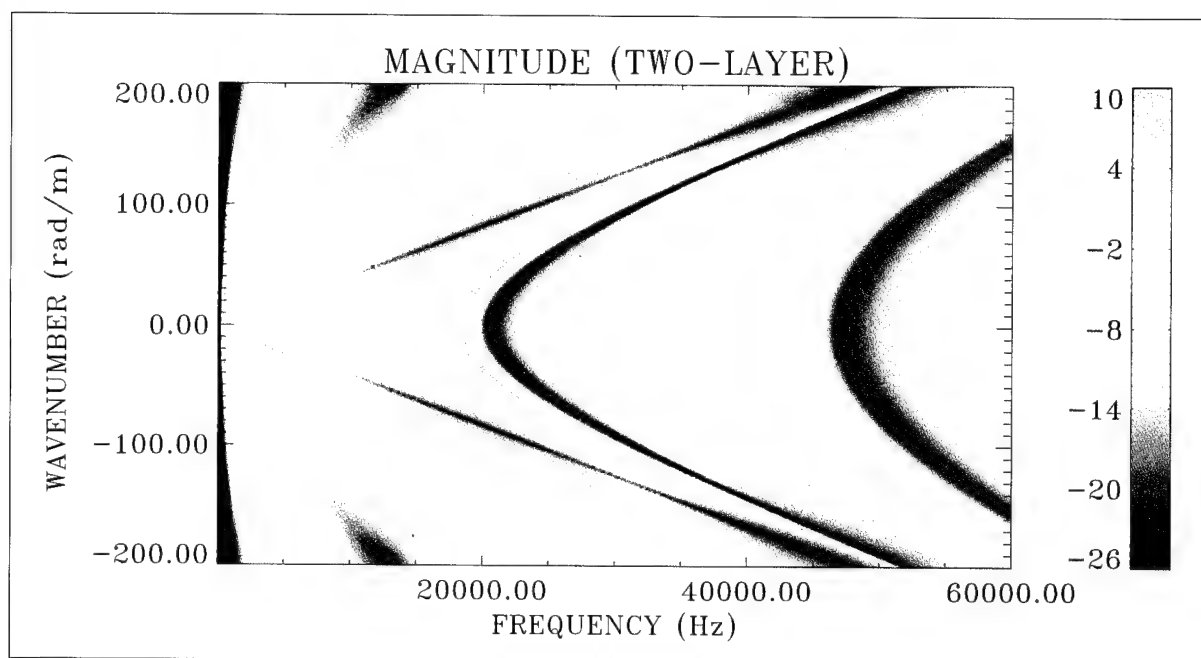


Figure D-1. Pressure Transfer Surface With Magnitude = $10\text{Log}(P_i(r_1)/P_o)^2$ at $r_1 = 1.1$ in. for Elasticity Model, Where $n = 0$ and Diameter = 3.00 in. (Two-Layer Cylinder)

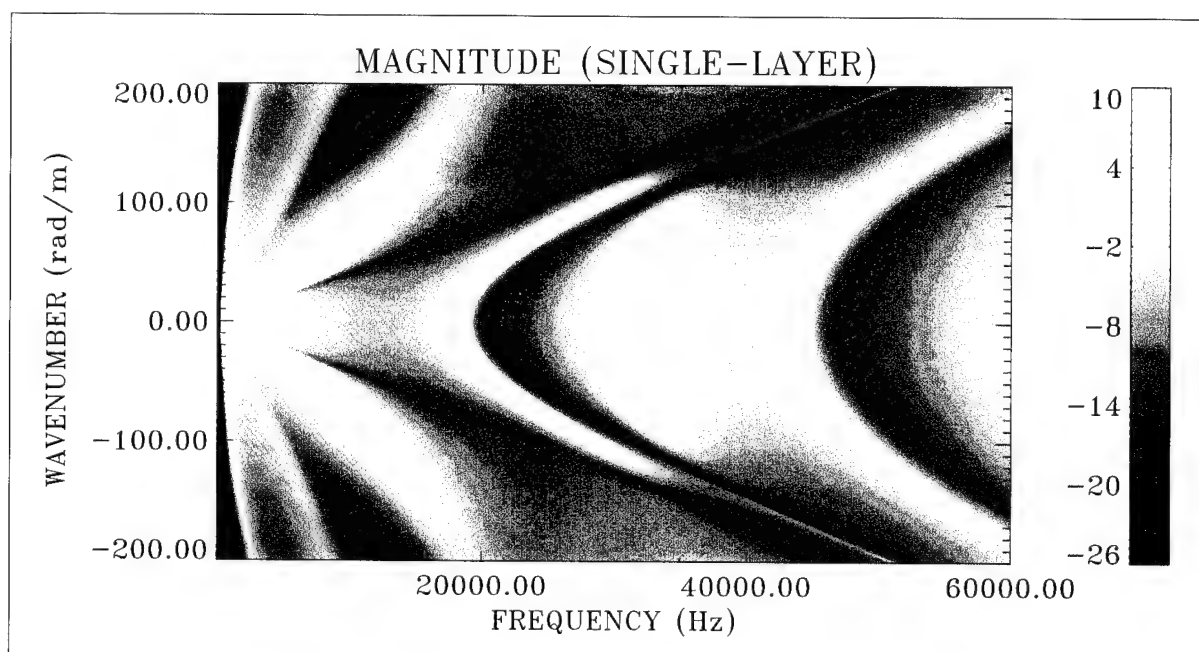


Figure D-2. Pressure Transfer Surface With Magnitude = $10\text{Log}(P_i(r_1)/P_o)^2$ at $r_1 = 1.1$ in. for Elasticity Model, Where $n = 0$ and Diameter = 3.00 in. (Single-Layer Cylinder)

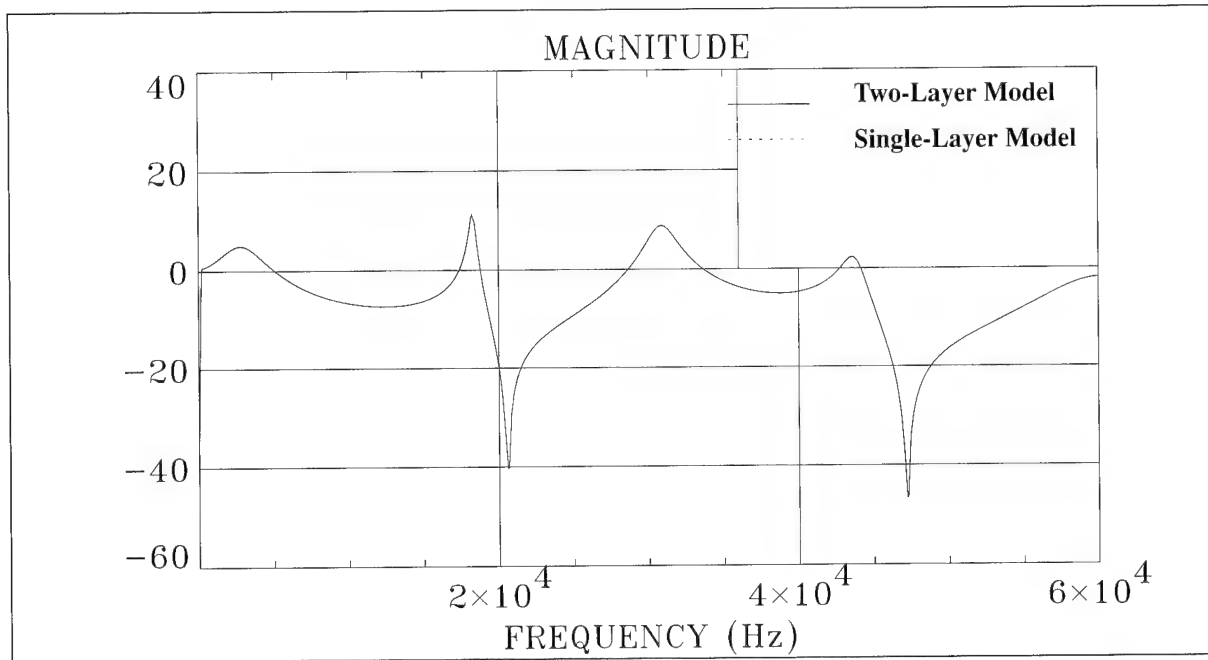


Figure D-3. Comparison of Two-Layer and Single-Layer Elasticity Models With Magnitude = $(10\text{Log}(P_i(r_1)/P_o)^2)$ at $r_1 = 1.1$ in., Where $n = 0$ and Diameter = 3.00 in.

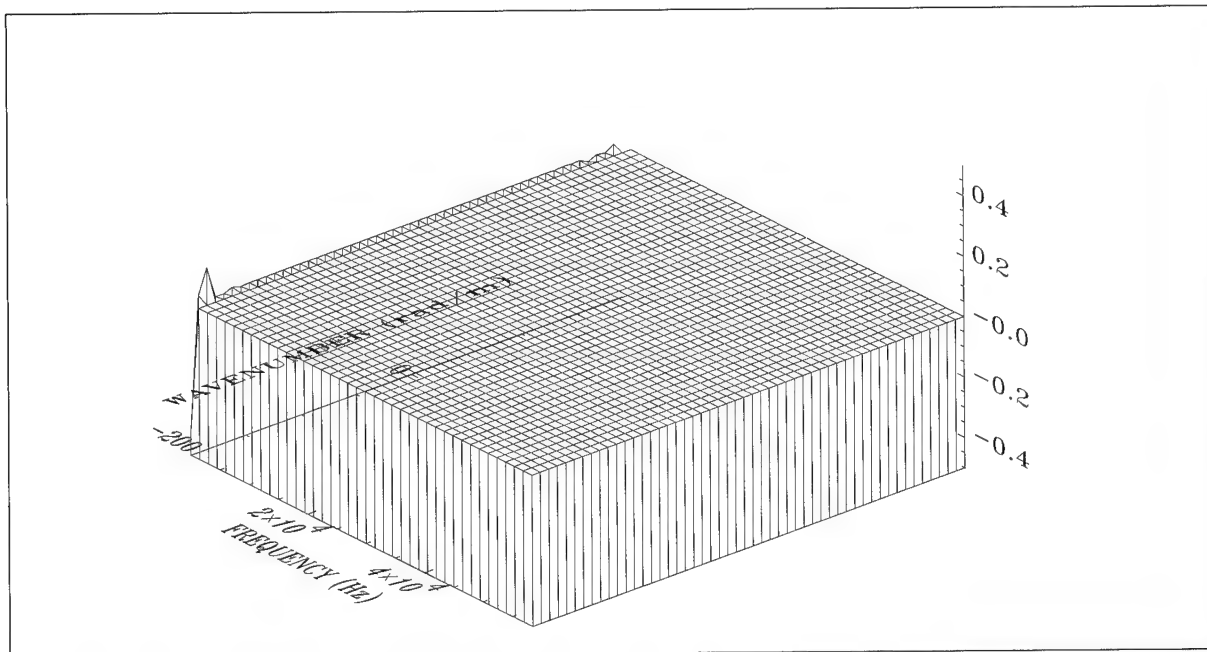


Figure D-4. Relative Difference Between Two-Layer and Single-Layer Surfaces With Magnitude = $(10\text{Log}(P_i^{M2}(r_1)/P_o)^2 - 10\text{Log}(P_i^{M1}(r_1)/P_o)^2)$ at $r_1 = 1.1$ in. for Elasticity Model, Where $n = 0$ and Diameter = 3.00 in.

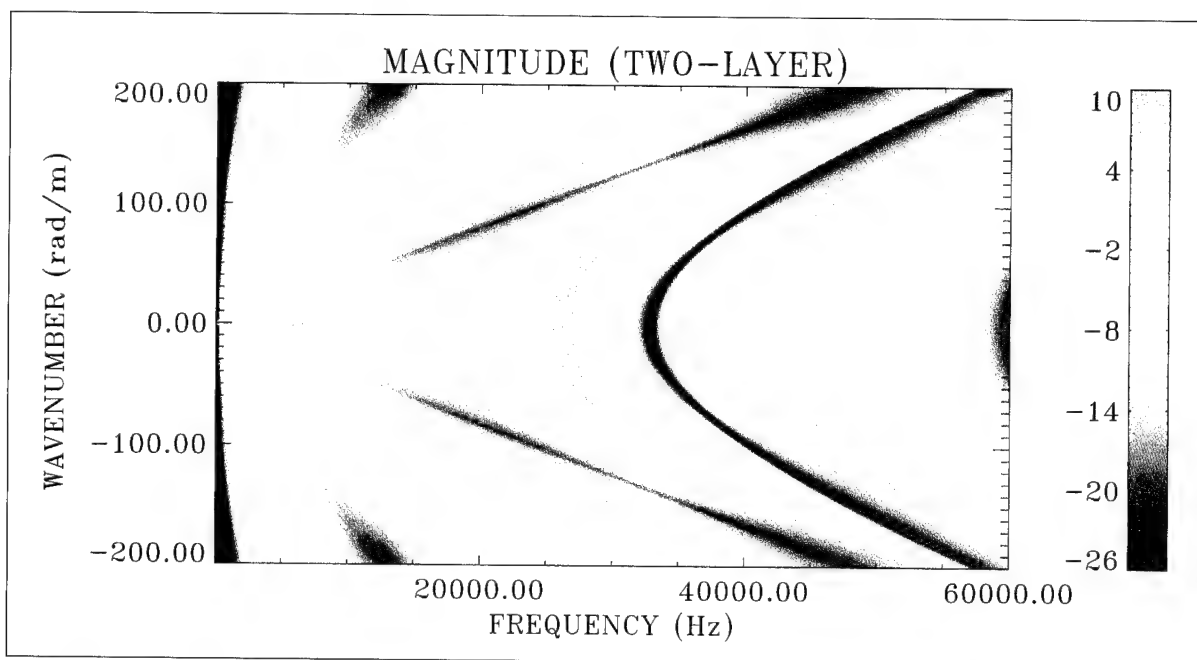


Figure D-5. Pressure Transfer Surface With Magnitude = $10\text{Log}(P_i(r_1)/P_o)^2$ at $r_1 = 1.1$ in. for Elasticity Model, Where $n = 1$ and Diameter = 3.00 in. (Two-Layer Cylinder)

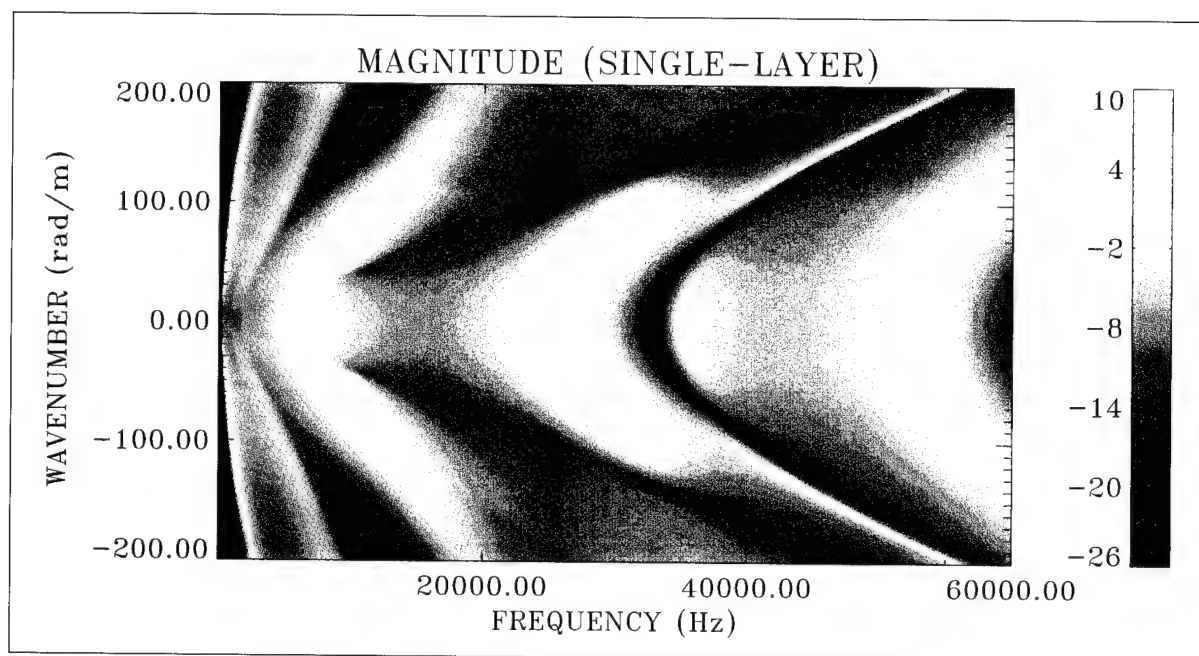


Figure D-6. Pressure Transfer Surface With Magnitude = $10\text{Log}(P_i(r_1)/P_o)^2$ at $r_1 = 1.1$ in. for Elasticity Model, Where $n = 1$ and Diameter = 3.00 in. (Single-Layer Cylinder)

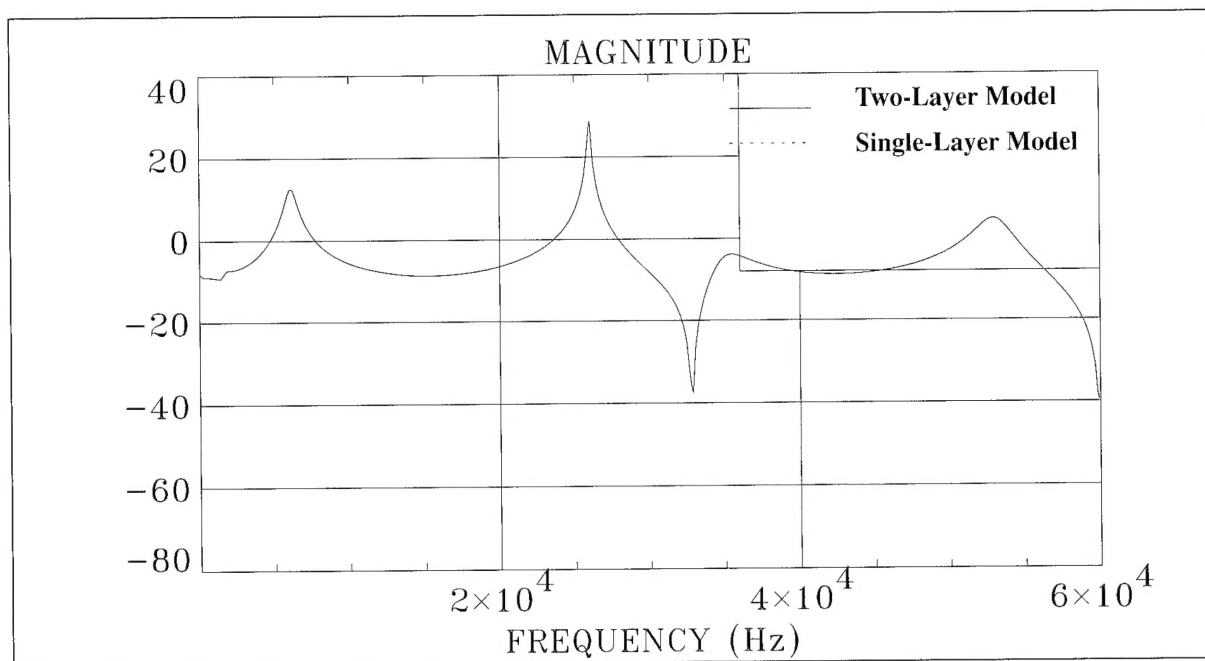


Figure D-7. Comparison of Two-Layer and Single-Layer Elasticity Models With Magnitude = $(10\text{Log}(P_i(r_1)/P_o))^2$ at $r_1 = 1.1$ in., Where $n = 1$ and Diameter = 3.00 in.

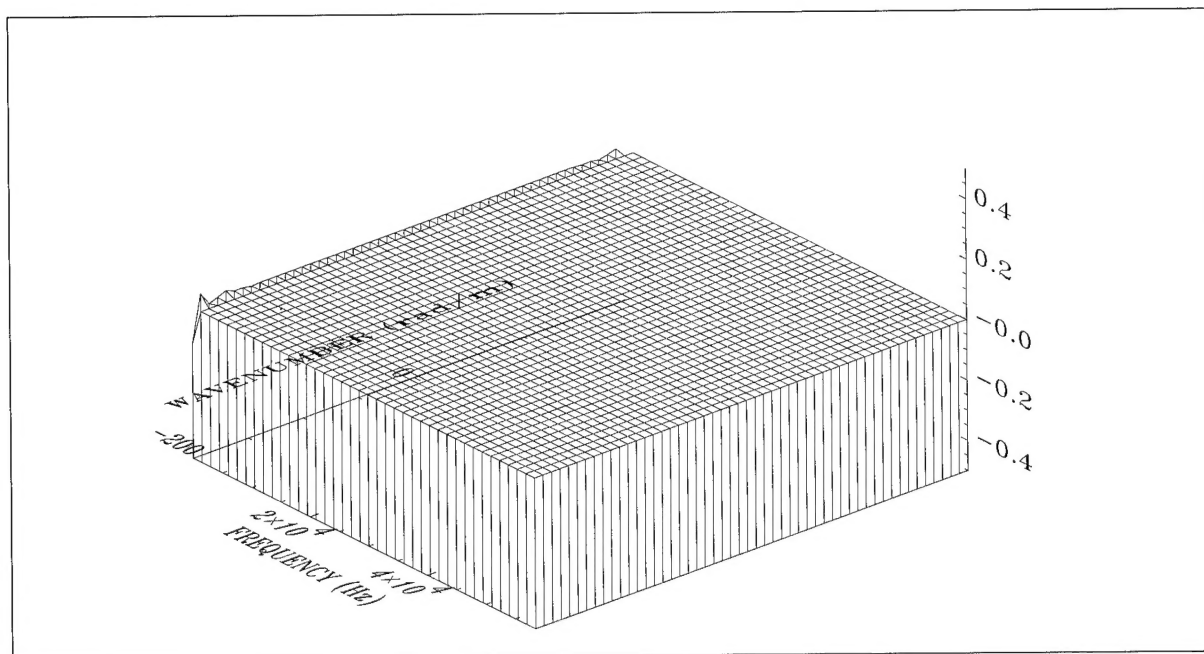


Figure D-8. Relative Difference Between Two-Layer and Single-Layer Surfaces With Magnitude = $(10\text{Log}(P_i^{M2}(r_1)/P_o)^2 - 10\text{Log}(P_i^{M1}(r_1)/P_o)^2)$ at $r_1 = 1.1$ in. for Elasticity Model, Where $n = 1$ and Diameter = 3.00 in.

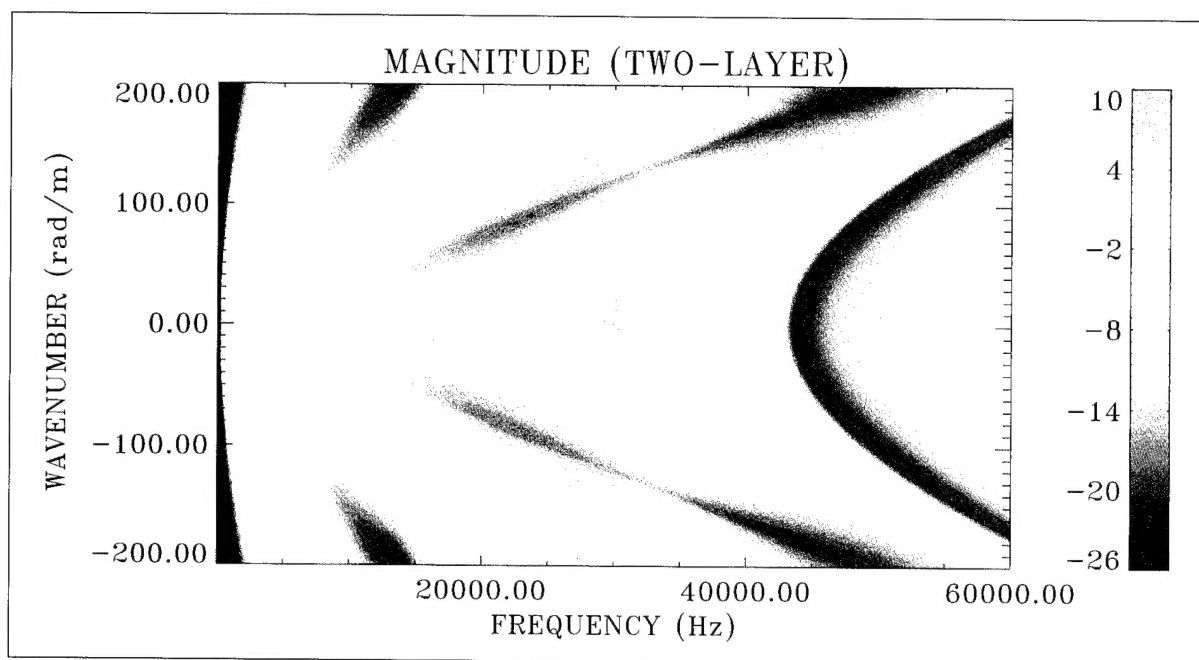


Figure D-9. Pressure Transfer Surface With Magnitude = $10\text{Log}(P_i(r_1)/P_o)^2$ at $r_1 = 1.1$ in. for Elasticity Model, Where $n = 2$ and Diameter = 3.00 in. (Two-Layer Cylinder)

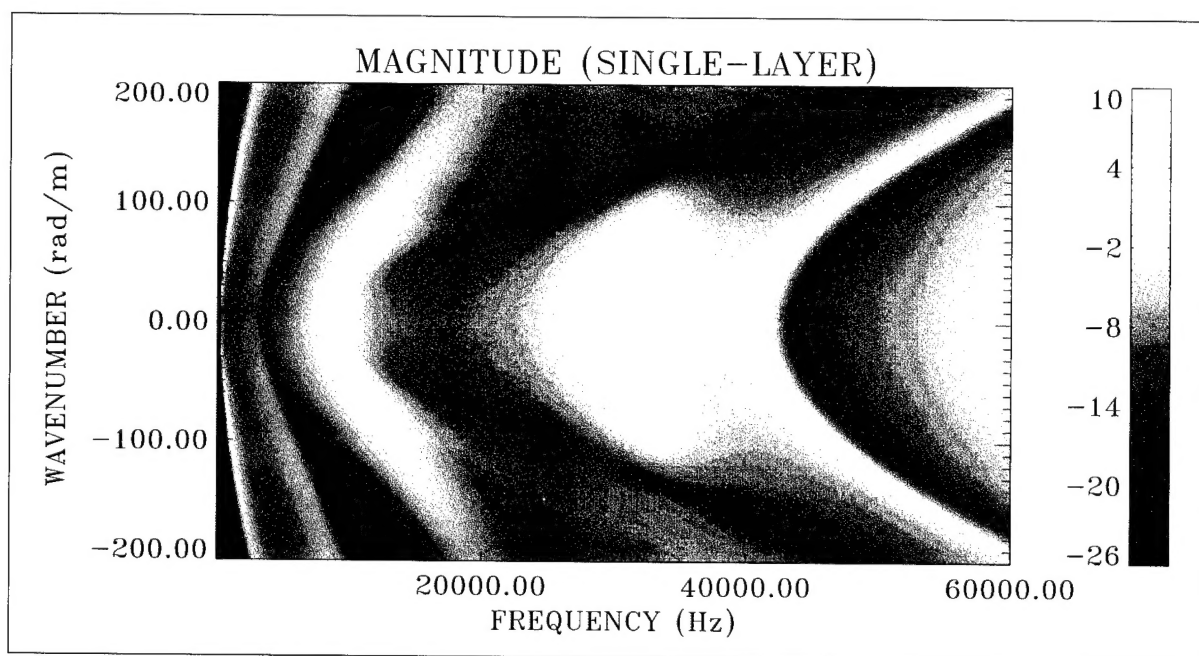


Figure D-10. Pressure Transfer Surface With Magnitude = $10\text{Log}(P_i(r_1)/P_o)^2$ at $r_1 = 1.1$ in. for Elasticity Model, Where $n = 2$ and Diameter = 3.00 in. (Single-Layer Cylinder)

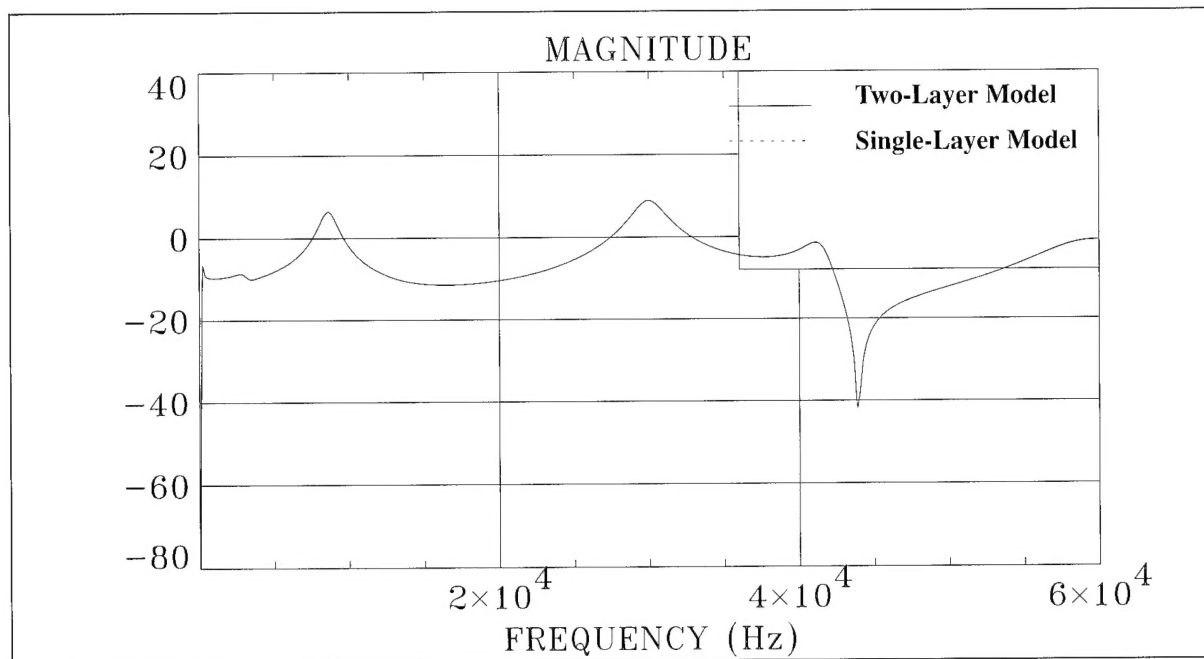


Figure D-11. Comparison of Two-Layer and Single-Layer Elasticity Models With Magnitude = $(10\text{Log}(P_i(r_1)/P_o))^2$ at $r_1 = 1.1$ in., Where $n = 2$ and Diameter = 3.00 in.

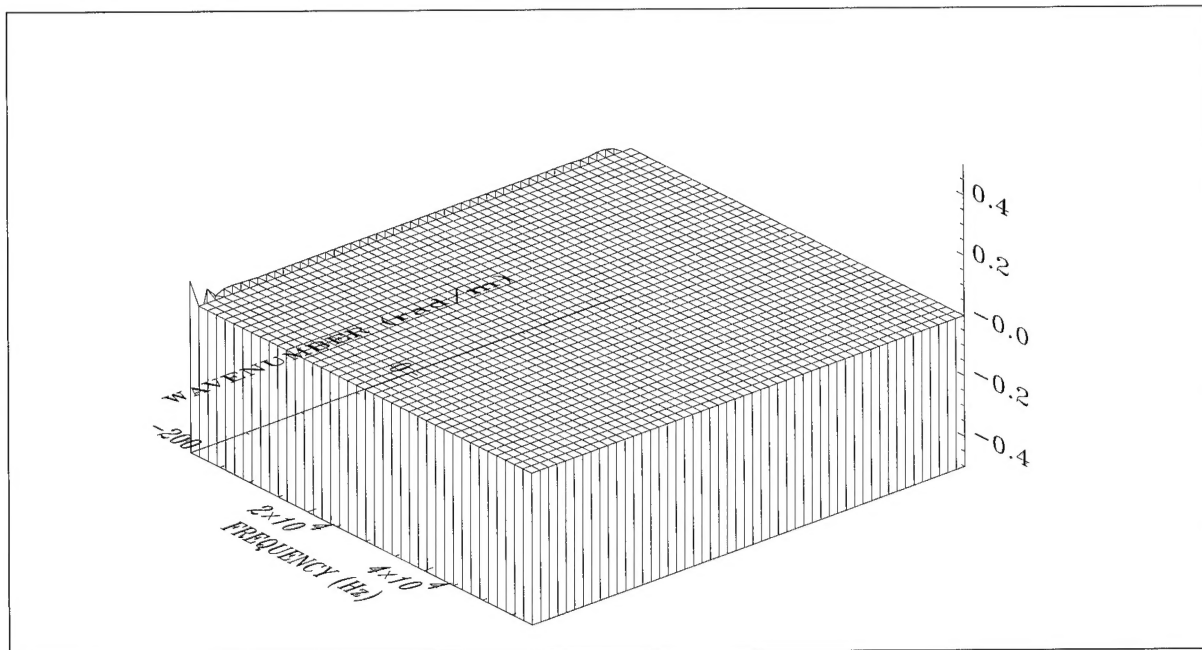


Figure D-12. Relative Difference Between Two-Layer and Single-Layer Surfaces With Magnitude = $(10\text{Log}(P_i^{M2}(r_1)/P_o))^2 - 10\text{Log}(P_i^{M1}(r_1)/P_o))^2$ at $r_1 = 1.1$ in. for Elasticity Model, Where $n = 2$ and Diameter = 3.00 in.

INITIAL DISTRIBUTION LIST

Addressee	No. of Copies
Defense Technical Information Center	12
Office of Naval Research (Code 321SS: K. Dial, S. Littlefield, R. Varley)	6
Naval Research Laboratory (A. Dandridge, S. Vohra)	2
Cambridge Acoustical Associates (J. Garrelick, J. Cole III)	2
Applied Measurement Systems, Inc., New London (J. Diggs, R. Hauptmann)	2
Michigan State University (C. R. MacCluer, C. J. Radcliffe)	2